ABSTRACT

Title of Dissertation: ASSESSING OCEAN SALINITY AS NATURE'S RAIN GAUGE

James Richard Reagan, Doctor of Philosophy, 2025

Dissertation Directed By: Professor James Carton
Research Scientist Semyon Grodsky
Assistant Professor Jacob Wenegrat
Assistant Professor Madeleine Youngs
NOAA Retiree Dr. Dan Seidov
Professor Michael Evans – Dean's Representative

Changes in the hydrological cycle can have profound impacts on society, from more frequent and severe droughts to extreme flooding. However, monitoring changes in the hydrological cycle is difficult from current observing platforms (namely satellites), and even more difficult to identify secular changes in the often-noisy data. Near-surface ocean salinity patterns mirror the distribution of evaporation and precipitation over the ocean: regions dominated by evaporation are saltier, while regions dominated by precipitation are fresher. Recently, ocean salinity has gained attention as a proxy for tracking global hydrological changes. Altering salinity in the ocean through changes in the hydrological cycle can impact global ocean circulation, which could have major downstream impacts on global climate.

Thus, this research focuses on the relationship between changing ocean salinity and the global hydrological cycle. The first chapter provides details on what ocean salinity is, why it is important, how it is measured, and what research gaps are addressed in this dissertation. The second chapter focuses on validating satellite-based surface salinity measurements with in situ observations to ensure that the global signals identified by satellites are reliable. The third

chapter examines how surface salinity relates to evaporation and precipitation in the dynamic and climatically important North Atlantic. The fourth chapter leverages a vigorous methodology designed to minimize sampling biases and properly preserve and propagate uncertainties to estimate robust salinity pattern amplifications (salty gets saltier, fresh gets fresher) over short (< 20 years) and long (> 60 years) time periods. We find salinity patterns have amplified at a rate of 4.89% per 50 years over the 1957/61 – 2019/23 pentadal record. Furthermore, we identify a 30–40-year period for when secular changes are identifiable (e.g., salty areas become saltier and fresh areas become fresher), and we detect and quantify an acceleration in the salinity pattern amplifications which may be indicative of an acceleration in the amplification of the hydrological cycle.

Finally, the fifth chapter addresses the future work we believe is critical to further our understanding of Earth's climate through the lens of ocean salinity. One of the most important questions that has evolved from this dissertation is how will salinity impact the Atlantic Meridional Overturning Circulation (AMOC) in a warming climate. We identified changes in observed salinity that may help maintain/enhance the AMOC; however, it is unclear if increased meltwater and hydrologic amplifications will counter those changes. Thus, to address this question we must leverage both numerical simulations and observations. Since these changes are happening on multi-decadal time scales, it is critical that we continue to collect near-global ocean salinity measurements for the foreseeable future.

ASSESSING OCEAN SALINITY AS NATURE'S RAIN GAUGE

by

James Richard Reagan

Dissertation submitted to the Faculty of the Graduate School of the
University of Maryland, College Park, in partial fulfillment
of the requirements for the degree of
Doctor of Philosophy
2025

Advisory Committee:
  Professor James Carton, Chair
  Research Scientist Semyon Grodsky
  Assistant Professor Jacob Wenegrat
  Assistant Professor Madeleine Youngs
  NOAA Retiree Dr. Dan Seidov
  Professor Michael Evans – Dean's Representative

Dedication

In loving memory of my mother, your love, strength, and wisdom will forever guide me.

Acknowledgements

The completion of this dissertation would not be possible without the help and guidance from many individuals. First and foremost, I would like to thank my wife, Jennifer, for the endless sacrifices she made so I could complete my dissertation. You truly are amazing. I want to acknowledge my children, Sophia and Michael, for their patience and understanding during this academic and professional journey. I hope my journey showed you the importance of never giving up on a dream. To my friends and family, thank you. You all were there for me when I needed you the most.

I want to acknowledge all of my Ocean Climate Laboratory colleagues at the National Centers for Environmental Information, both past and present! I truly love the work we do and I could never thank you all enough for the wisdom and support you have shown to me. I am not where I am today without your guidance.

I also want to say thank you to my advisor, Dr. Jim Carton. You showed me a great amount of patience, and never gave up on me. To the advisory committee, thank you for the constructive discussions and for helping to shape and improve my dissertation and research.

Table of Contents

List of Tables

List of Figures

Appendix Figures

List of Abbreviations

AMJ	April, May, June
AMO	Atlantic Multidecadal Oscillation
AMOC	Atlantic Meridional Overturning Circulation
APB	Autonomous Pinniped Bathythermograph
APDRC	Asia-Pacific Data Research Center
AQ	Aquarius
AQ251	Aquarius version 2.5.1
AQCAP	Aquarius Combined Active-Passive
AQCAP251	Aquarius Combined Active-Passive version 2.5.1
AR(1)	Autoregressive model order 1
BIC	Bayesian Information Criterion
CAP	Combined Active-Passive
CATDS	Centre Aval de Traitement des Données
CEC	Centre d'Expertise Scientifique
CGD	Climate and Global Dynamics
CI	Confidence interval
CONAE	Comisión Nacional de Actividades Espaciales
CORE	Coordinated Ocean-ice Reference Experiments
CTD	Conductivity, Temperature, Depth
DCMF	Divergent component of moisture fluxes
DMI	Dipole Mode Index
DRB	Drifting Buoy
ECMWF	European Centre for Medium-Range Weather Forecasts
ERA5	ECMWF Reanalysis version 5
ERA-I	ECMWF Reanalysis-Interim
ESA	European Space Agency
GCOS	Global Climate Observing System
GLD	Glider
GOOS	Global Ocean Observing System
GPCP	Global Precipitation Climatology Project
HMS	Her Majesty's Ship
IOBM	Indian Ocean Basin Mode
IOC	Intergovernmental Oceanographic Commission
ITCZ	Intertropical Convergence Zone
JAS	July, August, September
JFM	January, February, March
JPL	Jet Propulsion Laboratory
LOCEAN	Laboratoire d’Océanographie et du Climat: Expérimentations et Approches Numériques
MERRA-2	Modern-Era Retrospective Analysis for Research and Applications - version 2
MK	Mann-Kendall
MLR	Multiple Linear Regression
MLS	Mixed Layer Salinity
MMK	Modified Mann-Kendall
MRB	Moored Buoy

NA	North Atlantic
NADW	North Atlantic Deep Water
NAO	North Atlantic Oscillation
NASA	National Aeronautics and Space Administration
NCAR	National Center for Atmospheric Research
NCEP	National Centers for Environmental Prediction
NOAA	National Oceanic and Atmospheric Administration
NPGO	North Pacific Gyre Oscillation
NSS	Near-surface salinity
NSSB	Near-surface salinity budget
NW	Northwest
OAFlux	Objectively Analyzed air-sea Fluxes Project
OND	October, November, December
OSD	Ocean Station Data
PC	Principal Component
PCA	Principal Component Analysis
PDO	Pacific Decadal Oscillation
PFL	Profiling float
PIRATA	Prediction and Research Moored Array in the Atlantic
PMEL	Pacific Marine Environmental Laboratory
PNA	Pacific-North America index
PODAAC	Physical Oceanography Distributed Active Archive Center
PSS-78	Practical Salinity Scale 1978
RAMA	Research Moored Array for African-Asian-Australian Monsoon Analysis and Prediction
RFI	Radio frequency interference
RMSE	Root-mean-square-error
RSS	Remote Sensing Systems
SA	Absolute Salinity
SAC-D	Satélite de Aplicaciones Científicas
SAM	Southern Annular Mode
SE	Standard Error
SMAP	Soil Moisture Active Passive
SMOS	Soil Moisture and Ocean Salinity
SOI	Southern Oscillation Index
SPCZ	South Pacific Convergence Zone
SPG	Subpolar Gyre
SPNA	Subpolar North Atlantic
SSS	Sea surface salinity
SST	Sea surface temperature
STG	Subtropical Gyre
STNA	Subtropical North Atlantic
TAO	Tropical Atmosphere Ocean
TEOS-10	Thermodynamic Equation of Seawater – 2010
TRITON	Triangle Trans-Ocean Buoy Network
UOR	Undulating Oceanographic Recorder

US	United States
VIMFD	Vertically integrated moisture flux divergence
WHOI	Woods Hole Oceanographic Institution
WOA	World Ocean Atlas
WOCE	World Ocean Circulation Experiment
WOD	World Ocean Database

Chapter 1: Introduction

The focus of this dissertation is upper ocean salinity: how to measure it, why it varies, and what those variations reveal about the earth's hydrologic cycle.

1.1 Ocean salinity

99% of the salts in the ocean by mass consist of chloride, sodium, sulfate, magnesium, calcium, and potassium ions (Knauss, 1997). The major source of these is the chemical weathering of rocks while the major sink is salt deposits left behind by tectonic processes. Since the timescale of these processes are 10^7yr while the overturning timescale of the ocean is 10^3yr the ratio of ions is nearly uniform and the concentrations only vary with salinity (Hay et al., 2006). The exception to this rule is calcium which is used in plankton shell formation. Currently, there is, on average, 34.9 grams of salt for every 1 kilogram of seawater which contributes to a slight increase in the average density of seawater of 1,025 kg/m^3 over pure water.

1.1.1 Importance of ocean salinity

The ocean covers roughly 71% of Earth's surface, with the remaining 29% covered by land. It has been estimated that roughly 85% of total evaporation (liquid volume rate of ~$13\text{x}10^6$ m^3/s of freshwater removed) and 77% of total precipitation (~$12\text{x}10^6$ m^3/s of freshwater deposited) on Earth occurs over the ocean, with the remaining ~$1\text{x}10^6$ m^3/s returning to the ocean indirectly in the form of continental discharge (Durack, 2015; Schanze et al., 2010; Schmitt, 1995). By tracking these freshwater exchanges, we are able to monitor ~80% of the total water exchange between the atmosphere and the earth's surface (Durack, 2015).

Figure 1.1 illustrates the long-term pattern of evaporation minus precipitation (E-P) over the global ocean. Where there is net evaporation, freshwater is being removed from the ocean, and where there is net precipitation freshwater is being added to the ocean. While long-term patterns of E-P can be easily established, direct tracking of changes in freshwater fluxes over the ocean, which are small compared to the long-term means, remain clouded in uncertainty (Hegerl et al., 2015; Robertson et al., 2014). However, the adding and removing of freshwater alters the salinity and therefore ocean surface salinity patterns are highly correlated with evaporation and precipitation. This relationship has been known for nearly 100 years (Wüst, 1936). Figure 1.2 shows the long-term mean of surface salinity. High regions of salinity are in regions of high evaporation/low precipitation and low regions of salinity are in regions of high precipitation/low evaporation. This relationship between evaporation/precipitation and salinity allows for salinity to be used as a natural "rain gauge." However, it should be noted that there are only a few regions of the ocean where salinity is predominately a function of E-P (Yu, 2011).

Recent studies have found that changes in salinity are related to changes in the hydrological cycle (Cheng et al., 2020; Douville et al., 2024; Durack et al., 2012; Hosoda et al., 2009; Skliris et al., 2014). Many of these studies find that salty (dry) regions are becoming saltier (drier) and fresh (wet) regions are becoming fresher (wetter) which is directly related to an amplifying hydrological cycle in a warming world. An amplified hydrological cycle can lead to more severe droughts, more intense rainfall and floods, and difficulties with managing water resources (Ficklin et al., 2022; Polade et al., 2014; Polson et al., 2013; Wainwright et al., 2021; Zhang et al., 2007).

Salinity also plays a critical role in the general circulation of the ocean. While winds primarily drive ocean surface currents, the ocean's density structure is responsible for the deep ocean circulation. Seawater density is a function of both temperature and salinity, and thus the density driven circulation of the ocean is often referred to as the thermohaline circulation (Knauss, 1997). For many years it has been known that deep water is produced in the North

Atlantic (NA) (Broecker, 1991; Wüst, 1936) and occurs in this region because it is one of few locations in the global ocean where surface water can become dense enough to sink to great depths (1-4km depth). As near-surface water moves poleward from the salty subtropics to the subpolar North Atlantic along the Gulf Stream and North Atlantic Current, it loses its heat to the atmosphere, but mostly maintains its salty signature. As the water becomes colder and colder, it eventually becomes dense enough to sink to deep depths and becomes North Atlantic Deep Water (NADW) that flows equatorward at depth. This circulation is known as the Atlantic Meridional Ocean Circulation (AMOC).

The AMOC is responsible for redistributing heat from the tropics to the higher latitudes. At 26.5°N, it transports 1.3 petawatts of heat poleward (Johns et al., 2011). A disruption to the AMOC can cause significant impacts to the global climate. A simple box model experiment performed by Henry Stommel showed that changes in density brought upon through changes in temperature or salinity can result in abrupt shifts in overturning circulation (Stommel, 1961). More recently, hosing experiments in which freshwater is artificially added to the North Atlantic in deep water formation regions (symbolizing enhanced meltwater and/or precipitation), have been shown to create disruptions in the AMOC (Stouffer et al., 2007; Stouffer et al., 2006; Wei et al., 2024). However, these disruptions typically occur only after an excessive (and often times unrealistic) amount of freshwater is added. For example, the experiment employed by Stouffer et al. (2007) released 1Sv of freshwater into the North Atlantic every year for 100 years, which would raise sea level by 9 meters! Additionally, in some experiments (e.g., Haskins et al. 2020) the freshwater is added directly to the deep-water formation regions, which is not realistic since much of the freshwater, particularly in the Labrador Sea, comes in via boundary currents (Wei et al., 2024). Nonetheless, salinity changes can play a role in stabilizing/destabilizing the water column and thus impact the thermohaline circulation.

While this research focuses primarily on the importance of salinity from the perspective of it acting as a proxy for the global hydrological cycle, and its impact on density and stratification in the context of the overturning circulation; it is important to note that salinity, acting as a conservative tracer, is critical in tracking ocean water masses, is an important element in maintaining marine ecosystem health, is important in diagnosing mixed layers and barrier layers, and diagnosing global freshwater changes. For all these aforementioned reasons, salinity has been declared both an essential ocean and essential climate variable by the Global Ocean Observing System (GOOS) and the Global Climate Observing System (GCOS), respectively.

1.2 Measuring ocean salinity

Ocean salinity is measured through one of two ways: in situ or satellite.

1.2.1 *In situ* salinity observations

In situ is a Latin word that means "in place." Therefore, in situ ocean observations are observations that are made at a single point in time. For example, a research vessel out at sea that drops an instrument in the water and takes measurements would be an in situ observation. In situ salinity has been measured by two primary methods over the past ~150 years. The first method is through chemical titration, and this was the dominant method of measuring salinity from the late 19th century until the 1970's. This involved taking a water sample (often from a Nansen or Niskin bottle), and chemically titrating the sample for chlorinity with silver nitrate. This method would produce salinity values with an accuracy of +/- 0.02g/kg (Knauss, 1997). This method also assumed that the chemical composition of salts in seawater were constant throughout the global ocean, a reasonable assumption for the open ocean, but not in regions where the composition could be quite different (e.g., river outflows, marginal seas).

The second and more modern method for observing salinity is through measuring conductivity. The more salt ions in a sample of seawater, the higher its conductivity. The measured conductivity is then divided by the conductivity of a known standard solution of potassium chloride. This dimensionless ratio is then used in the practical salinity equation to compute the salinity value. The salinity value is dimensionless (unitless) and is on the Practical Salinity Scale 1978 (PSS-78) (Lewis, 1982). The accuracy of salinity measured through conductivity can range from +/-0.002 to +/-0.005 for Conductivity-Temperature-Depth (CTD) instruments out at sea to +/- 0.001 for samples drawn out of bottles and measured with salinometers in a lab. Salinometers are often used to help calibrate CTD sensors.

Just as the methods for observing salinity have evolved over time, so too have the units used to report it. When salinity measurements are mass-based—such as those derived from chemical titrations of bottle samples—the units are typically reported as parts per thousand (ppt) or grams of salt per kilogram of seawater (g/kg). This was especially common for bottle measurements prior to the adoption of the Practical Salinity Scale in 1978. As discussed previously, salinity derived from conductivity measurements is expressed using the PSS-78, which yields a dimensionless value. More recently, with the introduction of the Thermodynamic Equation of Seawater – 2010 (TEOS-10) (IOC et al., 2010), Absolute Salinity (SA) has been recommended for thermodynamic calculations, as it accounts for regional variations in seawater composition (Millero et al., 2008). The units of SA are grams of dissolved salts per kilogram of seawater (g/kg). In this research, most salinity data are reported as Practical Salinity (PSS-78). One exception may be salinity values from pre-1978 bottle samples, which were likely based on chlorinity titrations and thus reported in mass-based units (e.g., g/kg), making them not directly convertible to PSS-78 without additional information. However, in open-ocean conditions, particularly within the salinity range from 33 to 37, chlorinity-based values typically differ from PSS-78 by less than 0.01 units (Lewis et al., 1981), making them sufficiently comparable for use in large-scale and long-term analyses. Thus, because the analyses presented here focus primarily on open-ocean conditions, the use of pre-1978 bottle salinity measurements is considered appropriate.

1.2.1.1 Time evolution of in situ ocean salinity observations

Section 1.3.1 described the two major methods of determining ocean salinity: chemical titrations and conductivity. While these two methods dominate how in situ salinity is measured; the observing platforms for which these measurements are made has changed dramatically over the last 70 years. Unless otherwise noted, all in situ ocean profile data used in this research comes from the World Ocean Database (A. V. Mishonov et al., 2024).

The World Ocean Database is the largest quality-controlled, uniformly formatted, and freely accessible ocean profile database in the world. As of April 2025, it contained over 19.2 million ocean profiles with nearly ~11.5 million salinity profiles dating back to the HMS Challenger expedition in 1872. Figure 1.3 illustrates the temporal evolution of salinity profiles measured by various probe types from 1900-2024. From 1900 through the 1960's, mostly all salinity profiles were taken using bottles (OSD in Figure 1.3). In the early 1970's and through the 1980's, Conductivity, Temperature, and Depth (CTDs) were introduced and used in combination with bottle measurements; however, bottle measurements still outnumbered the number of CTD profiles during this time. From the 1990's to the year 2000, profiles from moored buoys (MRBs) and Undulating Oceanographic Recorders (UORs) were introduced, while bottle profiles began to decrease and CTDs became the dominant observing system.

As we entered the new millennium, the advent of autonomous instruments brought about a new revolution of ocean observations and monitoring. Drifting buoys (DRBs) and

Autonomous Pinniped Bathythermographs (APBs) have provided ocean data in previously unobserved ocean regions covered by ice. Gliders (GLD), while generally spatially limited, have provided unprecedented spatial and temporal data for coastal sections. Finally, profiling floats (PFL) from the Argo program have offered near-global coverage of ocean monitoring from 0-2000m depth (Roemmich et al., 2009).

Figure 1.4 shows the change in spatial coverage of ocean observations from the 1950's through the 2010's. As discussed previously, bottle and CTD data dominated salinity observations from the 1950's through the 1990's. Of note, is the hemispheric spatial inequities in data distribution with many more Northern Hemisphere salinity observations than Southern Hemisphere from the 1950's through the 1980's. The arrival of the World Ocean Circulation Experiment (WOCE) in the early 1990's helped improve the observation density and frequency in the Southern Hemisphere through single and repeat cruise transects during the 1990's (Woods, 1985). By the turn of the 21st century, the inclusion of autonomous instruments into the ocean observing system allowed for near-global coverage on seasonal time scales. There are very few regions that go unobserved during the 2000's and 2010's (Figs. 1.4f,g) due to the number of autonomous instruments, particularly through the Argo program, that are making ocean observations. However, it should be noted, while the density and spatial improvements of ocean observations have been noticeable the last two decades; it has coincided with the loss of high-quality bottle and CTD measurements. These shipboard measurements are critical to calibrating autonomous instruments, and acquiring biogeochemical properties of the ocean.

1.2.2 Satellite salinity observations

The Soil Moisture and Ocean Salinity (SMOS) satellite mission carried out by the European Satellite Agency (ESA) was the first satellite mission directed towards measuring global sea surface salinity from space. While the SMOS satellite launched in 2009, the idea of measuring surface salinity from space was discussed many years earlier (Lagerloef et al., 1995; Swift et al., 1983). Shortly after the SMOS mission launched in 2009, the Aquarius/Satélite de Aplicaciones Científicas (Aquarius/SAC-D) mission was launched in 2011. This mission was a joint mission between the National Aeronautics and Space Administration (NASA) and the Argentinean Space Agency (CONAE). Finally, the NASA Soil Moisture Active Passive (SMAP) mission launched in 2015.

While these are three different satellite missions, they all retrieve salinity measurements using the same underlying principles. They all use passive microwave radiometers measuring sea surface brightness temperature at the 1.4 gigahertz frequency. Brightness temperature (Tb) is a function of emissivity (ε) and sea surface temperature (SST):

$$\mathrm{Tb} = \varepsilon \cdot \mathrm{SST} \qquad (1)$$

By knowing the brightness temperature from the microwave radiometer, and SST from other sources (e.g., another satellite), you can estimate the emissivity. The emissivity is then a function of surface salinity (SSS), surface temperature, viewing angle of the antenna (θ), and polarization (p):

$$\varepsilon = \varepsilon(\mathrm{SST}, \theta, \mathrm{SSS}, p) \qquad (2)$$

Using the inverse of a forward emissivity model (f), you can then determine the salinity based on the emissivity, surface temperature, viewing angle, and polarization:

$$\mathrm{SSS} = f^{-1}(\varepsilon, \mathrm{SST}, \theta, p) \qquad (3)$$

This is a high-level overview of the general process, and there are a lot of corrective and additional processes specific to each satellite (Boutin et al., 2021a; Boutin et al., 2021b; Meissner et al., 2018; Reul et al., 2020).

1.3 Dissertation Structure and Research Gaps

1.3.1 Satellite Salinity Validation

Since the advent of satellite salinity measurements in 2009, a large effort has been made to assess and validate remotely sensed salinity observations using in situ data. These validation efforts primarily use Argo profiles and Argo gridded data products as their in situ data source (e.g., Boutin et al., 2012; Drucker et al., 2014; Lee 2016) or use Argo data and one other observing platform (e.g., moored buoys in Abe et al., 2014). However, since Argo floats typically drift at 1000m, and take profiles down to 2000m, they primarily observe only open ocean regions and not near-shelf. Additionally, Argo floats are rarely deployed in high latitude locations where sea ice may be a problem (sea ice will not allow the Argo float to reach the surface and transmit data or the ice could damage the float) and there was a propensity for Argo floats, especially floats before 2013, to not transmit data in very fresh and stratified regions like the Amazon outflow (Reverdin et al., 2024).

Thus, ***Chapter 2*** focuses on leveraging the World Ocean Database (WOD) (A. V. Mishonov et al., 2024) and the millions of ocean salinity profiles that it has aggregated from a variety of different probe types (e.g., bottles, CTD, gliders, Argo floats, etc.), to produce new monthly in situ salinity fields for comparison with Aquarius satellite salinity to ensure the indirect estimates of salinity from Aquarius were accurate and therefore able to be exploited. Utilizing WOD allows for comparisons with satellite salinity in regions not accessible to Argo (e.g., marginal seas, high latitudes, near-coast, etc.). Additionally, while a harmonic analysis of climatological in situ salinity was undertaken by Boyer et al. (2002), it had not yet been calculated for satellite sea surface salinity. We undertake this analysis to see how the annual cycle of Aquarius sea surface salinity compares to in situ. Much of ***Chapter 2*** was previously published in Reagan et al. (2014), but some updated comparisons between in situ and the SMOS and SMAP satellites were conducted and added to Appendix A.

1.3.2 North Atlantic Water Vapor Transfer and Salinity Contrasts

The ability for deep water to sink in the subpolar North Atlantic and drive global ocean circulation relies heavily on how salty the water is. The primary upstream source for this water is the subtropical North Atlantic, known for its very salty footprint due to evaporation greatly exceeding precipitation. Thus, for the AMOC to function, it is critical that this North Atlantic intra-basin salinity gradient be maintained. A key atmospheric source of moisture is evaporation in the northern tropics and subtropics, while a key sink is precipitation onto the northern subpolar gyre. However, it remains unclear whether intra-basin atmospheric moisture transport within the North Atlantic helps maintain these salinity gradients.

In ***Chapter 3***, we address this gap by testing the hypothesis that North Atlantic salinity gradients are correlated with intra-basin moisture transport. We explore the seasonal link between atmospheric and oceanic hydrologic cycles in the North Atlantic sector. The tropospheric circulation, including the trade winds and Hadley circulation, have a strong seasonal component with increasing net evaporation in the subtropics in summer and decreasing in winter. ***Chapter 3*** reveals a strong seasonal connection between near-surface salinity (NSS) in the subpolar gyre and atmospheric moisture transport from the subtropics, a result that offers the potential to use NSS observations as a proxy to track changes in atmospheric water transport. ***Chapter 3*** has been published in Reagan et al. (2018b).

1.3.3 Multi-year Salinity Trends

The Clausius–Clapeyron equation shows that a 3K increase in tropospheric temperature will increase saturation vapor pressure by 20% (Held et al., 2006; Trenberth, 2011). Climate models tend to increase specific humidity while maintaining a fixed relative humidity in the troposphere as temperatures rise. The impact, to quote Held et al. (2006), is that "...poleward vapor transport and the pattern of evaporation minus precipitation (E-P) increases proportionally to the lower-tropospheric vapor, and in this sense *wet regions get wetter and dry regions drier*".

As discussed in section 1.1.1, changes in global salinity patterns have been linked to shifts in the hydrological cycle (Cheng et al., 2020; Douville et al., 2024; Durack et al., 2012; Hosoda et al., 2009; Skliris et al., 2014), with salty (dry) areas getting saltier (drier) and fresh (wet) areas getting fresher (wetter). Most of these studies have focused on long (>30-year) time periods, estimated only basic uncertainties, and have not robustly accounted for natural variability.

In ***Chapter 4***, we build on the empirical framework developed by Durack et al. (2012) to estimate salinity pattern amplifications. Our goal is to understand how these amplifications evolve from 10 to 60+ years and if we can estimate when secular changes are identifiable. We improve uncertainty quantification by directly accounting for sampling biases and then incorporating these uncertainties in our analysis.

We also apply a more robust methodology to better capture and remove natural variability from our data. These improvements, combined with the use of a vastly expanded dataset (millions more profiles than Durack et al., 2012), enable us to determine robust estimates (and uncertainties) of salinity pattern amplifications from 1957/61-2019/2023. In addition, by leveraging recently released decadal salinity climatologies, we clearly identify an acceleration of salinity pattern amplifications over the last ~70 years. Finally, we examine the salinity contrast between the Atlantic/Pacific and how it relates to maintaining the AMOC.

1.3.4 Conclusions and Future Work

Chapter 5 summarizes the general conclusions of this research, highlights outstanding questions, and outlines future work needed to help resolve them.

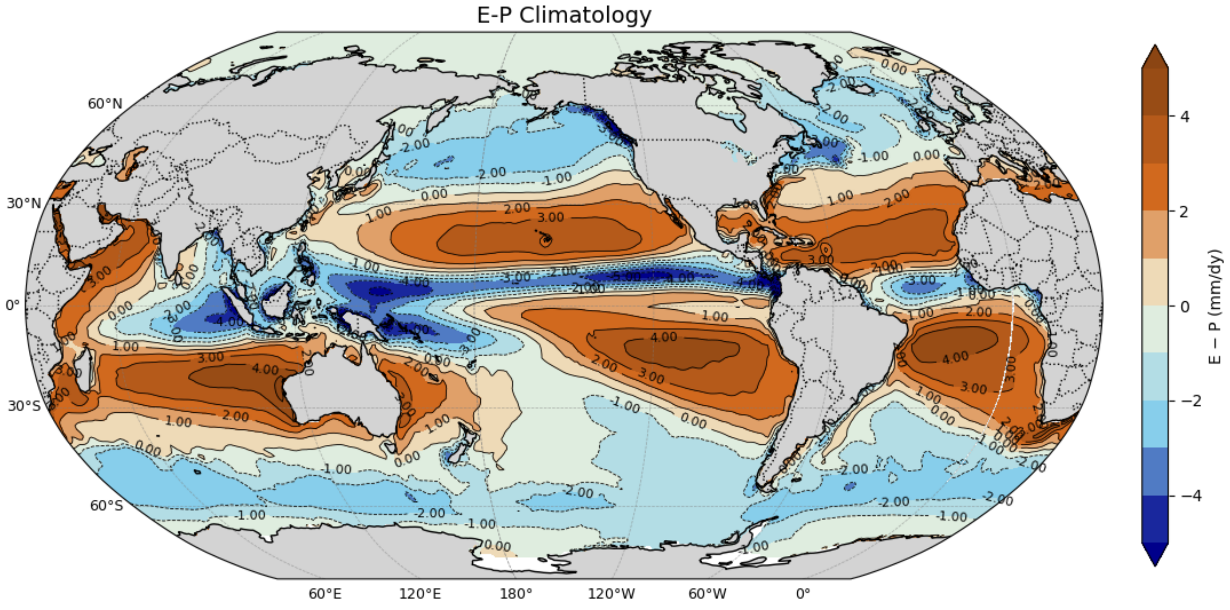

Figure 1.1: Global Climatology of Evaporation minus Precipitation (mm/dy) for 1979-2022. Evaporation data is from the OAFlux Project (Yu et al., 2008) and the precipitation data is from the GPCPv2.3 Project (Adler et al., 2003).

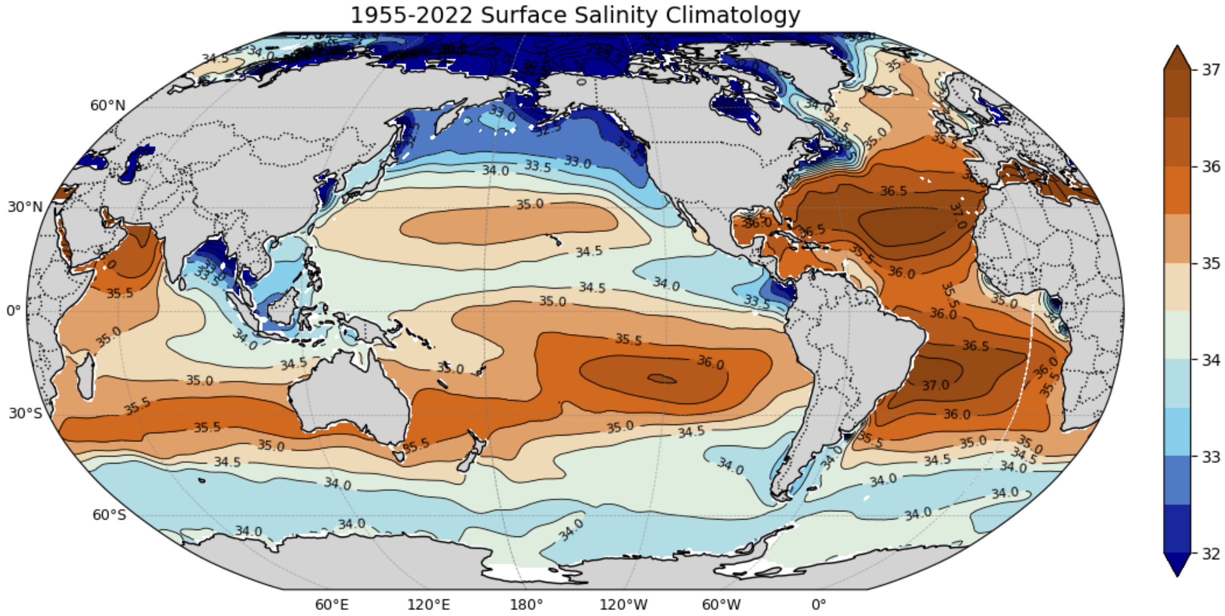

Figure 1.2: Global Climatology of Sea Surface Salinity. Data is from the World Ocean Atlas 2023 (Reagan et al., 2024b).

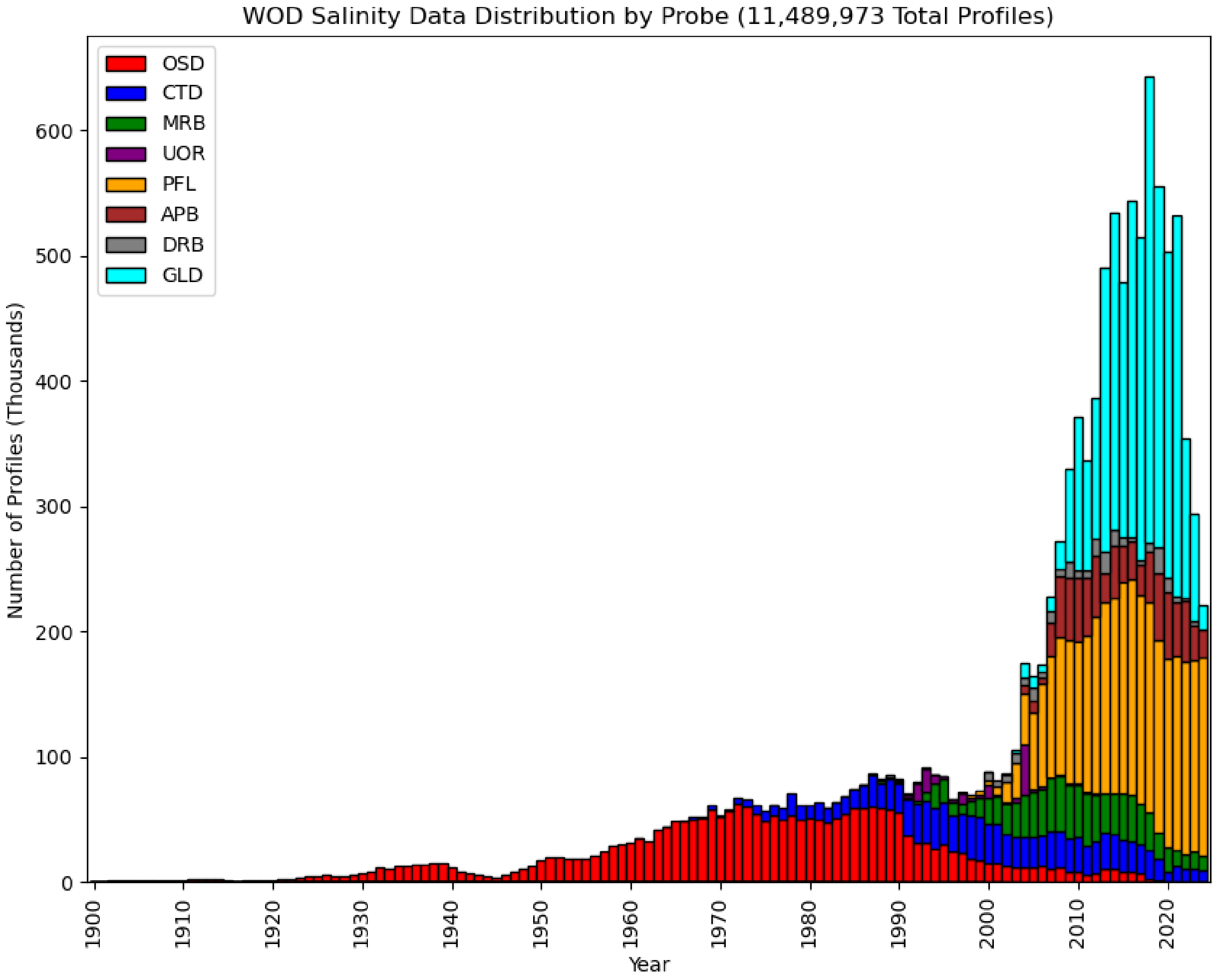

Figure 1.3: Yearly salinity data distribution by probe type within the World Ocean Database (A. V. Mishonov et al., 2024). OSD = Bottle; CTD = Conductivity, Temperature, Depth; MRB = Moored Buoy; UOR = Undulating Oceanographic Recorder; PFL = Profiling Floats; APB = Autonomous Pinniped Bathythermographs; DRB = Drifting Buoys, GLD = Gliders.

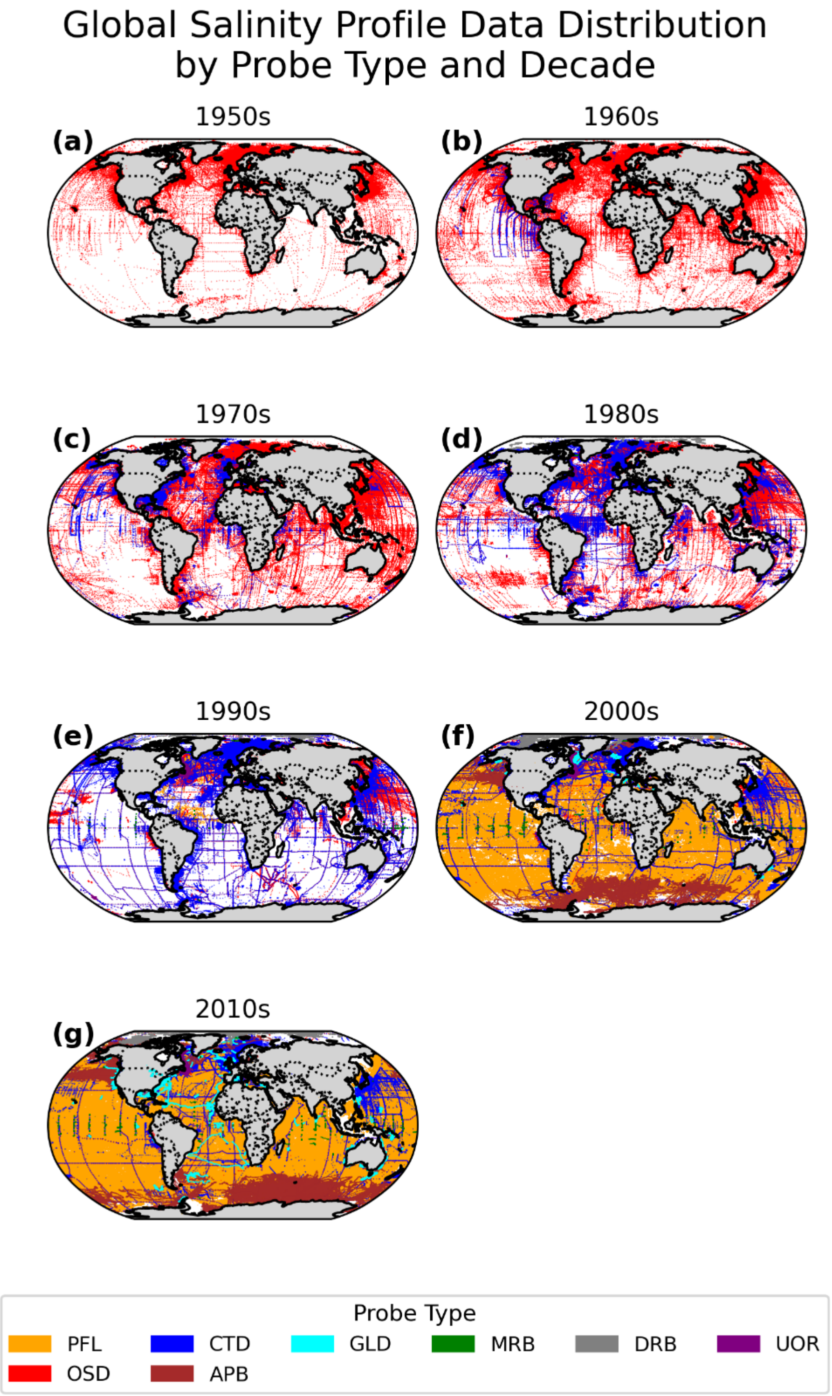

Figure 1.4: The temporal and spatial distribution of ocean salinity profile data within the World Ocean Database (A. V. Mishonov et al., 2024) by decade and probe type. Probe types are described in Fig. 1.3.

Chapter 2: Validation of satellite sea surface salinity with in situ measurements

Materials presented in this chapter have been published in the Journal of Geophysical Research- Oceans as Reagan et al. (2014) [https://doi.org/10.1002/2014JC009961]

Abstract: A new monthly sea surface salinity (SSS) product calculated from profile data within the World Ocean Database (WOD) is compared and contrasted with Aquarius SSS, both standard and Combined Active-Passive (CAP) products, from September 2011 through September 2013. Aquarius exhibits similar biases as shown in previous comparison SSS studies, with negative biases in the tropics transitioning to positive biases in the higher latitudes when compared to WOD SSS. These biases are generally much weaker in CAP than the standard version, indicating that the biases are strongly related to the differences in algorithms used to retrieve satellite SSS. Non-Argo data utilized in the study are shown to be of great use to validate Aquarius in regions with little to no Argo coverage and helps provide SSS measurements in regions where there are known errors in Aquarius retrievals. The annual cycle of WOD and Aquarius is found to be very similar, with Aquarius being generally more coherent and robust. All three products' annual cycles compared favorably to the World Ocean Atlas 2013. The interannual changes in all three products generally corresponded well to one another and to changes in evaporation and precipitation (E-P). Overall, Aquarius compares very well with in situ sea surface salinity fields under multiple comparison examinations; however, both products have their own strengths and weaknesses and a synthesis of the two should be used to study global scale SSS variability.

2.1 Introduction

Sea surface salinity (SSS) is an important variable of the ocean. A recent study by Durack et al. (2010) showed that over the past ~50 years salty regions of the ocean have become saltier and fresh regions fresher, suggesting a strengthening of the global hydrological cycle.

Furthermore, Durack et al. (2012) showed through the observed changes in SSS combined with global climate models that a global surface temperature increase of 1°C would increase the global hydrological cycle by an estimated 8 ± 5%. This agrees with the general idea that in a warming world the hydrological cycle will become stronger (Held et al., 2006) and dry regions dominated by evaporation will become drier and wet regions dominated by precipitation will become wetter.

In addition to SSS changes being a natural marker of changes in the global hydrological cycle, its importance to deep water formation and ocean circulation cannot be overstated. The thermohaline circulation depends on a delicate balance between temperature and salinity as do all density driven currents in the ocean. Broecker (1991) put forth the first generalized view of the thermohaline circulation and noted that changes in salinity due to changes in freshwater fluxes could result in changes in the thermohaline circulation. Multiple studies [e.g., Fichefet et al. (2003); Gregory et al. (2005); Rahmstorf et al. (1999)] have used models to evaluate changes in the thermohaline circulation in a warming world. For the most part, increases in freshwater fluxes causing a decrease in salinity resulted in a decrease in the strength of the thermohaline circulation in the North Atlantic. An important property of the thermohaline circulation is it redistributes heat from the tropics to high latitudes; thus, any changes in the thermohaline circulation would affect the global distribution of heat.

Therefore, it is critical to monitor SSS variability due to its status as an important marker for the hydrological cycle, and an important component of the thermohaline circulation. In recent years, the Aquarius/Satélite de Aplicaciones Científicas (SAC)-D (Lagerloef et al., 2008) and Soil Moisture and Ocean Salinity (SMOS) (Kerr et al., 2010) satellite missions have been measuring SSS on a near-global scale. A crucial component of these satellite missions is validation of the satellite SSS measurements. Monthly validation of satellite SSS measurements with in situ observations is possible due to the international project, Argo (Team, 1998), and its vast fleet of profiling floats.

Recent studies [e.g., Boutin et al., 2012; Lagerloef, 2013; Vinogradova et al., 2013] all compared satellite SSS measurements to in situ observations. In general, over the subtropical regions away from land, in situ and satellite SSS measurements match up very well. However, in tropical regions, high latitudes, river outflow, and coastal regions the differences can be quite large. A challenge in validating satellite data is that the footprints are much larger than single point in situ observations. SMOS has a footprint of ~40 km. Aquarius has three ellipsoidal footprints: 76 x 94 km, 84 x 120 km, and 96 x 156 km.

For this study we compare and analyze Level-3 gridded monthly Aquarius SSS to gridded in situ derived SSS. We choose to compare to gridded in situ fields rather than individual profiles due to Aquarius' larger footprint. This study expands on the previous analyses in two different ways. First, a new monthly SSS gridded dataset computed from not only Argo profiling data, but also from a multitude of other instruments (moored buoys, CTDs, bottles, gliders, and ice drifters) are used. The use of non-Argo data was vital because ~30% of the Argo data used in our study was discarded because the shallowest measurements were deeper than 5.25 m. We also look at the importance of non-Argo SSS data in regions where Argo floats are sparse and how it relates to Aquarius validation and regional SSS studies. Second, in addition to performing a direct comparison with the satellite data, a look at how the annual cycles compare is also completed by analyzing the first harmonic of the Fourier decomposition. These cycles are also compared to the annual harmonics of the World Ocean Atlas 2013 (Zweng et al., 2013) SSS climatology. The interannual changes of SSS are compared and contrasted between the in situ and satellite products. Finally, SSS and E-P interannual changes are discussed. For this study, all salinity values are on the Practical Salinity Scale 1978 (PSS-78) and are therefore unitless.

2.2 Data

For our comparison analyses, several difference plots are calculated from a multitude of various SSS and ancillary datasets that are described below. Unless otherwise noted, all gridded monthly fields are on a 1°x1° resolution for the time period of September 2011 through September 2013.

2.2.1 In Situ Analyzed Surface Salinity Fields

To create monthly in situ analyzed SSS fields we started with all available SSS in situ profile data from the World Ocean Database (http://www.nodc.noaa.gov/OC5/WOD/pr_wod.html) (Boyer et al., 2013) which is a product of the National Oceanographic Data Center. In our time domain of September 2011 – September 2013 there were a total of 426,212 salinity profiles. For this study, only salinity measurements less than 5.25 m from the surface were considered. A depth of 5.25 m was chosen as at this depth we are able to include many Argo profiling floats, and in addition, other instruments' shallowest measurements are often at least 1 m deep, and rarely at the sea surface due to the difficulty of obtaining measurements right at the sea surface. The depth is not extended any deeper than 5.25 m as it has been shown (see Fig. 5 in Henocq et al. (2010)) that increasing rainfall rates caused larger differences in salinity between 1 m and 10 m depths than 1 m and 5 m depths. This depth constraint eliminated 31.3% of Argo measurements for the period since many Argo floats shut off sensors below 5 m to prevent biofouling. It also eliminated 22.0% of measurements from other instrument types. Thus, a total of 305,576 profiles were in our depth range, of which 45,524 did not pass quality control checks leaving a total of 260,052 total profiles used in the analyses. For a full list of the quality control checks please review D. R.

Johnson et al. (2013). Table 1 illustrates the data distribution among different data types, with Argo profiling floats dominating the distribution. However, a substantial amount of SSS data is also attributed to CTD and moored buoys. All moored buoy data are daily means from the Pacific Marine Environmental Laboratory (PMEL) tropical moored buoy dataset. The moored buoy array network consists of the Tropical Atmosphere Ocean/Triangle Trans-Ocean Buoy Network (TAO/TRITON), Prediction and Research Moored Array in the Atlantic (PIRATA), and Research Moored Array for African-Asian-Australian Monsoon Analysis and Prediction (RAMA). Figure 2.1 illustrates the spatial distribution of SSS observations over our time domain. Argo data are in grey to emphasize the measurements from other instruments.

The gridding technique used to calculate the in situ analyzed SSS fields is very similar to the technique implemented when computing the World Ocean Atlas 2013 (WOA13) climatologies (Zweng et al., 2013), with a few differences. We begin by computing monthly mean anomalies for each month in our time domain. These are computed by taking the differences between the in situ SSS observations and the monthly climatological SSS value from the World Ocean Atlas 2009 (Antonov et al., 2010) at each 1°x1° grid point. Once all mean anomalies are calculated for each month, the mean anomalies are objectively analyzed following the same technique used in computing the salinity climatology for WOA13. For a detailed overview of the objective analysis procedure please see Zweng et al. (2013). Once the anomalies are objectively analyzed they then go through subjective quality control screening in which each monthly anomaly field is reviewed for "bullseyes". "Bullseyes" are concentric closed contours emanating from a specific location. These "bullseyes" often appear in the analyzed fields due to a single profile with an abnormally large anomaly compared to surrounding data. Bullseyes are not necessarily bad data; they often represent small or mesoscale anomalies not representative of the larger area. Data that produced these "bullseyes" are removed and the anomaly fields are rerun. Once these fields are finalized, they are added to their respective WOA09 monthly climatology yielding a full salinity field. It is important to note that because WOA09 is added to the salinity anomaly fields, regions of poor data coverage will essentially be the monthly climatology (see Figure 2.1 to locate data-poor regions). The monthly salinity anomalies are available at: http://www.nodc.noaa.gov/OC5/3M_HEAT_CONTENT/. We will refer to the WOD-derived SSS fields as WODSSS.

2.2.2 World Ocean Atlas 2013

The climatological decadal average monthly salinity fields from the World Ocean Atlas 2013 (http://www.nodc.noaa.gov/OC5/woa13/) are used in the comparison analysis as a baseline for what we expect the SSS fields from both Aquarius and the in situ derived fields to resemble. A full description of WOA13 salinity fields and how they are calculated can be reviewed in Zweng et al. (2013). Note that we use the decadal average monthly SSS fields, which are an average of the monthly climatology fields of each of the six decades (1955-1964, 1965-1974, 1975-1984, 1985-1994, 1995-2004, 2005-2012).

2.2.3 Aquarius

The Aquarius satellite observes SSS by measuring microwave emissions from the sea surface at the 1.413GHz frequency (L-band) using three microwave radiometers [Lagerloef et al. (2008)]. For this study we used the Level 3 Standard Mapped Image version 2.5.1 Aquarius/SAC-D monthly SSS fields. The data used were not separated based on ascending/descending phase. The initial reasoning for separation was due to seasonal biases, especially during the descending phase in the Southern Hemisphere (Lagerloef, 2013). However, version 2.5.1 has been shown to have these biases mostly eliminated [Lagerloef, personal communication, 2013], and thus for this study, especially in regards to comparing annual cycles, we use the combined phase data. All salinities less than zero and greater than 100 were masked out before analyzing the Aquarius v2.5.1 data. These erroneous values are mostly confined to high latitude regions where sea ice and/or land contamination caused errors in the salinity retrievals.

In addition to the aforementioned v2.5.1, we also utilized the Level 3 Standard Mapped Image CAP version 2.5.1 Aquarius/SAC-D monthly SSS fields. The major difference between the standard version 2.5.1 and the CAP version is that the CAP version uses a Combined Active-Passive (CAP) (Yueh et al., 2012) algorithm that enables wind speed/direction and sea surface salinity to be retrieved simultaneously from Aquarius data by minimizing the sum of squared differences between model and observations (Yueh et al., 2012). There is no dependence on the wind directions from the National Centers for Environmental Prediction (NCEP) like that of the standard version for Aquarius. Wind speed and direction are important components of calculating the surface roughness correction on which Aquarius sea surface salinity retrievals depend. The v2.5.1 CAP data set can also utilize a rain correction [Simon Yueh, personal communication, 2014]. When rain droplets strike the ocean surface it creates roughness which increases the brightness temperature that Aquarius measures; this ultimately reduces the measured SSS. This correction reduces surface freshening under rain [Simon Yueh, personal communication, 2014; Tang et al. (2014)]. For this study the rain corrected v2.5.1 CAP data set was used. We will refer to Aquarius v2.5.1 as AQ251 and Aquarius CAP v2.5.1 as AQCAP251.

2.2.4 Evaporation and Precipitation

The monthly gridded ocean evaporation data comes from the Woods Hole Oceanographic Institution (WHOI) Objectively Analyzed Air-sea Fluxes (OAFlux) project (http://oaflux.whoi.edu/dataproducts.html). The data were initially in units of cm·yr-1 and were converted into mm·dy-1. For a detailed analysis of how these fields are calculated please review Yu et al. (2008).

The monthly gridded precipitation data is from the Global Precipitation Climatology Project (GPCP). We use the GPCP Version 2.2 monthly gridded precipitation data. In a very general sense, the GPCP version 2.2 data is a merged product that combines satellite precipitation estimates with surface rain gauge observations (Adler et al., 2003). The monthly gridded data is in units of mm·dy-1. The initial gridded data were on a 2.5°x2.5° spatial scale. With all other comparison data on a 1°x1° grid, we used bi-linear interpolation to regrid the precipitation data on to a finer 1°x1° grid. For a full review of the GPCP Version 2.2 data please review Adler et al. (2003) and Huffman et al. (2009). We will refer to the WHOI OAFlux evaporation dataset as OAFlux and the precipitation GPCP Version 2.2 will be referred to as GPCP.

2.3 Discussion and Results

2.3.1 In situ Comparison

Multiple studies [e.g., Qu et al. (2014); Vinogradova et al. (2013)] use the Asia-Pacific Data Research Center (APDRC) gridded Argo data products as a validation data set for Aquarius. The APDRC uses a variational interpolation algorithm to map salinity onto a three-dimensional grid on standard levels (for more documentation see: http://apdrc.soest.hawaii.edu/projects/Argo/data/Documentation/). Because this dataset has been used for validating Aquarius in the past [e.g., Qu et al. (2014); Vinogradova et al. (2013)] , a comparison between our gridded SSS data and the APDRC Argo-only gridded data was conducted to ensure that our own SSS gridded dataset is comparable to the APDRC dataset.

The APDRC monthly mean fields from 09/2011-09/2013 (http://apdrc.soest.hawaii.edu/dods/public_data/Argo_Products/monthly_mean) were compared to the WODSSS monthly gridded fields. The monthly comparison statistics root-mean-square error (RMSE) and bias (APDRC – WODSSS) are shown in Figure 2.2. The RMSE remains below 0.20 for the entire 2+ year time period. There is a very small positive bias (APDRC>WODSSS) for most months, however, it never reaches above 0.02 for any given month.

Annual (09/2011-09/2013) scatter diagrams were also plotted (Figure 2.3a-d) to further evaluate the differences seen between WODSSS and APDRC. The statistics show that when comparing both datasets to AQ251 (Figures 2.3a,c), both WODSSS and APDRC are nearly identical with similar bias (~0.02), standard deviation of the differences (~0.24), and correlation (~0.97) with a slight edge to WODSSS. However, there are noticeable differences when both are compared to AQCAP251 (Figures 2.3b,d). While bias is doubled in WODSSS (-0.017 compared to -0.008 for APDRC), the standard deviation of the differences is improved by nearly 13% when using WODSSS. There is also a noticeable tailing-off feature in the APDRC plots where regions of low SSS are measured to be much higher than AQ251 and AQCAP251. This tailing-off feature is not evident in the WODSSS plots; however, there is a small positive bias in WODSSS for the same low surface SSS waters. These specific points are located near the Bay of Bengal.

Figure 2.4a illustrates the monthly RMSE for AQ251-WODSSS, AQCAP251-WODSSS, AQ251-APDRC, and AQCAP251-APDRC. The RMSE for both Aquarius products are slightly smaller for most months when using WODSSS as the "observed" SSS instead of APDRC. The 25 month RMSE average for AQ251-WODSSS is 0.304 and 0.314 for AQ251-APDRC, resulting in a very small -0.010 difference. Similarly, the 25 month average RMSE for AQCAP251-WODSSS is 0.266 and 0.281 for AQCAP251-APDRC, resulting in a small -0.015

difference. This indicates that on average AQ251 and AQCAP251 are slightly closer to WODSSS than APDRC. The monthly biases also exhibit similar magnitudes and month to month variability (Figure 2.4b). There also appears to be a low amplitude annual cycle in the monthly biases. These results compare very well with the recent Aquarius CAP analyses from Tang et al. (2014). There is also a noticeable difference in RMSE and bias when using AQ251 and AQCAP251 which will be discussed in the next section.

Overall, WODSSS compares very well to the APDRC SSS dataset. There is very little bias between the two (Fig. 2.2) and an RMSE that is below 0.20 for each month (Fig. 2.2). The slight Aquarius (both versions) validation improvement when using WODSSS as compared to APDRC is likely caused by a combination of additional data used in the WOD analyses, differences in the objective analyses, and using the background climatology in computing the analyzed fields (see section 2.1).

2.3.2 Aquarius SSS compared to WOD SSS

The average monthly differences (09/2011-09/2013) between AQ251/AQCAP251 and WODSSS are shown in Figure 2.5a,b. The zonal average of each difference is shown in Figure 2.5c. From Figure 2.5a and 2.5c large negative biases (AQ251<WODSSS) exist from roughly 25°S-25°N. The large negative biases in the tropics, especially in regards to AQ251, would appear to have a direct relation to surface freshening induced by rainfall along the Intertropical Convergence Zone (ITCZ) and South Pacific Convergence Zone (SPCZ). Vertical salinity stratification in high precipitation locales in the upper couple of meters has been analyzed in a few studies [Boutin et al. (2013); Drucker et al. (2014); Reverdin et al. (2012)]. Argo typically makes its shallowest salinity measurement near 5 m depth as this is when the CTD pump is turned off on its way to the surface (Riser et al., 2008). Aquarius is measuring the top 2 cm, thus any salinity stratification between 2 cm and 5 m will not be well-captured by the in situ fields.

However, recent work by Drucker et al. (2014) showed that while heavy precipitation events can cause large vertical salinity stratifications (>0.1) in the near-surface waters, they are often short lived and very infrequent, thus only contributing up to 0.03 bias when Aquarius is compared to Argo in the tropics. The zonal biases that are seen in Figure 2.5c are much greater than the 0.03 bias found by Drucker et al. (2014), thus salinity stratification is not the main source of negative biases in the tropical region.

Figure 2.5b shows the average monthly difference between AQCAP251 and WODSSS and the zonal average of these differences are shown in Figure 2.5c. There is a large decrease in the negative bias seen in the tropical regions when the CAP algorithm is utilized as compared to the standard Aquarius v2.5.1. Recent work by Tang et al. (2014) showed that the month to month bias (when compared to Argo) for the rain-corrected CAP data (the data that is used in this study) was shifted up by 0.03 when compared to the bias using the non-rain-corrected CAP data over the global ocean. Because this bias (0.03) is 3-4 times smaller than the zonal average bias improvement we see from AQ251 to AQCAP251 in Figure 2.5c, we conclude that the improvement in bias in the tropics seen in AQCAP251 when compared to AQ251 is a direct result of the usage of the CAP algorithm and not due to the addition of the rain correction. Thus, the biggest influence on bias in the tropics is the difference in the salinity retrieval algorithms between AQ251 and AQCAP251. Additionally, large river outflows such as the Amazon and Ganges-Brahmaputra contribute large negative biases. However, a change in the salinity retrieval algorithms (Figure 2.5a,b) has little effect on the differences seen in river outflow regions.

In the subtropical regions, in both Figures 2.5a and 2.5b, the WODSSS and AQ251/AQCAP251 appear to generally agree outside of coastal regions. Based on the annual salinity climatology from WOA13 (Zweng et al., 2013), the maximum SSS in each ocean basin occurs in the open ocean subtropical regions where evaporation dominates precipitation. With little precipitation, a weak wind field (due to the presence of subtropical high pressures), and a region well sampled by Argo (Figure 2.1), we'd expect Aquarius (both products) and WOD to agree. The agreement is spatially contained to a very small area centered around 30°N and 30°S. Large discrepancies near coastal locations are due to a combination of land contamination in satellite salinity retrievals (Zinc et al., 2007), and a lack of in situ data along the coast (Figure 2.1).

In the higher latitudes the zonal averages (biases) (Figure 2.5c) become positive, and in some cases are greater than 0.20 (i.e., 45°S for AQ251-WODSSS). There are several error sources in this region. In the high latitudes, measuring SSS is especially difficult due to cold sea surface temperatures (SST), high winds, and melting/freezing of sea ice. Aquarius measurements are less sensitive to SSS in cold SST regions. High winds increase the surface roughness of the ocean which increases the difficultly of accurately measuring SSS (Lagerloef et al., 2008). Melting/freezing of sea ice causes sea ice contamination errors in the SSS retrieval. There is a notable decrease in positive bias between AQCAP251 and AQ251 in the high southern latitudes (30°S-50°S). This large improvement in bias occurs in a region known for strong westerly winds (i.e., Roaring Forties) quite possibly signifying that the CAP algorithm is handling the roughness correction for high wind speeds better in this region. The same improvement in bias is not seen in the high northern latitudes likely because the biases in this region are more dominated by land and sea-ice contamination in the satellite SSS retrievals as well as radio frequency interference (RFI) errors. RFI errors cause high brightness temperatures which in turn cause low SSS values. These errors are mainly confined to the northeast Atlantic (near Europe), northwest Atlantic (US/Canada), and the northwest Pacific (China/Japan)

(Lagerloef, 2013). They can be seen in Figure 2.5a as low salinity values in the eastern North Atlantic. There is a noticeable decrease in the RFI-induced negative bias in both the northwest Pacific and northeast Atlantic from AQ251 (Figure 2.5a) to AQCAP251 (Figure 2.5b), implying that the CAP algorithm may be filtering the RFI out better than the standard version. However, the northwest Atlantic exhibits a positive bias in both AQ251 (Figure 2.5a) and AQCAP251 (Figure 2.5b). Thus, some other error source(s) must be contributing to these large positive biases as there is sufficient in situ data in this region (see Figure 2.1) and thus unlikely to be related to a lack of in situ data.

It should be noted that the North Pacific exhibits a strong positive bias (Figure 2.5a,b) in v2.5.1 for both Aquarius products, whereas this bias was much weaker in the standard version 2.0, and just slightly weaker in the CAP version 2.0. Figure 2.6a shows the North Pacific summer (July, August, and September) SSS difference between AQ251 and WODSSS. Figure 2.6b shows the average precipitation over this same time period. There is a lack of precipitation over the area of strongest SSS difference. Climatologically, during the summer months there is also a weak wind field in this region (Risien et al., 2008). With a weak wind field and little precipitation, the North Pacific biases cannot be explained through surface roughness issues or near-surface salinity gradients. It is likely that a change in the satellite retrieval algorithms from version 2 to version 2.5.1 caused this increase in bias.

Overall, the zonal average of the average monthly differences follow the same positive/negative bias pattern in both AQ251-WODSSS and AQCAP251-WODSSS (Figure 2.5c), with AQCAP251-WODSSS generally less biased than AQ251-WODSSS, especially in the tropical and Southern Ocean regions. In Figure 2.4 it is shown that AQCAP251 consistently produces smaller RMSE than AQ251 throughout the 2+ year time period, indicating AQCAP251 is measuring closer to in situ than AQ251. The 25 month average RMSE for AQ251 is 0.306 and AQCAP251 is 0.266 when compared to WODSSS. This represents an improvement of 13% when using AQCAP251. It is important to note that the improvement of RMSE when using AQCAP251 is a result of using the CAP algorithm and not the usage of the rain correction as Tang et al. (2014) found no real difference in RMSE between CAP with no rain correction and CAP with rain correction when compared to Argo. Subsequently, it indicates that utilizing the CAP algorithm makes a strong difference in the validation of the Aquarius instrument.

2.3.3 Non-Argo Measurements: Importance to Validation of Aquarius and Regional SSS Studies

There are regions of the global ocean (i.e., near coast, high latitudes) (see Figure 2.1) where the distribution of Argo profiling floats is simply not adequate for validation of satellite SSS measurements nor is it adequate for regional scale SSS studies. Non-Argo data (i.e., CTD, moored buoys, gliders, etc.) provide, in some regions, the data that is necessary to perform these tasks. Figure 2.7a shows the distribution of CTD SSS data and the number of months during our time domain in which no Argo floats surfaced within a one-degree box of the CTD measurement. Figure 2.7b is the same as Figure 2.7a, except for moored buoy, bottle, drifting buoy, and glider data combined. Off of the northeast coast of the United States, southeast coast of Canada, the North Sea, and off the coast of Japan there are many months of CTD SSS data where Argo floats never surfaced (Figure 2.7a). Near the northeast coast of the United States and southeast coast of Canada (80°W-40°W, 38°N-54°N) there are a total of 8,286 CTD profiles and 1,103 Argo profiles. The northern European waters (20°W-30°E, 45°N-80°N) contain 6,044 CTD profiles and 2,911 Argo profiles. Finally, coastal Japan (126°E-144°E, 30°N-42°N) contains 8,713 CTD profiles and 3,536 Argo profiles. In each of these regions the amount of CTD profiles at least doubles the amount of Argo profiles.

Figure 2.8a shows the September 2011 one-degree bin-averaged SSS data from CTD along the water ways between Norway and Svalbard. There is not a single Argo measurement made during this month in this region, however, there are numerous CTD measurements. The CTD measurements allow us to compare SSS measurements to Aquarius, which was done in Figure 2.8b. As shown, Aquarius has a positive bias greater than 1.4 in parts of this region. This high bias cannot be confirmed with Argo profiles because the most eastern extent of Argo data for this region is 17E throughout the 25 month time period; however, there are other months such as August 2012 (not shown) where there is a sufficient amount of CTD data that continues to show the high bias of Aquarius in this region. If Aquarius is to be used to study high latitudes, then Argo deployments in these regions need to be increased, and/or data outside of Argo floats will be needed to serve as a ground truth for Aquarius.

In addition to utilizing non-Argo data in regions where there is a lack of Argo data, we can also utilize non-Argo data in regions where there are Argo data. One example of this is to use moored buoy data to observe near-surface salinity stratification such as was done in Henocq et al. (2010). Many moored buoy observations shallowest measurements are made at 1 m depth, which is on average 4 or more meters shallower than Argo measurements. Henocq et al. (2010) found that, on a local scale, changes in SSS between 1m and 5m depths can reach 1.0 in rainy regions. We still have little understanding on the development and eventual dissipation of these stratification events, but with moored buoy data and other near surface measurements from other instruments, we can begin to build the bridge on what happens between the surface and 5-10 m depths during stratification events. So even though it has been shown that these precipitation induced salinity stratification events occur infrequently and on short time scales and minimally effect the global bias seen between Aquarius and Argo (Drucker et al., 2014), they are still important events to understand.

As shown in Figure 2.7a-b, there are many regions, especially near coasts, where Argo float data, by itself, does not meet the need for optimal validation of Aquarius data. Furthermore, there are a few regions (i.e., European coast, NW Atlantic) where it is known that Aquarius has RFI issues, and in these same regions we CTD data (and lack of Argo data). Thus, not only is supplementary data needed for validation purposes, it is vital for closing the gaps where Aquarius does not perform very well (i.e., RFI regions, coastlines, high latitudes, etc.). In addition, instrumentation outside of Argo (i.e., moored buoys, gliders, etc.) will assist in bridging the gap and helping our understanding of near surface salinity stratification events. Higher level products, like the blended satellite and in situ SSS product created by Xie et al. (2014), will need to utilize all SSS data available to accurately depict SSS. More near-surface instrumentation and measurements are also needed (Henocq et al., 2010; Lagerloef et al., 2008).

2.3.4 Annual Cycle

The annual cycle of WODSSS, AQ251, and AQCAP 251 were constructed through a Fourier decomposition of the 09/2011-08/2013 monthly fields. We first averaged the two year monthly fields then calculated the first harmonic of the Fourier series. The Fourier decomposition follows the methods used by Boyer et al. (2002). Figure 2.9(a-c) illustrates the amplitude of the first harmonic. The locations of largest salinity amplitudes (ITCZ, SPCZ, and river outflows) compares very well to those calculated by Boyer et al. (2002) in which they analyzed the annual cycle by applying a Fourier decomposition to the monthly climatological means of WOA98. In general, WODSSS, AQ251, and AQCAP251 annual amplitudes compare very well to one another.

Figure 2.10a,b shows the annual amplitude differences between AQ251 and WODSSS and AQCAP251 and WODSSS, respectively. AQ251 and AQCAP251 have larger amplitudes along most major river plumes, likely because Aquarius's larger footprint can more robustly and accurately depict SSS in these regions then can sparsely located in situ observations (see Figure 2.1). AQ251 and AQCAP251 also exhibit larger amplitudes along the ITCZ, likely for the same reasons. AQ251 exhibits much larger amplitudes in the northern North Atlantic and Nordic Seas region, whereas AQCAP251 is not larger than WODSSS in this region. This is likely related to the satellite salinity error sources discussed in section 3.2 (i.e., RFI, sea ice contamination, melting and freezing of sea ice, and difference in retrieval algorithms). Higher amplitudes in the Aquarius products along and just off the coast of Colombia and Ecuador in the equatorial Pacific are due to the low surface salinity waters being brought in from the south Pacific equatorial countercurrent (Boyer et al., 2002) and are likely better represented through Aquarius. Both AQ251 and AQCAP251 exhibit larger annual cycles near the Antarctic ice sheet, however, it is much larger in AQ251. This is likely related to melting and freezing of sea ice in addition to sea ice contamination errors; however, the larger amplitudes in AQ251 stretch further north which are more likely due to the salinity retrieval errors in the high wind speed and low SST waters. The lack of larger differences in AQCAP251 supports that it is a retrieval based issue. It is important to note that where there is a lack of in situ observations, the monthly field is in essence the WOA09 climatology, which will often yield a lower amplitude signal because the fifty-seven year time period covered in the climatology is much greater than the two years we are examining, and thus variability will be smoothed out a great deal.

The month in which maximum SSS (phase) occurs generally agrees between WODSSS, AQ251, and AQCAP251 (Figure 2.9e-h). The largest disagreements (Figure 2.10c,d) between the in situ and Aquarius phases are in the high southern latitudes near Antarctica. The phase for the Aquarius products near the Antarctic ice sheet is generally during the austral spring, where we would expect more melting and lower SSS values. The phase for WODSSS is generally around austral winter, where the freezing of sea ice should cause an increase in SSS due to brine rejection during the freezing process. Thus, this difference is likely a result of errors in the satellite salinity retrievals in this area due to the cold SST, windy conditions, and sea ice contamination. In addition to the high southern latitudes, we also notice large phase differences in the central/eastern North Atlantic and the central/eastern North Pacific. These occur due to very low salinity amplitudes in these regions and therefore large differences in the phase are expected.

The percent variance accounted for by the first harmonic is very similar in all three SSS products (Figure 2.9i-l). In general, higher values mirror regions of higher amplitude, which is expected. As was the case with the annual amplitudes, most percent variance differences (Figure 2.10e,f) between the Aquarius products and WOD occur due to the footprint of Aquarius and its ability to measure SSS over a more connected area than the in situ product.

There is a similar pattern when comparing the annual harmonic of the monthly climatological fields from WOA13 to the WODSSS, AQ251, and AQCAP251 (Figure 2.9). Comparing the annual harmonic of the WOA13 climatology to the WOA98 climatology which was used in Boyer et al. (2002), there is a noticeable decrease in amplitude of SSS in WOA13 (Figure 2.9d). This is a result of the dampening effect from averaging together six decadal monthly climatologies. Thus, when comparing WODSSS, AQ251, and AQCAP251 to the annual amplitude of WOA13 it is important to ensure the structures are similar, as it is expected that the amplitudes for WODSSS, AQ251, and AQCAP251 will be larger than that of WOA13.

The annual amplitude structure for all three are very similar to WOA13, as can be seen when reviewing Figure 2.9a-d. The phases and percent variance accounted for by the first harmonic between WOA13 and WODSSS, AQ251, and AQCAP251 are also very similar (Figure 2.9e-i).

Despite some technical limitations and reservations of analyzing the annual cycle with Aquarius as discussed by Lagerloef (2013); Aquarius agrees very well with the in situ derived annual cycle. When comparing the annual cycles of WODSSS, AQ251, and AQCAP251 (Figure 2.9) to that of Figure 3 in Boyer et al. (2002), there is very little change in the structure of the largest amplitudes and phases of the annual cycle. This is of importance because Figure 3 from Boyer et al. (2002) is based on WOA98, in which the majority of SSS data came from shipboard data (bottles, CTD). Thus, even with a large increase in SSS data from satellites and Argo, the annual cycle has remained unchanged in structure.

2.3.5 Interannual Variability Comparison

Monitoring SSS changes is vital to climate studies as changes in SSS over time have been linked to changes in the global hydrological cycle (Durack et al., 2012). If Aquarius is to be used to study SSS variability then we must first ensure that the changes Aquarius measures are similar to the changes in situ observations measure.

2.3.5.1 Changes in annual cycle

We first compare the interannual variability of all three SSS products' annual cycle. The first year is from September 2011 – August 2012 (denoted 11/12), and the second year is from September 2012 – August 2013 (denoted 12/13). As was done in section 3.3, a Fourier decomposition was applied to each year. Similarly, because SSS changes are often reflected by E-P changes, a similar Fourier decomposition of E-P for each year was performed.

Figure 2.11a-l illustrates the annual amplitude for 11/12, 12/13, and their difference (12/13 – 11/12) for WODSSS, AQ251, AQCAP251, and E-P. Focusing on the 12/13-11/12 salinity difference figures (Figure 2.11c,f,i), we see that all three salinity products exhibit similar changes in annual amplitude from 11/12 to 12/13. This can be more clearly illustrated when we examine the differences in year to year annual amplitude changes between AQ251 and WODSSS (Figure 2.12a) and the differences in year to year annual amplitude changes between AQCAP251 and WODSSS (Figure 2.12b). Outside of coastal locales and major river outflow regions, where the differences in interannual amplitude changes between Aquarius and WODSSS can be greater than 0.5, the magnitude of interannual changes in annual amplitude is very similar between the satellite and in situ products. Furthermore, when the Aquarius and WODSSS differences in interannual amplitude changes (Figure 2.12a,b) are compared to the differences in the two year averaged annual amplitudes (Figure 2.10a,b) the ITCZ feature in Figure 2.10a,b is removed in Figure 2.12a,b signifying that Aquarius and WOD are measuring similar year to year magnitude changes in the annual amplitude for this region, but Aquarius is measuring a higher two year averaged annual amplitude than WOD as seen in Figure 2.10a,b. Conversely, high values in river outflow regions and other coastal locales appear in both Figure 2.12a,b and Figure 2.10a,b signifying that not only are the two year averaged annual amplitudes different (Figure 2.10a,b), but the year to year changes in the magnitude of the annual amplitude are also different (Figure 2.12a,b). As discussed previously, we believe Aquarius is better able to resolve the SSS structure near river outflows due to a larger footprint and better coverage. In addition, there is normally little in situ data near the river mouths (Figure 2.1), and thus they are likely not being well represented in the in situ product. The interannual changes in phase generally agree between all three SSS products (Figure 2.12c,d) outside of the regions discussed in section 3.3.

Figure 2.11j-l shows the annual amplitude of E-P for 11/12, 12/13 and 12/13-11/12, respectively. Regions whose SSS variability is mostly influenced by E-P should share similar annual harmonic structure as these two have been shown to be closely related in annual harmonic analysis (Boyer et al., 2002). Based on Figure 2.11, the SSS annual amplitude from all three products closely resembles the E-P annual amplitude for much of the ocean in both 11/12 (Figure 2.11j) and 12/13 (Figure 2.11k). It is important to note that many of the regions with high E-P amplitude are very similar to the regions Yu (2011) depicted as being the locales where the dominant term in the mixed layer salinity (MLS) budget was E-P (see Figure 9 in Yu (2011)). In addition to E-P, Yu (2011) found that horizontal advection by both geostrophic and Ekman velocities, and vertical entrainment also played a major role in the MLS budget. Next, we compare the interannual changes in SSS for all three salinity products and compare their year to year changes to changes in E-P.

2.3.5.2 SSS and E-P: Interannual Similarities and Differences

The changes in salinity from 11/12 to 12/13 are illustrated in Figure 2.13(a-c). There is general agreement between all three products on which regions became saltier or fresher from 11/12 to 12/13. However, in some cases the magnitude of year to year SSS change is different (Figure 2.14a-c). Figure 2.14a is the difference between the absolute value of the 11/12 to 12/13 SSS change in AQ251 as compared to the absolute value of the 11/12 to 12/13 SSS change in WODSSS. Similarly, Figure 2.14b is AQCAP251 compared to WODSSS, and Figure 2.14c is AQCAP251 compared to AQ251. Figure 2.14a,b shows larger year to year changes in the satellite products along the SPCZ, off the coast of Ecuador/Colombia, and near numerous river outflow regions. These higher magnitudes are likely due to Aquarius' ability to resolve SSS in high variability regions better than WODSSS. Figure 2.14a and less so in Figure 2.14b show large year to year changes in high latitude regions when compared to WODSSS which is likely due to errors in Aquarius retrievals near sea-ice margins and in cold windy waters. WODSSS depicts larger changes than Aquarius (both products) in the southern Gulf of Mexico and the

South China Sea. The larger changes in the southern Gulf of Mexico and the South China Sea are likely due to spurious data sampling in the regions (see Figure 2.1). Figure 2.14c depicts AQCAP251 with slightly higher year to year changes in SSS compared to AQ251 along the ITCZ, SPCZ, and along the Amazon plume.

Figure 2.13d illustrates the 11/12 to 12/13 changes in E-P. There are only a few regions where E-P is the dominate term in the MLS budget. These regions are mainly confined to the ITCZ, SPCZ, and the western North Pacific (Yu, 2011). Comparing Figure 2.13d to Figure 2.13a-c, and focusing on the regions where SSS variability is dominated by E-P, there is a noticeable relationship with the interannual changes in SSS and the interannual changes in E-P over the western North Pacific and the SPCZ, but not over the ITCZ. The SPCZ progressed northward from 11/12 to 12/13. This resulted in an increase in SSS from where the original SPCZ was located in 11/12 to a decrease in salinity at its current location in 12/13. This is similar to what is seen between calendar years 2011 and 2012 (G. C. Johnson et al., 2013).

The ITCZ strengthened between 11/12 and 12/13 in the tropical Pacific (Figure 2.13d); however, the salinity reflection does not quite come through in the central tropical Pacific (Figure 2.13a-c). Typically, along the ITCZ there is a three month time lag between precipitation and salinity reflection (Delcroix, 1998), and there is a substantial increase in precipitation in this region from Jun-Aug 2012 to Jun-Aug 2013 (not shown). Thus, the salinity changes lag behind the precipitation changes. The decrease in salinity from the August-October 2012 time period to the August-October 2013 time period confirms this (not shown).

Overall WODSSS, AQ251, and AQCAP251 capture similar interannual changes between 11/12 and 12/13. The AQ251 and AQCAP251 are generally larger in the magnitude of these year to year changes in some regions (i.e., SPCZ region) with AQCAP251 being slightly larger in interannual changes than AQ251. The SSS changes are reflected in the E-P fields over regions where E-P is expected to dominate SSS variability (Yu, 2011). However, in regions where horizontal advection and other factors mostly determine the MLS budget the correlation between year-to-year change in SSS and E-P is weak or absent (e.g., Amazon outflow, eastern tropical Indian, northern North Pacific, etc.).

2.4 Conclusions

Overall, the Aquarius products compare very well to WODSSS. The negative bias of Aquarius in the tropics transitions to a positive bias in the higher latitudes when compared to WODSSS, consistent with other studies [i.e., Lagerloef (2013)]. It is found that the negative biases in the tropics and southern latitudes are greatly reduced when using the CAP algorithm, which implies that the majority of bias is retrieval-based and not near-surface salinity stratification. The effect on bias from near surface salinity stratification has recently been found to be quite small (0.03 in tropics) (Drucker et al., 2014). In addition to a reduction in the zonally averaged biases, the CAP algorithm exhibits a smaller RMSE than the standard Aquarius version when compared to WODSSS. The CAP algorithm improves RMSE by 13% over the standard version when compared to WODSSS.Strong differences between in situ and Aquarius (both products) also exist in coastal locations, river outflow boundaries, and high latitudes. Coastal locations are undersampled in our current in situ observation network (Figure 2.1) and Aquarius has multiple issues measuring SSS near coasts (land contamination, RFI in certain regions). River outflow regions also suffer from a lack of in situ observations (Figure 2.1) while Aquarius generally performs well in capturing the low salinity signature of the river discharge. Finally, high latitudes offer many error sources. There is a lack of in situ data, and in addition, Aquarius has difficulty measuring SSS accurately in high wind and low SST water. There is also the possibility of sea ice contamination.

The comparison analyses performed in this study further examined the annual cycle and relationships, where both in situ and Aquarius exhibited similar SSS annual cycles with both Aquarius products generally depicting a more robust and coherent annual cycle than WODSSS. These annual cycles were also similar to the long-term (fifty-seven year) mean of the World Ocean Atlas 2013 climatology, albeit much more robust. The SSS annual cycles compared reasonably well to the E-P annual cycle, a dominant factor in determining SSS variability in some regions of the ocean (i.e., ITCZ, SPCZ). Further analysis examined the year to year variability of SSS by reviewing changes in SSS in addition to changes in the SSS annual cycle. The satellite and in situ products depicted similar interannual variability with both Aquarius products exhibiting slightly larger year to year changes in certain regions (i.e., SPCZ) than WODSSS.

The WODSSS fields provide a strong comparison dataset for Aquarius SSS products. The WODSSS improves on routine validation datasets such as the Argo-only gridded product from APDRC by utilizing additional SSS data from non-Argo instruments (e.g., moored buoy and CTD). Furthermore, the additional data used in WODSSS allows validation in regions where little to no Argo data is available. Some of these regions (i.e., NW Atlantic, Arctic, coastal, etc.) are also regions of highly questionable Aquarius data, and thus not only does it allow opportunity of validation in these regions, but it also improves on the Aquarius measurement. Thus, to study global sea surface salinity variability going forward, a synthesis of in situ and Aquarius data should be utilized.

2.5 Additional Results

Updated results not previously published have been added to Appendix A. These updates include comparisons between in situ near-surface salinity fields and the following monthly satellite surface salinities: Aquarius Level-3 Standard Mapped Image version 5.0 and two level-3 products from the Soil Moisture Active Passive (SMAP) satellite. This includes the version 5.0 monthly SMAP product from the Jet Propulsion Laboratory at NASA, and the version 6.0 monthly SMAP product from the Remote Sensing Systems (RSS). We also include a comparison between in situ and Soil Moisture Ocean Salinity (SMOS) level-3 debiased version 9 data (9-day) produced by the Centre Aval de Traitement des Données SMOS (CATDS) - Centre d'Expertise Scientifique (CEC) - Laboratoire d'Océanographie et du Climat: Expérimentations et Approches Numériques (LOCEAN); however, it should be noted that the CATDS-CEC-LOCEAN data product is debiased and uses an in situ climatology field in its debiasing methodology. It should not be considered an independent product as the in situ salinity imparts substantial information onto the fields. This produces unrealistically small differences when comparing the data to in situ observations (see Figures A.13-A.16).

Most of the conclusions drawn from our 2024 publication still stand today. Satellite salinity provides us an unprecedented look at how salinity changes in both time and space. However, knowing where it measures well (open ocean, warm SSTs) and where it struggles (near-coast, cold SSTs) has remained quite consistent a decade later. The 2014 discussion on the importance of in situ data, particularly outside of Argo, continues to hold weight in 2025. Argo still does not measure along coast, and with the problem of land contamination in satellite salinity retrievals, we are reliant on in situ observations to provide us with coastal salinity monitoring. Additionally, for high latitude regions where satellite retrievals suffer due to windy and cold ocean conditions, in situ observations are often our only option.

Table 2.1: Data distribution used in computing monthly WODSSS fields from 09/2011 – 09/2013

Argo	CTD	Moored Buoys	Glider	Bottle	Drifting Buoys	Total
162,090 (105,355 have delayed-mode quality control)	30,338	40,787	23,528	3,256	53	260,052

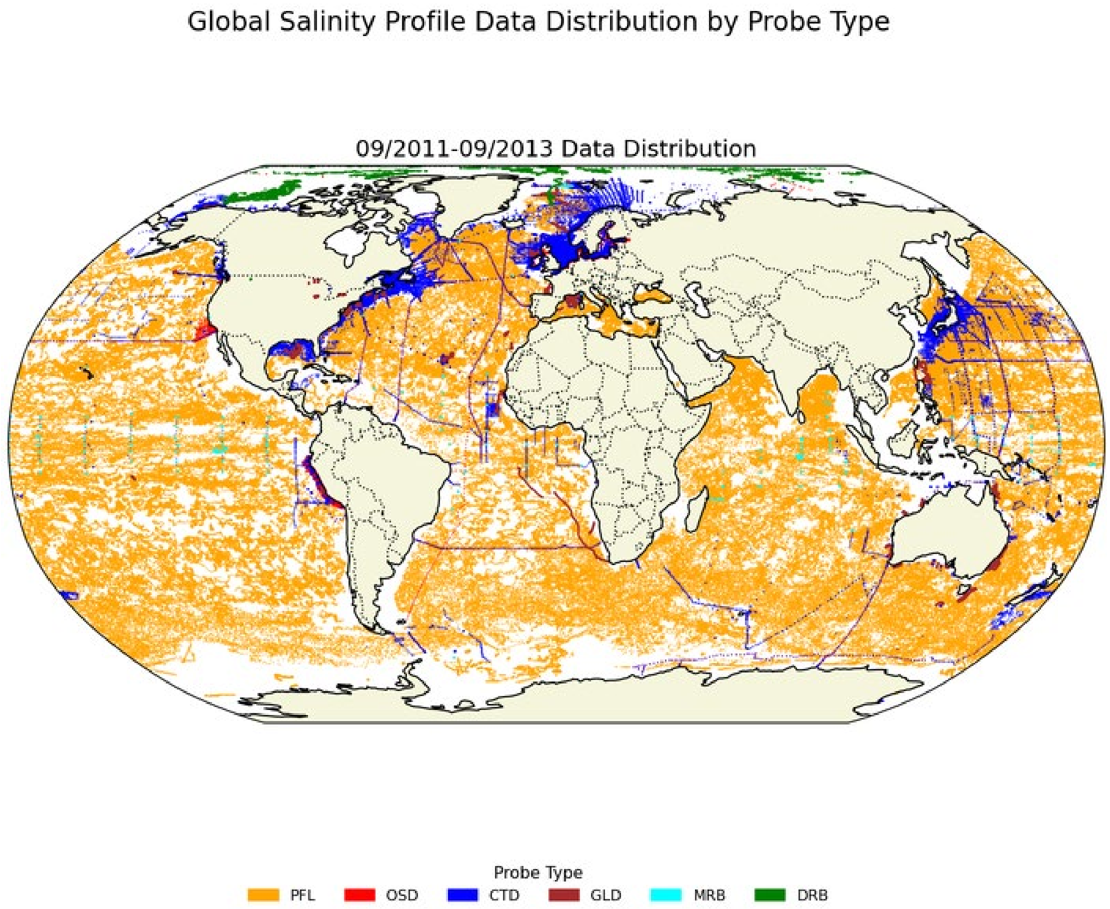

Figure 2.1: Data distribution of all SSS in situ observations used in the monthly WODSSS analyses from 09/2011 – 09/2013 (Orange = Argo floats, Dark Red= Glider, Red = Bottle, Green= Drifting Buoy, Blue = CTD, Turquoise= Moored Buoy).

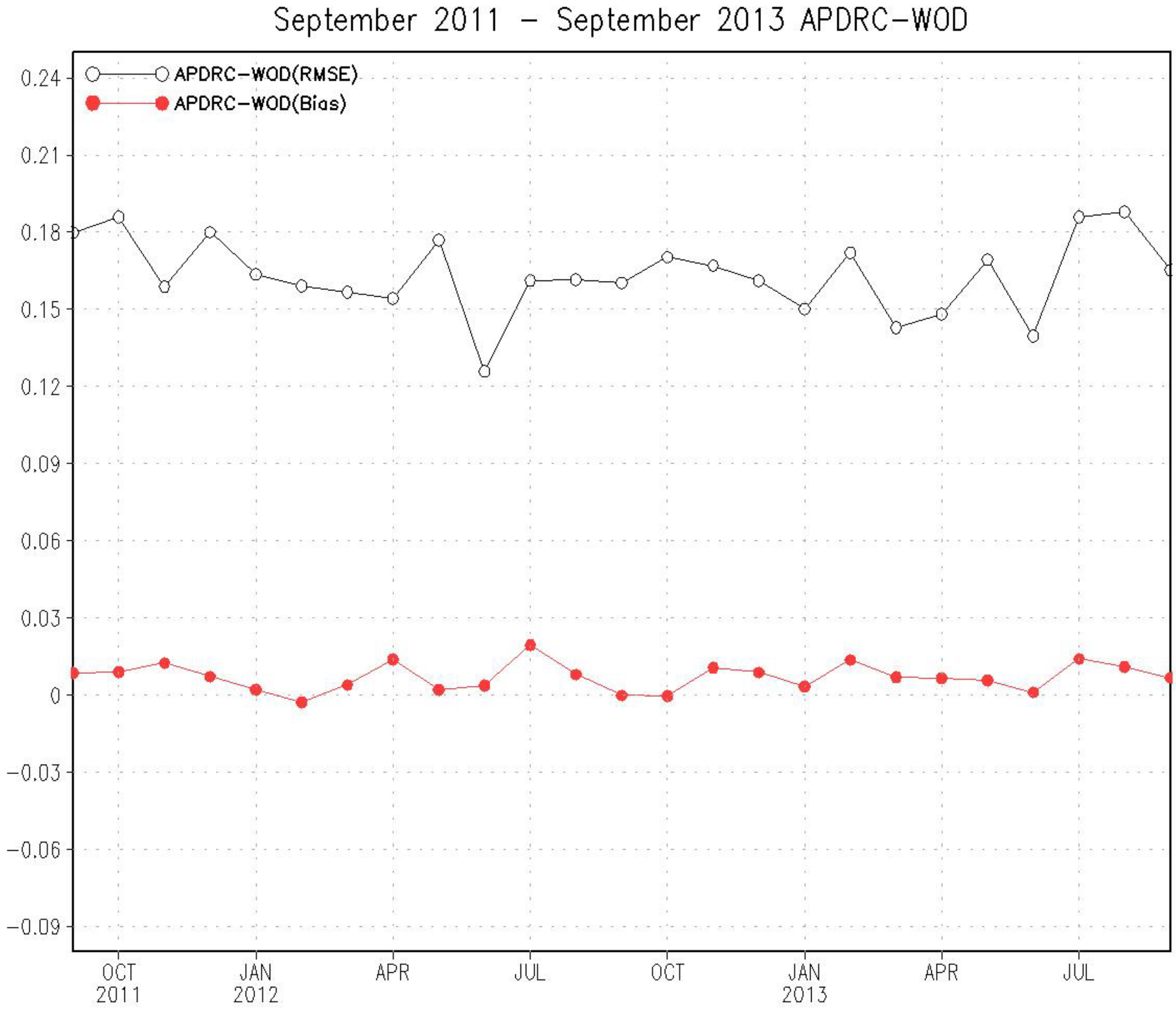

Figure 2.2: Time series of monthly comparison statistics (RMSE and Bias) between APDRC and WOD SSS.

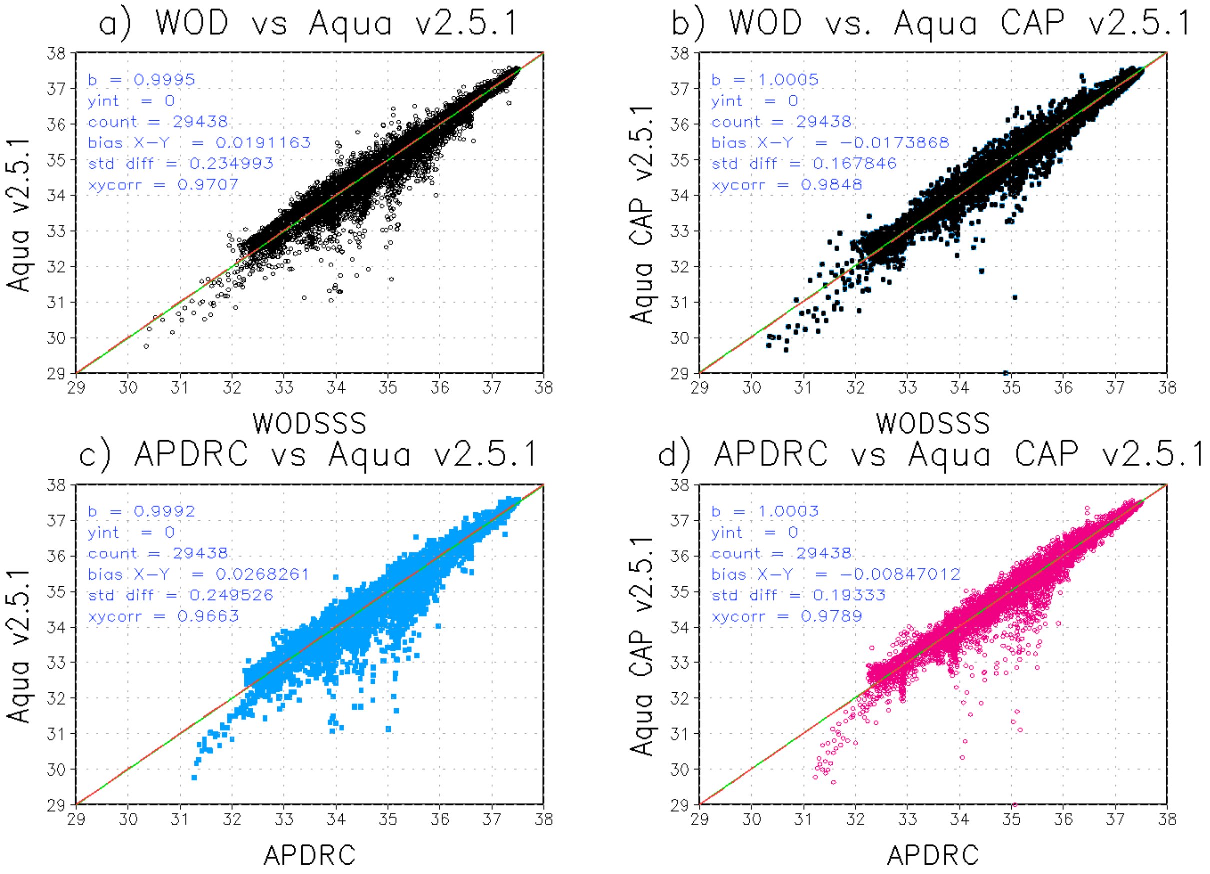

a) WOD vs Aqua v2.5.1

b) WOD vs. Aqua CAP v2.5.1

c) APDRC vs Aqua v2.5.1

d) APDRC vs Aqua CAP v2.5.1

Figure 2.3: Annual (09/2011-09/2013) scatter plots with comparison statistics for a) WODSSS and AQ251 b) WODSSS and AQCAP251 c) APDRC and AQ251 and d) APDRC and AQCAP251.

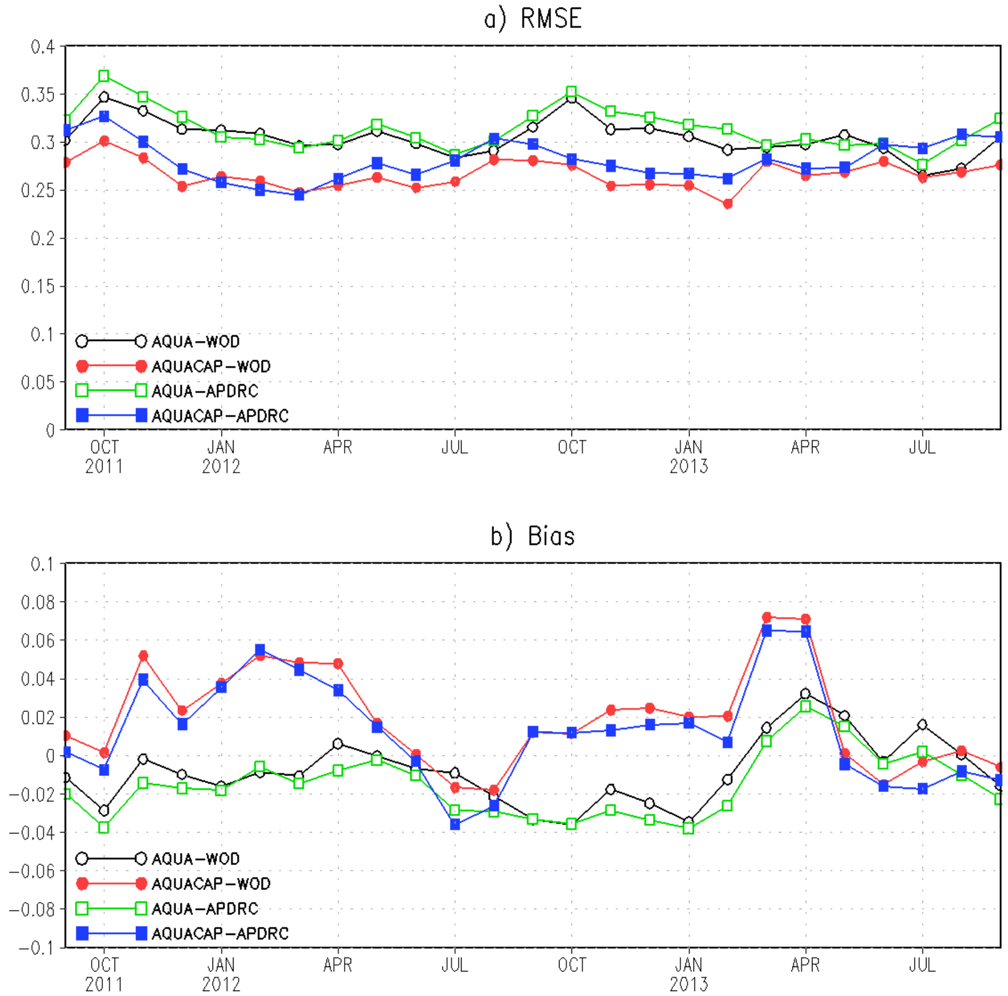

Figure 2.4: Monthly time series plots for September 2011 – September 2013 of a) root-mean-square error (RMSE) and b) bias for AQ251-WODSSS, AQ251-APDRC, AQCAP251-WODSSS, and AQCAP251-APDRC over the ocean from 60°S-60°N.

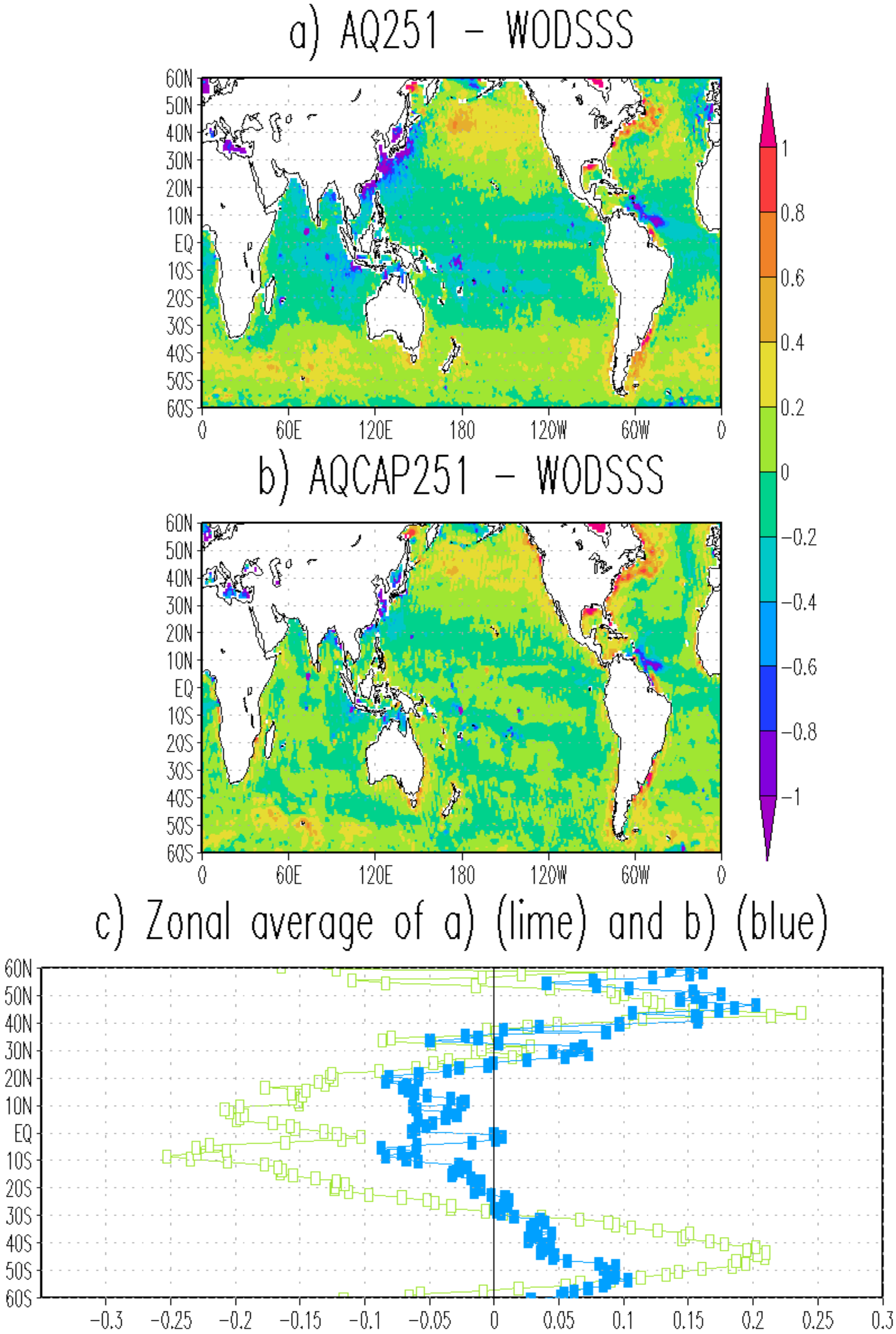
a) AQ251 - WODSSS

b) AQCAP251 - WODSSS

c) Zonal average of a) (lime) and b) (blue)

Figure 2.5: a) 09/2011-09/2013 average monthly difference between WODSSS and AQ251. b) Same as (a) except for AQCAP251 c) Zonal average of both (a) (lime) and (b) (blue).

a) Aqua−WOD Summer 2012

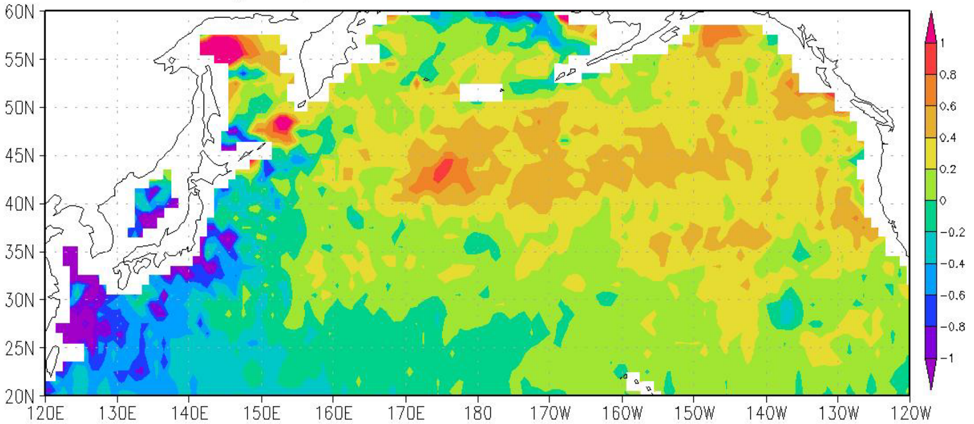

b) Precipitation Summer 2012

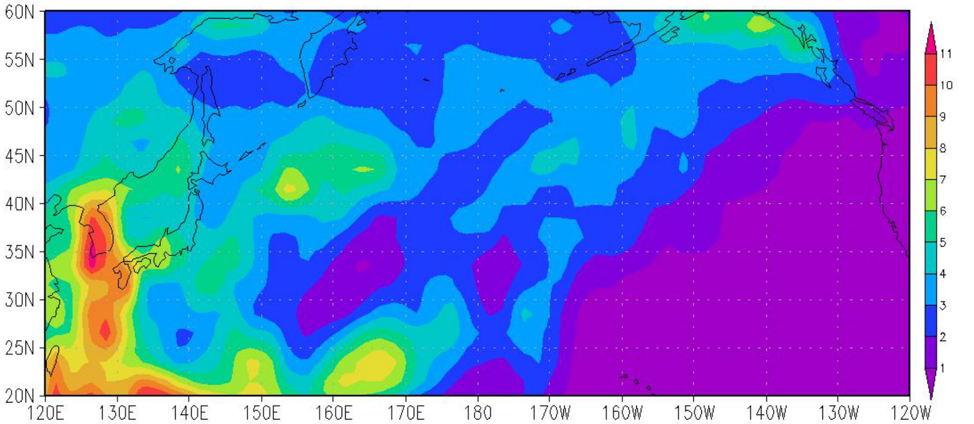

Figure 2.6: Summer (July, August, September) 2012 a) SSS differences between AQ251 and WODSSS and b) average precipitation (mm/dy).

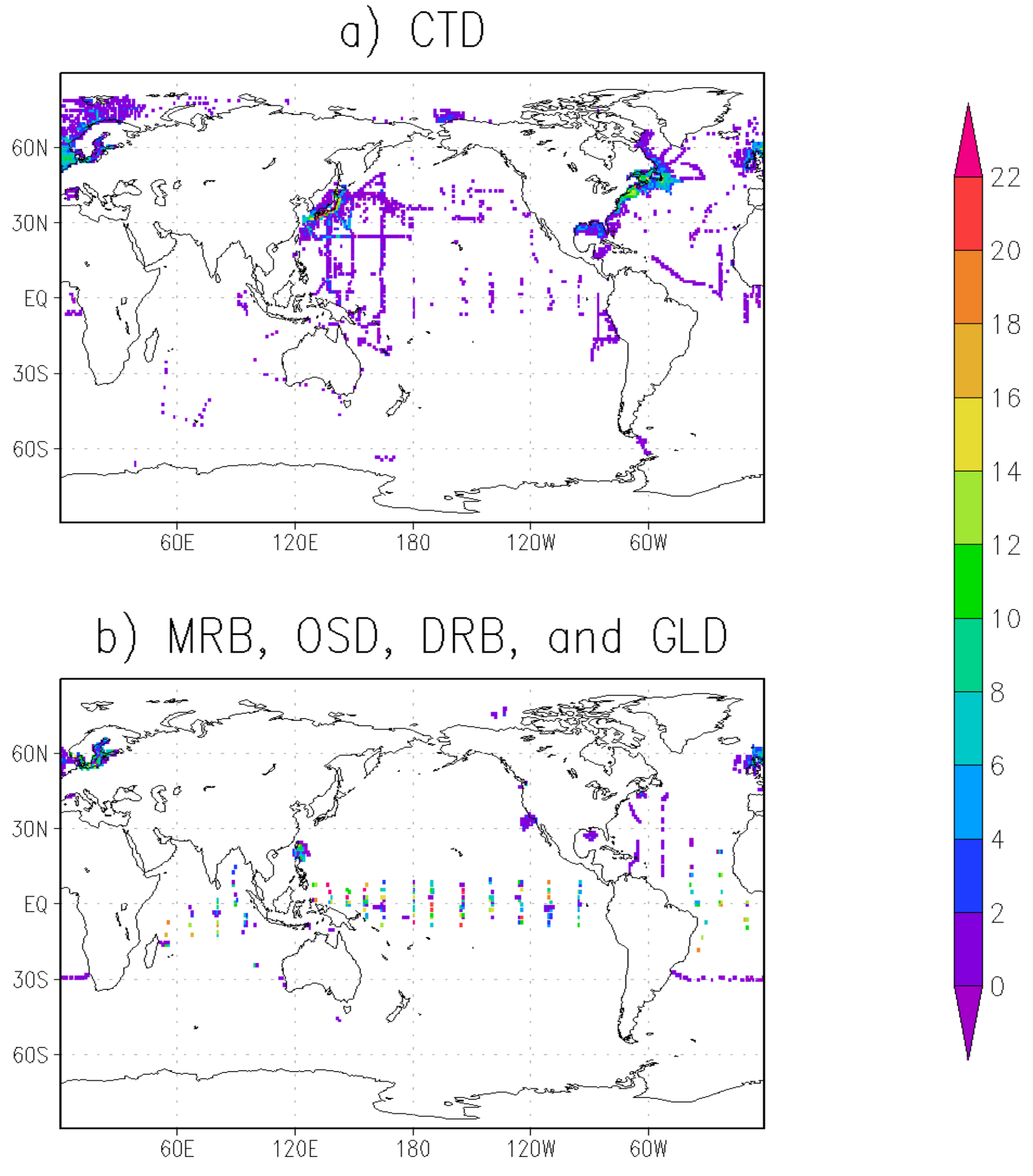

Figure 2.7: Number of months between 09/2011 – 09/2013 in which there was a a) CTD or b) MRB (moored buoy), OSD (bottle), DRB (drifting buoy), and GLD (glider) observation within a one degree grid box that had no Argo measurement during the same month.

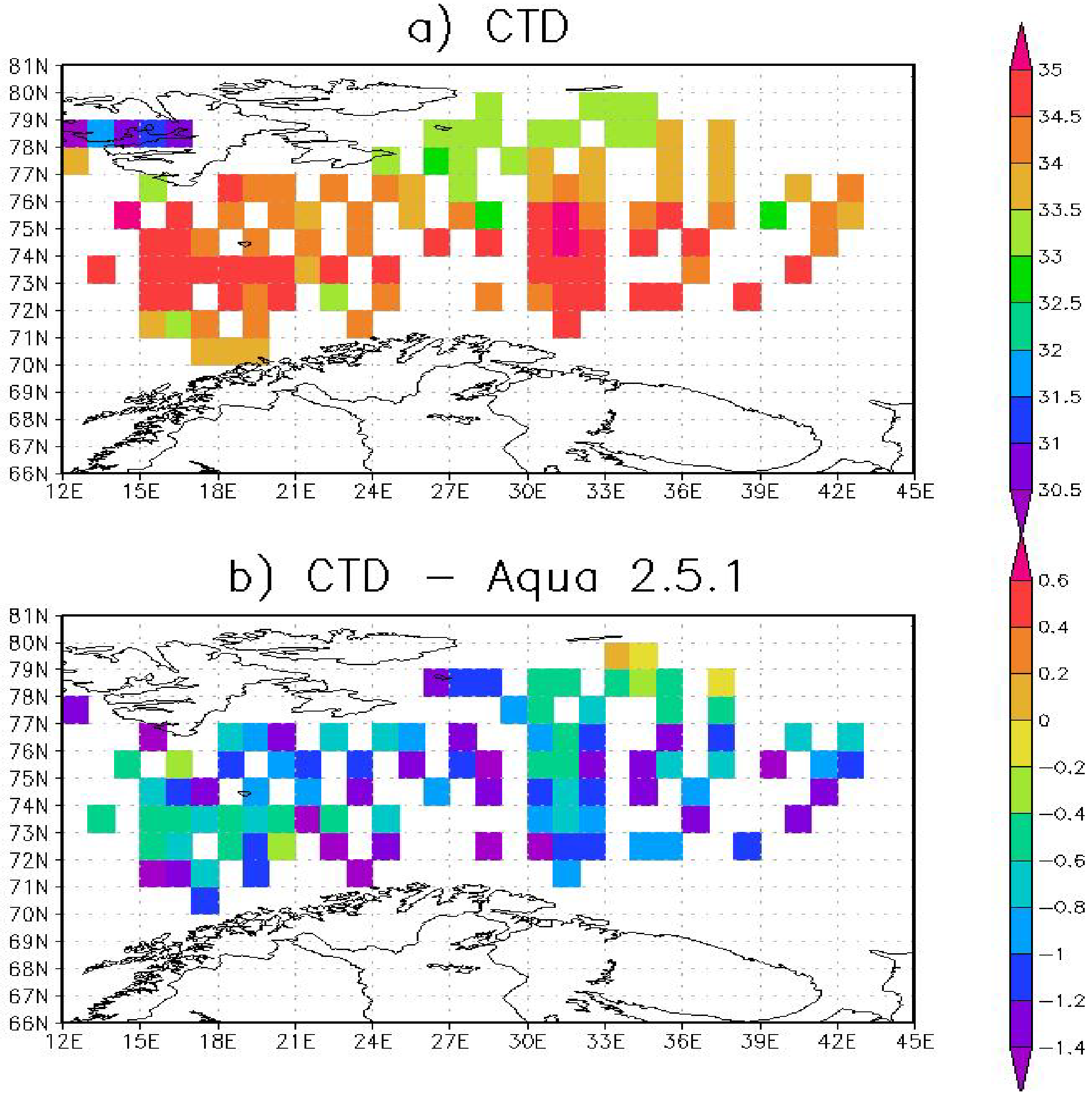

Figure 2.8: September 2011 a) one-degree bin averaged CTD SSS and b) difference between CTD one-degree bin average and AQ251.

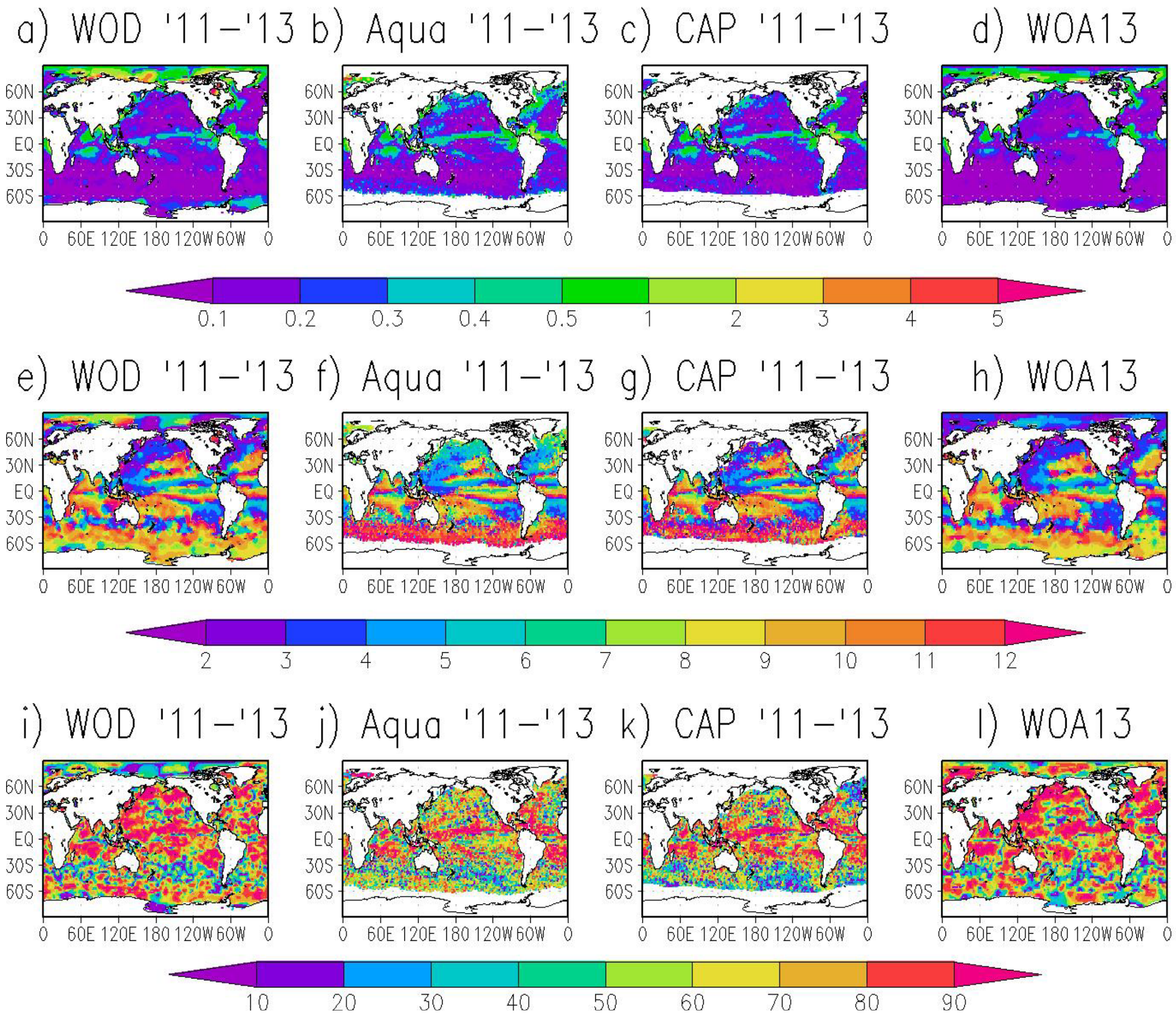

Figure 2.9: Amplitude of the first harmonic (09/2011-08/2013) for a) WODSSS , b) AQ251, c) AQCAP251 , and d) WOA13; phase (month of maximum SSS) of first harmonic for e) WODSSS , f) AQ251 , g) AQCAP251 , and h) WOA13; percent variance accounted for by first harmonic for e) WODSSS , f) AQ251 , g) AQCAP251 , and h) WOA13; percent variance accounted for by first harmonic for i) WODSSS , j) AQ251 , k) AQCAP251 , and l) WOA13.

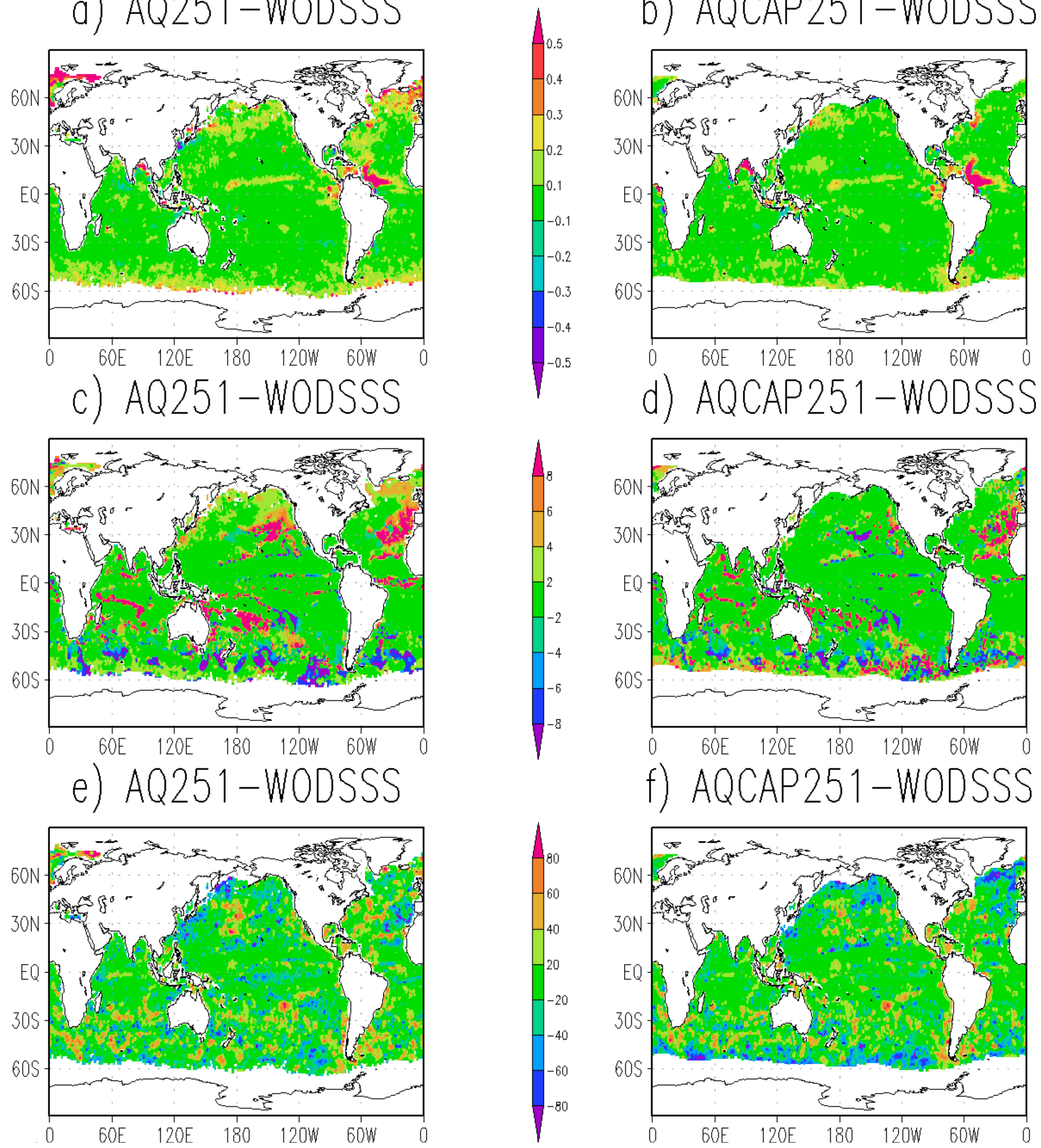

Figure 2.10: Difference in the first harmonic (09/2011-08/2013) for a) AQ251 – WODSSS amplitude, b) AQCAP251 – WODSSS amplitude, c) AQ251-WODSSS phase, d) AQCAP251-WODSSS phase, e) AQ251-WODSSS percent variance, and f) AQCAP251-WODSSS percent variance.

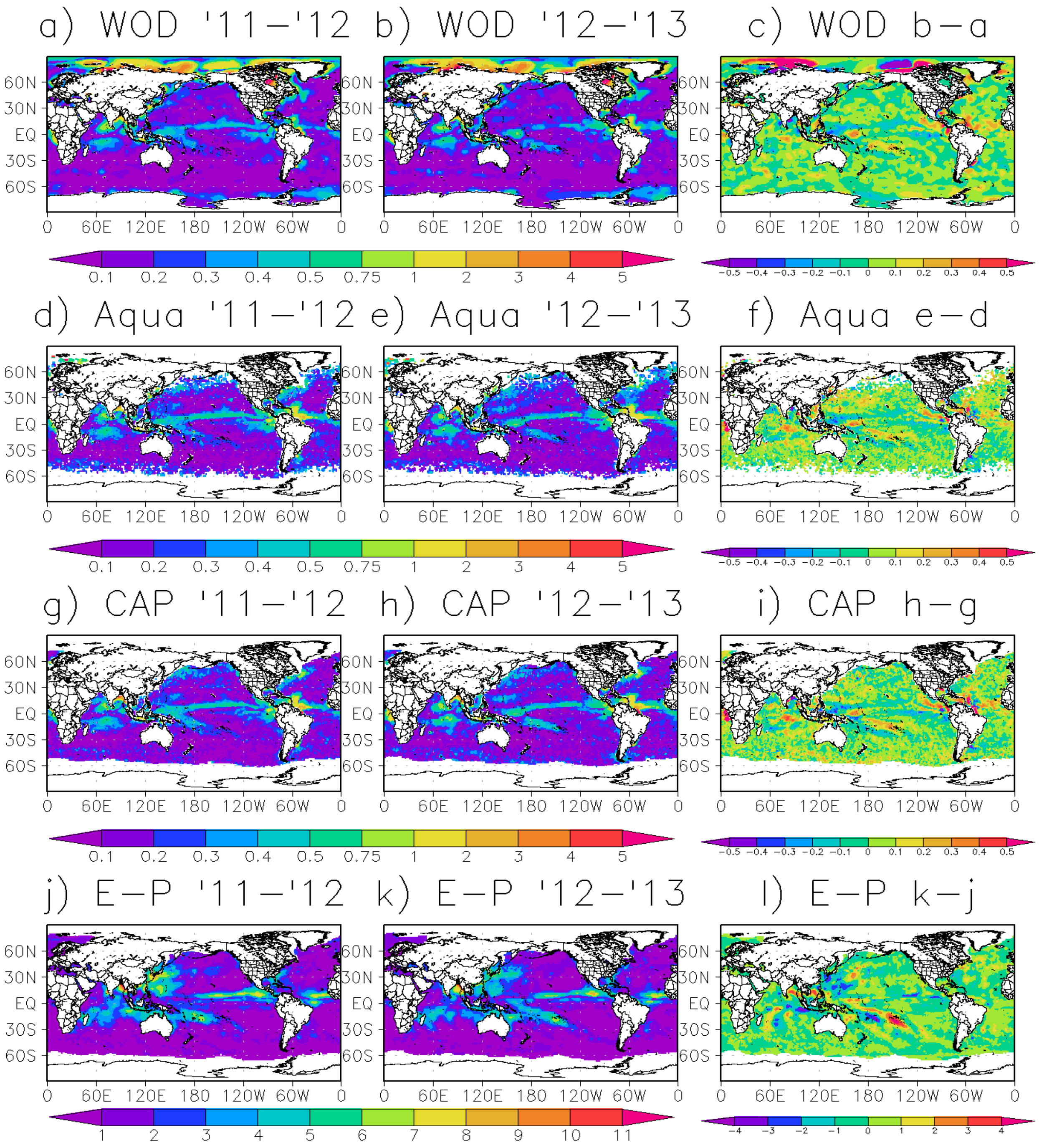

Figure 2.11: Amplitude of the first harmonic for a) WODSSS 09/2011-08/2012, b) WODSSS 09/2012-08/2013, c) WODSSS Amplitude difference (b-a), d) AQ251 09/2011-08/2012, e) AQ251 09/2012-08/2013, f) AQ251 Amplitude difference (e-d), g) AQCAP251 09/2011-08/2012, h) AQCAP251 09/2012-08/2013, i) AQCAP251 Amplitude difference (h-g), j) E-P 09/2011-08/2012, k) E-P 09/2012-08/2013, and l) E-P Amplitude difference (k-j).

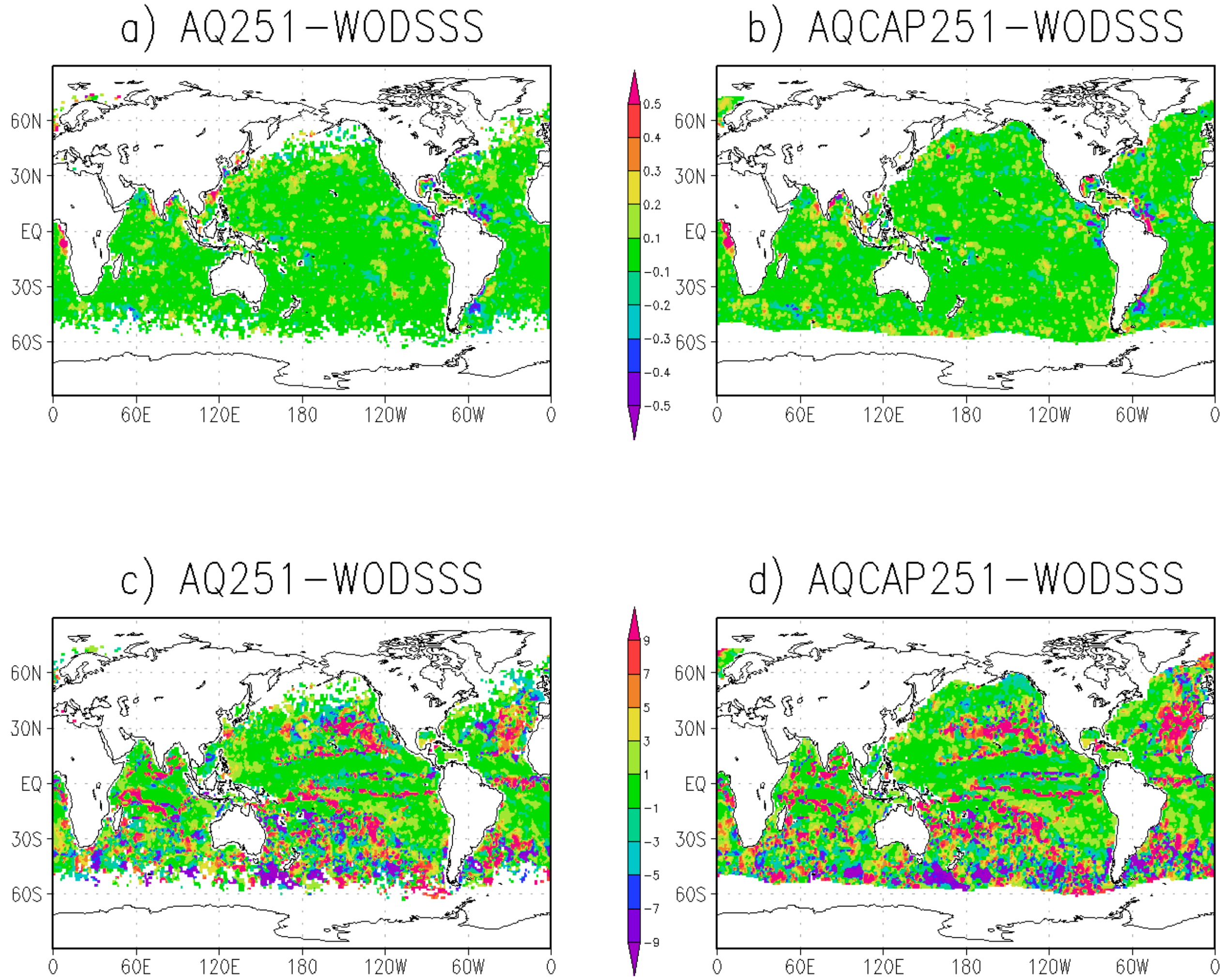

Figure 2.12: Interannual (09/2012-08/2013 - 09/2011-08/2012) differences in a) annual amplitude for AQ251-WODSSS (Fig. 2.11f-2.11c), b) annual amplitude for AQCAP251-WODSSS (Fig. 2.11i-2.11c), c) phase for AQ251-WODSSS, and d) phase for AQCAP251-WODSSS.

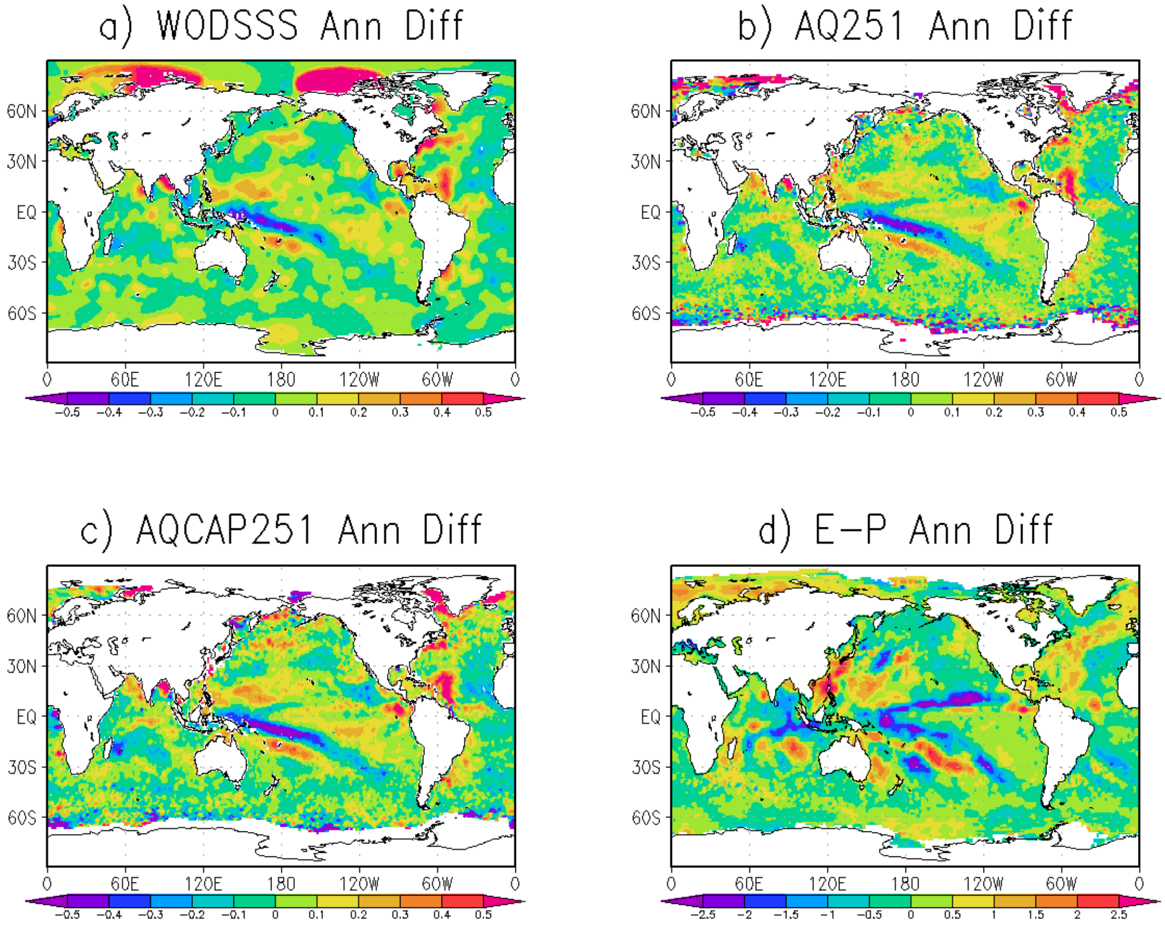

Figure 2.13: Annual difference between 09/2012-08/2013 and 09/2011-08/2012 for a) WODSSS b) AQ251 c) AQCAP251, and d) OAFlux Evaporation – GPCP v2.2 Precipitation (mm/dy).

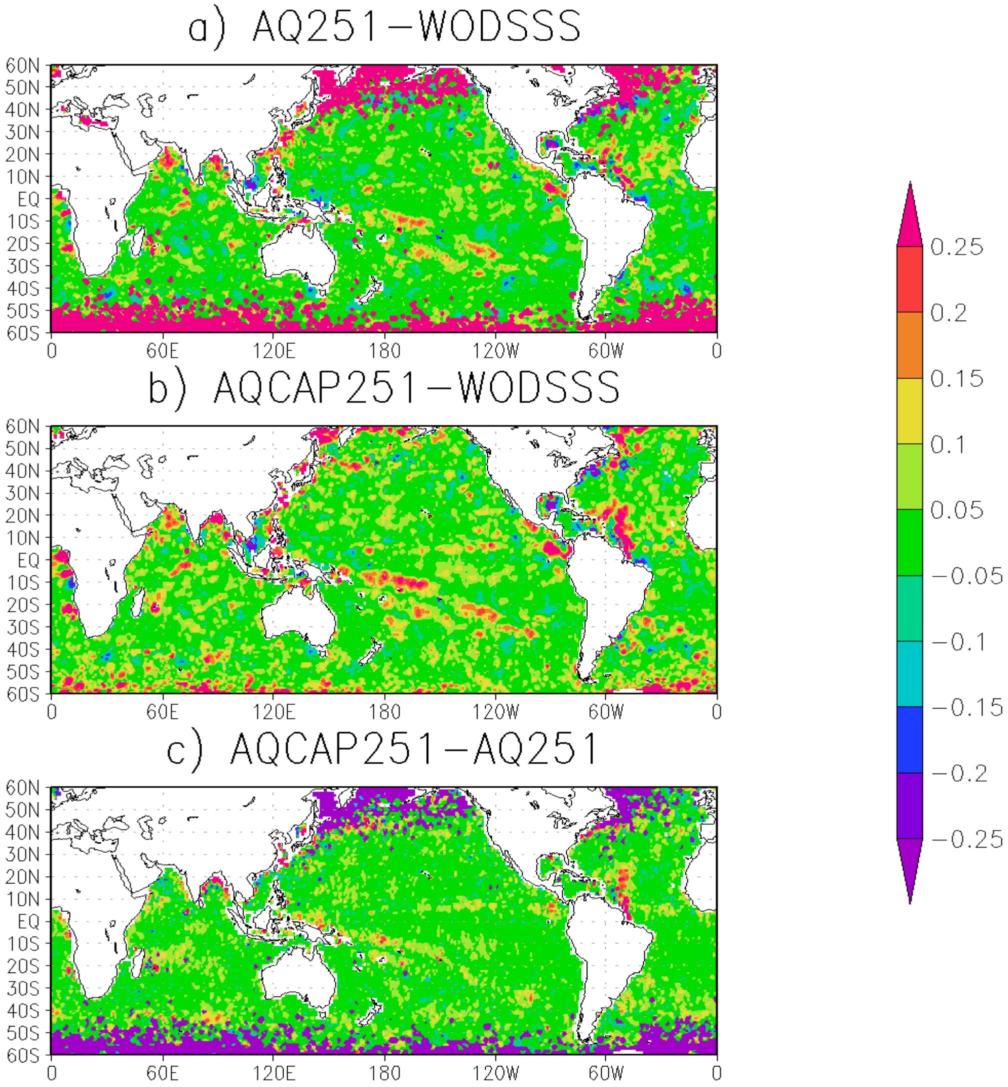

Figure 2.14: Absolute interannual (12/13-11/12) differences between a) AQ251 and WODSSS (Fig 2.13b-2.13a), b) AQCAP251 and WODSSS (Fig 2.13c-2.13a), and c) AQCAP251 and AQ251 (Fig 2.13c-2.13b).

Chapter 3: Water vapor transfer and near-surface salinity contrasts in the North Atlantic

Materials presented in this chapter have been published in *Nature Scientific Reports* as Reagan et al. (2018b) [https://doi.org/10.1038/s41598-018-27052-6]

Abstract: Maintaining North Atlantic (NA) intra-basin near-surface salinity (NSS) contrast between the high NSS (>37.0) in the subtropical NA (STNA) and low NSS (<35.0) in the subpolar NA (SPNA) has been shown to be important in sustaining the strength of the Atlantic Meridional Overturning Circulation. Evaporation (E) exceeding precipitation (P) in the STNA is primarily responsible for the high NSS there, whereas P dominating E in the SPNA contributes to its low NSS. With a basic understanding of NA intra-basin moisture transport, a correlation analysis was conducted between E-P/NSS over the NA subpolar gyre (SPG) and E-P across the rest of the NA over the 1985–2012 time period. Significant anti-correlations exist between E-P/NSS over the NA SPG and E-P over the central/northern STNA. This suggests that during times of high E over the central/northern STNA there is high (low) precipitation (NSS) over the SPG demonstrating a relationship likely exists between E over the STNA and NSS over the SPG. The maximum anti-correlated area is poleward of the maximum E-P location in the STNA, which is examined. These results provide a first step to ultimately utilizing NSS in the NA as a proxy for estimating changes in the hydrological cycle.

3.1 Introduction

The North Atlantic (NA) is the saltiest of all ocean basins (Zweng et al., 2013) with strong and highly variable intra-basin sea surface salinity contrasts (Reverdin et al., 2007), which are essential for the Atlantic Meridional Overturning Circulation (AMOC) (Seidov et al., 2003; Stouffer et al., 2007)—the major element of the world ocean thermohaline circulation interconnecting all major ocean basins (Broecker, 1991; Gordon, 1986). Very salty surface water in the subtropical North Atlantic (NA) is a prominent feature of near-surface salinity (NSS, here defined as the average salinity between 0 and 10m depths) distribution, with salinity exceeding 37.0 (dimensionless on the PSS-78 Scale). These high NSS values in the NA subtropical gyre are due to evaporation (E) substantially exceeding precipitation (P) (Schmitt, 1995, 2008).

Over 77% of global P and 85% of global E occurs over the ocean (Durack, 2015; Schmitt, 1995, 2008). While most of P and E occurs over the ocean, their historical estimates are plagued by large uncertainties in satellite observations (Lagerloef et al., 2010; Schanze et al., 2010), and assessing long-term change of E minus P (E-P) directly from measurements is therefore not feasible (Hegerl et al., 2015; Robertson et al., 2014). The satellite observation record (~1979-present) is also too short to assess long-term water cycle changes when compared to multi-decadal variability, and in situ data pre-1979 is full of large data gaps over the ocean (Hegerl et al., 2015). Evaporation and precipitation, particularly the difference (E-P), has also been shown to be largely uncertain when assessing the global ocean water cycle using state of the art atmospheric reanalyses (Yu et al., 2017). However, since global NSS changes are directly associated with E-P (Wüst, 1936), it is, in principle, possible to assess E-P indirectly through knowledge of the NSS variability (Durack et al., 2012; Skliris et al., 2014; Skliris et al., 2016; Terray et al., 2012; Vinogradova et al., 2017; Yu et al., 2017).

The AMOC functionality may be impacted by the long-term changes in NSS due to variability of the Earth's water cycle which can modulate the high-latitude convective and mixing processes essential for the sinking branch of the AMOC (Buckley et al., 2016). It has been observed that salty regions of the ocean are becoming saltier and fresh regions fresher over the past ~40-60 years (Boyer et al., 2005; Durack et al., 2010) which has been directly related to an amplification of the global hydrological cycle (Durack et al., 2012; Hosoda et al., 2009; Skliris et al., 2014), albeit with varying rates (Skliris et al., 2016).

Through some estimates using multi-decadal climatologies of E and P (Schmitt, 2008), the dominance of E over P yields a 1.16 Sverdrups (1 Sv = 106m3sec-1) rate of freshwater loss in the Atlantic Ocean, whereas the dominance of P over E in the Pacific Ocean yields a rate of freshwater gain of 0.5 Sv across the sea surface. With E dominating the Atlantic and P dominating the Pacific, an amplification of this pattern would lead to further salinification of the Atlantic and freshening of the Pacific. This salinity inter-basin dipole has been amplifying since the 1950's (Boyer et al., 2005; Durack et al., 2010; Skliris et al., 2014) and is primarily sustained by ~0.5 Sv of water vapor over the subtropical Atlantic being transported across Central America and deposited as precipitation in the equatorial Pacific (Singh et al., 2016). However, very little water vapor is transported from the Pacific and deposited as precipitation in the Atlantic due to the blocking of moisture transport by the Rocky Mountains (Schmittner et al., 2011).

Models have shown that the inter-basin moisture transport—termed an "Atmospheric Bridge" (Marsh et al., 2007)—and resulting NSS contrasts between the Pacific and Atlantic is a key controlling mechanism of the global thermohaline circulation (Marsh et al., 2007; Seidov et al., 2002, 2005). Additionally, this inter-basin salinity amplification is projected to continue (Terray et al., 2012). Marsh et al. (2007) argued that the long-term fate of the AMOC is sensitive to two processes by which high Atlantic surface salinity is maintained, the Atmospheric Bridge and the Agulhas Leakage. In freshwater "hosing" model simulations (Marsh et al., 2007; Seidov et al., 2005; Stouffer et al., 2007; Stouffer et al., 2006), high-latitudinal freshening and thus subtropical-subpolar NSS contrast in the NA have risen as an important if not key factor (Seidov et al., 2003; Stouffer et al., 2007) impacting the AMOC, while similar freshening in the Southern Ocean did not inflict noticeable AMOC change (Stouffer et al., 2007).

The NSS intra-basin contrasts in the NA are especially important, as they are essential for the AMOC dynamics. Singh et al. (2016) showed that most of the P in the NA is sourced from the NA with very little moisture contribution from other ocean basins. To assess long-term ocean climate change, it is of paramount importance to understand how the salinity contrasts within the NA are being built and maintained. In our research we address one specific aspect of this broader task, namely—to uncover possible correlations between E-P and NSS in the subtropical and subpolar regions of the NA. The implications of detecting and quantifying such correlations may be far reaching—utilizing NA in-situ NSS observations as a proxy for estimating E-P.

Although the inter-basin water vapor exchange and inter-basin salinity contrasts are well documented, some ambiguity still exists regarding the connection between the intra-basin E and P distribution and salinity contrasts in all oceans. In more general terms, it is not yet well known how the spatial variability of the hydrological cycle correlates with the changes of the intra-basin NSS contrasts. This study aims to address this ambiguity.

3.2 Results and Discussion

The subtropical-subpolar NA atmospheric moisture transport is an effective and rapid (on the order of days to weeks) mechanism of freshwater transport between positive and negative E-P regions in the NA and is, along with advection of freshwater into the subpolar North Atlantic, one of the main candidates for maintaining the observed inter-gyre NSS contrasts. The mechanism of this moisture transport is schematically depicted in Figure 3.1. Over the subtropical NA (STNA, approximate area shown in green box of Figure 3.2a), where E>P, water vapor is produced and then diverges away from the NSS maximum salinity region. Although the strength and direction of the divergence of water vapor from the STNA varies with seasons (Li et al., 2016a, 2016b), in all four seasons it is captured and precipitated in four different regions: (i) along the Atlantic Intertropical Convergence Zone (ITCZ), (ii) in the eastern tropical Pacific ITCZ (via the aforementioned Atmospheric Bridge), (iii) off the East Coast of North America, and (iv) in the subpolar North Atlantic (SPNA, approximate area shown in red box of Figure 3.2a). Since the ITCZ dynamics and potential impacts on tropical NSS is outside our focus on the extratropical NSS interconnections, only the SPNA and STNA NSS contrasts and their relations to the hydrological cycle are the subject of this study.

In the atmosphere, water vapor transported to the East Coast of North America is typically captured within eastward/northeastward moving mid-latitude cyclones that generally originate due to baroclinic instability caused by sharp temperature gradients off the East Coast of North America. These storms are stronger and more frequent in winter due to increased baroclinic instability. They generally follow a similar northeast trajectory (i.e., storm tracks) directing them and their associated precipitation to the subpolar and northeast Atlantic regions (Bengtsson et al., 2006; Chang et al., 2002; Hoskins et al., 2002; Shaw et al., 2016). Excess E over P along the Gulf Stream path and in the STNA also provides moisture for NA atmospheric rivers (Ramos et al., 2016) throughout the year (Eiras-Barca et al., 2016). Alternatively, a north/northwestward moisture transport from the E>P STNA region (see the schematics in Figure 3.1) can cause convergence in the SPNA leading to precipitation, particularly during certain seasons.

There are two major pathways for water vapor produced in the STNA to be transported and deposited (as precipitation) in the SPNA: the indirect pathway (i.e., water vapor is captured in a mid-latitude cyclone and transported along the NA East Coast storm track) and the direct pathway (i.e., north/northwestward moisture divergence from STNA with convergence over SPNA), as the scheme in Figure 3.1 suggests. For the indirect pathway, the latency between water vapor production in the STNA and deposition in the SPNA is at most a week or two, with the direct pathway requiring just several days.

The rate of freshening in the subpolar gyre (SPG) depends on the amount of water vapor transported northward from the subtropical gyre (STG) that precipitates over the SPG leading to P dominating E. For our analysis, we computed the monthly climatological distribution of evaporation minus precipitation (E-P) averaged over the time period between 1985 and 2012 (Figure 3.2a) using the Objectively Analyzed air-sea Fluxes (Yu et al., 2008) (OAFlux) monthly evaporation fields and the Global Precipitation Climatology Project version 2.2 (Adler et al., 2003) (GPCP) monthly precipitation fields (full description and reasoning of data selection, data processing, and calculations can be found in Methods). The maximum of E-P (>4.0 mm/day) occurs in the southeast NA, between 15°N and 40°N centered around 30°W and 20°N. There is also a secondary maximum along the US east coast following the Gulf Stream path. E-P slowly decreases to the north, with P beginning to exceed E at about 40°N and with the maximum negative E-P (<-4.0 mm/day) occurring southeast of Newfoundland. On average, the SPNA has E-P rates of roughly -2.0 mm/day.

To assess the STNA-SPNA moisture connection, a geographic E-P correlation analysis was performed using the OAFlux evaporation and GPCP precipitation fields. Figure 3.2b represents the correlations between the area-averaged E-P in the SPG (subset region of SPNA identified as the red rectangle in Figure 3.2b) and E-P throughout the rest of the NA over the three decadal time period from 1985-2012 (1985-1994, 1995-2004, and 2005-2012). High positive correlations (>0.5) exist in not only the SPG (where the area-averaged E-P was calculated), but also along the Gulf Stream path. High anti-correlations (<-0.5) extend from the central STNA to the northeast STNA, along the region of decreasing E-P (as shown in Figure

3.2a). This is consistent with other reanalyses and hybrid E-P products (see Appendix B Figure B.1). Hence, when E-P increases (i.e., increased water vapor production) in the central and northeastern regions of the STNA, E-P decreases (i.e., increased precipitation) in the SPG. This can be clearly seen in Figure 3.2c showing the area-averaged 36-month time series of E-P for the subpolar (red box in Figure 3.2b) and subtropical (green box in Figure 3.2b) regions. The full time series has a -0.71 correlation ($p<0.0001$), with late boreal summer/early fall being most noticeably anti-correlated. Other reanalyses and hybrid E-P products show similarly strong anti-correlated time series of intra-basin E-P (see Appendix B Figure B.2). During this time, the northern subtropics experience maximum E-P (i.e., maximum evaporation), while the SPG has minimum E-P (i.e., maximum precipitation). Additionally, the positive correlation between E-P over the Gulf Stream path and the SPG E-P (Figure 3.2b) indicates that they share a similar seasonal cycle of precipitation, which is likely due to their strong connection through the storm tracks as shown in Figure 3.1. Essentially, Figure 3.2 implies that the water vapor produced over the central and northeastern STNA is transported both directly and indirectly to the SPG where it is deposited as precipitation.

The E-P relationship between the STNA and SPNA is rather straightforward; E-P is primarily based on the convergence/divergence of vertically integrated moisture fluxes (Byrne et al., 2015). NSS, on the other hand, is affected by many other factors besides E-P (Yu, 2011), but understanding the SPNA NSS relationship with the STNA E-P is essential to eventually estimating E-P from NSS (or vice-versa) in the North Atlantic. This first step towards a better understanding of intra-basin relations between E-P and NSS can be viewed as a starting point for future work on utilizing subpolar NSS measurements as a proxy for estimating NA E-P.

The correlation between the SPG NSS (SPG-NSS) and NA E-P (Figure 3.3a) shows a pattern similar to the SPG E-P and NA E-P correlation (Figure 3.2b). All NSS calculations are based on the World Ocean Atlas 2013 (Zweng et al., 2013) (WOA13) fields. The positive correlations of E-P (~0.4-0.6) in the SPG with the area averaged SPG NSS (red box in Figure 3.3a) illustrates that local E-P plays a role in the near-surface salinity budget (NSSB) in the subpolar area, but E-P may not dominate all other terms in the NSSB (i.e., advection, meltwater, entrainment, etc.) (Yu, 2011). This is especially so during certain seasons (e.g., during spring when sea ice melts and thus augments E-P in freshening the sea surface). There is a large E-P area that extends from the northcentral STNA to the northeastern STNA where the SPG NSS and E-P are significantly (95%, $r<-0.330$) anti-correlated (Figure 3.3a). The pattern in this region is very similar to the area with significant anti-correlation in Figure 3.2b. Thus, when there is high E-P in the northcentral to northeastern STNA region, there is low NSS in the SPG.

A time series in both areas may help better illustrate these inter-relations. Figure 3.3b shows the same area-averaged regions of Figure 3.2b (green box = northern subtropics, red box = SPG), but plots SPG NSS rather than E-P. The SPG NSS and the STNA E-P 36-month time series were then normalized to allow plotting on the same figure (Figure 3.3b). During late summer/early fall when E-P is at maximum in the northern subtropics, NSS is at its lowest in the SPG. The correlation is -0.64 ($p<0.0001$) between the area-averaged NSS of the SPG and E-P over the northern subtropics. This means that the additional water vapor produced in the northcentral/northeastern STNA region during high E-P periods is likely transported, via both direct and indirect pathways, to the SPG where it falls as precipitation lowering NSS. The NSS and E-P do not anti-correlate quite as strongly as seen in Figure 3.2b because NSS in the SPG is shaped by more than just local E-P as discussed previously (Yu, 2011). The region of highest anti-correlations between SPG NSS and NA E-P in Figure 3.3a and the corresponding area-averaged time series in Figure 3.3b are consistent with other reanalyses and hybrid E-P products (see Appendix B Figures B.3 and B.4), with some reanalyses extending the area of significant anti-correlations across the entire North Atlantic (Appendix B Figure B.3).

The highest anti-correlations in Figure 3.3a are to the north (latitude range of ~30°-40°N) of the E-P maximum in the STNA (see Figure 3.2a). While this may be counter-intuitive, the 1985-2012 seasonal averages of the divergent components of the vertically integrated moisture flux (DCMF) vectors over the NA (Figure 3.4a-d, black vectors) from the Modern-Era Retrospective analysis for Research and Operations – Version 2 (MERRA-2) (Gelaro et al., 2017) imply that the anti-correlation in Figures 3.2b and 3.3a are located in regions where the divergent component of the moisture flux is directed poleward away from the region of maximum E-P. Additionally, the vertically integrated moisture flux divergence (VIMFD) is slightly positive (Figure 3.4a-d, orange shades) but becomes negative (Figure 3.4a-d, blue shades) at the northern extent of this STNA region characterized by significant anti-correlations. The divergent components of the moisture fluxes converge (Figure 3.4a-d, blue shades) in the SPNA with additional convergence in spring and summer along the storm track area in the STNA. This is generally consistent with other reanalyses (see Appendix B Figures B.5 and B.6). In a statistically steady state of the atmosphere, and more general 2-D formulation, E-P is balanced by the divergence of the horizontal moisture flux, $E - P = \nabla \cdot \mathbf{F}$, where F is the vector of horizontal moisture flux integrated over the depth of the atmosphere (Byrne et al., 2015), thus the convergence (divergence) regions in Figure 3.4a-d indicate where P (E) exceeds E (P). It should be noted that there exists high anti-correlations between E-P along the near-coast of North America and SPG NSS (Fig. 3.3a). They are likely due to unrelated anti-correlated seasonal cycles as there is little to no moisture production (Fig. 3.4a-d, orange shades) in this region that can be transported to the SPG, and thus no easily seen physical mechanism linking the two. Additionally, the DCMF (Fig. 3.4a-d, vectors) in this region is mainly north-northwestward and not directed towards the central SPG.

Examination of the meridional component of the divergent moisture fluxes (see Figure 3.4a-d, vectors) demonstrate that, after taking the zonal average across 60°W-20°W over the 20°N-75°N domain, the poleward divergent moisture fluxes are strongest between 35° and 45°N for nearly all seasons (Figure 3.5a-d, black line). Importantly, these poleward divergent fluxes are strongest (~60 kg*m-1*sec-1) in summer (Figure 3.5c, black line), coinciding with the highest E-P in the northern subtropics (Figures 3.2c and 3.3b). Additionally, the zonal average of the vertically integrated moisture flux divergence (Figure 3.5a-d, red line) shows that the strongest convergence (~-2 mm*day-1) in the subpolar regions (50°-60°N) also occurs in late summer (Figure 3.5c, red line). These findings are consistent with another state-of-the-art reanalysis and differ somewhat from an older generation reanalysis (see Appendix Figures B.7 and B.8). However, the moisture fluxes from all products agree on the significant impact that the meridional component of divergent moisture fluxes can have on the redistribution of moisture in the North Atlantic and the role it can play in sustaining the NSS inter-gyre contrast.

Bringing all analyses together, it can be reasonably concluded that during late summer when E-P is at its maximum in the northern subtropics (Figure 3.2c- black line) there are near-maximum poleward divergent moisture fluxes (Figure 3.5c, black line) occurring in the vicinity at the same time. The poleward transport of this excess moisture yields ample amounts of available precipitable water, and with maximum convergence also occurring in summer (Figure 3.5c, red line) over the SPG we see this moisture fall as precipitation in the SPG leading to lower

NSS there (Figure 3.3b, red line). This seasonal cycle explains why such strong anti-correlations exist between E-P over the subtropics and E-P/NSS over the SPG.

3.3 Conclusions

The NA intra-basin NSS contrast and intra-basin moisture transport are connected and are essential components in maintaining the AMOC functionality. Although this focal point in ocean climate dynamics has been intensely investigated (see recent review (Buckley et al., 2016)), the connection between NA intra-basin water vapor production, transfer, and deposition and the inter-gyre NSS contrast remained largely underexplored. The provided correlation analysis in this study between NSS and E-P over the NA aims at improving the understanding of the role the hydrological cycle plays in maintaining the NA inter-gyre NSS structure. The major conclusions are the following:

Subtropical E-P is significantly (95%, r<-0.330) anti-correlated with subpolar E-P in the NA and is consistent with multiple hybrid and reanalysis E-P products. The strong anti-correlations occur mainly between 30° to 40°N in the subtropics, which is also near the area where the poleward divergent component of the moisture fluxes are strongest. It implies that a significant amount of water vapor produced in the northcentral and northeastern STNA is transported poleward and deposited as precipitation in the SPG inferring substantial extra-tropical intra-basin redistribution of freshwater.

The same processes cause significant anti-correlations (95%, r<-0.330) between the subtropical E-P and subpolar NSS in the NA implying the seasonal cycle of E-P (particularly summer) over the northern subtropical NA and subpolar NSS are connected through intra-basin moisture transports.

In late summer, the E-P is at its maximum over the northern subtropical NA, and so is the strength of the poleward-directed moisture fluxes. This allows ample moisture to be pumped poleward where it converges over the subpolar region (also max in summer) and precipitates. Subsequently, the precipitation freshens the near-surface leading to decreased NSS.

In summary, the intra-basin moisture transport from the STNA is immensely important for maintaining intra-basin NSS contrasts. Future work in utilizing observed subpolar NSS as a proxy for estimating historical and current changes in the hydrological cycle is needed as there is a clear and coherent relationship between those two. Additionally, if the estimates of E over P substantially improve, it may permit the usage of E-P estimates over the subtropical NA to forecast changes in subpolar NSS, which can carry many different and far fetching implications.

3.4 Methods

This study operates with four different variables of the ocean-atmosphere system in the North Atlantic Ocean: near-surface salinity, evaporation, precipitation, and moisture fluxes. For each of these variables, monthly decadal climatologies were calculated for the 1985-1994, 1995-2004, and 2005-2012 decades. For moisture fluxes, in addition to the three aforementioned monthly climatologies, seasonal climatologies were also calculated.

3.4.1 Data

All gridded data used in this study and in the Supplementary Information (Appendix B) were interpolated to a 1°x1° spatial grid. For original data that was of a finer resolution than 1°x1°, the data were interpolated using box-averaging. For original data that was of a coarser resolution than 1°x1°, the data were interpolated using bilinear interpolation. Salinity data is a dimensionless quantity reported on the PSS-78 Scale. All evaporation, precipitation, and vertically-integrated moisture divergence data were converted to units of mm*day-1. Moisture fluxes were, if necessary, converted to kg*m-1*sec-1. For all fields, with the exception of salinity which is already available as monthly decadal climatologies, the decadal monthly climatologies were calculated from the monthly fields by averaging all months within each decade of interest. For example, the January 1985-1994 evaporation decadal climatology was compiled by averaging the monthly evaporation from January 1985, January 1986, and so on through January 1994. Thus, all decadal climatologies computed and used in this study were presented on the same temporal and spatial resolutions. Below is a brief description of all datasets used and where they can be acquired.

3.4.1.1 Salinity

The monthly decadal climatological salinity data are from the World Ocean Atlas 2013 Version 2 (WOA13) (Zweng et al., 2013) (available at: https://www.nodc.noaa.gov/OC5/woa13/). The WOA13 salinity fields were calculated using in situ profile data from the World Ocean Database (Boyer et al., 2013). The WOA13 provides gridded climatological salinity fields for the 1955-1964, 1965-1974, 1975-1984, 1985-1994, 1995-2004, and 2005-2012 decades as well as an average of those six decades. For this study, only the monthly fields for the last three decades (i.e., 1985-1994, 1995-2004, and 2005-2012) were used. Additionally, near-surface salinity was defined to be the average of the first three levels (i.e., 0, 5, and 10m) of the WOA13 salinity fields. The 0-10m average salinity was used rather than just the 0m salinity for two reasons: 1.) mixed layer depth in the subpolar region is generally greater than 10m throughout the year (de Boyer Montégut et al., 2004) yielding well-mixed salinity in the 0-10m depth range and 2.) to ensure instruments whose shallowest measurements are made at depths greater than 5m (i.e., many Argo floats shallowest measurements are made between 5-10m) are included in our analysis.

3.4.1.2 Evaporation

The evaporation data is from the Woods Hole Oceanographic Institute (WHOI) Objectively Analyzed air-sea Fluxes (OAFlux) Project (Yu et al., 2008) (available at:

http://oaflux.whoi.edu/index.html). The original evaporation data are monthly from January 1958 through September 2015 in units of cm*yr-1.

For the Supplementary Information (Appendix B), additional evaporation products were used and underwent similar transformations to establish the decadal climatologies. These products include the following reanalyses: the European Centre for Medium-Range Weather Forecasts (ECMWF) Reanalysis-Interim (Dee et al., 2011) (ERA-I), the Modern-Era Retrospective analysis for Research and Applications – Version 2 (Gelaro et al., 2017) (MERRA-2), and the NCEP/NCAR Reanalysis 1 Project (Kalnay et al., 1996) (NCEP). Additionally, we also utilized the evaporation data from the Coordinated Ocean-ice Reference Experiments version 2 (Large et al., 2009) (COREv2).

3.4.1.3 Precipitation

The precipitation data is from the Global Precipitation Climatology Project (GPCP) (Adler et al., 2003) (available at: https://www.esrl.noaa.gov/psd/data/gridded/data.gpcp.html). For this study, version 2.2 of the data was used. The original precipitation data were monthly 2.5°x2.5° fields from January 1979 through September 2015 in units of mm*day-1.

For the Supplementary Information (Appendix B), additional precipitation products were used and underwent similar transformations to establish the decadal climatologies. These products include the following reanalyses: ERA-I, MERRA-2, and NCEP. Additionally, we also utilized the COREv2 precipitation data. The COREv2 precipitation data blends multiple precipitation products, some of which merge in situ and satellite observations. Additionally, the evaporation data in COREv2 is, at least partially, derived from variables provided by reanalysis output (Large et al., 2009). Therefore, because the COREv2 E-P dataset is a mixture of in situ observations, satellite observations, and reanalysis data, we consider it a hybrid E-P product in this study.

3.4.1.4 Evaporation minus Precipitation (E-P)

We combine the OAFlux evaporation and GPCP precipitation fields to assemble E-P. These selected products have been successfully utilized in many recent studies relating ocean salinity and the water cycle (Ren et al., 2014; Skliris et al., 2014; Skliris et al., 2016; Vinogradova et al., 2017; Yu, 2011; Yu et al., 2017). Additionally, the OAFlux evaporation and GPCP precipitation were also found to be in good agreement with in situ measurements and, when combined with river runoff data, do a good job at closing off the oceanic freshwater budget (Schanze et al., 2010).

3.4.1.5 Moisture Fluxes

The zonal and meridional moisture flux data is from the Modern-Era Retrospective analysis for Research and Operations – Version 2 (Gelaro et al., 2017) (MERRA-2) reanalysis. The data is available at: https://gmao.gsfc.nasa.gov/reanalysis/MERRA-2/data_access/. The original MERRA-2 moisture fluxes were monthly 0.5°x0.625° in units of kg*m-1*sec-1. One of the primary focuses of MERRA's (MERRA-2's predecessor) development was an improved representation of the global water cycle, and that focus continued with MERRA-2's development (Bosilovich et al., 2017; Gelaro et al., 2017), which justified our selection of this product for moisture flux related analysis.

For the Supplementary Information (Appendix B), additional moisture fluxes were used and underwent similar transformations to establish the decadal climatologies. These products include the following reanalyses: ERA-I and NCEP.

The ERA-I and NCEP evaporation minus precipitation and moisture flux data were made available through the National Center for Atmospheric Research (NCAR) Climate and Global Dynamics (CGD) Climate Analysis Section's Data Catalog (available at: http://www.cgd.ucar.edu/cas/catalog/index.html). The COREv2 evaporation and precipitation data were made available through the Research Data Archive at the National Center for Atmospheric Research (available at: https://rda.ucar.edu/datasets/ds260.2/).

3.4.2 Decadal Averaging and Correlation Analysis

For NSS, E, and P analyses, we only used the three decadal climatologies spanning from 1985 through 2012. While there is NSS, E, and P data predating this time period, the launch of microwave imaging satellites in 1987 allowed for improved estimates of certain water flux parameters (e.g., wind speed), thus a discontinuity in the E and P data arises around 1987 (Schanze et al., 2010). Our earliest decade begins in 1985 which is pre-1987; however, we see little difference in the E and P fields whether we use 1988-1994 or the 1985-1994 period, likely due to the large amount of averaging that the data undergoes to form decadal climatologies. Some atmospheric reanalyses do contain E, P, and moisture flux fields before the satellite era (~1979), but the lack of in situ data before 1979, particularly over the oceans, causes a severe lack of data being assimilated into the reanalysis models. Appendix B Figure B.9 illustrates the area-averaged monthly decadal averages of E-P over the 1957-2002 period from the ERA-40 reanalysis (Uppala et al., 2005) in the subpolar and subtropical NA. There is a clear degradation of the seasonal cycle of E-P during the 1957-1964 and 1965-1974 periods (as compared to the latter 3 decades) over the subpolar NA, likely due to the misrepresentation of precipitation in the subpolar NA. Thus, we confine this study to the 1985-2012 period. The ERA-40 data was acquired from the Asia-Pacific Data-Research Center (http://apdrc.soest.hawaii.edu/data/data.php).

The correlation calculations performed in this study and additional results provided in the Supplementary Information (Appendix B) were done through calculating the area-average E-P and NSS in the subpolar gyre (we defined the subpolar gyre as the area encompassing 310°-330°E and 50°-60°N), and correlating the 36 month time series (3 decadal monthly climatologies) to each grid point's E-P time series in the NA. Additionally, we computed the area-average E-P over the northern subtropics (defined as the area encompassed by 315°-345°E and 32°-38°N) to be used in the time series plots and was also used to compute the time series correlations with area-average SPG NSS and E-P. For all correlation calculations, the data were de-trended using simple linear regression. The sample size (i.e., time period) for each correlation calculation is 36 (N = 12 months * 3 decades) with 34 degrees of freedom (N-2).

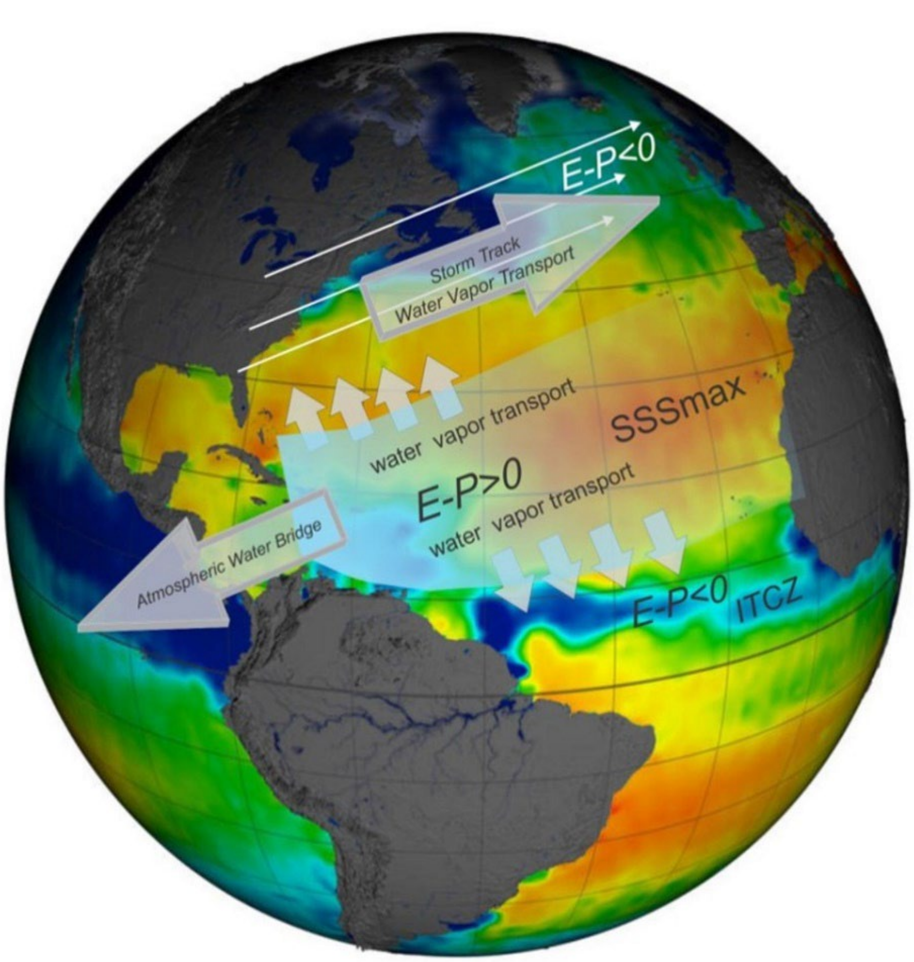

Figure 3.1: Schematic of the North Atlantic moisture transport. The background image with colored shadings of salinity is from the Aquarius satellite and courteous of NASA's Goddard Space Flight Center Scientific Visualization Studio (https://svs.gsfc.nasa.gov/4046). Evaporation minus precipitation (E-P) is indicated by the white shadings, and atmospheric moisture transport is shown by the various arrows.

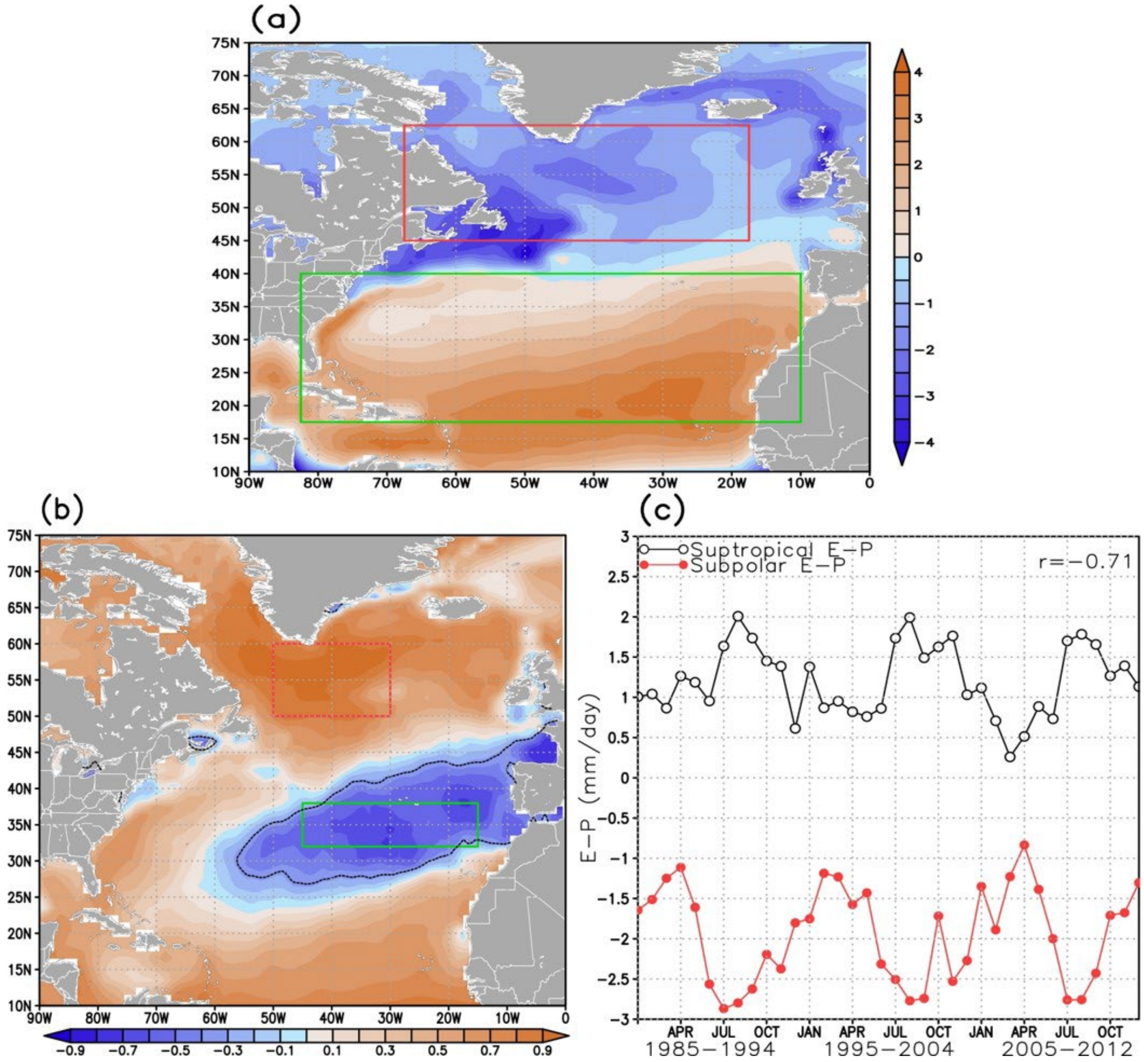

Figure 3.2: The 1985-2012 North Atlantic (a) Climatological E – P (mm*day-1), (b) correlation between the areal averaged subpolar gyre E-P (red-contoured rectangle in b) and the E-P over the rest of the North Atlantic Ocean, and c) time series of E-P over the subpolar NA (red box in b) and E-P over the subtropical NA (green box in b). Correlations and time series are based on the 1985-1994, 1995-2004, and 2005-2012 monthly climatological E and P fields (N=36). The red box in (a) designates the subpolar North Atlantic (SPNA) region and the green box designates the subtropical North Atlantic (STNA). Black dotted line in (b) represents the region where correlation is lower than -0.330 (95% CI).

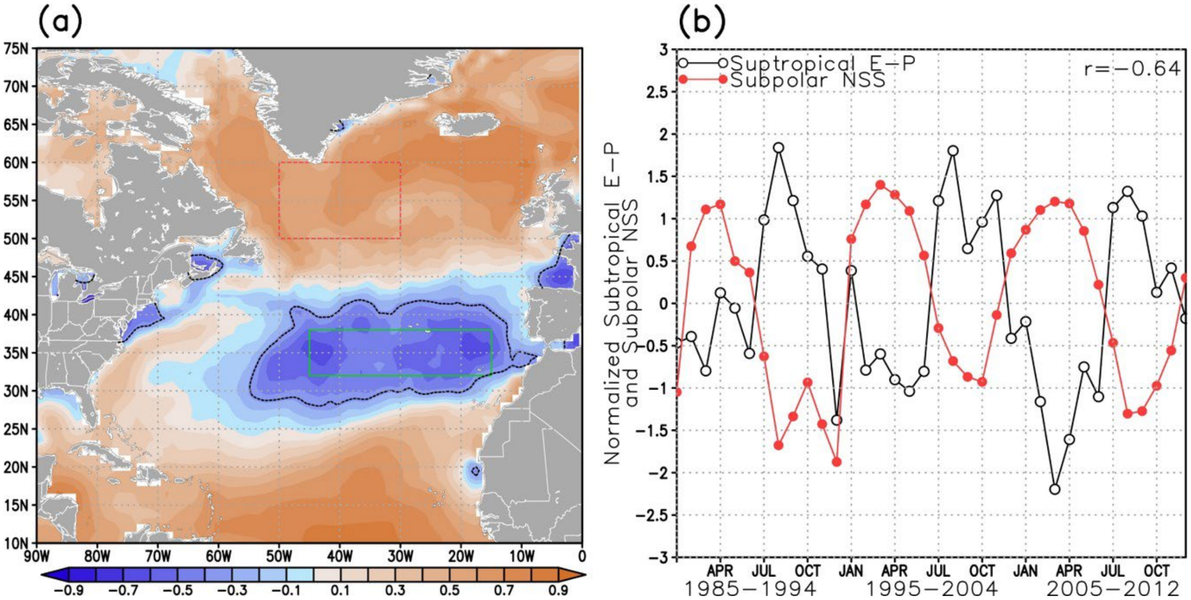

Figure 3.3: Similar to Figure 3.2, but a) represents correlation between area-average subpolar NSS (red box) and NA E-P and b) is the normalized time series of NSS from the red box in (a) and E-P from the green box in (a). Black dotted line in (a) represents the region where correlation is lower than -0.330 (95% CI).

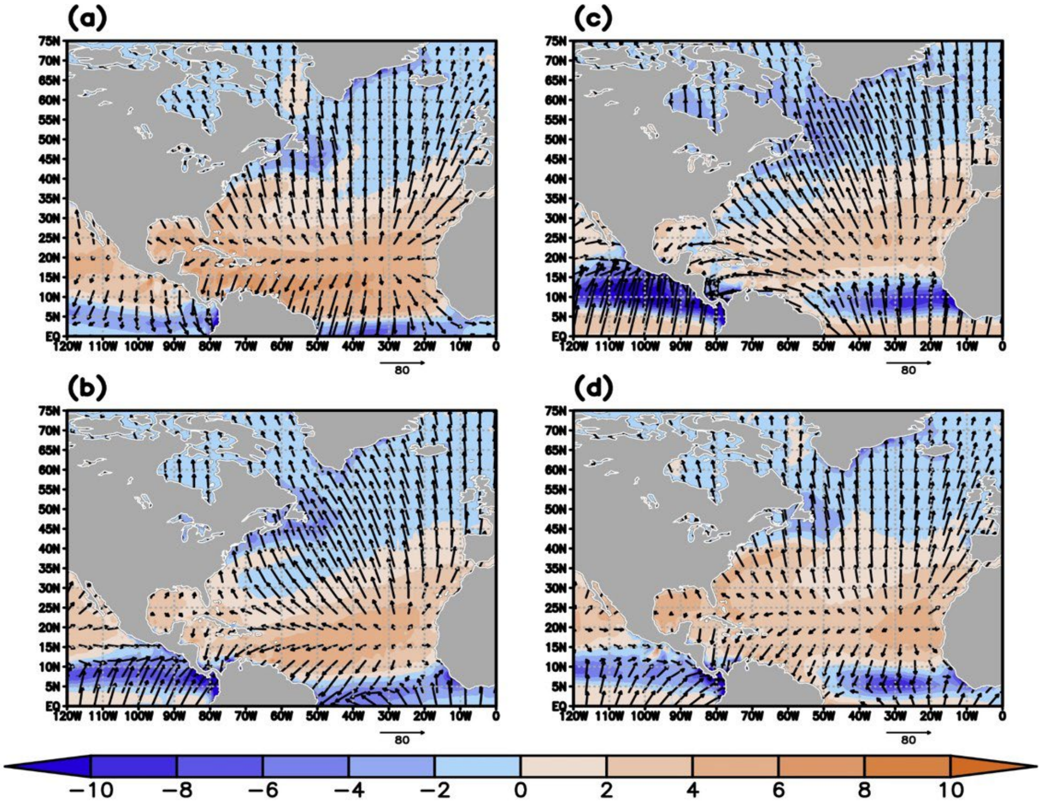

.

Figure 3.4: The 1985-2012 seasonal average of the vertically integrated moisture flux divergence (VIMFD, mm*day-1, shaded) and the divergent component of the moisture fluxes (DCMF, kg*m-1*sec-1, vectors) for a) winter (JFM), b) spring (AMJ), c) summer (JAS), and d) fall (OND). Orange shades represent moisture divergence and blue shades represent moisture convergence.

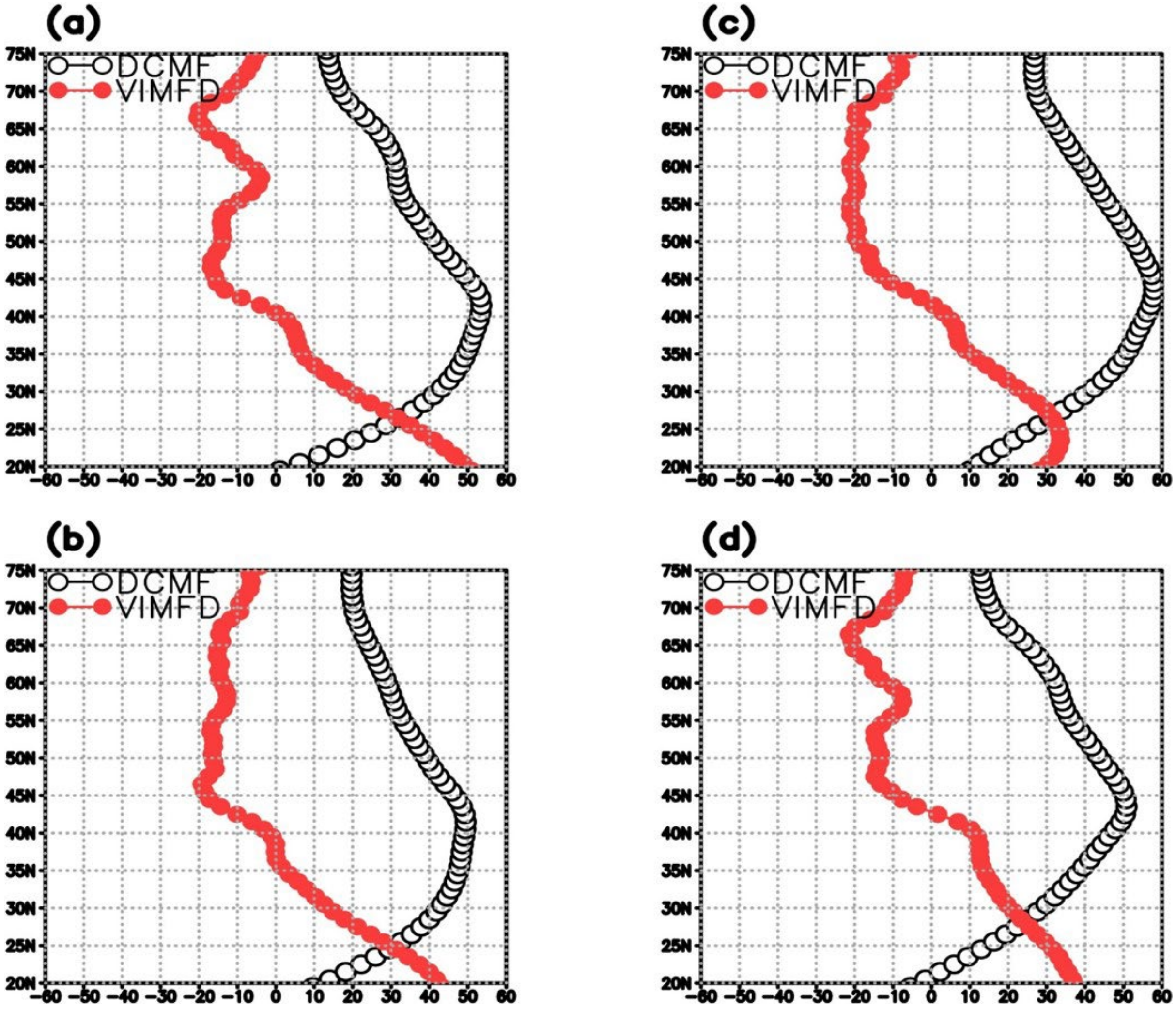

Figure 3.5: The 1985-2012 zonal average of the meridional component of the DCMF (kg*m-1*sec-1, black line) and of the VIMFD (10*mm*day-1, red line) for a) winter (JFM), b) spring (AMJ), c) summer (JAS), and d) fall (OND). The zonal average was taken over the 60°W-20°W area (see Figure 3.4a-d).

Chapter 4: Long- and short-term trends in near-surface salinity from 1957/61-2019/23

Abstract: The global hydrological cycle is expected to amplify in a warming world where dry regions become drier and wet regions wetter. However, identifying secular changes is difficult due to the indirect methods of observing evaporation and precipitation (E-P) and the large noise that is often present. Salinity patterns are a fingerprint of E-P, and their amplifications have been used as a proxy to estimate amplifications in the hydrological cycle. This study implements an empirical framework put forth by Durack et al. (2012) to estimate salinity pattern amplifications, but leverages a robust methodology that removes natural variability using a novel approach, accounts for and propagates mapping uncertainty, and utilizes millions of additional profiles not available to Durack et al. (2012). We find over the 1957/61-2019/23 time period that salinity patterns have amplified at a rate of 4.89% per 50yr (CI 95: 3.83% to 6.06%) and are accelerating at a rate of 1.22 ± 0.64 % per 50yr per decade. Furthermore, we find that secular changes in salinity (i.e., salty areas become saltier and fresh areas fresher) are identifiable between 30- and 40-years, and the Atlantic/Pacific salinity contrast has been increasing over the same 1957/61-2019/23 time period which has been shown to help maintain the Atlantic Meridional Overturning Circulation. Finally, we highlight the importance of utilizing global climate models in future work to see if we can reproduce these findings, and if so, what exactly is driving them.

4.1 Introduction

A warming climate has the capacity to hold more moisture following the Clausius-Clapeyron relationship. A saturated atmospheric boundary layer responds to increases in SST by increasing saturation vapor pressure by approximately 7%/K. Such an increase can increase the strength of the tropospheric hydrologic cycle potentially causing the ‘dry gets drier, and wet gets wetter' paradigm (Held et al., 2006; Seager et al., 2012; Seager et al., 2010; Trenberth, 2011). However, energy budget considerations likely limit the increase in global-mean precipitation to be closer to 2-3%/K (O'Gorman et al., 2012; Trenberth, 2011). An amplified hydrological cycle can lead to increased chances of natural hazards, such as floods and droughts (Hirabayashi et al., 2008; Trenberth, 2011).

Most of Earth's hydrological cycle takes place over the ocean. The ocean covers 71% of the planet's surface and experiences 85% of global evaporation and 77% of global precipitation (Durack, 2015; Schanze et al., 2010; Schmitt, 2008). Precipitation (P) estimates over the ocean are primarily made through satellites, which indirectly measure precipitation through complex algorithms that relate radiances observed by the satellite to precipitation rate (Adler et al., 2003). Evaporation (E) is mainly estimated through a bulk aerodynamic method which requires knowledge of sea surface temperature (SST), air temperature, wind speed, and specific humidity (Yu et al., 2008). Due to the indirect methods of observing E-P over the ocean, and a lack of direct observations (e.g., evaporation pan, rain gauges) for sufficient validation, E-P estimates and associated changes are riddled with uncertainty over the ocean (Durack, 2015; Lagerloef et al., 2010). Additionally, secular changes in E-P are small when compared to natural variability making them even more difficult to detect (Hegerl et al., 2015).

When the ocean exchanges freshwater with the atmosphere the salt content per unit mass of water (salinity) is altered in the mixed layer. On seasonal time scales, in addition to air-sea freshwater fluxes, salinity can be modified by advection, entrainment, and horizontal diffusion. Each of these terms can dominate the mixed layer salinity budget in different regions of the global ocean at seasonal time scales (Yu, 2011). However, for longer time scales (e.g., decadal) salinity patterns are maintained by a balance of advection, mixing, and freshwater fluxes

(Durack, 2015). Since advection and mixing primarily redistribute salinity within the ocean, long-term changes in salinity are reflective of changes in freshwater forcing (Skliris et al., 2014).

Many recent studies have explored the relationship between near-surface and vertically integrated salinity changes and changes in the hydrological cycle (Boyer et al., 2005; Cheng et al., 2020; Douville et al., 2024; Durack et al., 2012; Gould et al., 2021; Hosoda et al., 2009; Shi et al., 2024; Skliris et al., 2014; Skliris et al., 2016; Terray et al., 2012; Zika et al., 2018). A common conclusion that many of these studies have come to is that fresh regions of the ocean, where precipitation dominates evaporation, have become fresher, and salty regions of the ocean, where evaporation dominates precipitation, have become saltier. These findings are consistent with the "rich get richer" mechanism where wet regions become wetter (i.e., enhanced precipitation) and dry regions become drier (i.e., enhanced evaporation) in a warming world (Chou et al., 2004; Chou et al., 2009; Held et al., 2006).

Durack et al. (2012) put forth an empirical framework to estimate salinity pattern amplification rates. The salinity pattern amplification rate quantifies how much the spatial contrast in salinity has changed. For example, Durack et al. (2012) estimated that sea surface salinity patterns from 1950 to 2000 amplified at a rate of ~8% (there was also 0.5°C of warming during this time). Thus, relative to the climatological salinity pattern, the salty-fresh contrast increased by 8%. They related this to, through leveraging multiple global climate models, a hydrological cycle amplification rate of ~4% per 0.5°C of warming. Skliris et al. (2014) estimated a surface salinity pattern amplification of 4.5% over a similar 50-year time period (they estimated the hydrological cycle amplification rate to be 4.7 ± 2.5% per °C from 1950-2010), and Cheng et al. (2020) estimated a pattern amplification over the 0-2000m water column of 5.2% ± 0.4% from 1960-2017 (equating this to a 2.6 ± 4.4% $°C^{-1}$ hydrological cycle amplification). There is also evidence that the amplification in salinity patterns are accelerating (Cheng et al., 2020; Skliris et al., 2014). Additionally, Zika et al. (2018) estimated salinity pattern amplifications of 2.04 ± 1.2% over 1957-2016 and directly attributed those amplifications to changes in the hydrological cycle. This amplification rate removed the effects from ice melt and ocean surface warming. The latter was found to play a major role in stratifying the upper ocean and impeding the ability for salinity to diffuse.

The previous studies have all found significant long-term salinity pattern amplifications and have related them to an amplified hydrological cycle; however, many questions still remain. How have salinity pattern amplifications grown over time? Are salinity pattern amplifications evident over the Argo profiling era (2005-present)? Are the salinity pattern amplifications consistent across the three major ocean basins (Atlantic, Pacific, Indian)? There has been evidence of salinity pattern amplification acceleration (Cheng et al., 2020; Skliris et al., 2014), but there's been no quantification of this acceleration. Can this be quantified? Despite their uncertainty, is there evidence of pattern amplifications within various E-P products?

This study sets out to answer the aforementioned questions utilizing the empirical methodology put forth by Durack et al. (2012), but with improvements we feel provide a more accurate assessment of the long and short-term salinity pattern amplifications. These improvements include using additional ocean salinity profile data not available to Durack et al. (2012), critically assessing and leveraging salinity mapping uncertainty, and using principal components and a multiple linear regression model to help remove natural variability from the salinity data. These improvements are further documented in section 4.2.3 – Improvements Over Prior Studies.

4.2 Methods

The methodology of this study is organized in the following manner: data used, what is pattern amplification and spatial pattern correlation and how is it calculated, and what improvements were made in our methodology that are advances over prior studies. A very broad diagram illustrating the methodology to derive pattern amplification and spatial pattern correlations in this study is shown in Figure 4.1.

4.2.1 Data

4.2.1.1 Salinity Data

The main data source for this study is the gridded salinity anomalies from the National Centers for Environmental Information (NCEI). We primarily use the pentadal (5-year running means from 1957-1961 through 2019-2023) and the annual (years 2005-2023) salinity anomalies in this study. The salinity anomalies are derived from quality controlled observational data on standard levels within the World Ocean Database (WOD) (A. V. Mishonov et al., 2024). For example, to derive the 2010-2014 pentadal salinity anomalies, all observational data from 2010-2014 are used (*i.e.,* Argo floats, CTD, bottle, glider, moored buoys, and ice drifting buoys). First, observational anomalies are calculated by removing the appropriate monthly climatology, from the World Ocean Atlas 2009 (Antonov et al., 2010), from the profile. Second, all anomalies are then bin-averaged into 1°x1° grid boxes. Finally, the mean anomalies are objectively analyzed following a modified Cressman approach (Barnes, 1964). Further details on this process can be found in the World Ocean Atlas 2023 Salinity documentation (Reagan et al., 2024b). Additionally, Boyer et al. (2005) contains a detailed description of the salinity anomaly calculations.

For this study, an average of the 0m and 10m analyzed fields were used. The 0m salinity anomaly fields are derived from WOD profiles whose shallowest measurement is 5.25m or less, which precludes some measurements, especially from Argo floats whose shallowest measurement is typically between 5 and 10m. Therefore, to increase the robustness of our salinity fields, the 10m salinity anomaly fields are also used. The 10m fields are derived from observational data whose shallowest measurement must be less than or equal to 10m. Due to these not being "surface" fields, we use the term near-surface salinity (NSS) to describe the average 0-10m salinity fields. Salinity is a unitless dimension in this study and is reported on the PSS-78 scale unless otherwise stated.

4.2.1.2 Net freshwater flux

The first E-P product comes together from two separate sources. The evaporation (E) data comes from the Objectively Analyzed air-sea Fluxes Project (OAFlux) at the Woods Hole Oceanographic Institution (WHOI) (Yu et al., 2008). The precipitation (P) data comes from the Global Precipitation Climatology Project (GPCP) (Adler et al., 2003). Since E-P computed from OAFlux and GPCP is not internally consistent like the below-mentioned products, a check on its mass conservation was carried out. The global ocean average E-P from OAFlux and GPCP was 0.14mm/day, which is within the range of uncertainty for satellite-based E-P estimates (Gutenstein et al., 2021).

The second and third E-P products we analyze are from the Modern-Era Retrospective analysis for Research and Applications, Version 2 (MERRA-2) (Gelaro et al., 2017), and the European Center for Medium Range Weather Forecasts Reanalysis version 5 (ERA5) (Hersbach et al., 2020), respectively. Both of these products contain their own internally consistent E-P estimates.

The OAFlux and GPCP products are observationally based products, and the MERRA-2 and ERA5 are reanalysis. All E-P products were regridded to a 1°x1° horizontal grid, and resampled to monthly, seasonal, annual, and pentadal time resolutions. All units were made to be mm/day. Uncertainties were provided for the OAFlux and GPCP products.

4.2.2 Salinity Pattern Amplification and Spatial Pattern Correlation

We use the empirical method for determining salinity pattern amplifications and spatial pattern correlations formulated by Durack et al. (2012), with some modifications that are discussed in section 4.2.3. The salinity pattern amplification is a quantification of how the contrast between fresh and salty regions of the ocean has intensified over time relative to a climatological baseline. The spatial pattern correlation identifies how strong the relationship is between climatologically fresh (salty) regions and their respective salinity trends. Salinity pattern amplifications are reported as a percentage change over 50 years, and the spatial pattern correlation is unitless.

First, NSS climatological anomalies are calculated for each 1° grid square. This is computed by taking the 0-10m average of the WOA09 annual climatology and removing the calculated 0-10m global climatological average value (in this study it was 34.62). Next, linear trends computed using linear regression were compiled for each relevant time period using the pentadal and annual NSS anomalies (denoted NSSa moving forward).

The next step is to calculate the zonal average of the linear trends and the NSS climatological anomalies for each major ocean basin. These points were then aggregated over all three basins, and a least squares regression was fitted with the zonal climatological anomalies being the independent variable and the zonally-averaged trends being the dependent variable.

The computed slope of this line represents the pattern amplification (multiplied by 100 for percent) and the correlation of the points represents the spatial pattern correlation. For example, a pattern amplification of 5% over 50 years means the salinity contrast of the climatological pattern has increased by 5%. Or, digging deeper, a salty point in the subtropical North Atlantic whose climatological anomaly is 2.00 (relative to the global average of 34.62) has now increased to 2.10 (2.00 x 1.05). A spatial pattern correlation of 0.7 means there is a strong relationship between climatologically fresh (salty) regions and regions experiencing freshening (salinification) trends. A highly correlated and positively amplified pattern indicates freshening in climatologically fresh regions and salinification in climatologically salty regions.

4.2.3 Improvements over Prior Studies

Numerous studies have investigated and quantified salinity pattern amplifications (Cheng et al., 2020; Durack et al., 2012; Skliris et al., 2014; Zika et al., 2018). However, this study improves on prior studies' methodologies by using and/or performing the following: utilizing current and historical ocean salinity data from WOD, only analyzing trends with sufficient data throughout the associated time period, removing natural variability from salinity and E-P data using a novel approach, and performing a strict accounting of uncertainty and weighing the uncertainty in calculations. The robust methodology implemented in this study will help provide improved estimates on historical and current salinity pattern amplifications and associated metrics.

4.2.3.1 Improved Temporal and Spatial Salinity Data Coverage

This study leverages more than 10 million ocean salinity profiles from the World Ocean Database (WOD) (A. V. Mishonov et al., 2024) in the creation of the 1957/1961-2019/2023 pentadal salinity anomaly fields. The 1950-2008 analysis period used by Durack et al. (2012) used ~1.6 million ocean profiles. If we were to intersect our analysis with the dates used in Durack et al. (2012), we would utilize ~4.0 million historical ocean profiles. Thus, not only does this study extend beyond the Durack study by 15 years and leverages millions of Argo ocean profiles during that time, it also uses more than 2.4 million historical ocean profiles during the 1957-2008 time period that were unavailable to Durack et al. (2012). With such considerable spatial heterogeneity and temporal biases in historical in situ salinity observations (see Fig. C.1, 1.3 and 1.4), incorporating millions of additional historical profiles improves the salinity anomaly representation and decreases the uncertainty.

4.2.3.2 Accounting for Natural Variability

This study reviews short and long-term salinity pattern amplifications. Both long-term and short-term salinity (and E-P) changes can be influenced by natural variability. Thus, to assist in removing some of the natural variability signal, we developed a multiple linear regression model (MLR). The model is built from the principal components (PCs) of the following detrended climate indices: Southern Oscillation Index (SOI), Pacific Decadal Oscillation (PDO), North Atlantic Oscillation (NAO), Atlantic Multidecadal Oscillation (AMO), Southern Annular Mode (SAM), Dipole Mode Index (DMI), Pacific-North American Index (PNA), Indian Ocean Basin Mode (IOBM), and the North Pacific Gyre Oscillation (NPGO). The significant PCs were identified using the Autoregressive model order 1 – AR(1) as the null model and Monte Carlo significant testing (Evans et al., 2001). This is a modern application of the Rule-N from Preisendorfer (1988). The first two PCs of the climate indices were found to be significant at the 95% confidence level. However, once the model was tested with both salinity and E-P data, only the first PC for all data products had the lowest Bayesian Information Criterion (BIC) and is therefore the only PC that was used in the MLR. The MLR was then used to remove the natural variability signal and the residuals were then left to analyze. A full outline of this procedure is provided in section C.1 of Appendix C.

It should be noted that, unless otherwise stated, the multiple linear regression to help account for natural variability has been applied and removed from the data, and the weighted least squares regression was used for both temporal and spatial regression computations.

4.2.3.3 Leveraging and Accounting for Uncertainty

This study, unlike many previous salinity amplification studies, assesses, leverages, and propagates the uncertainty originating in the original gridded salinity (and E-P) anomaly fields through to the final results. This strict accounting of uncertainty, along with its utilization in the analysis, allows for a more robust estimate of pattern amplifications and spatial pattern correlations. The details of uncertainty assessments, propagation, and significant testing used in this study is detailed below and in Appendix sections C.2, C.3, and C.4

4.2.3.3.1 Mapping Uncertainty and Linear Trend Estimation

Each gridded salinity anomaly field has an associated field of mapping uncertainties, one of which we designate as the standard error of the analysis. The standard error of the analysis fields are computed by calculating the difference between the bin-averaged anomaly and the objectively analyzed anomaly at each grid box for which there is a bin-averaged value (*i.e.,* observations). The standard error of these differences is then calculated within a radius of 669km. This radius corresponds to the second pass of the three-pass objective analysis scheme applied to create the salinity anomaly fields. This is approximately the size of the decorrelation length scale beyond which salinity anomalies are no longer significantly spatially correlated. As it may be expected, grid points with few observations nearby will incur larger uncertainties than grid boxes with many observations in its vicinity. More information regarding this uncertainty calculation can be found in the supplement of Levitus et al. (2012).

Additionally, since the pentadal salinity anomalies are running 5-year means, each time step is highly correlated with time steps before and after (we use the mid-point year as the "date" for the pentadal field). Thus, this effectively reduces our sample size from ~67 years down to ~13 independent time periods for the pentadal analysis. The uncertainty provided by the standard error of the analysis is used as a weighting factor in the linear trend estimate of the salinity anomalies at each grid point, and the reduced number of independent samples is utilized in calculating the uncertainty of the trend at each grid point. The details for how we calculate and use weighting in the linear trends, account for the autocorrelation in the running 5-year pentadal means, and propagate uncertainty through the calculations can be found in section C.2 of Appendix C.

4.2.3.3.2 Minimum Criteria for Trend Computations (3/50 Rule)

Assessing salinity trends at each grid point is a prerequisite of computing salinity pattern amplifications. However, there are large data-free regions in early pentads (see Fig. C.1). If we compute trends for grid points that have no data within or nearby for most of the time period, we are going to have an untrustworthy trend. As discussed in section 4.2.1, the analyzed salinity anomaly fields are created through objectively analyzing ocean profiles. The objective analysis uses a three-pass scheme with decreasing radii of influence (see Reagan et al. (2024b) for additional information). The smallest radius of influence is 446km, which means the data within this radius of influence imparts the most influence on that grid point’s final value. Therefore, we only compute trends for NSSa grid points that have at least three measurements within the smallest radius of influence (i.e., 446km) during at least 50% of the time period being analyzed (denoted the 3/50 rule). For example, for proper calculation of the 1971/1975-2010/2014 NSSa linear trend, we require at least 20 pentads for which the grid point had at least three measurements made within 446km. This approach helps ensure that the calculated trends were computed using sufficient historical data at each grid point.

4.2.3.3.3 Trend Significance Testing

Since salinity and E-P are both noisy variables in both time and space, we introduce a significance test using a modified Mann-Kendall trend test to determine whether or not a trend is significant (Hamed et al., 1998; Kendall, 1970; Mann, 1945). This test does not care about the distribution of the data, but simply looks at whether the data is consistently going up or down over time. Its implementation in this study is documented in section C.3 of Appendix C.

The modified Mann-Kendall trend test is performed for each valid grid point. We recognize that a small percentage of points will be significant simply by random chance due to multiple hypothesis testing. Thus, it is important to stress that the significant masks that are visible in the spatial trend maps (e.g., Fig. 4.2) should be used to only identify broad regions of significance and not individual grid points.

4.2.3.3.4 Zonal Averaging and Error Bounds of Pattern Amplifications

Thus far we've only discussed error propagation and uncertainty for the trend calculation at each grid point; however, uncertainty also must be carefully considered when we take the zonal means of each trend (and its uncertainty) during the second step of the pattern amplification and spatial pattern correlation calculation. Since the objective analysis that produces the salinity anomaly fields for this study uses a three-pass algorithm with three different radii of influence, there will be spatial correlations that exist between grid points (and their trends) that are up to 880km apart (largest radii of influence). Thus, to account for this spatial correlation, uncertainties were propagated along the latitudinal belt taking into account the covariance between the standard errors of nearby grid points. This acts to increase the uncertainty of the zonally-averaged trends. The accounting of this is documented in section C.4 of Appendix C.

Finally, once the zonally averaged salinity anomalies and zonally averaged trends are ready to be fitted with a weighted linear regression, there are generally greater than 300 data points. With a sample size that large, it can be easy to achieve significance. However, since there is a lot of uncertainty that has propagated through the trend and zonal average calculations, we implement a new method to test for whether or not the pattern amplification (i.e., the fitted weighted slope) is significant. We employ a Monte Carlo simulation in which we group the zonally averaged trends into 10-degree latitude bins for each basin, and then randomly sample two points out of each bin and randomly add or subtract 1.96*standard error (SE). A weighted linear regression is performed on the subsampled data and that slope is stored until 500 simulations have taken place. The minimum and maximum of the slopes from the 500 simulations are then recorded as the upper and lower bounds of the pattern amplification (weighted slope between zonally averages anomalies and zonally averaged trends).

4.3 Results and Discussion

The results of our analyses are presented below. It is organized by assessing and diagnosing long-term salinity and E-P trends and pattern amplifications, testing the robustness and identifying the time of emergence of salinity pattern amplifications, analyzing short-term trends and pattern amplifications, identifying and calculating the acceleration of salinity pattern amplifications, and estimating basin pattern changes and their relation with AMOC.

4.3.1 Long-term trends and pattern amplifications in salinity and E-P

The 1957/61 – 2019/23 linear trend in near-surface salinity reveals broadscale freshening in climatologically fresh regions, and salinification in climatologically salty regions (Fig. 4.2). This finding is consistent with many other studies (e.g., Durack et al. (2012), Skliris et al. (2014)). There is significant salinification in the Atlantic centered in both the Northern and

Southern Hemisphere subtropical basins, along with freshening at the higher latitudes. The Pacific exhibits significant freshening along the Intertropical Convergence Zone (ITCZ), the western tropical Pacific, and the higher latitudes, and salinification in the subtropical regions. The Indian basin has significant salinification in the Arabian Sea, and along the subtropical regions near 30°S, with freshening in in the eastern tropical region including northwest of Australia. All these trends work to amplify the climatological pattern where salty regions are becoming saltier and fresh regions are becoming fresher. Based on the empirical method for determining pattern amplifications and spatial pattern correlations put forth by Durack et al. (2012) and discussed in section 4.2.2, we estimate that the salinity pattern has amplified by 4.89% per 50yr (CI 95: 3.83% to 6.06%), and is spatially correlated at 0.75 (Fig. 4.3). This is slightly more than half of the 50-year 8% amplification rate that Durack et al. (2012) estimated, but is in line with other estimates (Cheng et al., 2020; Skliris et al., 2014; Zika et al., 2018). If we assume that roughly half of the amplification rate is due to warming and ice mass loss as found by Zika et al. (2018), then our salinity pattern amplification would be ~2.45% which would be directly attributable to an amplification in the hydrological cycle.

Global observational E-P estimates are only available since 1979 (beginning of the satellite era), and therefore do not stretch as far back in time as salinity observations. The expectation is that evaporative dominated regions will become more evaporative and precipitation dominated regions will become more precipitative in a warming world (Held et al., 2006; Seager et al., 2012; Seager et al., 2010; Trenberth, 2011); however, that is not evident over the 1979-2022 time period when analyzing E-P trends from OAFlux (E) and GPCP (P) (Fig. 4.4). The ITCZ appears to strengthen as expected, but there are other regions that trend in the opposite direction of what is expected to happen. For example, the Northern North Pacific and

Northern North Atlantic, both precipitation dominated regions have experienced enhanced E-P, whereas the subtropical North Pacific has experienced a decrease in E-P. Nearly the entire Indian basin has increasing E-P in regions that are expected to decrease in E-P, and vice-versa. Applying the same empirical method for identifying amplification and spatial pattern correlations in salinity, shows that E-P has not amplified over the 1979-2022 period, and has no spatial pattern correlation (Fig. 4.5). This is quite different from the expected amplification of 2-3%$°C^{-1}$ in a warming world (O'Gorman et al., 2012; Trenberth, 2011). Some E-P reanalysis products do a better job at capturing an amplified hydrological cycle (see Appendix Figures C.2, C.3, C.4, C.5), but as was discussed in the introduction, many observational products still struggle with identifying secular changes in E-P (Hegerl et al., 2015). Thus, we will focus the rest of this study on salinity's fingerprint on the hydrological cycle.

4.3.1.1 Robustness of the Salinity Pattern Amplification and Time of Emergence

There are clear temporal and spatial biases in the salinity observation distribution (Appendix Fig. C.1) which could impact linear trend calculations based on what starting and ending year is chosen. To test the robustness of the salinity pattern amplifications calculated for the full time period (Fig. 4.3), we chose six non-overlapping starting pentads (1960-1964, 1965-1969…,1985-1989) and analyzed their pattern amplifications through the end of the time period (Fig. 4.6). Despite some noisiness during the first 10-20 years, all converged near the 63-year pattern amplification (4.89%), and all fell within the 63-year pattern amplification's 95% CI, confirming the robustness of this method.

Despite efforts to remove dominant modes of natural variability through multiple linear regression, some residual natural variability likely remains, particularly in shorter-term trends. Therefore, to examine the emergence of the long-term salinity pattern amplification signal, it is necessary to analyze how pattern correlations and amplification estimates evolve with increasing trend duration.

For short-term trends (10–20 years), pattern correlations are low and amplification estimates are highly variable. The trend-to-noise ratio (TNR), defined as the trend divided by the standard error of the trend, also remains below 2 during this time period meaning the secular changes are difficult to tease out from the noise. However, as the trend durations increase, there is a steady, nearly linear, improvement in pattern correlation (i.e., salinification [freshening] is occurring in climatologically salty [fresh] regions), while the pattern amplification stabilizes and its associated uncertainty diminishes (Fig. 4.7). Remarkably, the average pattern amplification from 10-years to 63-years ranges between 2.9-6.3% for all trend durations, although confidence increases greatly the longer the trend duration is. The spatial pattern correlations increase linearly until they approach ~35-year durations, at which time it is approaching 0.7 and slowly increases to nearly 0.80 between 50–60-year durations, before falling back slightly to 0.75 as the trend duration approaches 63 years. The TNR increases linearly from near 0 at 10-year trend durations to ~7 at 45-year durations, becoming greater than 2 at around 20-year durations indicating when secular changes begin to emerge. The TNR increases linearly from 45 to 63-year durations, albeit at a slower pace than the first 45 years, reaching a peak of ~8.6 at 63-years.

When decomposing trend durations by specific starting years, peaks and valleys in pattern amplification begin to emerge (Fig. 4.8). While 10- and 20-year pattern amplifications remain too noisy to reveal consistent signals, the 30- and 40-year durations offer a glimpse into periods when salinity patterns amplified at a notably higher rate. For 30-year trends, a peak emerges for start years between 1971 and 1975 (trends ending between 2000–2004), while for 40-year trends, a peak occurs for start years between 1968 and 1971 (trends ending between

2007–2010). Both of these peaks occurred just before the Pacific climate shift of 1976–1977 (Mantua et al., 1997), and this shift may have contributed to the enhanced salinity pattern amplification observed during these periods. While we attempted to remove the dominant modes of natural variability, it is possible that a natural signal still exists in our data, particularly for multi-decadal modes of variability. Further analysis is warranted to understand why these peaks and valleys in the salinity pattern amplifications emerge.

The time of emergence, defined as the point at which secular changes are clearly identifiable relative to noise (i.e., internal variability), is often determined by exceeding some signal-to-noise ratio threshold (SNR) (Giorgi et al., 2009; Hawkins et al., 2012; Tebaldi et al., 2013). The thresholds typically range from 1 to 2, but can be unique to the particular application (Hawkins et al., 2012). If we use a TNR of 2 as our threshold, 20-years (see Fig. 4.7, bottom plot) would be identified as the time of emergence for the salinity pattern amplifications (i.e., when we begin to see the climatologically salty areas becoming saltier and climatologically fresh regions becoming fresher).

However, we must use a more comprehensive criteria to identify secular salinity pattern amplifications since it is clear that at 20-years, even though the average TNR is greater than or equal to 2 (Fig. 4.7), there are multiple instances where the TNR is less than 2 and salinity pattern amplifications are variable and insignificant (error bars cross zero) for various starting years (Fig. 4.8; 20-year subplot). At 30-years, the average TNR is ~4, and the average pattern amplification and spatial pattern correlation is 6.3% and 0.6, respectively (Fig. 4.7). However, there are a few early and late starting years where 30-year pattern amplifications are insignificant and TNR is less than 2 (Fig. 4.8). Finally, at 40-years, the average pattern amplification and spatial pattern correlation is 6.2% and 0.7, respectively with an average TNR of 5.5 (Fig. 4.7).

For each individual 40-year period, the TNR is greater than 2 and the pattern amplifications remain significant. Thus, based on both the cumulative metrics from Fig. 4.7, and the individual starting years of Fig. 4.8, we conclude that the time of emergence for salinity pattern amplifications is between 30 and 40 years.

4.3.2 Short term near-surface salinity trends

The 2005-2023 near-surface salinity trends show some fresh regions getting fresher and some salty regions getting saltier, but the pattern is very noisy when compared to the long-term salinity trends (compare Fig. 4.2 to Fig. 4.9). This is even more apparent when looking at the salinity pattern amplifications over the 19-year window where there has been no significant salinity pattern amplification (Fig. 4.10). Despite our best efforts to remove natural modes of variability, there is likely a large amount of internal variability unaccounted for that influences this 19-year time period. Furthermore, based on our previous analysis and Figures 4.7 and 4.8, we should not expect a 19-year window to pick up secular changes in pattern amplifications or correlations. Additionally, there have been major El Niño and La Niña events during this time period, along with shifts in the Pacific Decadal Oscillation.

4.3.3 Changing salinity patterns

Recent studies have shown that salinity pattern amplifications are accelerating (Cheng et al., 2020; Skliris et al., 2014). To achieve a robust estimate on whether salinity patterns are amplifying at an accelerated rate, we reviewed changes in near-surface salinity between the first decadal climatology (1955-1964) of the World Ocean Atlas 2023 Salinity (Reagan et al., 2024a), and the six decadal climatologies that followed: 1965-1974, 1975-1984, 1985-1994, 1995-2004, 2005-2014, and 2015-2022. Decadal climatologies use all available in situ data within the WOD 2023 (A. V. Mishonov et al., 2024) for that particular decade and are objectively analyzed and quality controlled. We treat these decadal changes from the 1955-1964 baseline as "trends", and normalize them to a 50-year time period.

There is a clear evolution over time that salty regions are becoming saltier and fresh regions are becoming fresher; however, it is difficult to ascertain whether these evolutions over time are accelerating by simply reviewing Fig. 4.11. To better quantify the changes, we calculated the pattern amplification rates and spatial pattern correlations for each decade (Fig. 4.12) compared to the 1955-1964 baseline. Reviewing all six decades, the pattern amplifications (spatial pattern correlations) between the 1955-1964 baseline and 1965-1974 is -1.50%/50yr (-0.16), 1975-1984 is 0.35%/50yr (0.16), 1985-1994 is 1.33%/50yr (0.32), 1995-2004 is 2.72%/50yr (0.48), 2005-2014 is 3.69%/50yr (0.65), and 2015-2022 is 5.03%/50yr (0.76). There is a marked increase in both salinity pattern amplifications and spatial pattern correlations over time. Since salinity pattern amplifications are presented as a percentage change over 50 years, then the change in time of the amplifications would provide us with an estimate of the pattern amplification acceleration. Taking a weighted least squares regression yields a significant acceleration of 1.22 ± 0.64 % per 50yr per decade. This means that for every successive decade, the salinity pattern amplification increases by 1.22%/50yr per decade starting from 1965-1974.

The increases in pattern amplification and spatial pattern correlations over time are not dependent on the baseline climatology. The same analyses were conducted using 1965-1974, 1975-1984, and 1985-1994 as the baseline, and in each case pattern amplifications and spatial pattern correlations grew with time (see Appendix Figures C.6, C.7, and C.8). Thus, this acceleration is robust and not altered by changing the baseline decadal climatology (and therefore changing data distributions; Appendix Fig. C.1). Additionally, decades 2005-2014, and 2015-2022 are used in the analysis, both of which are dominated by Argo, yet amplifications still increase between the two diminishing the idea that Argo (and its associated data distribution) is responsible for the acceleration (see Fig. 4.12 and Appendix Figures C.6, C.7, C.8).

We can physically interpret the acceleration of salinity pattern amplifications as climatologically salty (fresh) regions becoming saltier (fresher) at an increasing rate over time. This may have severe implications for the hydrological cycle.

4.3.4 Basin Amplifications and Their Implications

The Atlantic is a net evaporative basin and the Pacific is a net precipitative basin, with Atlantic moisture being transported across Central America and deposited in the Pacific (Schmitt, 2008). The strong evaporation, along with the Agulhas leakage (Gordon, 1986), helps maintain the high Atlantic salinity. The Atlantic Meridional Overturning Circulation (AMOC), a critically important current system that redistributes heat from the equator to the poles, has been shown to maintain or strengthen when the Atlantic/Pacific salinity contrast is preserved or enhanced (Seidov et al., 2002, 2003; Stouffer et al., 2007). The AMOC, despite slight weakening in recent decades, has been resilient to change; a direct reflection of the relationship it has with the stability of the Gulf Stream (A. Mishonov et al., 2024; Seidov et al., 2019). Furthermore, a study by Stendardo et al. (2020) showed that the negative freshwater fluxes (negative due to the high salinity) from the subtropical North Atlantic to the subpolar North Atlantic are on the same order as the positive freshwater fluxes from the Arctic to the subpolar North Atlantic. Therefore, the health of the AMOC is related to both the Atlantic/Pacific salinity contrast, and to the changes in subtropical North Atlantic salinity.

For the global ocean, salinity pattern amplifications and spatial pattern correlations are significant and quite robust (Fig. 4.2). However, it is not clear if one ocean basin drives this result or if all three ocean basins experience similar changes, and therefore we analyze the pattern amplifications for each major ocean basin. The 1957/1961-2019/2023 salinity pattern amplification and spatial pattern correlation for the Atlantic basin is 5.23% per 50yr (CI95: 3.70% to 7.50%) and 0.79, respectively (Fig. 4.13a). The Pacific basin experienced a pattern amplification of 3.22% per 50yr (CI95: 1.09% to 5.23%) and spatial pattern correlation of 0.49 (Fig. 4.13b). The Indian basin does not experience a significant salinity pattern amplification (Fig. 4.13c). However, it should be noted that the Indian basin has a significant dipole in its salinity pattern structure, with much of the eastern side being fresh and the western side being salty (see black contours of Fig. 4.2). This salinity contrast is not well represented in zonal mean salinity anomalies (a prerequisite for the salinity pattern amplification calculation) and therefore future work should look to isolate these two regions.

With significant salinity pattern amplifications evident in both the salty Atlantic and fresh Pacific, it is reasonable to assume that the Pacific and Atlantic salinity contrast has increased over the last 63 years. By splitting the Atlantic and Pacific into salty and fresh regions based on their respective basin-average salinity (Fig. 4.14), we compute 63-year area-average time series for each fresh/salty region within each basin. The salty regions of the Atlantic, which are primarily in the subtropics (Fig. 4.14), have experienced an increase of salinity at the rate of 0.127±0.052 per 50yr, with fresh regions not experiencing significant changes (Fig. 4.15a). Conversely, the fresh regions of the Pacific (Fig. 4.15b) have experienced significant freshening on the order of -0.080±0.026 per 50yr, with insignificant changes in the salty regions.

Over the 2005-2023 period (Argo-era), the rate of salinity change is even larger than what is seen over the 63-year time period, with salty regions of the Atlantic becoming more saline at a rate of 0.160±0.082 per 50yr (Fig 4.16a), and the fresh regions of the Pacific becoming fresher at a rate of -0.114±0.055 per 50yr (Fig. 4.16b). Additionally, the fresh regions of the Atlantic also experienced significant salinification over the 2005-2023 period (Fig. 4.16a). The Indian does not experience significant changes in fresh or salty regions over the shorter and longer time periods (Fig. 4.15c, Fig. 4.16c).

We present strong evidence that the Atlantic and Pacific basins have been trending saltier and fresher, respectively, over the 1957/61-2019/23 time period. There is also evidence of an acceleration of these changes over the past two decades, which is consistent with the acceleration in salinity pattern amplifications found in section 4.3.3. The E-P asymmetry between the Atlantic and Pacific accounts for nearly half of the observed Atlantic-Pacific salinity contrast (Ferreira et al., 2018); therefore, this increase in salinity contrast between the two basins suggests an amplification of the hydrological cycle.

In addition to the enhanced salinity contrast between the Atlantic and Pacific, which has shown to help maintain the AMOC, salinification in the subtropical North Atlantic could also play an important role in maintaining AMOC functionality. The Atlantic is getting saltier, both over the long-term (Fig. 4.15a) and short-term (Fig. 4.16a), with even fresh regions of the Atlantic getting saltier over the 2005-2023 time period. Stendardo et al. (2020) showed that high salinity transport from the subtropics to the subpolar regions could be as important as freshwater intrusion from the Arctic in helping to shape the salinity of the subpolar region which is critical for AMOC dynamics.

4.4 Conclusions

This study presented a robust and updated estimate of salinity pattern amplification using a sophisticated methodology rooted in the empirical framework put forth by Durack et al. (2012) over 10 years ago. Durack et al. (2012) showed how salinity pattern amplifications can be used to track changes in the hydrological cycle. Our work extends 15 years beyond their study and leverages millions of profiles that were unavailable to them. Additionally, we applied a novel approach to remove natural variability from the data, and carefully propagated mapping uncertainties across time and space. We tested the robustness of the method using different starting years, and identified when secular changes were clearly distinguishable from internal variability (i.e., time of emergence). We leveraged recently released decadal climatologies from the World Ocean Atlas 2023 (Reagan et al., 2024b) to identify an acceleration in the salinity pattern amplifications. Finally, we analyzed how the Atlantic/Pacific salinity contrast has changed over the 1957/61-2019/23 time period and related these findings to how it may impact AMOC. The conclusions of this study are summarized as follows:

- Over the 63-year time period, from the 1957-1961 pentad through the 2019-2023 pentad, climatologically fresh (salty) regions of the global ocean have become fresher (saltier) at a rate of 4.89% per 50yr (CI 95: 3.83% to 6.06%), relative to the 1955-2006 baseline (WOA09) (Fig. 4.3). This is consistent with previous observational studies and is indicative of an intensifying global hydrological cycle. This suggests that the hydrological cycle amplification would be ~2.45% over the same time period, as warming and ice mass loss accounts for roughly half of the amplification rate (Zika et al., 2018).
- Despite temporal and spatial heterogeneity in salinity data distributions during early time periods (Fig. 4.1), the salinity pattern amplifications were insensitive to different starting years with convergence near ~5% per 50 years (Fig. 4.6) by the end of the record (2019/23); highlighting their robust nature.
- For short-term trends (10-20 years), salinity pattern amplifications and spatial pattern correlations were highly variable and low, respectively. Thus, despite

attempts to remove natural variability using multiple linear regression, there appears to be some internal variability not accounted for.

- We identify the time period between 30 and 40 years as the time of emergence for salinity pattern amplifications. During this time, the secular changes (e.g., fresh regions become fresher, salty regions become saltier) emerge and are clearly identifiable relative to noise.
- This study reveals a statistically significant acceleration in the salinity pattern amplification rate between 1955 and 2022 of 1.22 ± 0.64 % per 50yr per decade. This suggests that not only are climatologically fresh (salty) regions becoming fresher (saltier), but they are doing so at an increasing rate which could potentially mean the hydrological cycle is not only amplifying, but also accelerating.
- The Atlantic and Pacific salinity contrast has amplified over the 1957/61-2019/23 time period. The Atlantic's salty areas have become saltier (rate of 0.127±0.052 per 50yr), and the Pacific's fresh areas have become fresher (-0.080±0.026 per 50yr). These rates have increased over the 2005-2023 time period, suggesting an acceleration of the inter-basin salinity contrast, consistent with the conclusion made above, which may be important for maintaining/enhancing the strength of the AMOC.

This study has provided new and improved estimates of long-term salinity pattern amplifications, an approximation of the time period needed to identify secular changes in salinity, quantification of the acceleration of the salinity pattern amplification during recent decades, and identified a growing Atlantic/Pacific salinity contrast. All of these results were based solely on observational data. Thus, one of the next steps we would like to take is to begin to relate these observational changes to global climate models. If we apply the same robust methodology, do we see similar salinity pattern amplifications? If so, is it primarily freshwater fluxes driving them? Is there an acceleration in salinity pattern amplifications over time? Do secular changes in the model emerge around the same time period as the observational data? Are there time periods of rapid amplification and other time periods of slow amplification, and what is driving them? Addressing these questions will allow for validation of the model, but also provide valuable insight on what drives these changes. This is difficult to ascertain from observational data alone.

One of the bigger questions that remains, and one that has eluded researchers for many decades, is how will salinity change in the subpolar North Atlantic in a warming world and how will those changes impact AMOC? From this study, we have identified that the Atlantic and Pacific salinity contrasts are growing and the subtropical North Atlantic is getting saltier, both of which help maintain/enhance AMOC (Seidov et al., 2002, 2003; Stendardo et al., 2020; Stouffer et al., 2007). However, how do these factors compare with increasing freshwater advection from Greenland and the Arctic to the subpolar North Atlantic that is expected in a warming world?

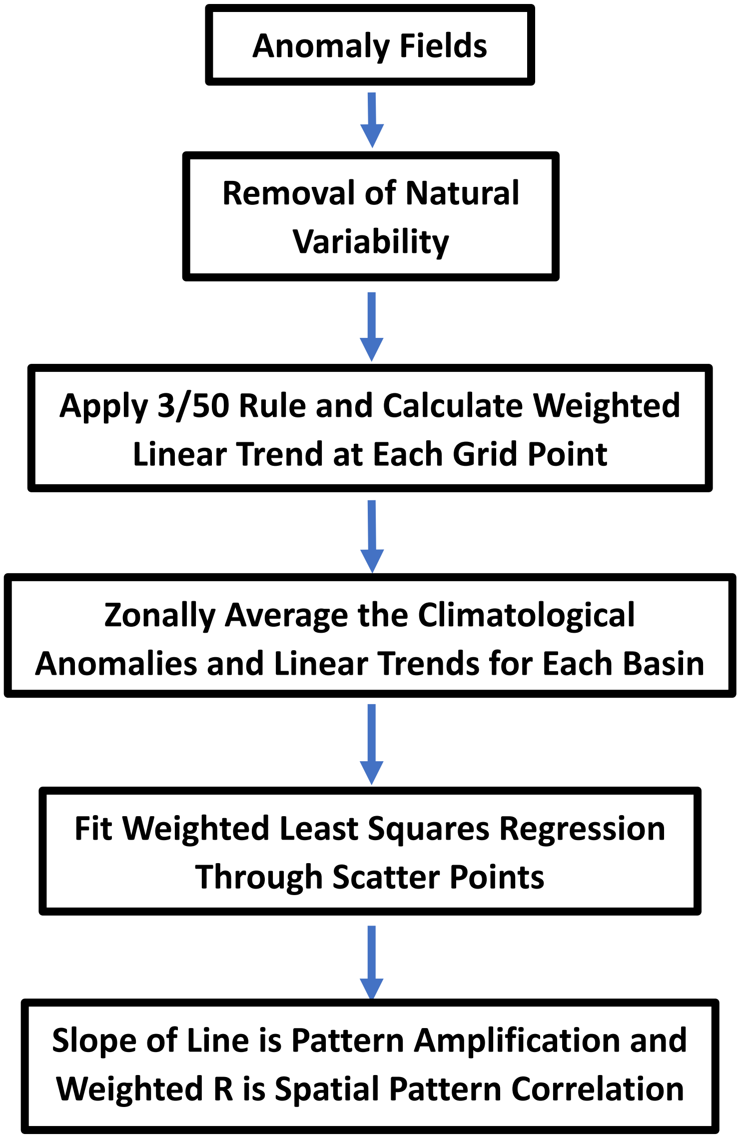

Figure 4.1: Schematic illustrating the various steps to calculate pattern amplification and spatial pattern correlations in this study. Please review section 4.2 for a more complete description of each step.

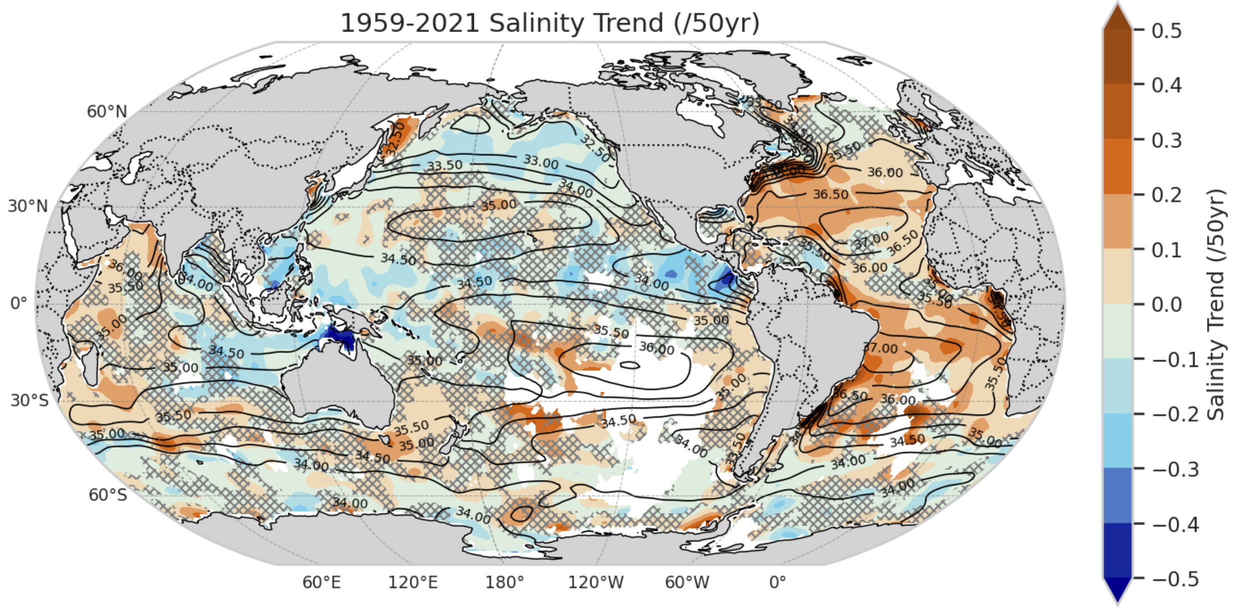

Figure 4.2: The linear trend of near-surface salinity from the 1957/1961 pentad through the 2019/2023 pentad. Orange shadings represent regions of increasing salinity, blue shadings show regions of decreasing salinity. Hatching covers regions where the trend was not significant at the 95% level using the modified Mann-Kendall test. Black contours show the climatological near-surface salinity mean. White regions had insufficient data.

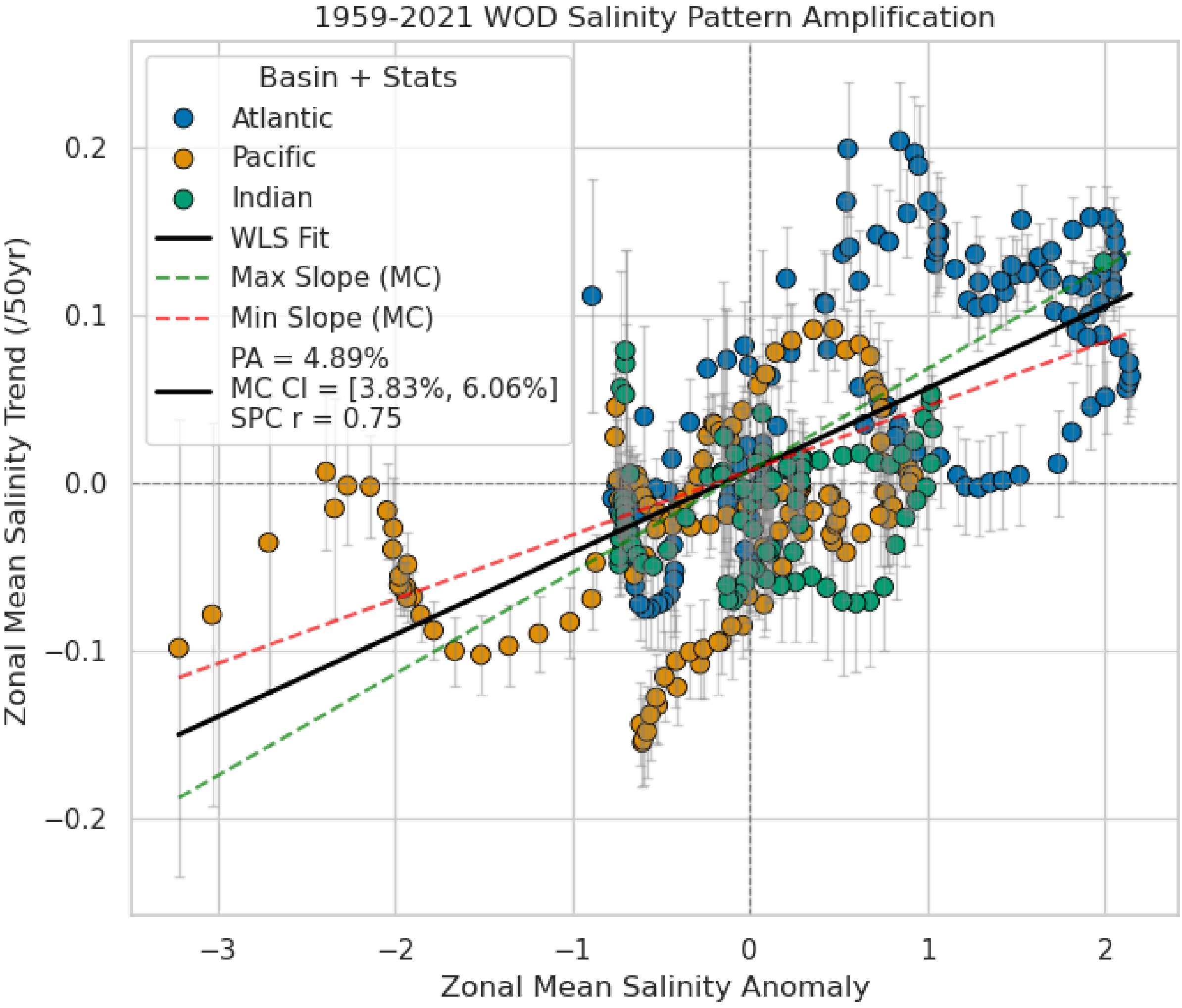

Figure 4.3: The 1957/1961 through 2019/2023 near-surface salinity pattern amplification and spatial pattern correlation. The different colored dots represent the zonally-averaged trends and climatological near-surface salinity anomalies for each ocean basin (Atlantic = Blue, Pacific = Orange, Green = Indian) along each 1-degree latitudinal belts within that basin. The black line represents the weighted least squares regression, and the red and green lines represent the 95% confidence interval based on the minimum and maximum slopes from 500 Monte Carlo simulations.

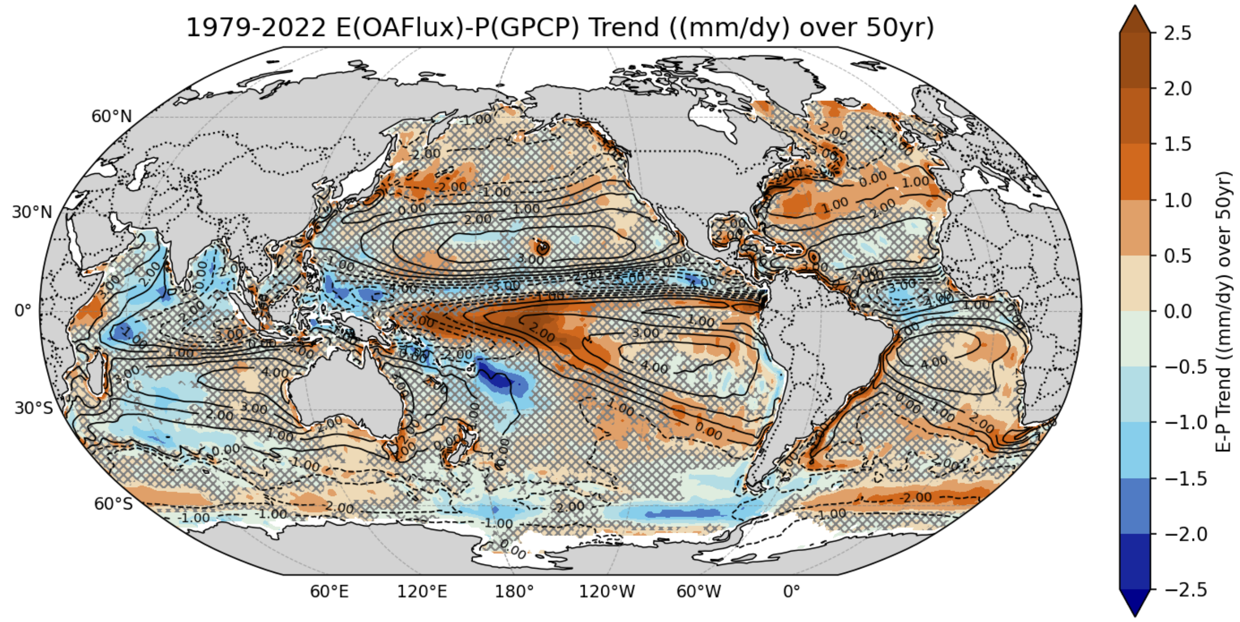

Figure 4.4: Linear trend of net freshwater flux during 1979-2022. Net freshwater flux here is the difference between OAFlux evaporation and GPCP precipitation. Units are mm/day per 50yr. Orange shows regions of increasing E-P, blue shows regions of decreasing E-P. Hatching covers regions where the trend was not significant at the 95% level using the modified Mann-Kendall test. Black contours show the climatological mean net freshwater flux. White regions had insufficient data.

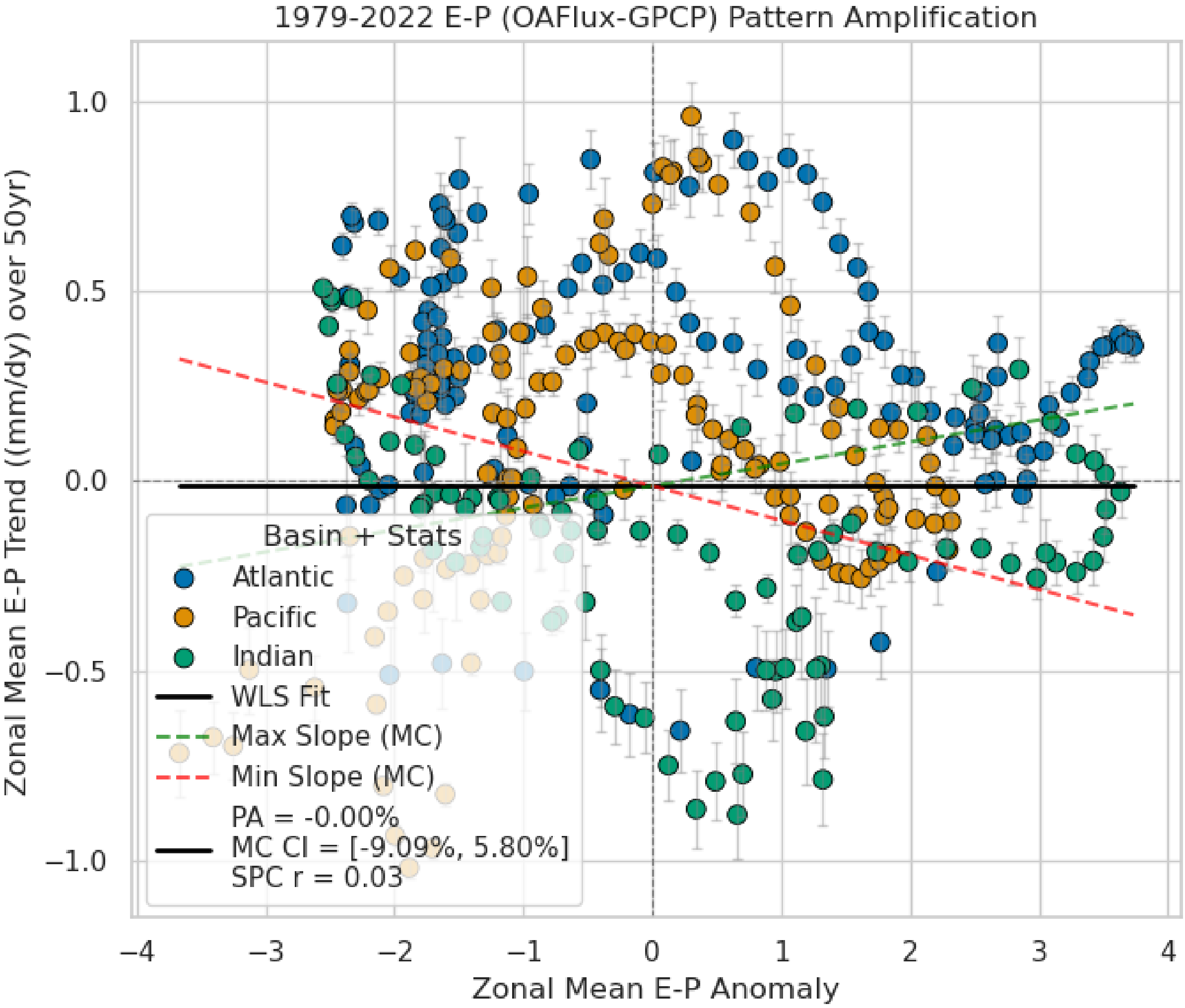

Figure 4.5: The 1979 – 2022 E (OAFlux)-P (GPCP) pattern amplification and spatial pattern correlation. The different colored dots represent the zonally-averaged trends and climatological E-P anomalies for each ocean basin (Atlantic = Blue, Pacific = Orange, Green = Indian) along each 1-degree latitudinal belts within that basin. The black line represents the weighted least squares regression, and the red and green lines represent the 95% confidence interval based on the minimum and maximum slopes from 500 Monte Carlo simulations.

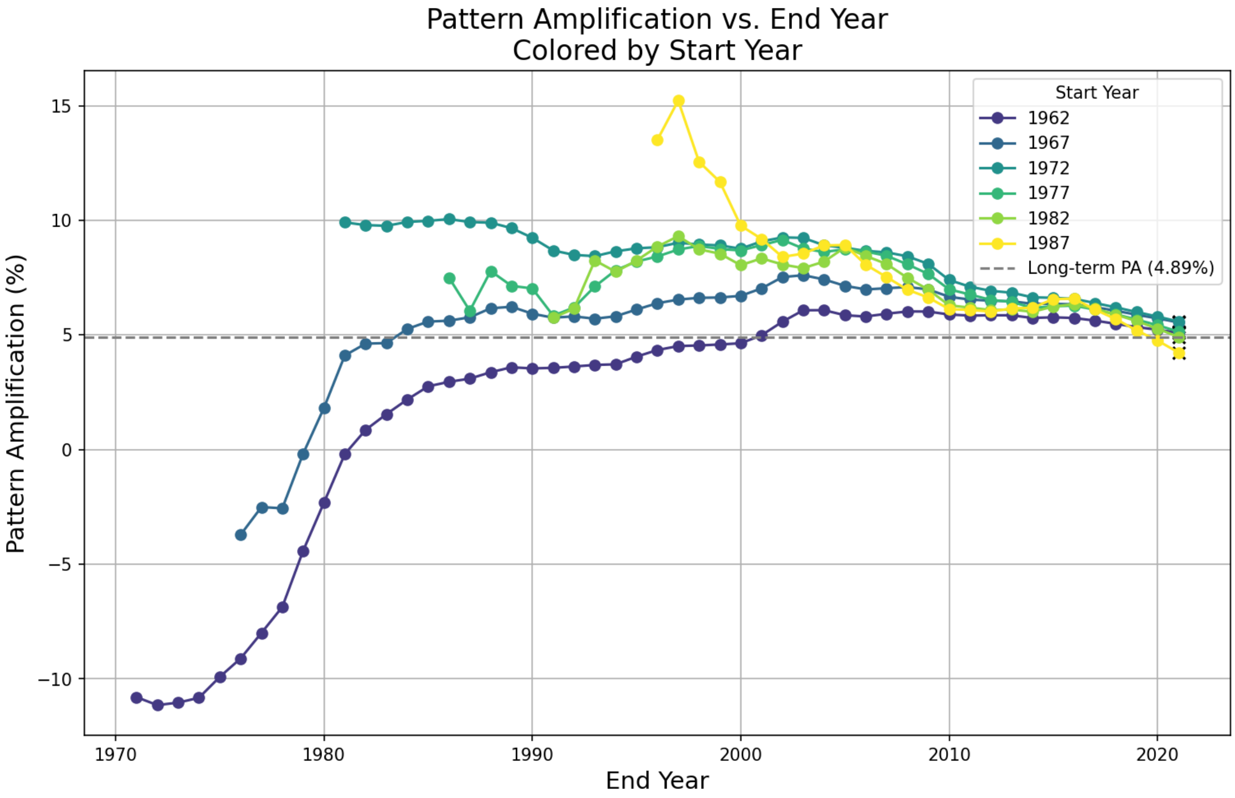

Figure 4.6: Time evolution of near-surface salinity pattern amplifications for different starting pentads. The center year is plotted for each pentad (e.g., 1962 is 1960/64 pentad).

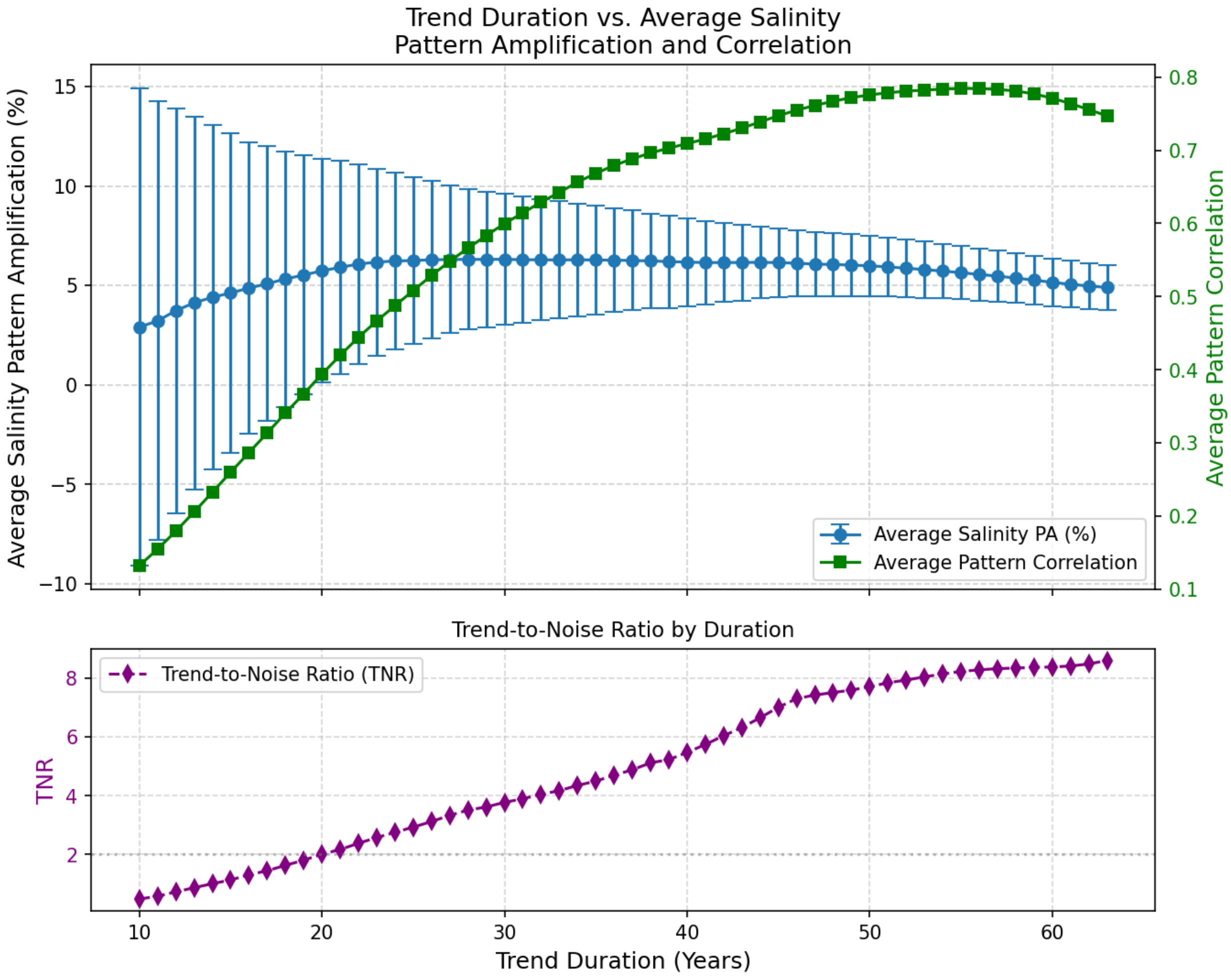

Figure 4.7: Average pattern amplification (blue; with average 95% uncertainty as error bars), spatial pattern correlations (green), and trend-to-noise ratio (purple) of all 10-year to 63-year trends. Each trend duration is aggregated from the entire 1957/61-2019/23 pentadal time period. For example, the 10-year trend duration contains the average of 1957/61-1966/70, 1958/62-1967/71,…,2010/14-2019/2023.

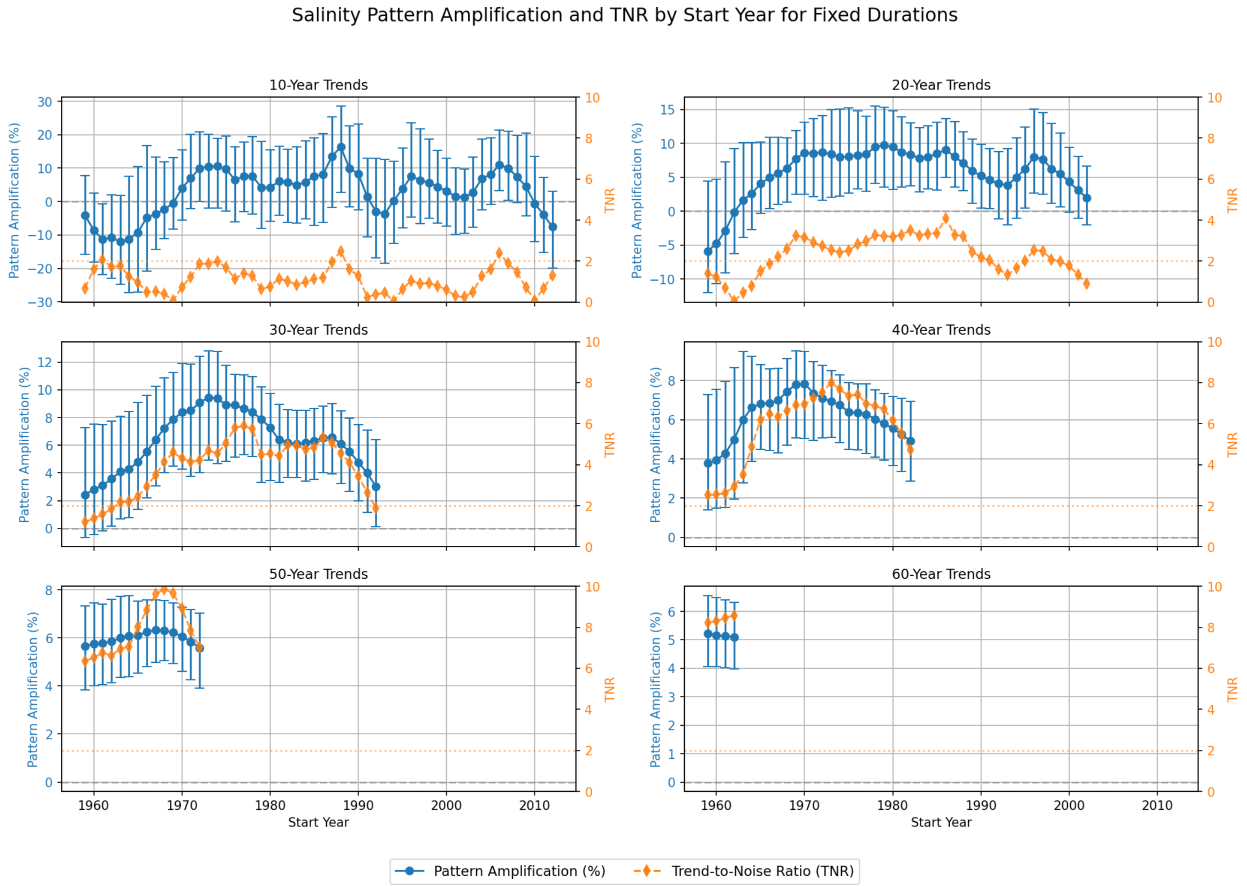

Figure 4.8: Salinity pattern amplification by start year grouped into 10, 20, 30, 40, 50, and 60-year trend durations.

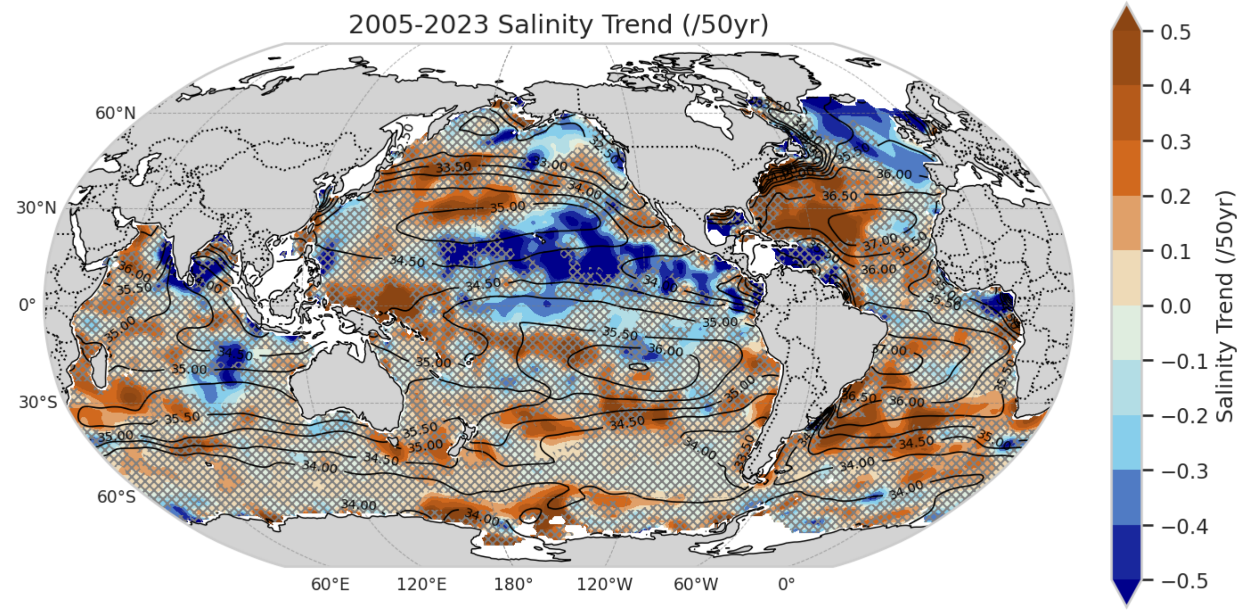

Figure 4.9: Trend in near-surface salinity during a recent 19-year period (2005 –2023) using annual salinity anomalies (see text for discussion). Orange shadings show regions of increasing salinity, blue regions show regions of decreasing salinity. Hatching covers regions where the trend was not significant at the 95% level using the modified Mann-Kendall test. Black contours show the climatological near-surface salinity. White regions had insufficient data.

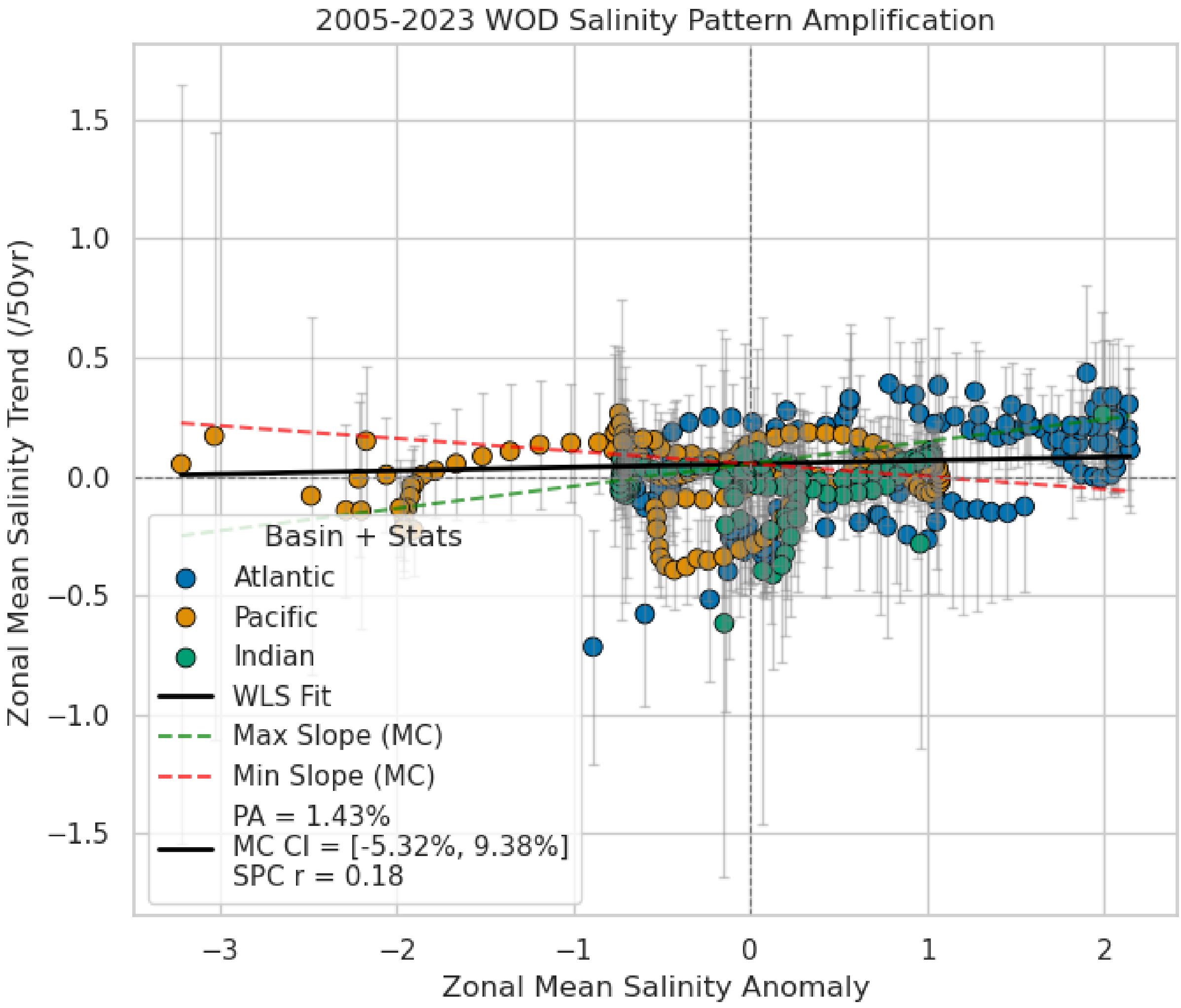

Figure 4.10: The 2005–2023 near-surface salinity pattern amplification and spatial pattern correlation. The different colored dots represent the zonally-averaged trends and climatological near-surface salinity anomalies for each ocean basin (Atlantic = Blue, Pacific = Orange, Green = Indian) along each 1-degree latitudinal belts within that basin. The black line represents the weighted least squares regression, and the red and green lines represent the 95% confidence interval based on the minimum and maximum slopes from 500 Monte Carlo simulations.

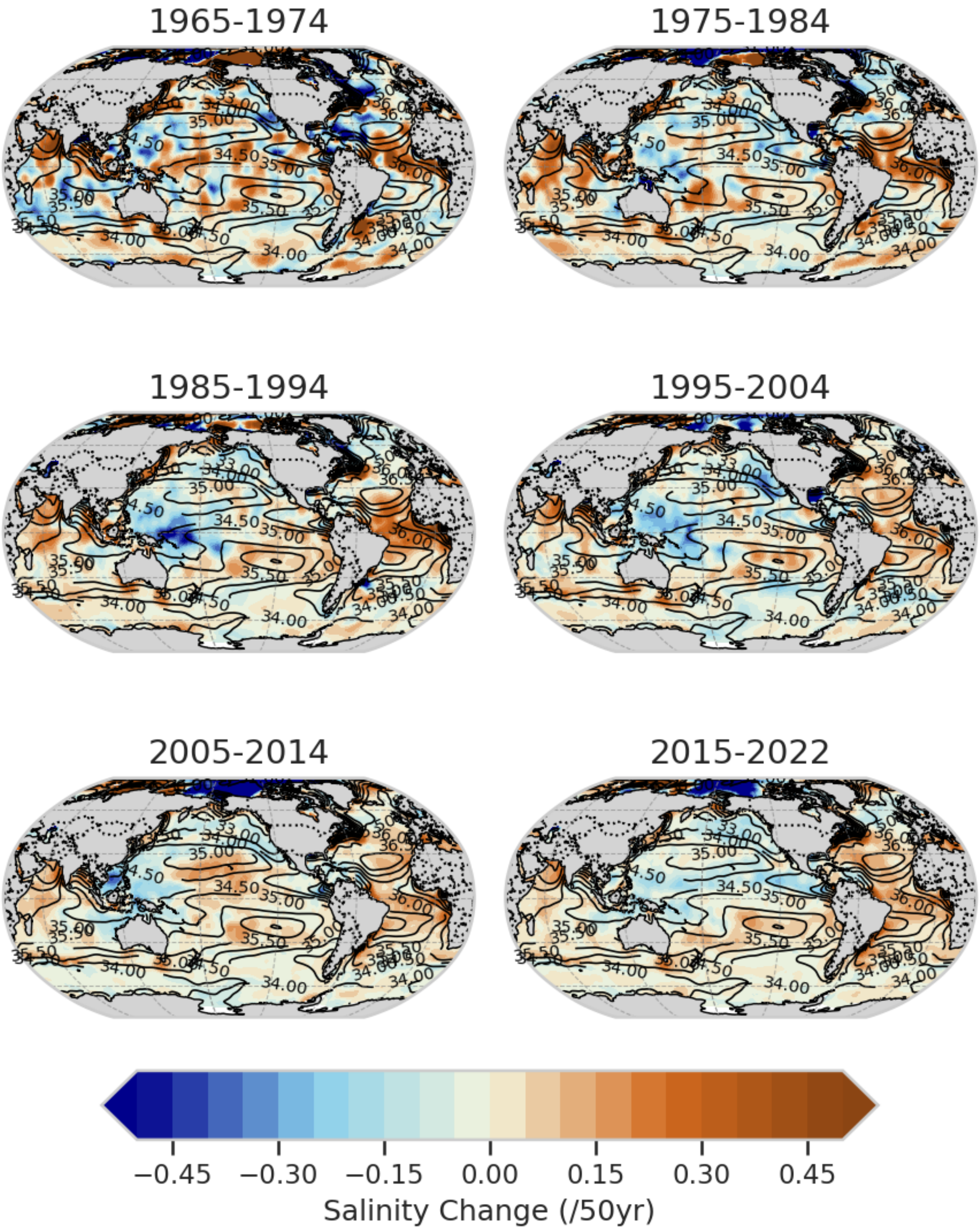

Figure 4.11: Near-surface salinity change between the 1955-1964 decadal climatology and (from top left to bottom right) 1965-1974, 1975-1984, 1985-1994, 1995-2004, 2005-2014, and 2015-2022 from the World Ocean Atlas 2023 (Reagan et al., 2024b). Orange shades show regions where the difference is positive (i.e., salinification). Blue shades show regions where the difference is negative (i.e., freshening). No attempt has been made to determine significance. Black contours show the 1955-2022 near-surface climatological mean.

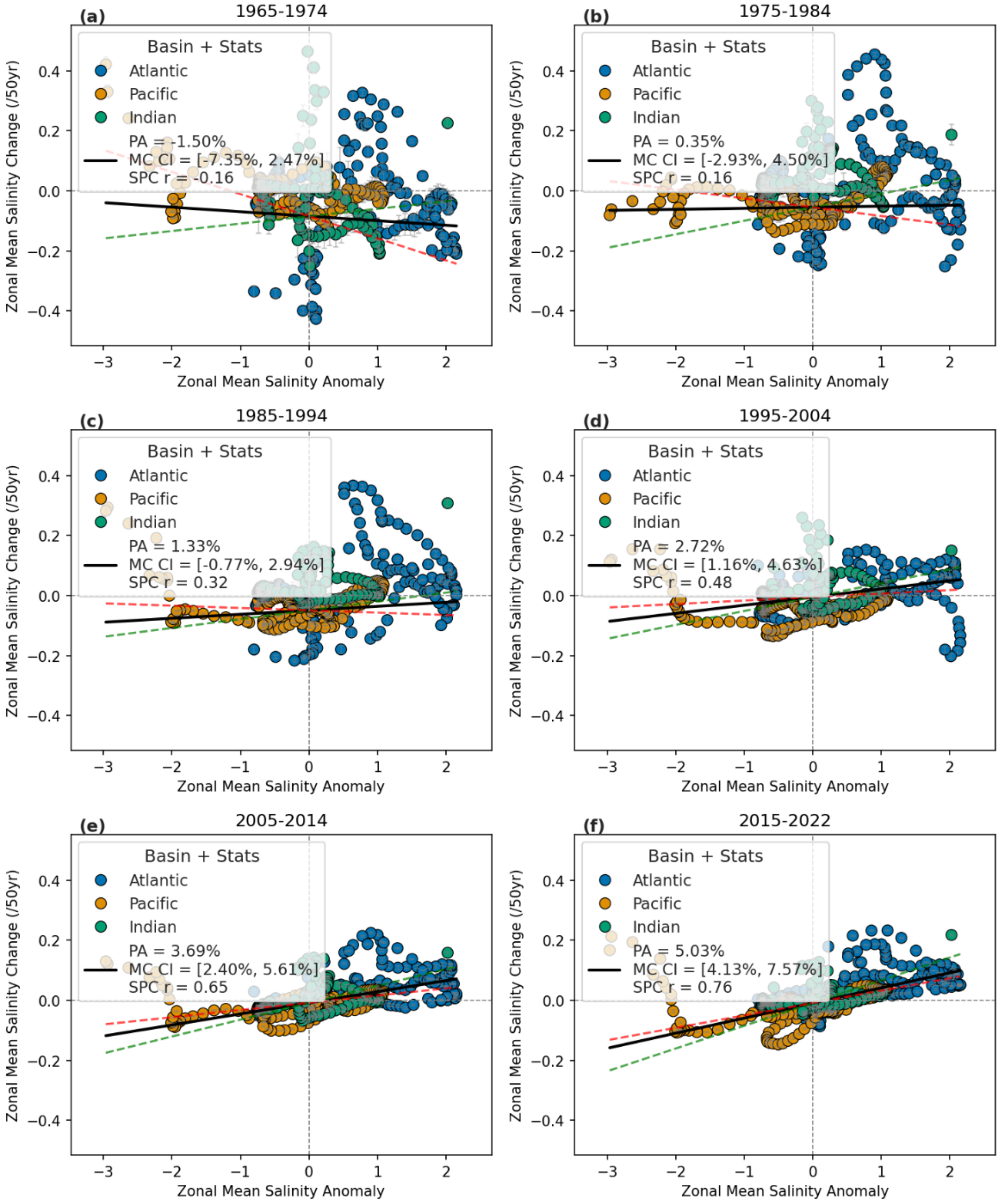

Figure 4.12: Near-surface salinity pattern amplification and spatial pattern correlations for the differences between the 1955-1964 decadal climatology and a) 1965-1974, b) 1975-1984, c) 1985-1994, d) 1995-2004, e) 2005-2014, and f) 2015-2022. The different colored dots represent the zonally-averaged differences between the climatology and the 1955-1964 climatology and the climatological near-surface salinity anomalies for each ocean basin (Atlantic = Blue, Pacific = Orange, Green = Indian) along each 1-degree latitudinal belts within that basin. The black line represents the weighted least squares regression, and the red and green lines represent the 95% confidence interval based on the minimum and maximum slopes from 500 Monte Carlo simulations, respectively. The climatologies are from the World Ocean Atlas 2023 (Reagan et al., 2024b).

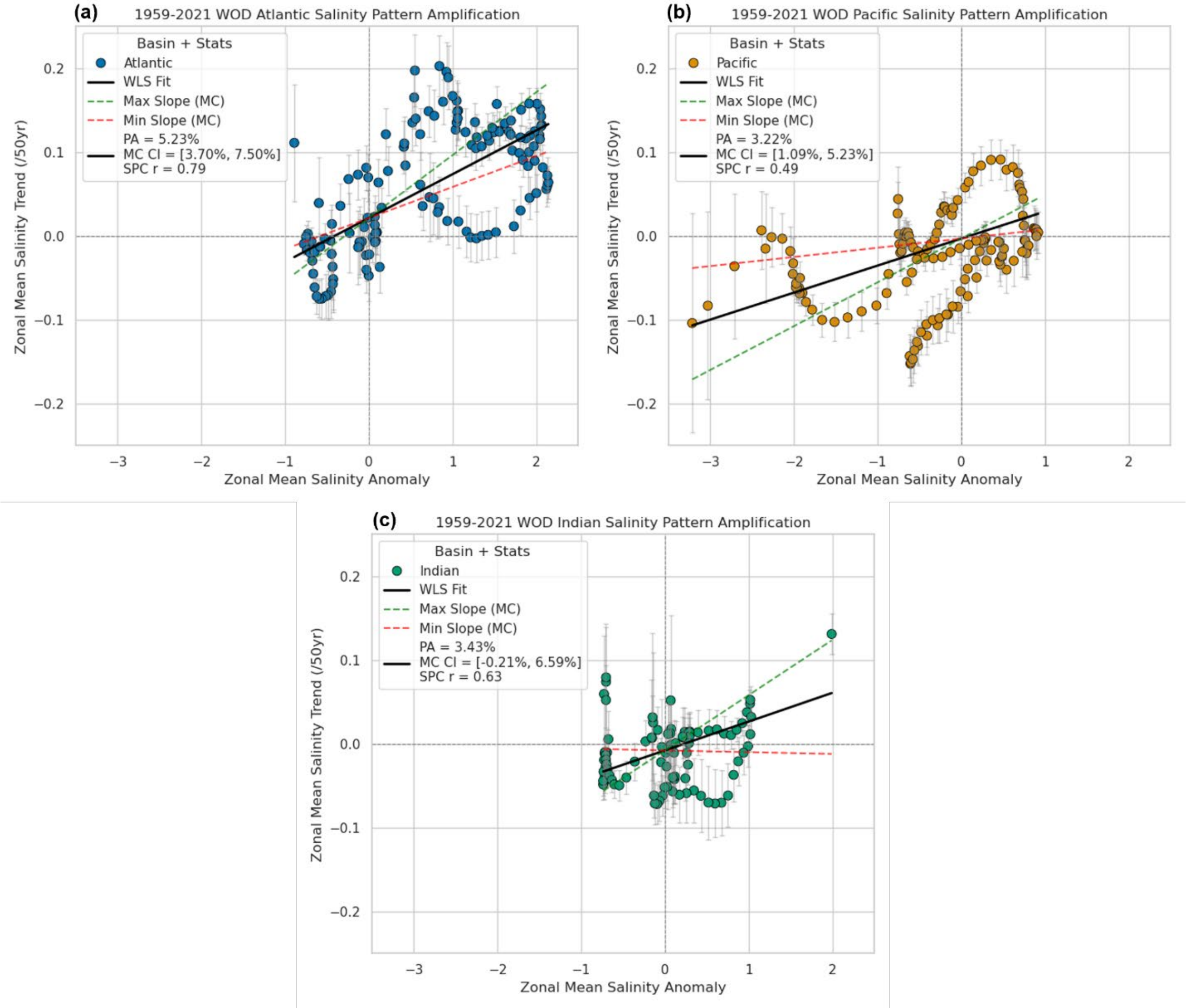

Figure 4.13: The 1957/1961 through 2019/2023 near-surface salinity pattern amplification and spatial pattern correlations for: a) Atlantic, b) Pacific, and c) Indian basin. The different colored dots represent the zonally-averaged trends and climatological near-surface salinity anomalies for each ocean basin (Atlantic = Blue, Pacific = Orange, Green = Indian) along each 1-degree latitudinal belts within that basin. The black line represents the weighted least squares regression, and the red and green lines represent the 95% confidence interval based on the minimum and maximum slopes from 500 Monte Carlo simulations.

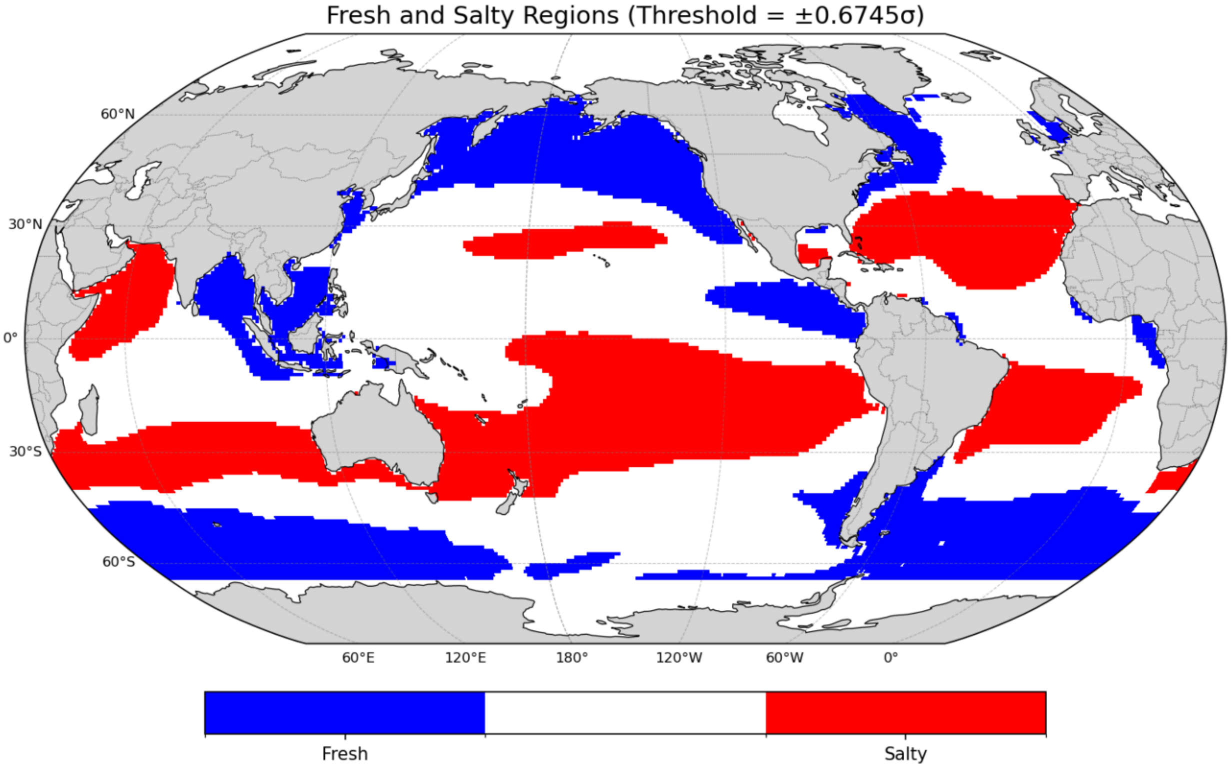

Figure 4.14: Fresh (blue) and salty (red) regions for each major ocean basin as identified by being greater than (for salty) and less than (for fresh) 0.6745 standard deviations away from the basin-average near-surface mean.

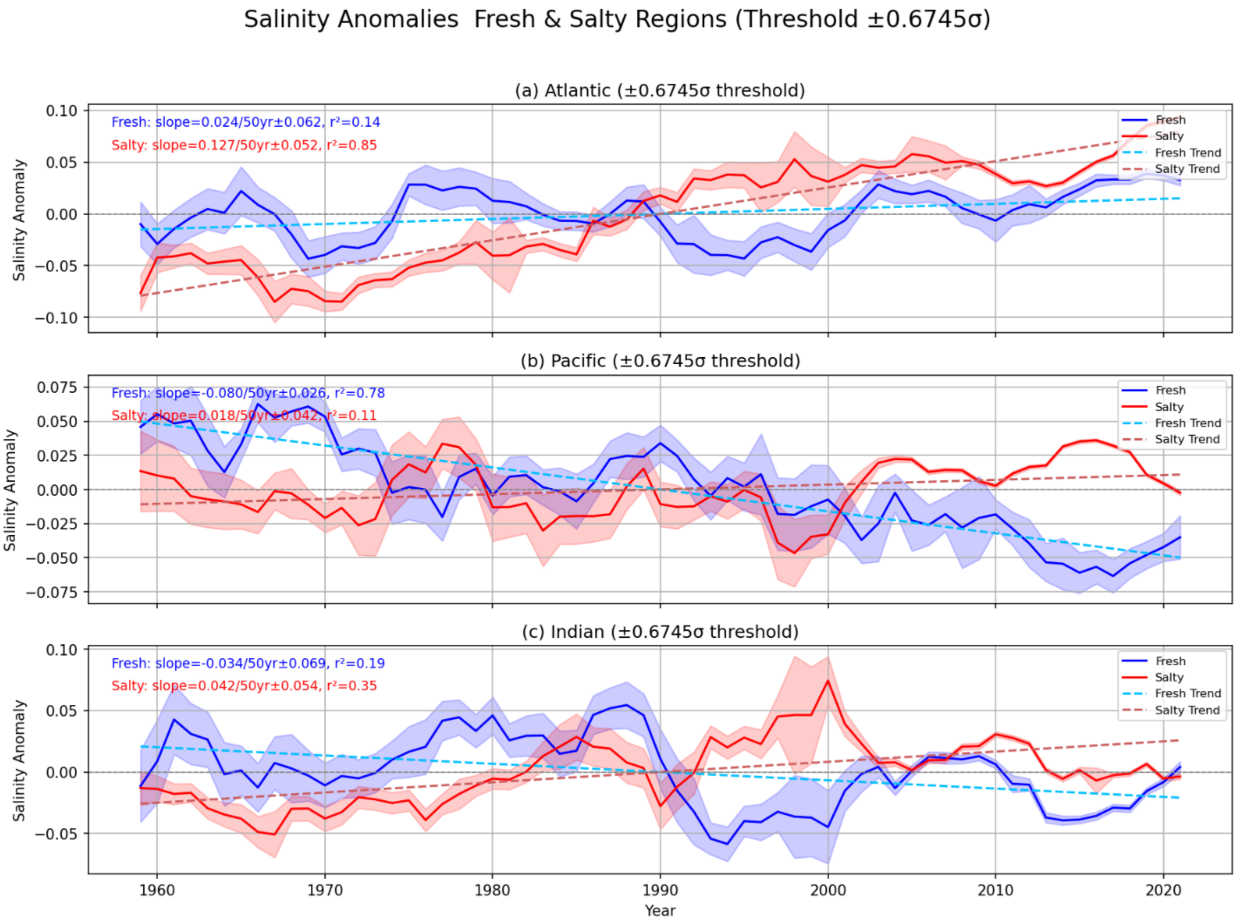

Figure 4.15: Area-average pentadal near-surface salinity anomalies from 1957/61-2019/23 based on salty (red) and fresh (blue) regions in Figure 4.14. Dotted lines represent the fitted linear regressions.

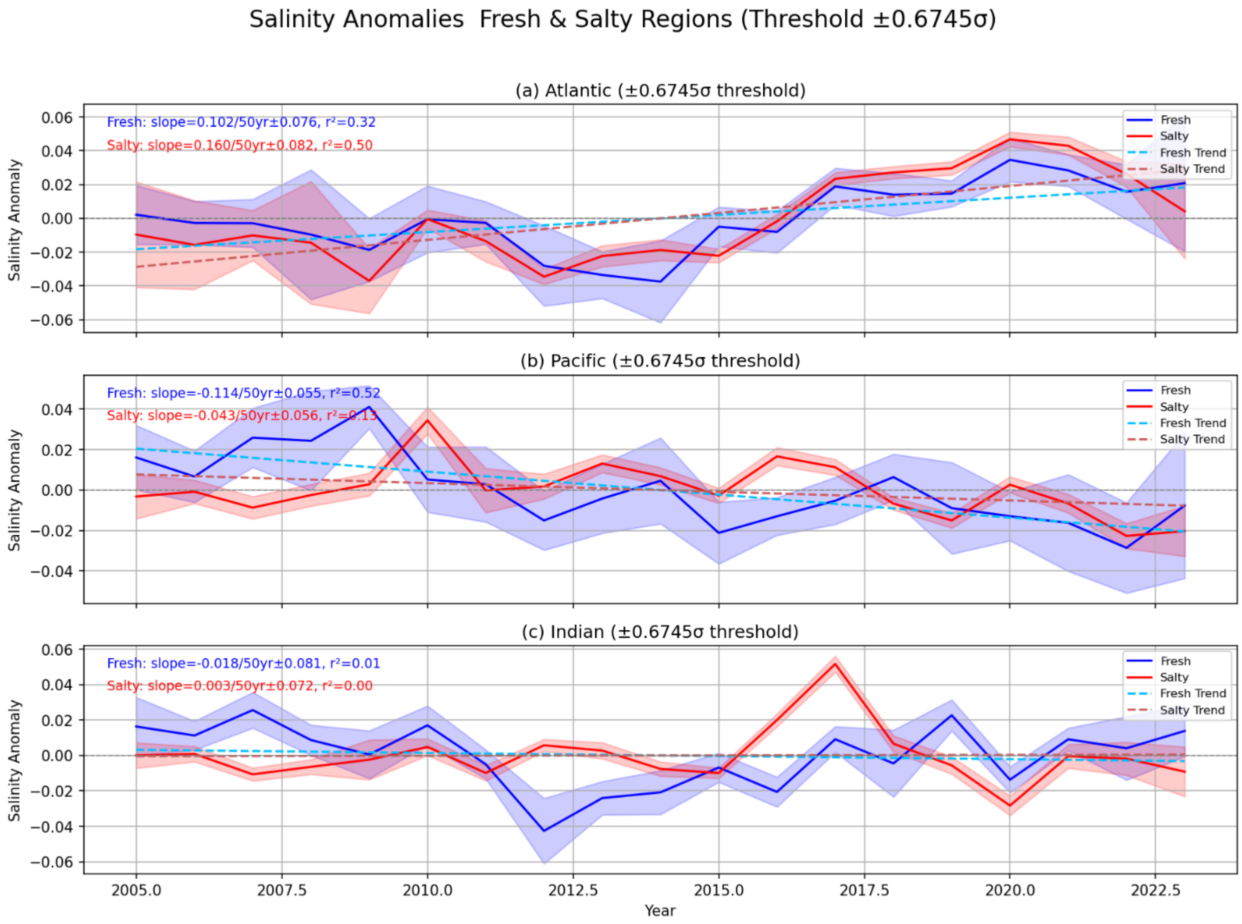

Figure 4.16: Area-average annual near-surface salinity anomalies from 2005-2023 based on salty (red) and fresh (blue) regions in Figure 4.14. Dotted lines represent the fitted linear regressions

Chapter 5: Conclusions and Future Work

5.1 Conclusions

This body of work revolved around assessing near-surface salinity as nature's rain gauge. Monitoring changes in the hydrological cycle is difficult with current observational products of evaporation and precipitation. There are considerable amounts of uncertainty in the data (Durack, 2015; Lagerloef et al., 2010), and natural variability can drown out the much smaller secular signal that we are looking to find (Hegerl et al., 2015). However, salinity has been found to be a proxy for estimating changes in the hydrological cycle (Durack et al., 2012). With the introduction of remotely sensed salinity observations within the last 15 years and a treasure trove of historic and current in situ measurements, this research set out to deliver a firmer understanding and unveil new relationships between salinity and the global and regional water cycle.

To help address this question, we first set out to investigate how accurate are remotely sensed salinity observations when compared to in situ measurements. Most satellite products compared reasonably well to in situ observations within the World Ocean Database, but there are strengths and weaknesses that users should be cautious of. Next, we investigated North Atlantic intra-basin moisture transport and its relationship with near-surface salinity, identifying a strongly correlated seasonal cycle of E-P in the subtropics with near-surface salinity in the subpolar region on decadal time scales. Finally, we adapted the salinity pattern amplification framework formulated by Durack et al. (2012) to investigate both short- and long-term changes in salinity patterns. We employed a robust and carefully detailed methodology focused on minimizing sampling biases and improving the representation of uncertainties. We found the following: salinity patterns have amplified at a rate of 4-5%/50yr (consistent with other studies, evidence that the hydrological cycle has also amplified) over the 1957/61-2019/23 pentadal time period (63 years), secular changes in salinity are identifiable between 30- and 40-year time periods, there has been a significant acceleration in salinity pattern amplifications over recent decades, and there has been a widening of the Atlantic/Pacific salinity contrast which could play a critical role in the Atlantic Meridional Overturning Circulation (AMOC) dynamics. Overall, all three chapters have helped improve our knowledge of the intricate relationship between the hydrological cycle and salinity, but many questions still remain unanswered.

5.2 Future Work

5.2.1 Subpolar North Atlantic Mixed Layer Salinity Budget

The biggest question that evolved from the work done in Chapter 3 was whether or not evaporation minus precipitation (E-P) in the subpolar region of the North Atlantic can play a major role in changing near-surface salinity (NSS) on decadal time scales. Of course, subpolar NSS is critical in helping to maintain the AMOC as it plays a major role in ensuring near-surface water becomes dense enough to sink and any changes to NSS could have major impacts on the overturning circulation (Dixon et al., 1999; Fichefet et al., 2003; Stouffer et al., 2006). We found significant negative correlations between E-P in the subtropical North Atlantic and NSS (and E-P) in the subpolar North Atlantic, and linked them through seasonal moisture transports over the North Atlantic on seasonal decadal time scales. This means that when E-P was at its maximum in the subtropical North Atlantic (boreal summer), NSS (and E-P) were at their minimum in the subpolar North Atlantic, and they were linked by maximum poleward moisture fluxes between the subtropical and subpolar North Atlantic during boreal summer. Of course, correlation does not mean causation. Thus, a new hypothesis emerges: E-P can play a significant role in altering the mixed layer salinity in the subpolar North Atlantic on decadal time scales.

This will require us to investigate the mixed layer salinity (MLS) budget in the subpolar North Atlantic, which is presented below and adapted from Ren et al. (2011):

$$\partial S_m/\partial t = [(E - P)/h_m]\cdot S_m - (u_e \cdot \nabla S_m) - (u_g \cdot \nabla S_m) + (w_e \cdot \Delta S)/h_m + \nabla^2 S_m + (I \cdot S_m)/h_m \quad \textbf{(1)}$$

(a) (b) (c) (d) (e) (f) (g)

Where S_m is mixed layer salinity, E-P is the freshwater flux from evaporation and precipitation, h_m is the mixed layer depth, u_e is Ekman velocity, u_g is geostrophic velocity, w_e is entrainment velocity, and I is the sea ice contribution. The terms are: a – salinity tendency, b – freshwater flux, c – Ekman advection, d – geostrophic advection, e – entrainment, f – horizontal diffusion, and g – sea ice melting/freezing.

Yu (2011) performed a global analysis of the mixed layer salinity (MLS) budget and found that E-P was not the dominant term over the subpolar North Atlantic. However, this analysis did not separate the dominant terms by season and therefore it is unclear whether or not freshwater fluxes dominate at any time period (particularly during boreal summer). Additionally, based on our work in Chapter 4, we know salinity patterns are amplifying and are directly related to an amplified hydrological cycle. Thus, in the subpolar region where P > E, we would expect more precipitation in a warming world and the potential for it to impart greater influence on the salinity budget. Therefore, through reanalysis products (e.g., Simple Ocean Data Assimilation) and global coupled climate models (e.g., CMIP6), we can investigate the mixed layer salinity budget on decadal time scales to begin to understand the role atmospheric freshwater fluxes have on salinity in the subpolar North Atlantic.

This analysis will also address one of the key questions that arose from Chapter 4 and that is does the salinification of the subtropical North Atlantic and its eventual poleward advection into the subpolar North Atlantic help offset (or dominate) the anticipated increase in freshwater advection from the Arctic and Greenland into the subpolar North Atlantic in a warming world. The analysis of the mixed layer salinity budget should help address this question as we can split the advection into salty and fresh advection components. This work will also help address many of the questions posed at the end of section 4.4.

5.2.2 Refining Regions of Salinity Pattern Amplification

The salinity pattern amplification and spatial pattern correlations presented in Chapter 4 assumed large scale salinity anomalies are mostly zonal. This is not unreasonable to assume for most of the major ocean basins, but this assumption fails in some key areas, most notably the Indian basin north of 30°S. The climatological salinity pattern of the Indian basin (see black contours of Fig. 4.2) shows mostly fresh areas (< 35) on the eastern side and salty areas (> 35) on the western side. The eastern side is dominated by precipitation and areas that receive excessive river run off (e.g., Bay of Bengal), whereas the western side is dominated by evaporation (e.g., Arabian Sea). When computing the salinity pattern amplifications, a zonal average at each latitude is taken of the climatological anomalies (climatology – global average [34.62]) and the salinity trends. This is an issue in the Indian basin since the large-scale salinity pattern is not zonal and therefore amplifications are eventually deemed insignificant (see Fig. 4.13c).

For future work, we can better capture salty, fresh, and transition areas so that averages, zonal or otherwise, are over a more common area. For example, we could employ the methodology used to determine the salty and fresh regions in Fig. 4.14 where we identified climatologically fresh and climatologically salty regions based on grid values that were >= 0.6745 standard deviations away from the basin-average near-surface mean. The 50% of grid points not labeled fresh or salty in each ocean basin can be labeled as the transition zone. The expectation is this will provide us with a more robust estimate of salinity trends and amplifications. We could test this approach in the future work discussed in 5.2.1.

5.2.3 Subsurface Salinity Changes on Isopycnal Surfaces

This dissertation has primarily focused on surface salinity changes, but salinity is a conservative tracer, and outside of mixing, these changes should be observed at depth as the water flows along isopycnals. We have conducted numerous studies of subsurface salinity changes, documenting how they have changed from one year to the next and over the entire Argo-era (2005-present) (Reagan et al., 2016, 2017, 2018a, 2019, 2020, 2021, 2022, 2023, 2024a), but these analyses have all occurred on standard depth surfaces (meters). Future work should focus on creating salinity anomaly analyses on isopycnal surfaces and examining both short and long-term variability. For example, if we were to recompute salinity pattern amplifications on certain isopycnal surfaces (rather than just at the near-surface) we would likely develop a more robust metric of salinity pattern amplification since we are isolating water masses by density. We could also detect how these isopycnals have changed over time in response to changing salinity and what implications that may have on global ocean circulation.

5.3 Closing Remarks

The first quarter of the 21st century has provided us with an unprecedented number of ocean observations from both satellites and in situ instruments. We have witnessed a change in the global ocean observing system which was once dominated by observations taken aboard research-vessels to the current day system where observations are mostly taken by autonomous instruments (e.g., Argo profiling floats, gliders; see Fig 1.3, 1.4). Satellite salinity provides us with near-global views of surface salinity in just a matter of days, whereas autonomous instruments out at sea, like the Argo profiling floats, are sampling down to 2000m every 10 days and providing near-global coverage. The insights we have been able to glean from the new observing paradigm is truly remarkable. Who knew that surface salinity anomalies could help predict terrestrial precipitation (Li et al., 2022; Li et al., 2016a; Liu et al., 2018), or that they could play a major role in the rapid intensification of hurricanes (Balaguru et al., 2020). I believe we are just touching the tip of the iceberg in terms of how we can use all of this salinity data. With artificial intelligence becoming a mainstay in oceanographic and climate research, the value of salinity data is only going to grow moving forward. It is critical that the current global ocean observing system be maintained. From ensuring safe shipping routes to monitoring ecosystem change, the ocean observing system plays a critical role in our everyday lives. I will finish this dissertation with one request, that we maintain a global baseline of ocean observations made from research vessels. These observations are of the highest quality, but the number of them have been dropping over for the last couple of decades due to cost and the advent of autonomous instruments (Fig. 1.3, 1.4). However, without these high-quality observations, we would have no way to validate and calibrate our autonomous instruments. They go hand and hand.

Appendices:

Appendix A: Supplementary Material for Chapter 2

A.1: Updated Satellite Salinity Comparisons with In Situ

The following satellite salinity datasets were compared to in situ salinity fields from the National Centers for Environmental Information. All data, if not already in proper spatial and temporal dimensions, were regridded onto a 1°x1° horizontal grid, and monthly means were computed. Ice fraction information from the SMAP JPL product was used across all products to remove any potential ice contamination.

Aquarius v5.0: This is the level-3 version 5.0 monthly salinity standard mapped image (Lee et al., 2012). The following is the dataset citation:

NASA Aquarius project. 2017. Aquarius Sea Surface Salinity Products. Ver. 5.0. PO.DAAC, CA, USA. Dataset accessed [2025-03-13] at https://doi.org/10.5067/AQR50-3Y3DE

Soil Moisture Active Passive (SMAP) – Jet Propulsion Laboratory (JPL): This is the level-3 version 5.0 monthly combined/active passive salinity standard mapped image (Fore et al., 2016). The following is the dataset citation:

JPL. 2020. JPL CAP SMAP Sea Surface Salinity Products. Ver. 5.0. PO.DAAC, CA, USA. Dataset accessed [2025-03-13] at https://doi.org/10.5067/SMP50-3TMCS

SMAP – Remote Sensing System (RSS): This is the level-3 version 6.0 monthly salinity standard mapped image. The following is the dataset citation:

Remote Sensing Systems (RSS). 2024. SMAP Sea Surface Salinity Products. Ver. 6.0. PO.DAAC, CA, USA. Dataset accessed [2025-03-13] at https://doi.org/10.5067/SMP60-3SMCS

CATDS-CEC-LOCEAN Soil Moisture Ocean Salinity (SMOS) – This is the level-3 version 9.0 debiased 9-day salinity product. The data reference is:

Boutin J., Vergely J.-L., Khvorostyanov D. (2024). SMOS SSS L3 maps generated by CATDS CEC LOCEAN. debias V9.0. SEANOE. https://doi.org/10.17882/52804#109630.

*As was noted in Chapter 2, the debiased SMOS product is not independent of in situ observations as they are used extensively in the debiasing stage. Therefore, please use caution when drawing any conclusions from the in situ – SMOS comparison.

Updated Comparisons:

Aquarius v5.0 vs WOD – The large-scale differences that were seen between Aquarius v2.5.1 and WOD in Reagan et al. (2014) mostly persist in the most recent comparison between Aquarius v5.0 and WOD. Aquarius v5.0 does appear to have a better handle on radio frequency interference (RFI) as the salinity differences near Europe and Asia are much improved (Fig. A.1). However, the zonal average of the differences shows a very similar pattern that we encountered with Aquarius v2.5.1 in that there are positive differences in the higher latitudes with negative differences in the subtropical and tropical latitudes (Fig. A.3). The high latitude difference is likely still due to the colder SSTs and windy conditions wreaking havoc on the satellite salinity retrieval. Overall, Aquarius v5.0 does appear to have made incremental improvements over Aquarius v2.5.1.

SMAP JPL vs WOD – SMAP JPL v5.0 exhibits mostly positive differences when compared to WOD (Fig. A.5). The differences are greater than 0.3 for much of the high latitudes which is clearly evident in the zonal average difference plot (Fig. A.7). The only region that exhibits negative differences is in the 20°S-40°S area of the Southern Ocean. Overall, there does appear to be a significant positive bias in the SMAP JPL v5.0 data based on Fig A.6.

SMAP RSS vs WOD - SMAP RSS v6.0 appears to have removed a lot of the bias present in the SMAP JPL v5.0 product. This is likely due to SMAP RSS v6.0 using in situ data fields for calibration, and leveraging different geophysical models. There is clear improvement when comparing SMAP RSS v6.0 (Fig A.9) to SMAP JPL v5.0 (Fig A.5). The zonal-average differences compared to in situ show small differences for all latitudes outside of the tropical region where there is a negative bias (Fig. A.10). Overall, outside of known regions of satellite salinity retrieval difficulty (e.g., coasts, high latitudes, etc.), SMAP RSS v6.0 performs quite well when compared to WOD.

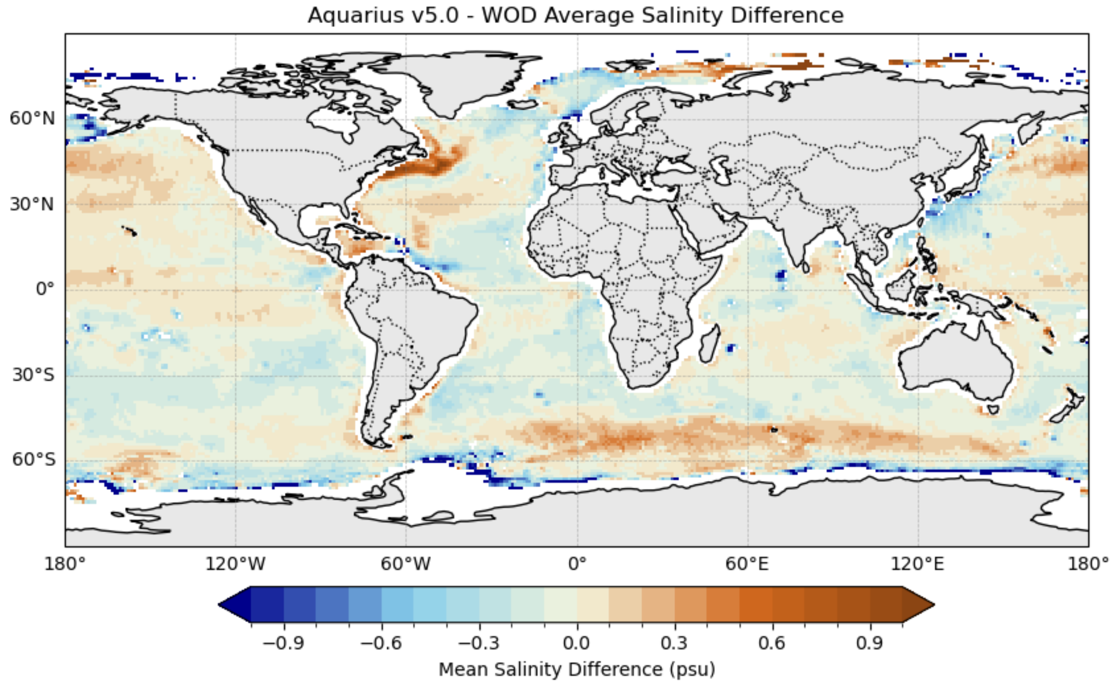

Figure A.1: Average monthly difference for Aquarius v5.0 minus in situ near-surface salinity from 09/2011-06/2015.

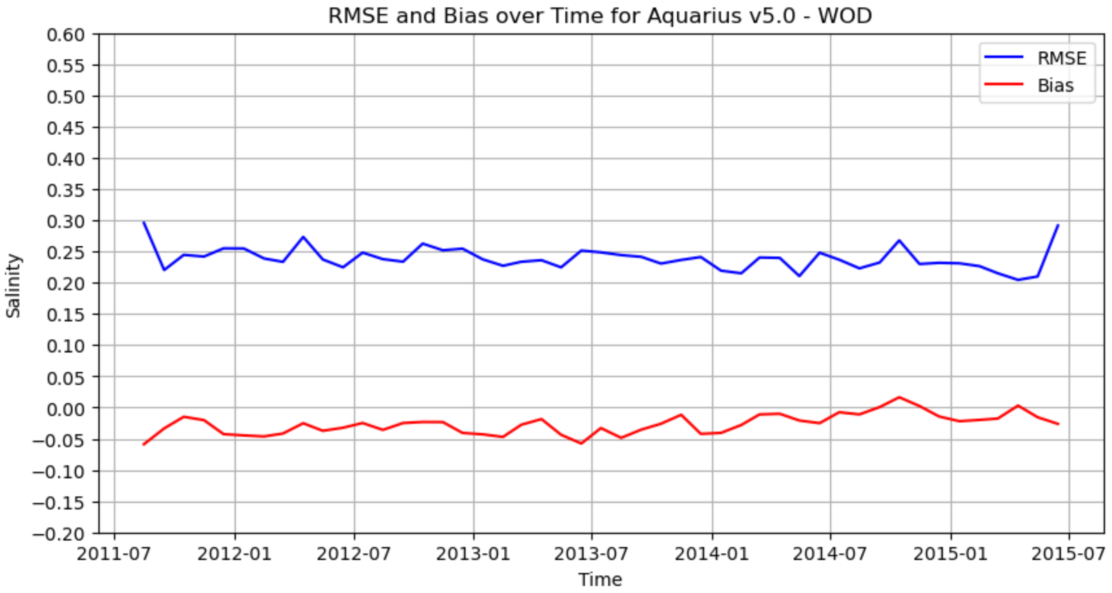

Figure A.2: Root mean squared error (blue) and bias (red) for Aquarius v5.0 minus in situ near-surface salinity from 09/2011-06/2015.

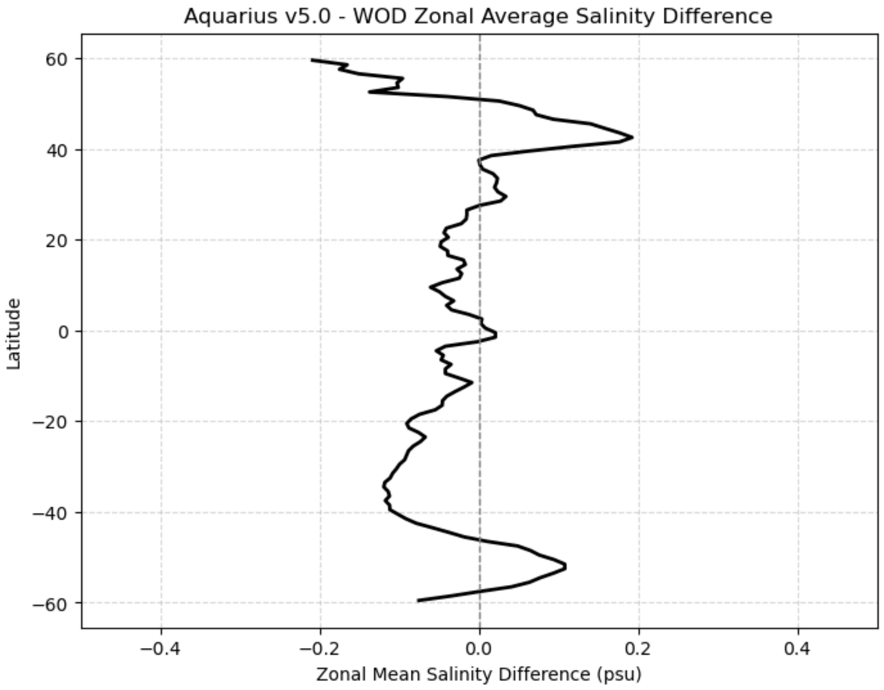

Figure A.3: Zonal average difference for Aquarius v5.0 minus in situ near-surface salinity from 09/2011-06/2015.

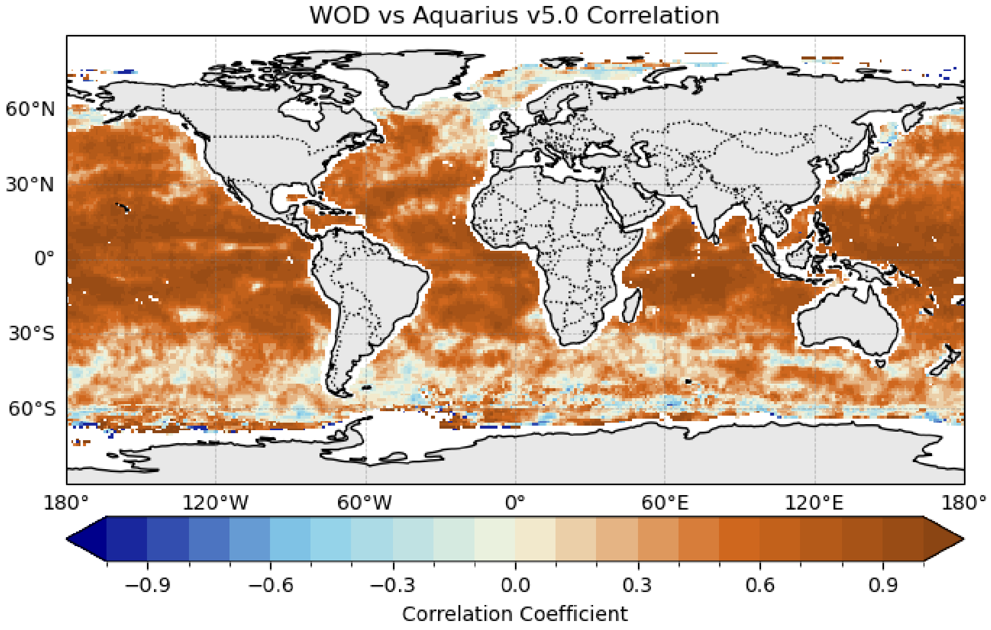

Figure A.4: Correlation between Aquarius v5.0 and in situ near-surface salinity from 09/2011-06/2015.

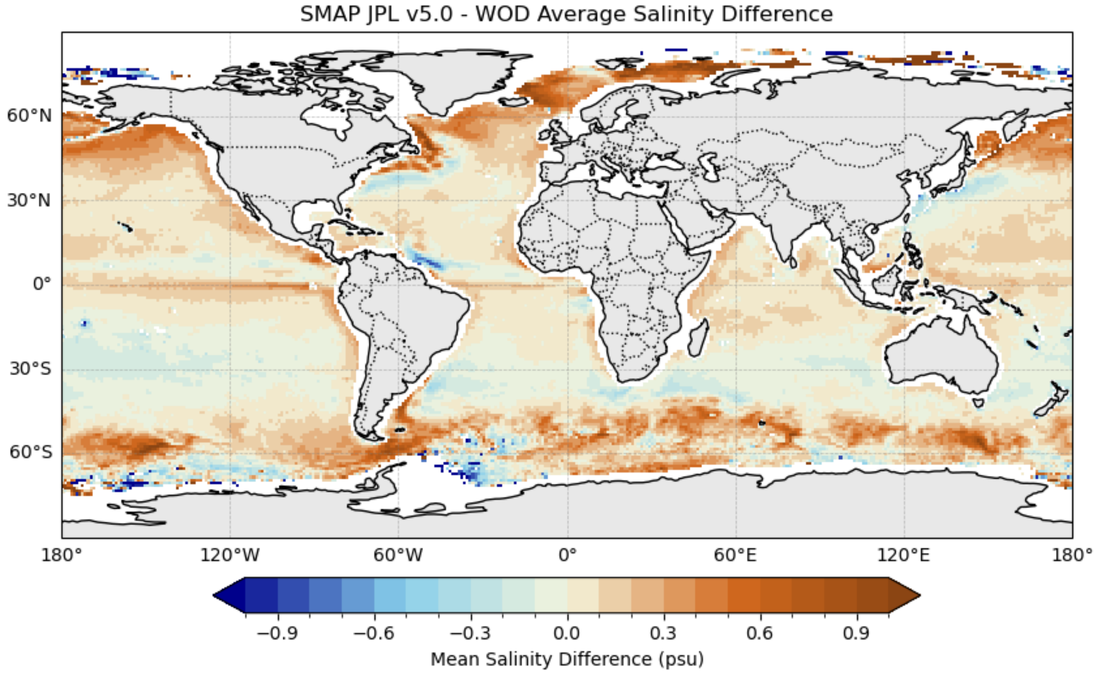

Figure A.5: Average monthly difference for SMAP JPL v5.0 minus in situ near-surface salinity from 04/2015-12/2023.

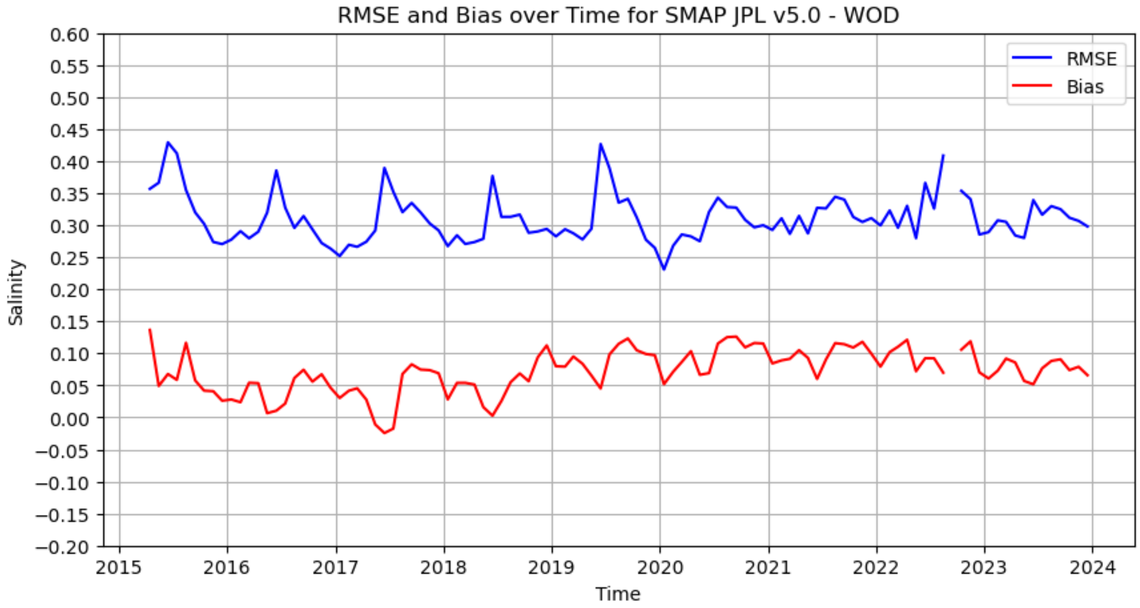

Figure A.6: Root mean squared error (blue) and bias (red) for SMAP JPL v5.0 minus in situ near-surface salinity from 04/2015-12/2023.

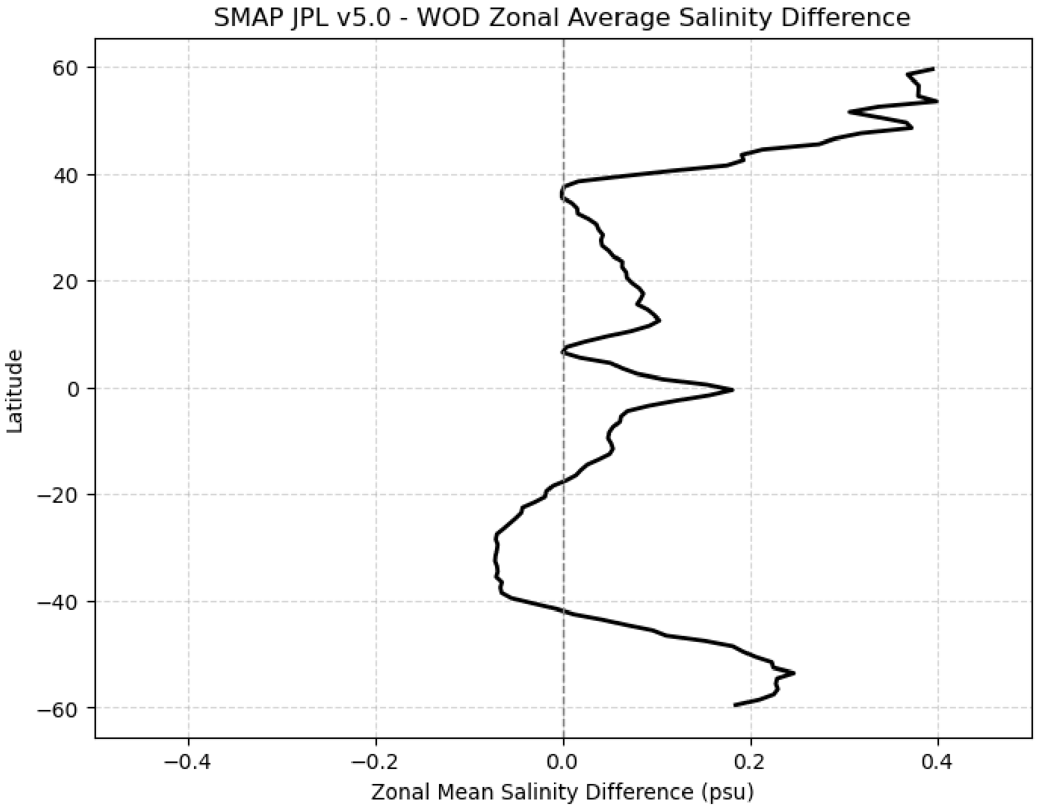

Figure A.7: Zonal average difference for SMAP JPL v5.0 minus in situ near-surface salinity from 04/2015-12/2023.

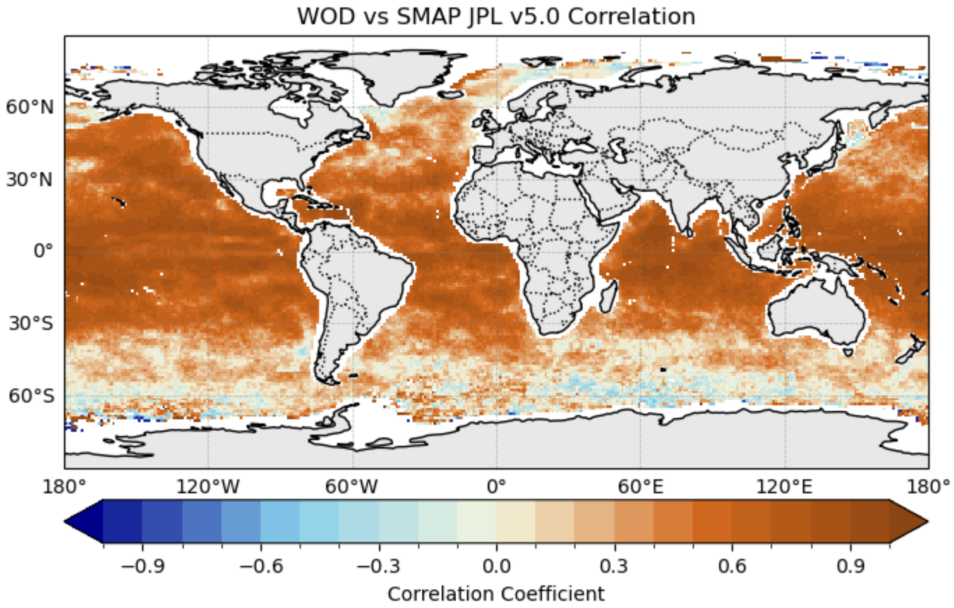

Figure A.8: Correlation between SMAP JPL v5.0 and in situ near-surface salinity from 04/2015-12/2023.

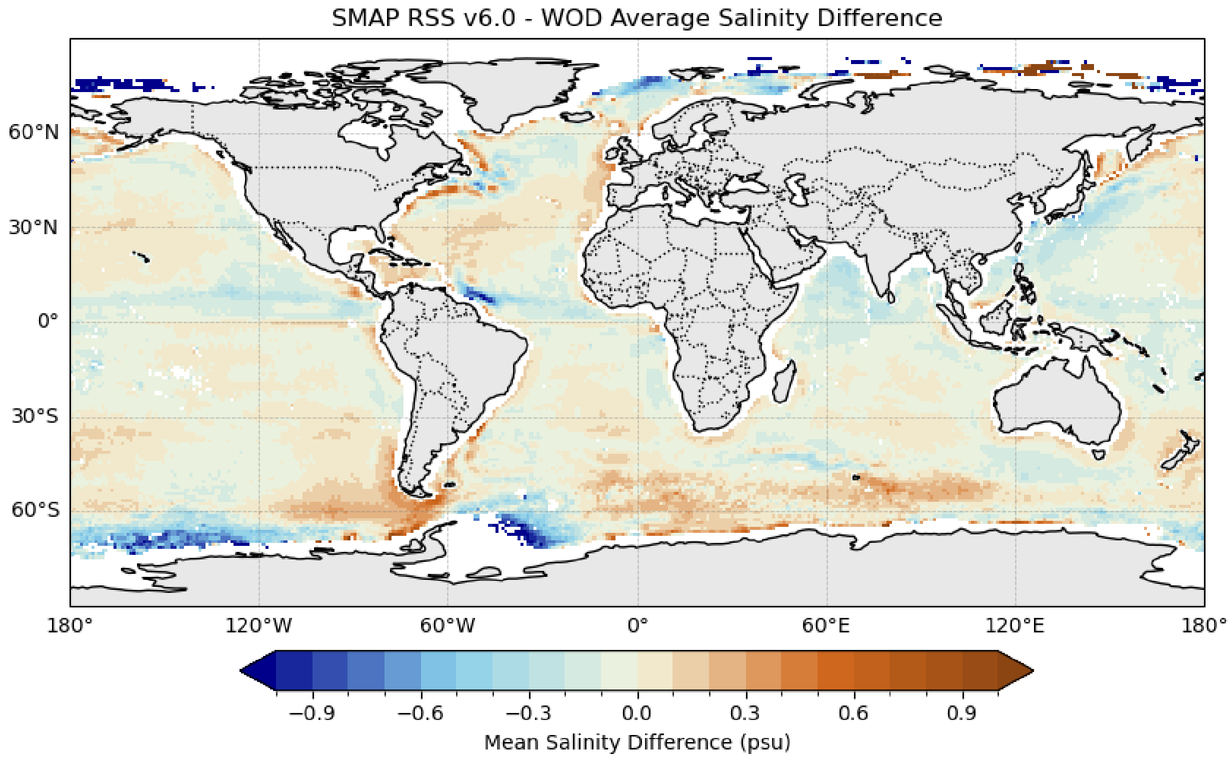

Figure A.9: Average monthly difference for SMAP RSS v6.0 minus in situ near-surface salinity from 04/2015-12/2023.

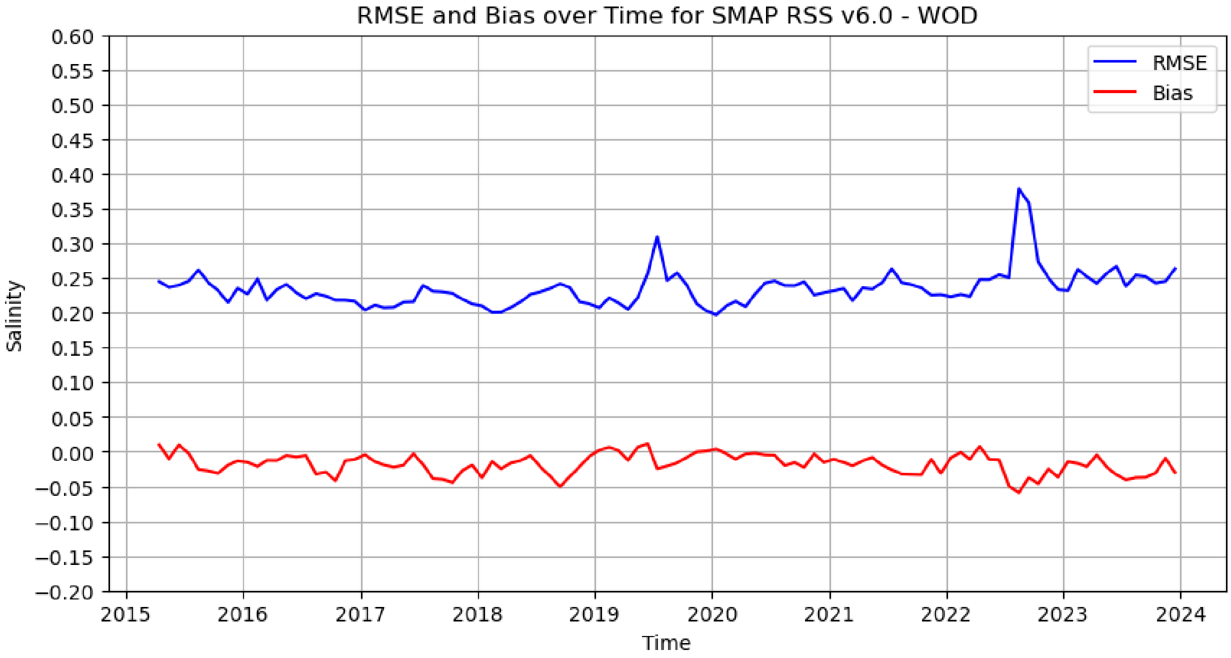

Figure A.10: Root mean squared error (blue) and bias (red) for SMAP RSS v6.0 minus in situ near-surface salinity from 04/2015-12/2023.

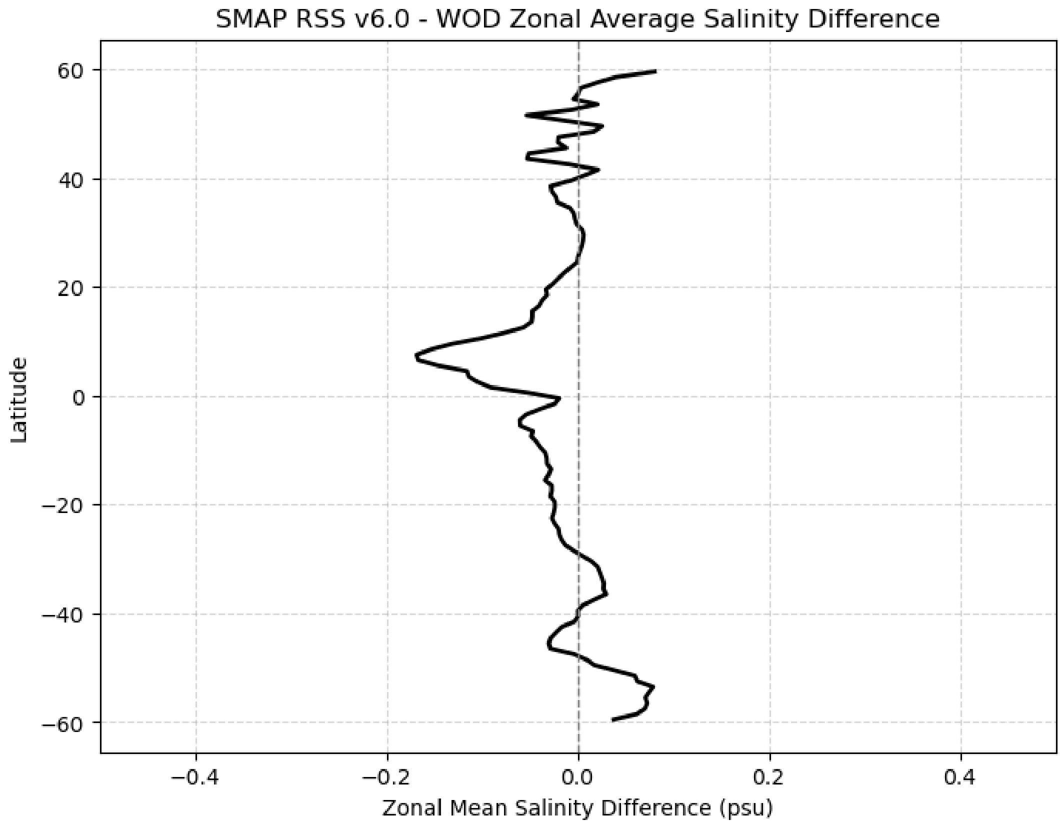

Figure A.11: Zonal average difference for SMAP RSS v6.0 minus in situ near-surface salinity from 04/2015-12/2023.

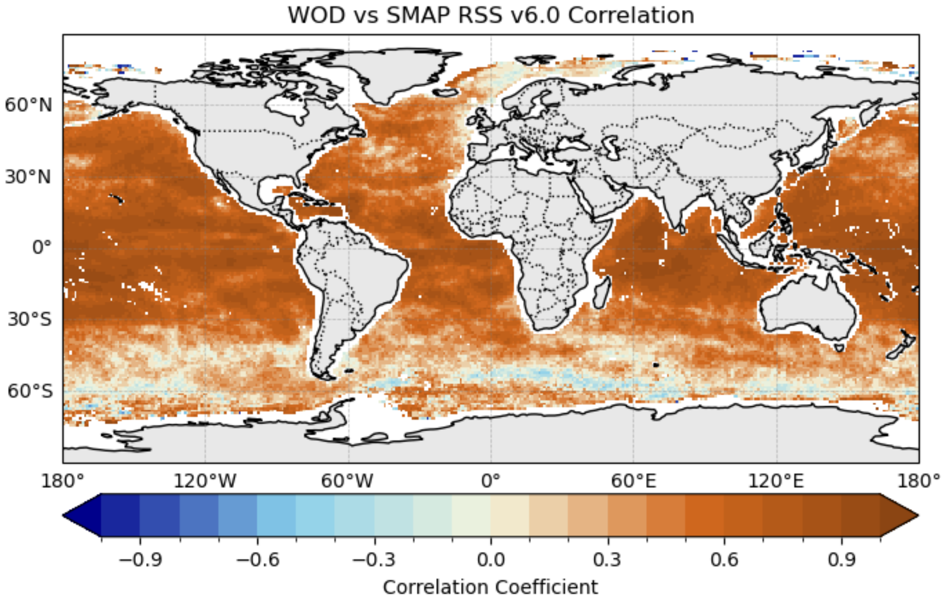

Figure A.12: Correlation between SMAP RSS v6.0 and in situ near-surface salinity from 04/2015-12/2023.

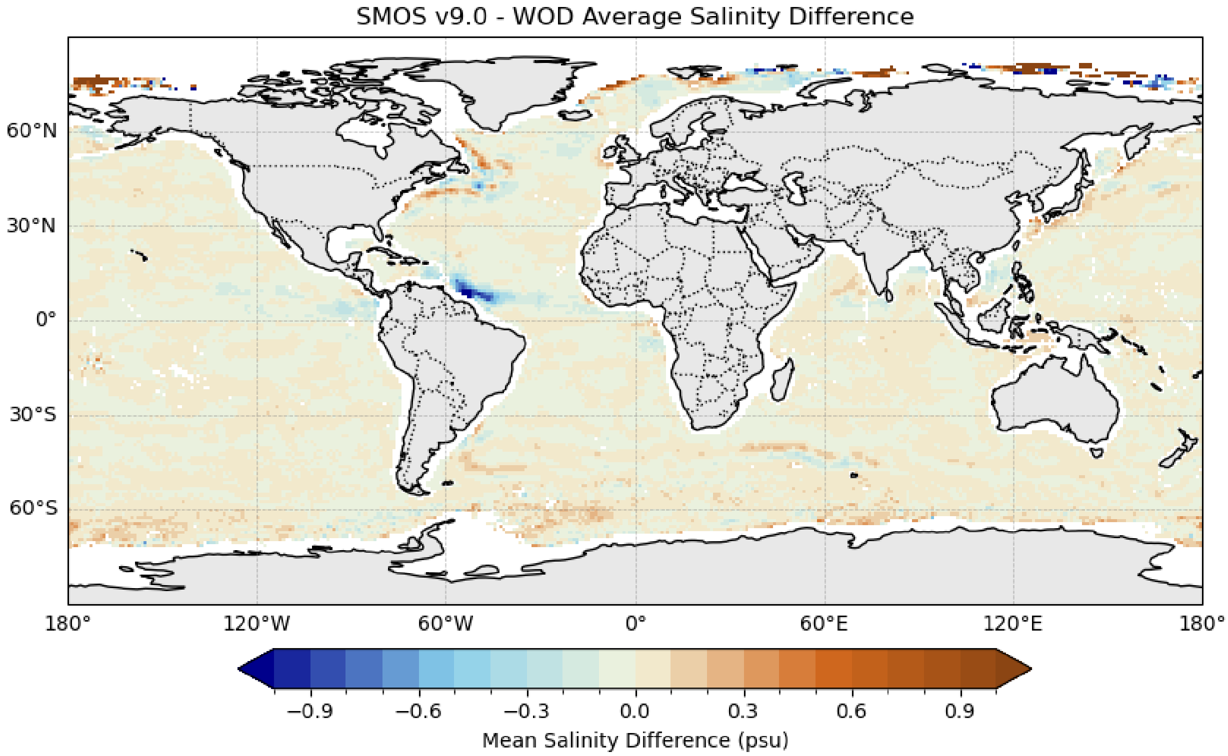

Figure A.13: Average monthly difference for SMOS debiased v9.0 minus in situ near-surface salinity from 01/2010-12/2023.

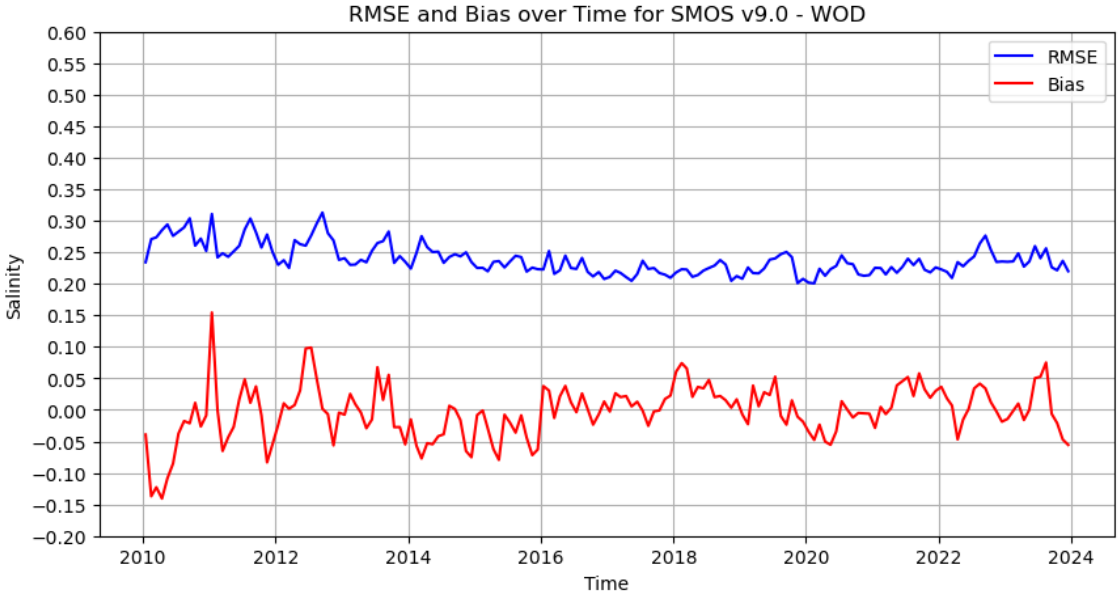

Figure A.14: Root mean squared error (blue) and bias (red) for SMOS debiased v9.0 minus in situ near-surface salinity from 01/2010-12/2023.

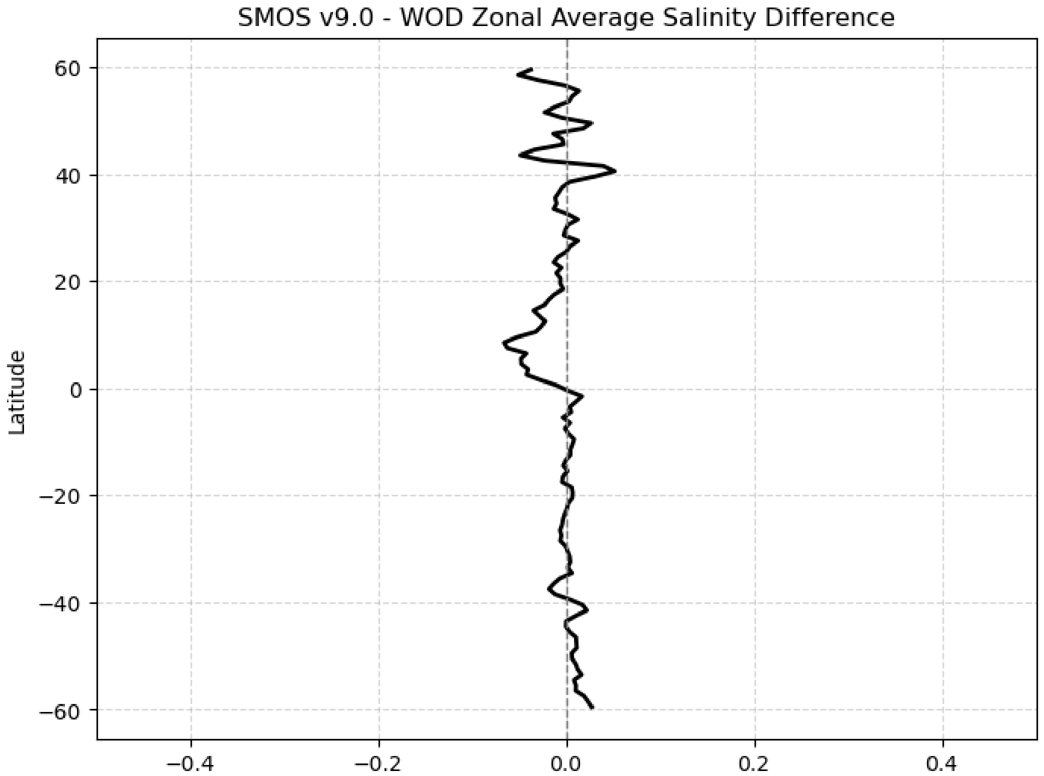

Figure A.15: Zonal average difference for SMOS debiased v9.0 minus in situ near-surface salinity from 01/2010-12/2023.

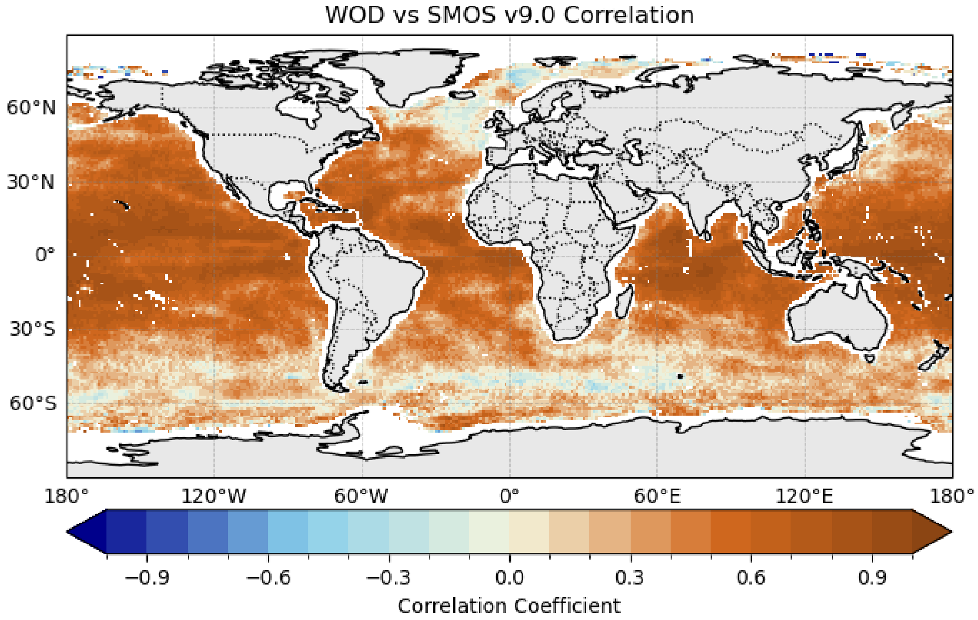

Figure A.16: Correlation between SMOS debiased v9.0 and in situ near-surface salinity from 01/2010-12/2023.

Appendix B: Supplementary Material for Chapter 3

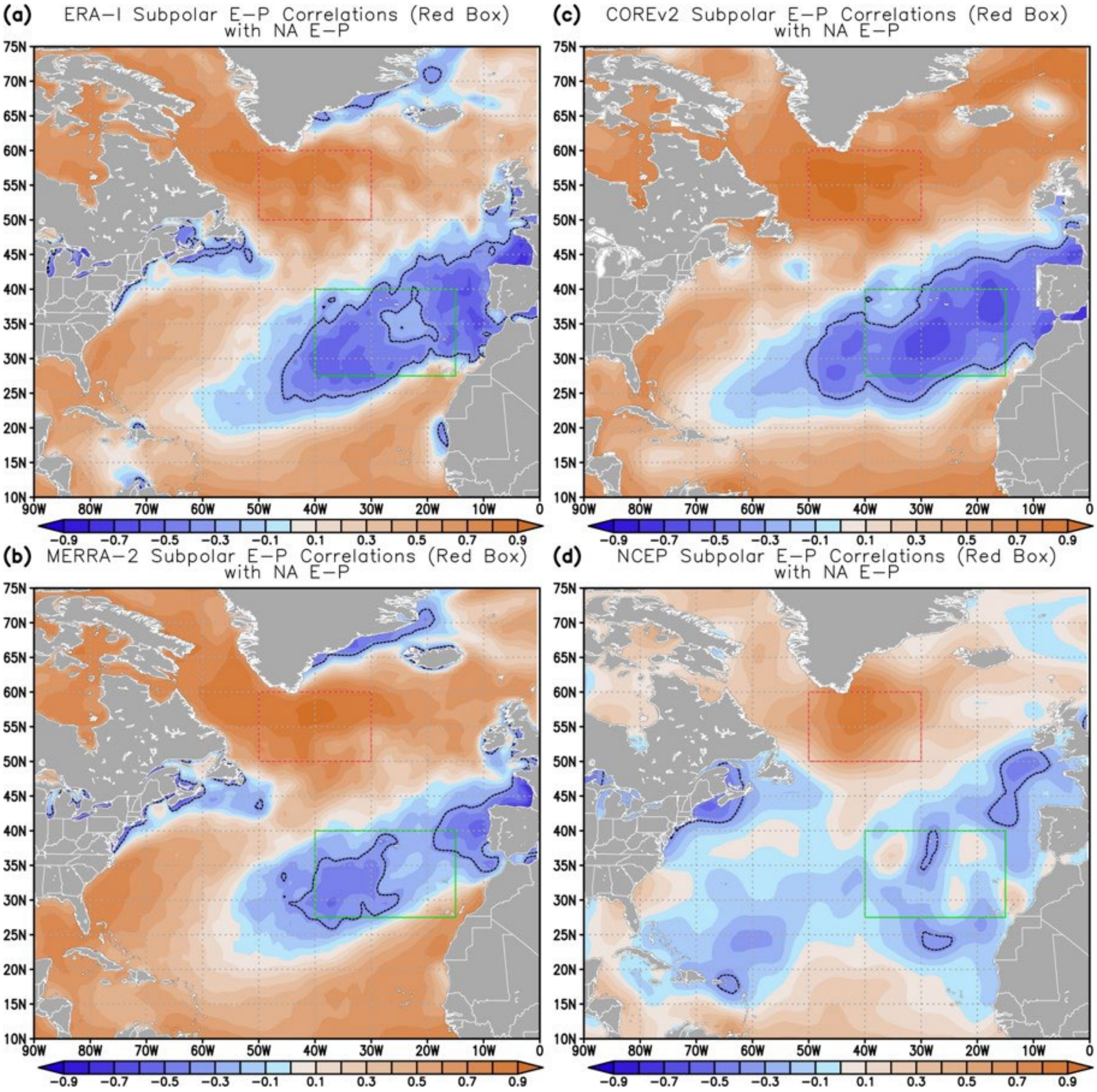

Figure B.1: The 1985-2012 North Atlantic correlation between the area-averaged subpolar gyre E-P (red-contoured rectangle) and the E-P over the rest of the North Atlantic Ocean for a) ERA-I reanalysis, b) MERRA-2 reanalysis, c) COREv2, and d) NCEP/NCAR reanalysis. Shaded correlations are based on the 1985-1994, 1995-2004, and 2005-2012 monthly climatological E and P fields (N=36). The black dotted line represents the region where correlation is lower than -0.330 (95% CI). The red-contoured box has the following boundaries: 310-330°E and 50-60°N. This figure is similar to Fig. 3.2b in the main text.

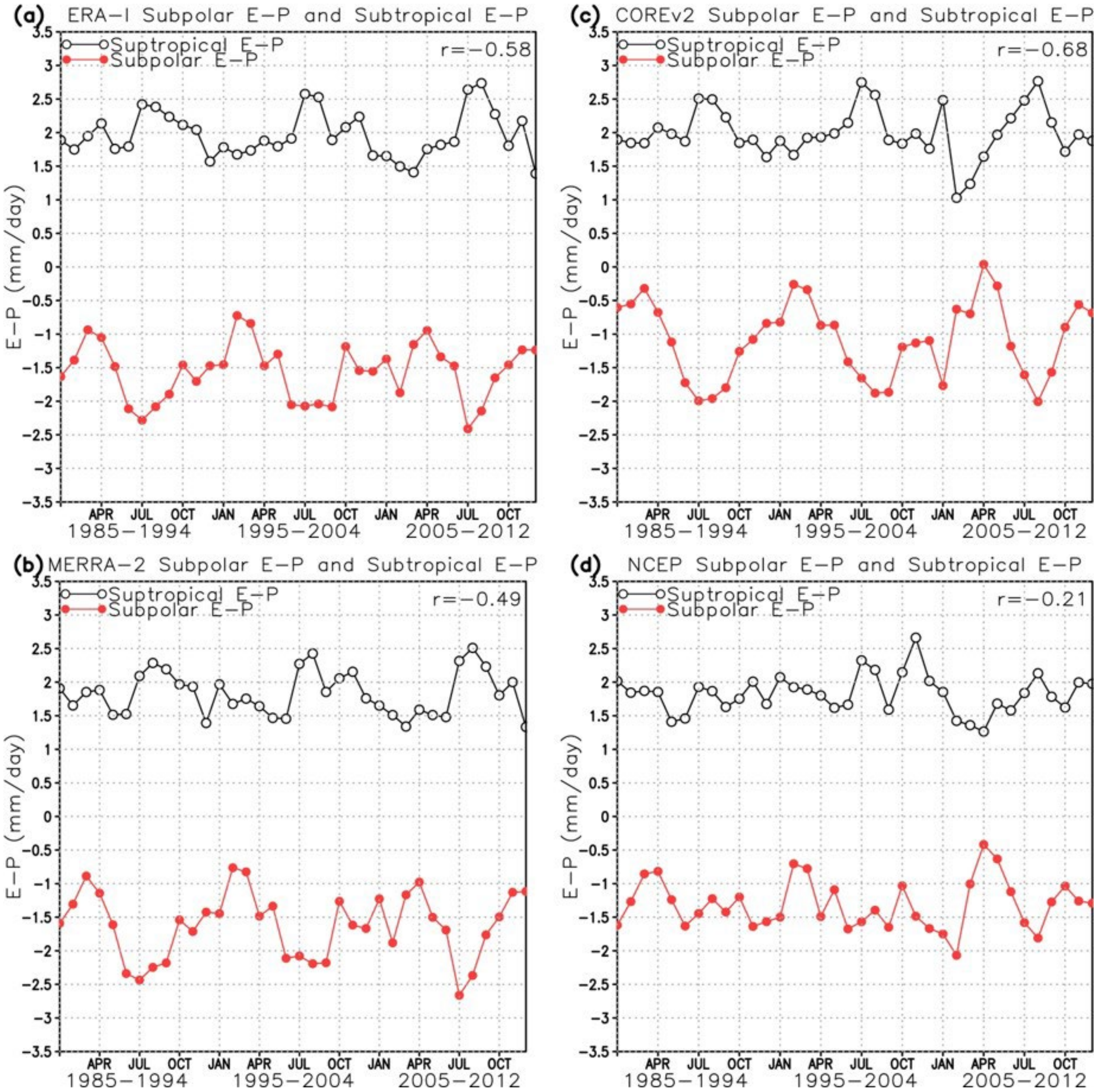

Figure B.2: The 1985-2012 North Atlantic time series of area-averaged E-P over the subpolar NA (red box in Appendix B Fig. B.1) and E-P over the subtropical NA (green box in Appendix B Fig. B.1) for a) ERA-I reanalysis, b) MERRA-2 reanalysis, c) COREv2, and d) NCEP/NCAR reanalysis. Time series and corresponding correlation between the two time series in each plot is based on the 1985-1994, 1995-2004, and 2005-2012 monthly climatological E and P fields (N=36). The red box in Appendix B Fig. B.1 has the boundaries: 310-330°E and 50-60°N and the green box has the boundaries: 320-345°E and 27.5-40°N. This figure is similar to Fig. 3.2c in the main text.

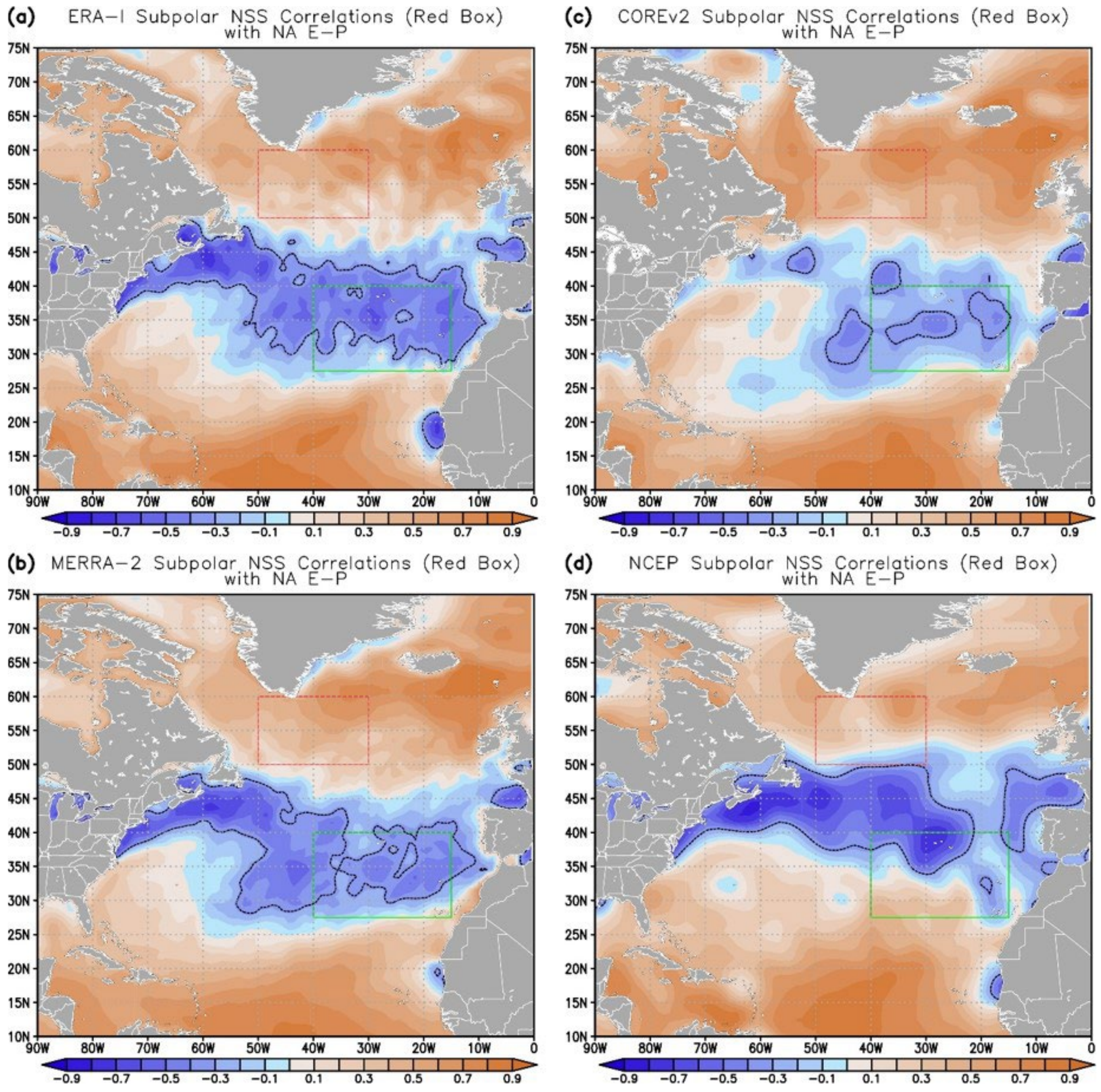

Figure B.3: Similar to Appendix B Fig B.1, but represents correlations between area-average subpolar NSS (red box) and NA E-P for a) ERA-I reanalysis, b) MERRA-2 reanalysis, c) COREv2, and d) NCEP/NCAR reanalysis. The black dotted line represents the region where correlation is lower than -0.330 (95% CI). Boundaries remain the same from Appendix B Fig. B.1. This figure is similar to Fig. 3.3a in the main text.

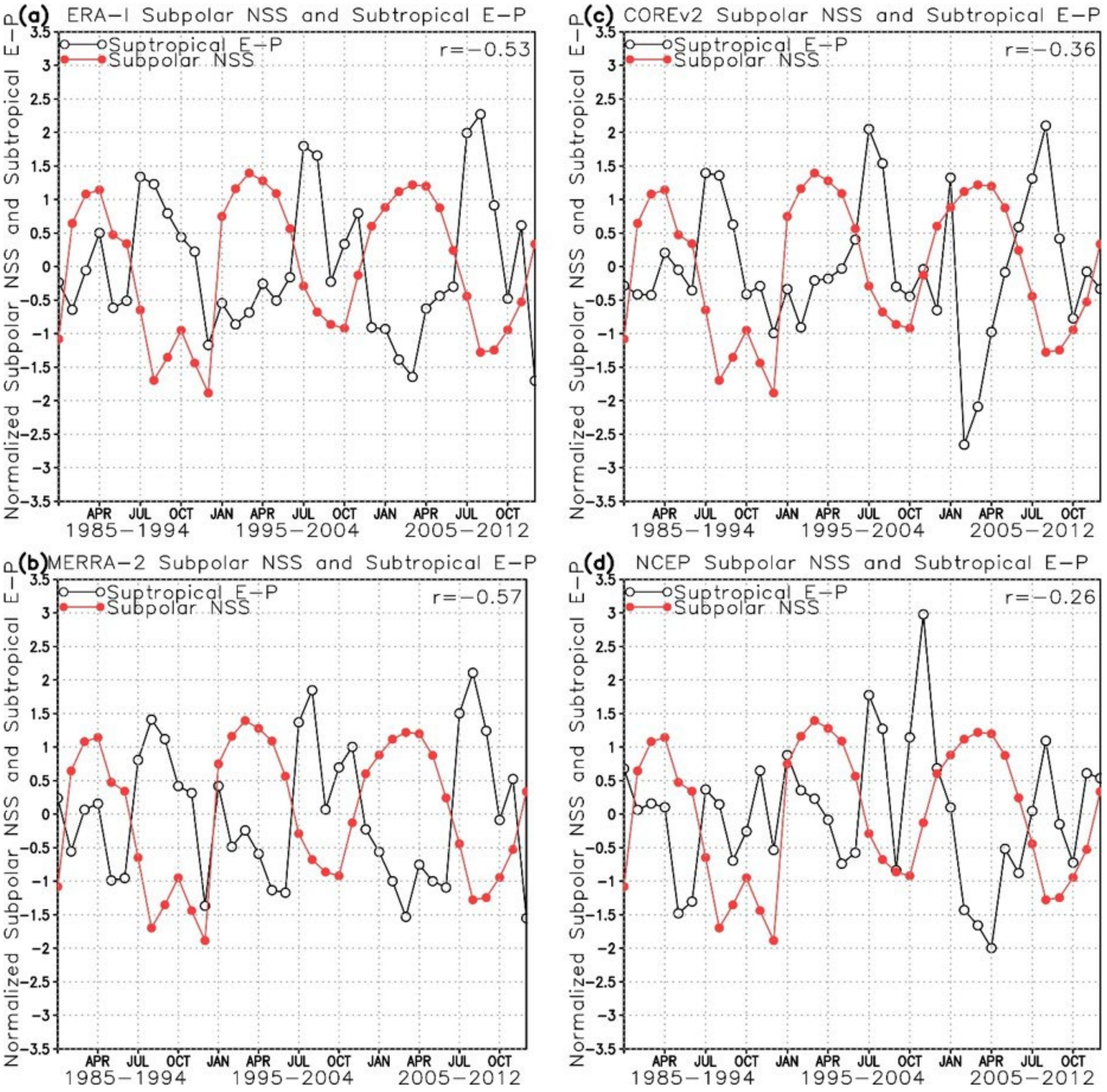

Figure B.4: Similar to Appendix B Fig B.2, but represents the time series of area-averaged NSS over the subpolar NA (red box in Appendix B Fig. B.3) and E-P over the subtropical NA (green box in Appendix B Fig. B.3) for a) ERA-I reanalysis, b) MERRA-2 reanalysis, c) COREv2, and d) NCEP/NCAR reanalysis. Boundaries remain the same from Fig. B.2. This figure is similar to Fig. 3.3b in the main text.

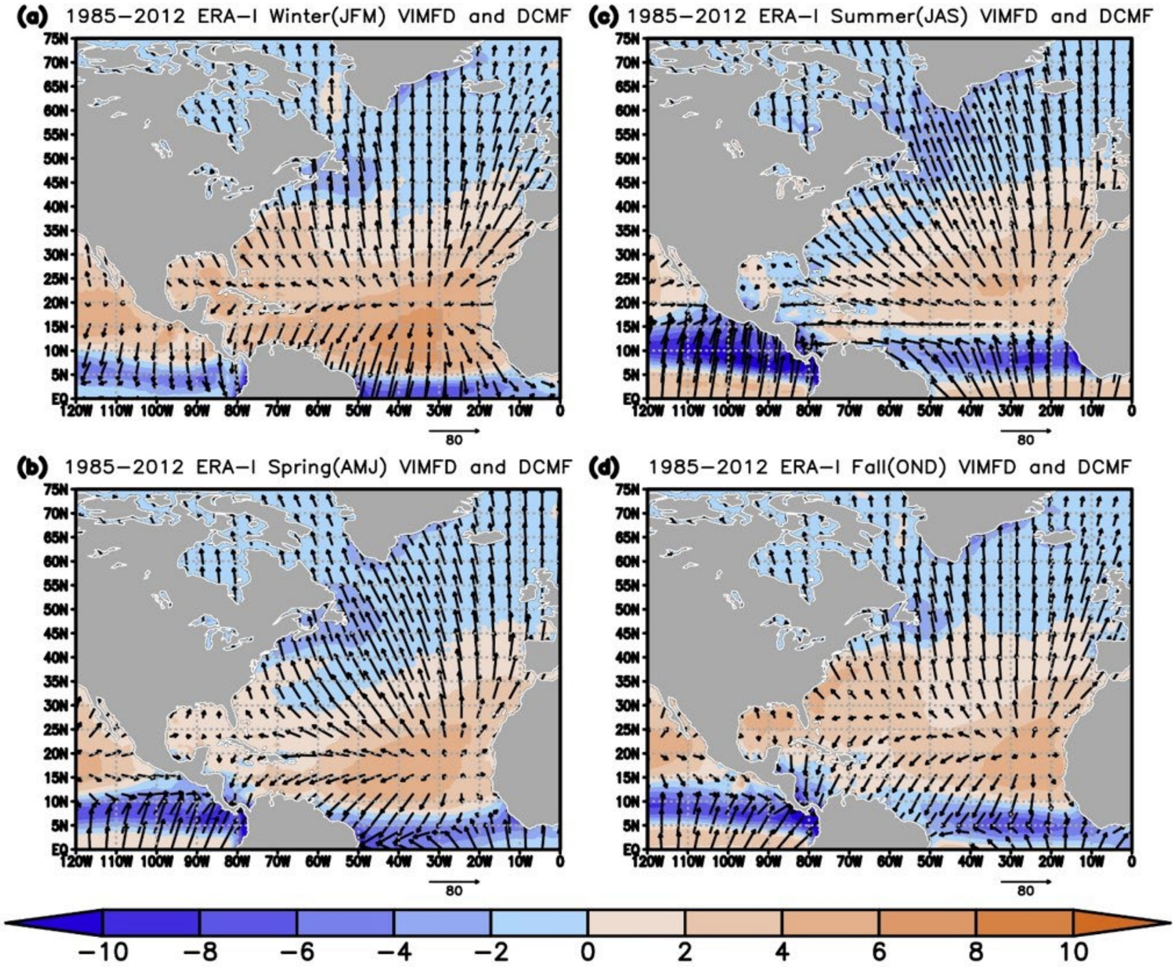

Figure B.5: The 1985-2012 seasonal average of the vertically integrated moisture flux divergence (VIMFD, mm*day-1, shaded) and the divergent component of the moisture fluxes (DCMF, kg*m-1*sec-1, vectors) for ERA-I reanalysis during a) winter (JFM), b) spring (AMJ), c) summer (JAS), and d) fall (OND). Orange shades represent moisture divergence and blue shades represent moisture convergence. This is similar to Fig. 3.4 in the main text.

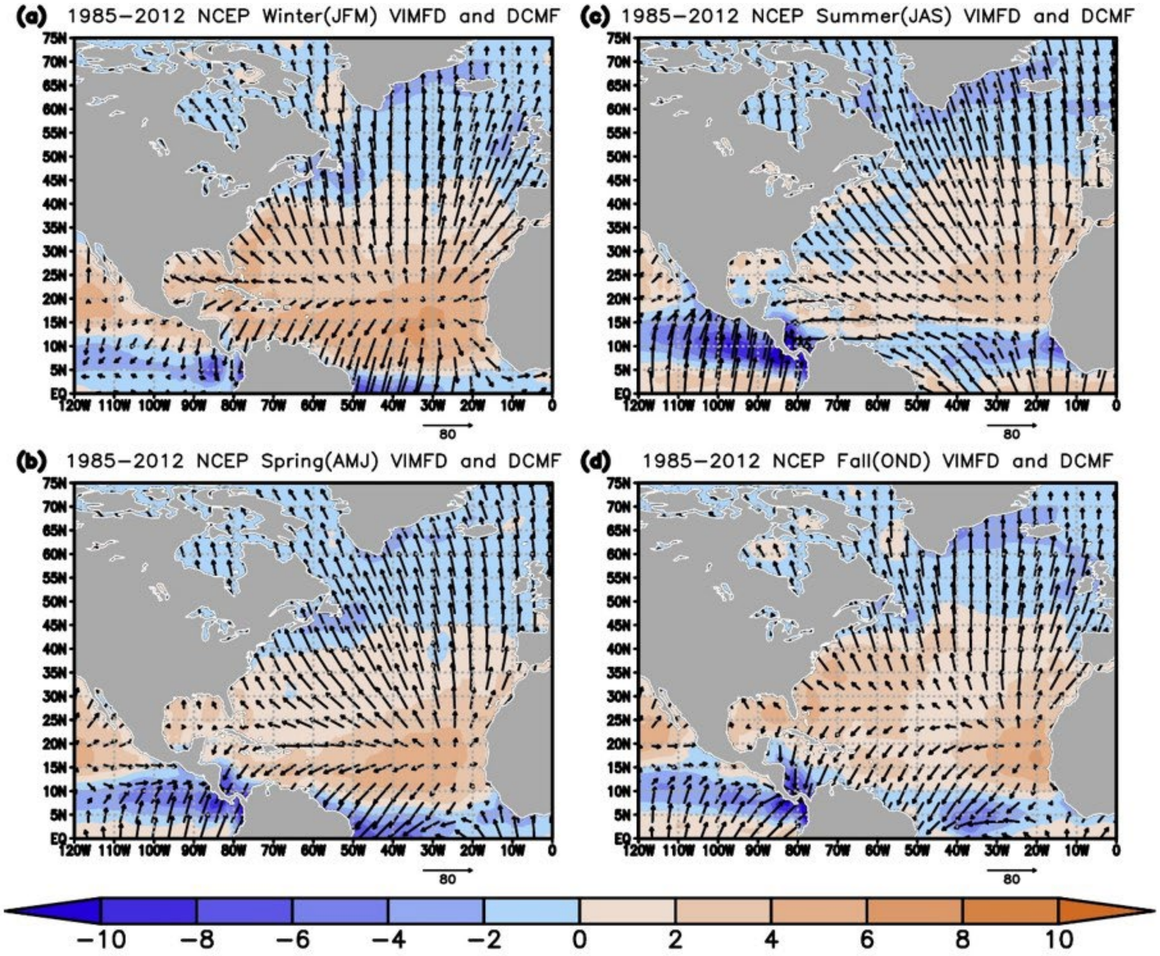

Figure B.6: The 1985-2012 seasonal average of the vertically integrated moisture flux divergence (VIMFD, mm*day-1, shaded) and the divergent component of the moisture fluxes (DCMF, kg*m-1*sec-1, vectors) for NCEP/NCAR reanalysis during a) winter (JFM), b) spring (AMJ), c) summer (JAS), and d) fall (OND). Orange shades represent moisture divergence and blue shades represent moisture convergence. This is similar to Fig. 3.4 in the main text.

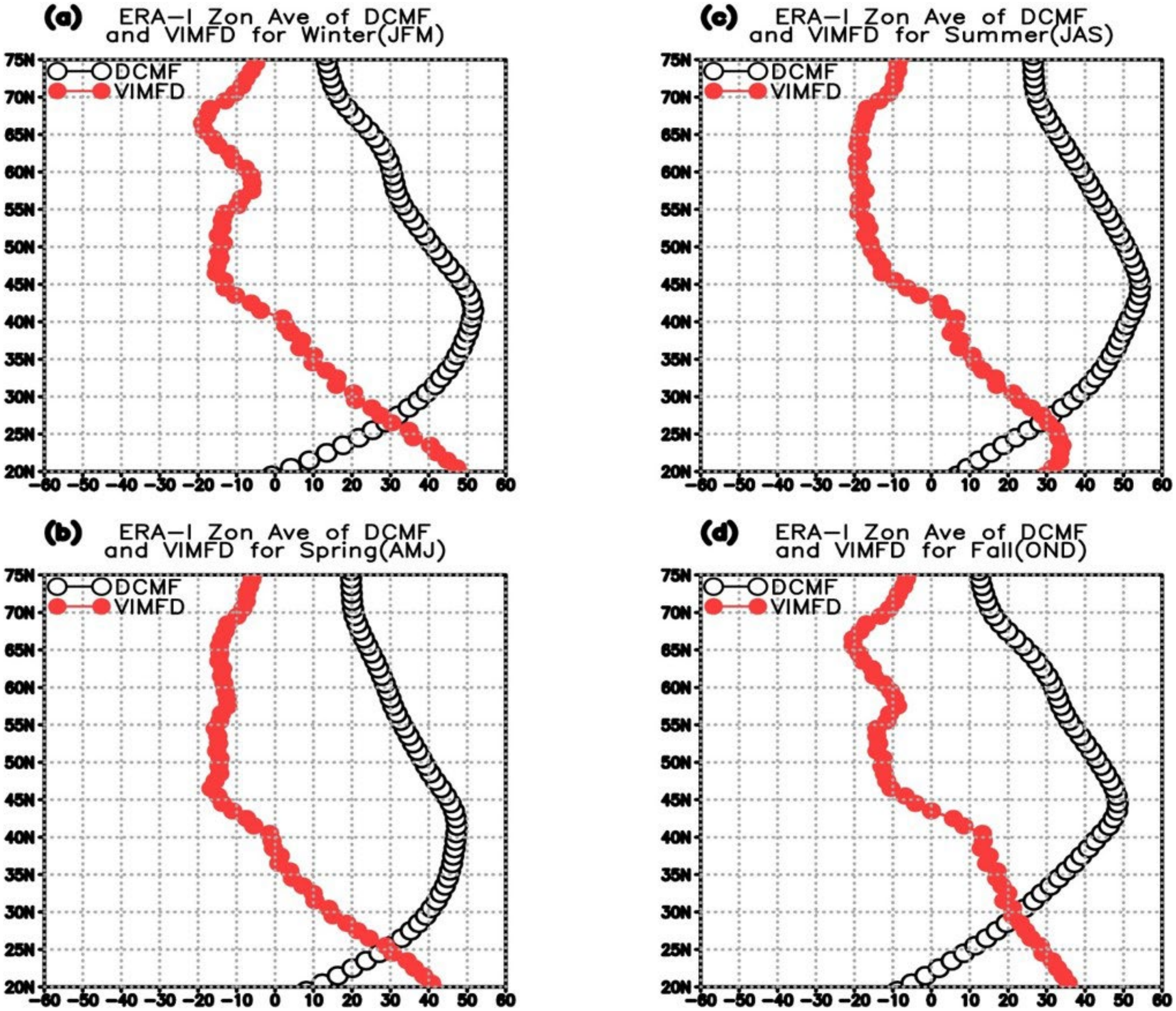

Figure B.7: The 1985-2012 zonal average of the meridional component of the DCMF (kg*m-1*sec-1, black line) and of the VIMFD (10*mm*day-1, red line) for ERA-I reanalysis during a) winter (JFM), b) spring (AMJ), c) summer (JAS), and d) fall (OND). The zonal average was taken over the 60°W-20°W area (see Appendix B Fig. B.5a-d). This is similar to Fig. 3.5 in the main text.

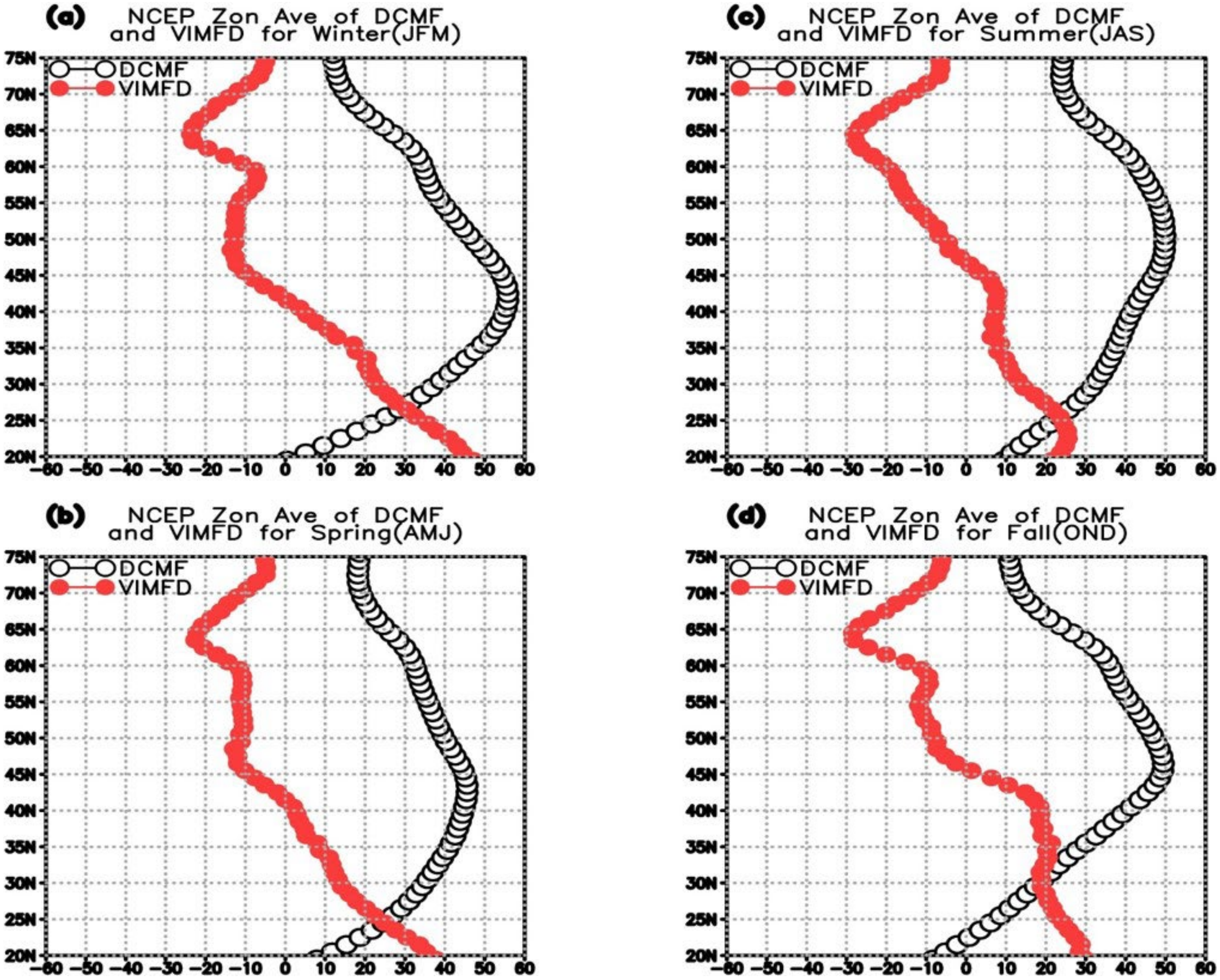

Figure B.8: The 1985-2012 zonal average of the meridional component of the DCMF (kg*m-1*sec-1, black line) and of the VIMFD (10*mm*day-1, red line) for NCEP/NCAR reanalysis during a) winter (JFM), b) spring (AMJ), c) summer (JAS), and d) fall (OND). The zonal average was taken over the 60°W-20°W area (see Appendix B Fig. B.6a-d). This is similar to Fig. 3.5 in the main text.

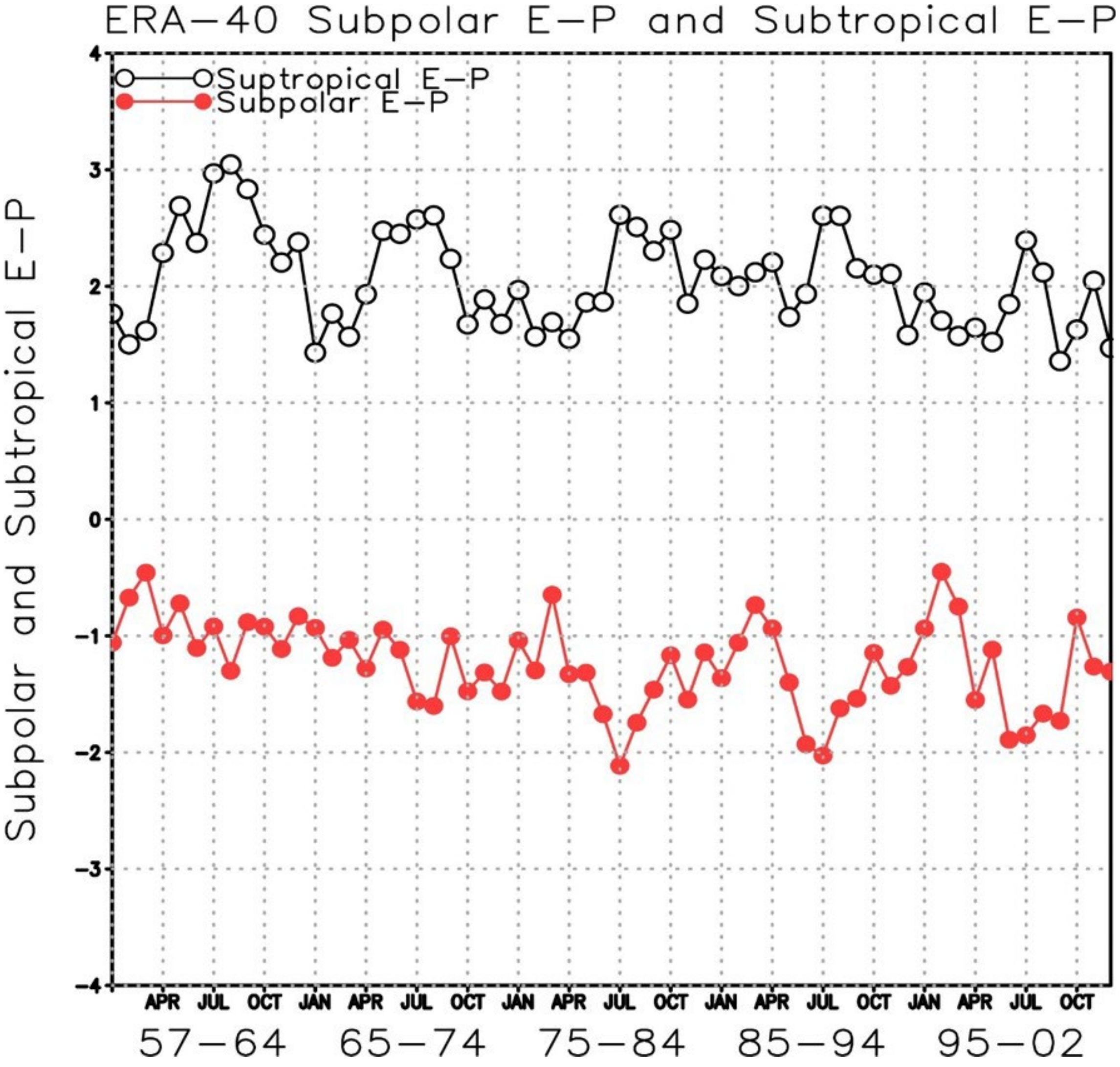

Figure B.9: Area-average E-P for five monthly decadal averages from 1957-2002 calculated from the ERA-40 reanalysis over the subpolar NA (red line, boundaries: 310-330°E and 50-60°N) and subtropical NA (black line, boundaries: 320-345°E and 27.5-40°N). Note the degraded seasonal E-P signal in the subpolar NA for the 1957-64 and 1965-1974 decades which is likely due to poor representation of precipitation in the ERA-40 reanalysis in the subpolar NA during this time. The seasonal signal improves once satellite data begins to be assimilated (~1979) into the ERA-40 reanalysis.

Appendix C: Supplemental Material for Chapter 4

C.1 Removal of Natural Climate Variability through Multiple Linear Regression

Our salinity and E-P pattern amplification analyses are focused on identifying secular changes, and therefore we attempted to remove the natural variability from salinity (or E-P) using a multiple linear regression (MLR) model. To build the model, we first detrended the climate indices using a simple linear regression (see Appendix C.2). We then normalized the nine monthly detrended climate indices: Southern Oscillation Index (SOI), Pacific Decadal Oscillation (PDO), North Atlantic Oscillation (NAO), Atlantic Multidecadal Oscillation (AMO), Southern Annular Mode (SAM), Dipole Mode Index (DMI), Pacific-North American Index (PNA), Indian Ocean Basin Mode (IOBM), and the North Pacific Gyre Oscillation (NPGO). We normalized each index as follows:

$$Xn_k = (X_k - \mathrm{mean}(X_k)) / \mathrm{stdev}(X_k)$$

where Xn_k is the normalized climate index and X_k is the non-normalized climate index.

Since SOI, PDO, DMI, and others are not completely independent of one another, we performed a principal component analysis (PCA) against the 9 detrended and normalized climate indices which yielded 9 orthogonal PCs. Following Evans et al. (2001), significant PCs were identified using AR(1) to simulate synthetic time series with the same autocorrelation as the input climate indices and Monte Carlo significant testing. This is a modern application of the Rule-N from Preisendorfer (1988).

To minimize the likelihood of overfitting, we fit multiple linear regression models using 1 through N PCs (where N is the number of significant PCs) in order to compare their performance. Then we used the Bayesian Information Criteria (BIC) to select the best model. The multiple linear regression model can be represented as:

$$y = X\alpha + \varepsilon$$

where y are the salinity (or E-P) values, X is the design matrix with dimensions of n x k (n is the number of time steps and k is the number of significant PCs), α is the regression coefficient vector, and ε is the residual error vector. By solving for α, we get the following:

$$\hat{\alpha} = (X^T X)^{-1} X^T y$$

Once the regression coefficient vector is computed, we can compute the total contribution from the selected PCs (derived from the nine climate indices) for each time period by using:

$$\hat{y}(t) = \alpha_0 + \Sigma\, \alpha_k X_k(t)$$

where $\hat{y}(t)$ is the predicted signal that is explained by the selected PCs at some point in time t, α_0 is the intercept, and α_k is the regression coefficient for the k^th^ principal component element $X_k(t)$ at time t. Finally, to calculate the residual signal (*y_residual(t)*) that is not explained by the selected PCs, we can take the original data (*y_original(t)*) and remove the predicted signal ($\hat{y}(t)$) that is explained by natural variability:

$$y\_residual(t) = y\_original(t) - \hat{y}(t)$$

For this study, we identified the first two PCs as significant at the 95% significance level. MLR models were built with the first PC and the first plus second PC, and BIC values were calculated. A grid point was included in the MLR salinity analysis if, for at least 75 percent of the time, there was at least one observation within its smallest radius of influence (this is the radius used in the objective analysis procedure that maps the salinity observations to the gridded fields). This limitation was set to ensure the time series at each grid point was long enough to capture natural variability. It was not necessary to apply this criterion to the gap-free E-P products. The white grid points in Figure C.9 did not meet this criterion in the pentadal salinity analysis and were therefore removed from further analysis in this study.

The model with the lowest BIC value was selected as the final model for our study and was used to remove the natural variability from each grid point. Based on the BIC results, the first PC yielded the lowest BIC, and thus the best model for our analysis (Figure C.10). The variance explained by the MLR model on the pentadal salinity time series shows that the first PC is predominately associated with natural variability in the tropics, and is likely dominated by the SOI, PDO, and DMI (Figure C.11). Similarly, the annual salinity and annual E-P (for all three products) also found that the first PC yielded the lowest BIC and was selected as the best model.

C.2 Ordinary Least Squares and Weighted Least Squares Regression

The trends in salinity and E-P were computed using both ordinary least squares and weighted least squares regression. The simple linear regression model is defined as:

$$y = \beta_0 + \beta_1 x + \varepsilon$$

where x is the time variable in fractional years, rescaled to start from zero, y is the observed salinity (or E-P) at each time step, β_0 is the estimated y-intercept (value at 0 time), and β_1 is the estimated linear trend (units/50yr) [all trends were scaled to 50 years]. The slope (β_1) is estimated by:

$$\beta_1 = \Sigma((x_i - \bar{x})(y_i - \bar{y})) / \Sigma((x_i - \bar{x})^2)$$

where x_i is time at the timestep i, $\bar{x}$ is the time mean, y_i is salinity (or E-P) at the timestep i, and $\bar{y}$ is the salinity mean. The standard error of the slope is defined by:

$$SE\_\beta_1 = \mathrm{sqrt}(\Sigma(y_i - \hat{y}_i)^2 / (dof \times \Sigma(x_i - \bar{x})^2))$$

Where $\hat{y}_i$ is the fitted value of the model at timestep i and dof is the degrees of freedom (N-2) where N is the number of time periods. The coefficient of determination (R^2), is estimated by:

$$R^2 = 1 - (\Sigma(y_i - \hat{y}_i)^2 / \Sigma(y_i - \bar{y})^2)$$

Where $\Sigma(y_i - \hat{y}_i)^2$ is the residual sum of squares and $\Sigma(y_i - \bar{y})^2$ is the total sum of squares. The t-statistic is calculated by:

$$t = \beta_1 / SE\_\beta_1$$

and the two-tailed probability value (p-value) which tests for whether or not the slope significantly differs from zero is given by:

$$p = 2 \times sf(|t|)$$

where *sf* is the survival function and provides the probability that a value from a t-distribution is greater than *t.* The 95% confidence interval is given by:

$$CI_{95}\% = \beta_1 \pm 1.96 \times SE\_\beta_1$$

For this study, we also compute the weighted least square regression to account for the uncertainty in the spatial-temporal fields. The weights are given by:

$$w_i = 1 / \sigma_i^2$$

where w_i is the weight given to the salinity (or E-P) value at a given time, and σ_i is the uncertainty of the value (when squared it is the variance). Thus, the more uncertainty a value has, the less it is weighted. The weighted slope then becomes:

$$\beta_1 w = \Sigma[w_i(x_i - \bar{x}\_w)(y_i - \bar{y}\_w)] / \Sigma[w_i(x_i - \bar{x}\_w)^2]$$

where $\bar{x}\_w$ is the weighted mean of time and $\bar{y}\_w$ is the weighted mean of the salinity (or E-P) data. The weighted standard error is then:

$$SE\_\beta_1 w = \mathrm{sqrt}(\Sigma[w_i(y_i - \hat{y}_i)^2] / (dof \times \Sigma[w_i(x_i - \bar{x}\_w)^2]))$$

Since some of the data we use are running pentadal means, it is important to calculate the effective sample size by taking into account the autocorrelation at each grid point in the data. This effective sample size, which we designate *n_eff*, can be determined by:

$$n\_eff = N(1 - r) / (1 + r)$$

where N is the number of time periods and r is the autocorrelation coefficient determined by:

$$r = [\sum(i=1 \text{ to } N-1)\ (y_i - \bar{y})(y_{i-1} - \bar{y})] / [\sum(i=1 \text{ to } N)\ (y_i - \bar{y})^2]$$

The *n_eff* is then used in the standard error calculation to determine the new degrees of freedom (dof = n_eff-2). The autocorrelation acts to decrease the number of independent data points and thus increases the standard error through decreasing the degrees of freedom.

Finally, we have made our best attempt to perform linear trend computations only on data with normally distributed residuals. However, despite our best efforts of removing natural variability from the data, there is a possibility that multi-decadal shifts resulting from natural variability could remain, albeit muted, in the data.

C.3 Modified Mann-Kendall Significance Test

While we calculate the 95% confidence intervals using the methods above, to test for whether or not salinity (or E-P) trends are significant we also employ a modified Mann-Kendall trend test (Hamed et al., 1998). The traditional Mann-Kendall (MK) test (Kendall, 1970; Mann, 1945) looks to see if there is a consistent trend upwards or downwards in the data without assuming the data follows some sort of distribution, and the modified Mann-Kendall (MMK) trend test accounts for autocorrelation within the data (Hamed et al., 1998). Thus, because salinity and E-P time series can be very noisy, we believe the MMK test is better suited to detect significant trends over time. The MK test (S) statistic is defined by:

$$S = \Sigma\, \Sigma\ \mathrm{sgn}(y_j - y_i), \text{ for all } j > i$$

where y_j is the salinity (or E-P) value at a later time j, y_i is the salinity (or E-P) value at the current time i. If $y_j - y_i > 0$, then $\mathrm{sgn}(y_j - y_i)$ equals +1, if $y_j - y_i = 0$, then $\mathrm{sgn}(y_j - y_i) = 0$, and finally, if $y_j - y_i < 0$, then $\mathrm{sgn}(y_j - y_i) = -1$. This is done for all pairs where $j > i$, the total sum is the S statistic. The variance of the S statistic (*Var(S)*) is calculated by (with autocorrelation, r):

$$\mathrm{Var}(S) = [n(n-1)(2n+5)/18] \times [1 + (2(n-1)(n-2)r)/(9n(n+1))]$$

Where n is the number of time steps and r is the autocorrelation calculated previously. The MK z-score is then calculated, in a piecewise function, by:

$$z = [\ (S-1)/\sqrt{\mathrm{Var}(S)},\ \text{if } S>0;\ 0 \text{ if } S=0;\ (S+1)/\sqrt{\mathrm{Var}(S)},\ \text{if } S<0\ ]$$

with the p-value determined by:

$$p = 2 \times (1 - \Phi(|z|))$$

where $\Phi(|z|)$) is the cumulative distribution function of the standard normal distribution**.** The p-value will determine whether or not the trend is significant or not (e.g., p=0.04 is significant at the 95% level).

C.4 Spatial Correlation – Impact on Uncertainty Propagation

The salinity anomaly fields are calculated using a modified Cressman approach (Barnes, 1964), and therefore nearby grid points are spatially correlated with each other through the radius of influence used in the objective analysis. We must take this spatial correlation into account when we compute the zonal means of the salinity trends and propagate their uncertainties. To do this, we first take the correlation length and convert it into degrees of longitude:

$$L = \mathrm{corr\_km} / (111.32 \times \cos(\mathrm{lat}))$$

where L is the correlation length scale in degrees longitude, *corr_km* is the largest radius of influence applied during the objective analysis procedure in km (880km), and *lat* is the latitude in degrees. Next, the covariance is estimated by:

$$\mathrm{Cov}_{ij} = \sigma_i \times \sigma_j \times \exp(-\mathrm{abs}(\Delta\lambda_{ij}) / L)$$

where Cov_{ij} is the covariance between grid cells I and j, σ_i and σ_j are the standard errors of the values at the i and j grid cells, and $\Delta\lambda_{ij}$ is the absolute value of the longitudinal distance in degrees between the i and j grids. Finally, the aggregated zonal standard error (*stderr_zonal*) across the latitudinal band is then calculated by:

$$\text{stderr\_zonal} = \sqrt{[(1 / n^2) \times \Sigma\Sigma \, \text{Cov}_{ij}]}$$

where *n* is the number of grid cells within the latitudinal band with data.

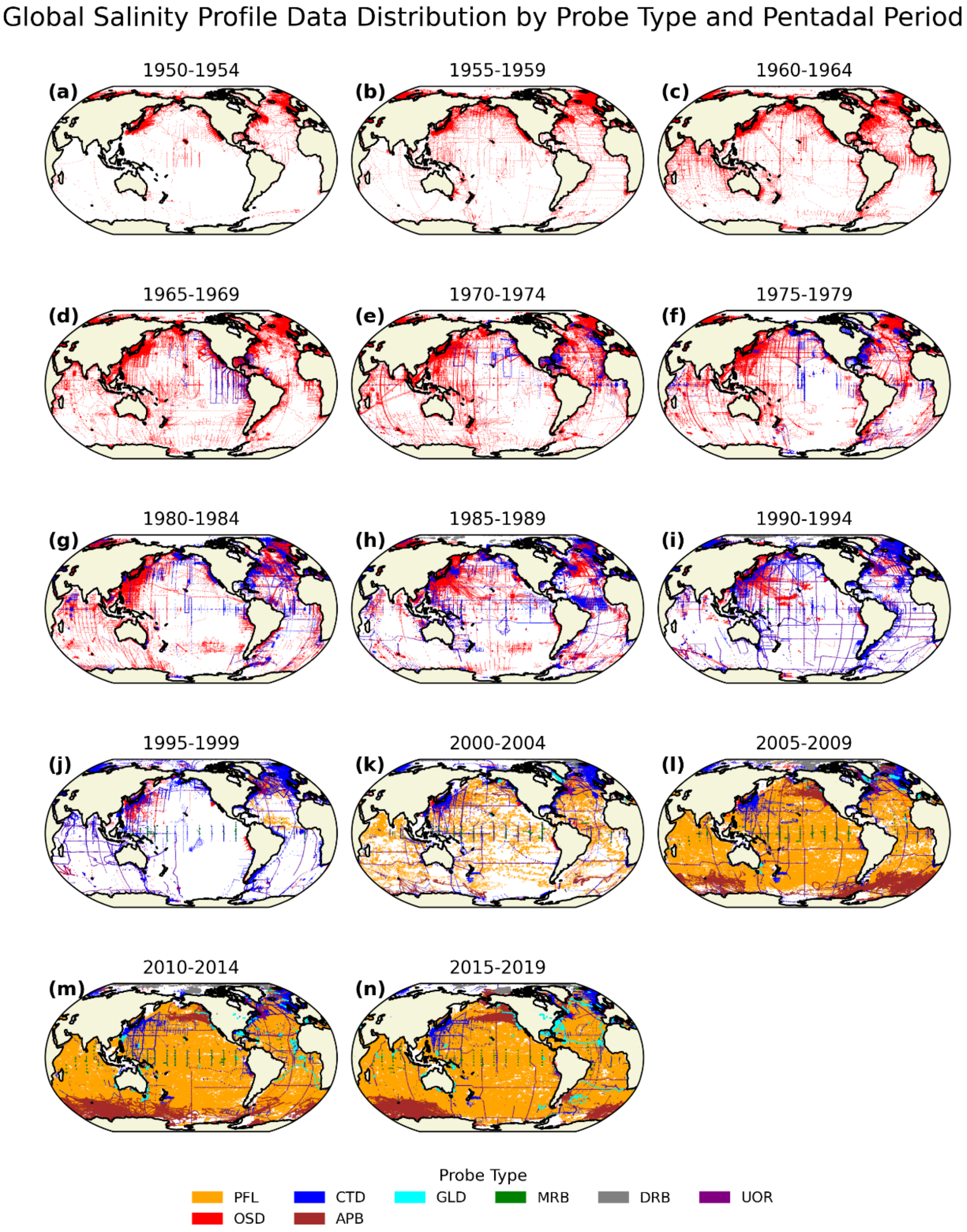

Figure C.1: Spatial distribution of salinity profiles for each pentad from 1950-54 through 2015-19 contained in the World Ocean Database and used to calculate the annual and pentadal salinity anomaly fields. OSD = bottle, CTD = Conductivity, Temperature, Depth, MRB = Moored Buoy, DRB = Drifting Buoy, UOR = Undulating Oceanographic Recorder, APB = Autonomous Pinniped Bathythermograph, GLD = gliders, and PFL = Profiling Floats.

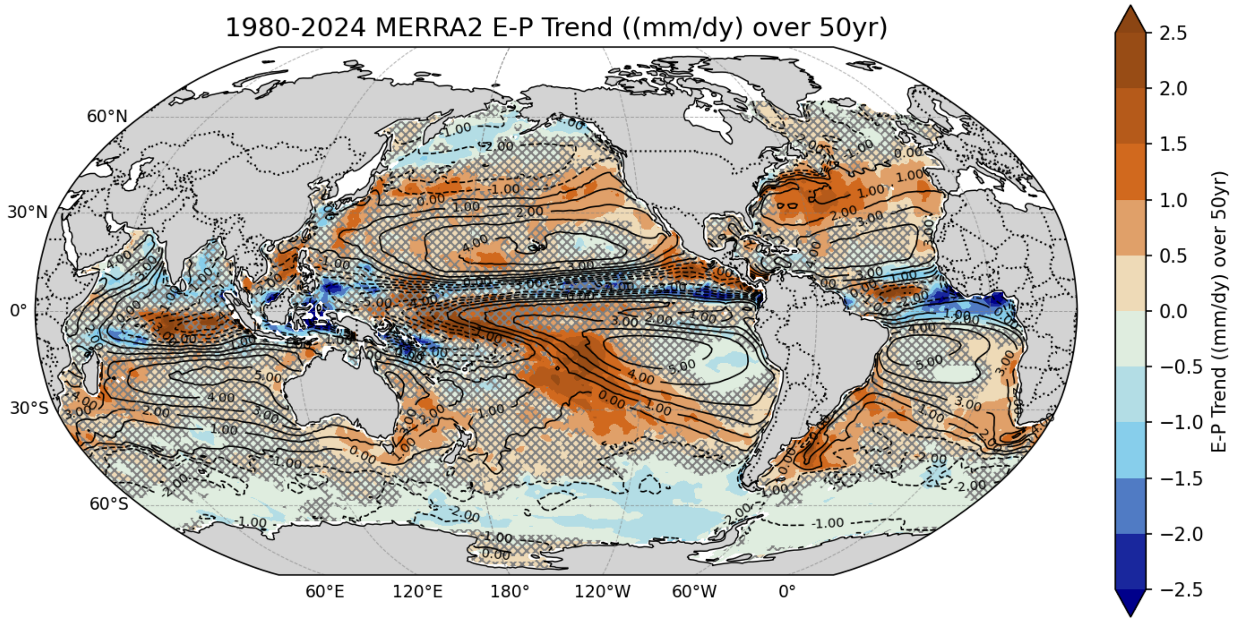

1980-2024 MERRA2 E-P Trend ((mm/dy) over 50yr)

Figure C.2: The 1980-2025 linear trend in MERRA-2 E-P standardized to a 50-year time period. The units are in mm/day over 50 years. Orange shadings represent regions of increasing E-P, blue regions represent regions of decreasing E-P. Hatchings represent regions where the trend was not significant at the 95% level using the modified Mann-Kendall test. Black contours represent the climatological E-P mean and white regions had insufficient data for a trend to be computed.

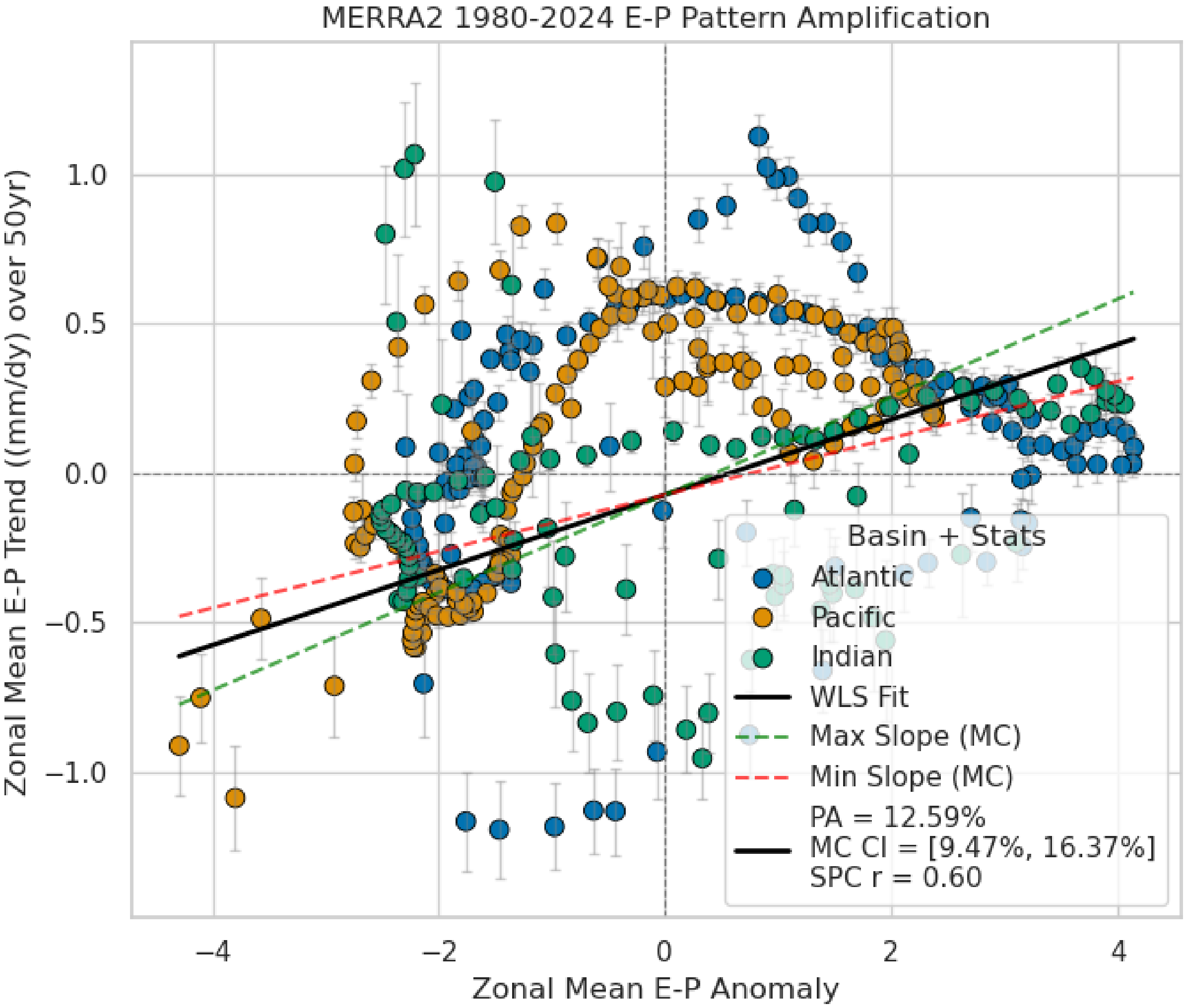

Figure C.3: The 1980-2024 MERRA-2 E-P pattern amplification and spatial pattern correlation, standardized to a 50-year time period. See section 4.2.2 for full description of pattern amplifications and spatial pattern correlations.

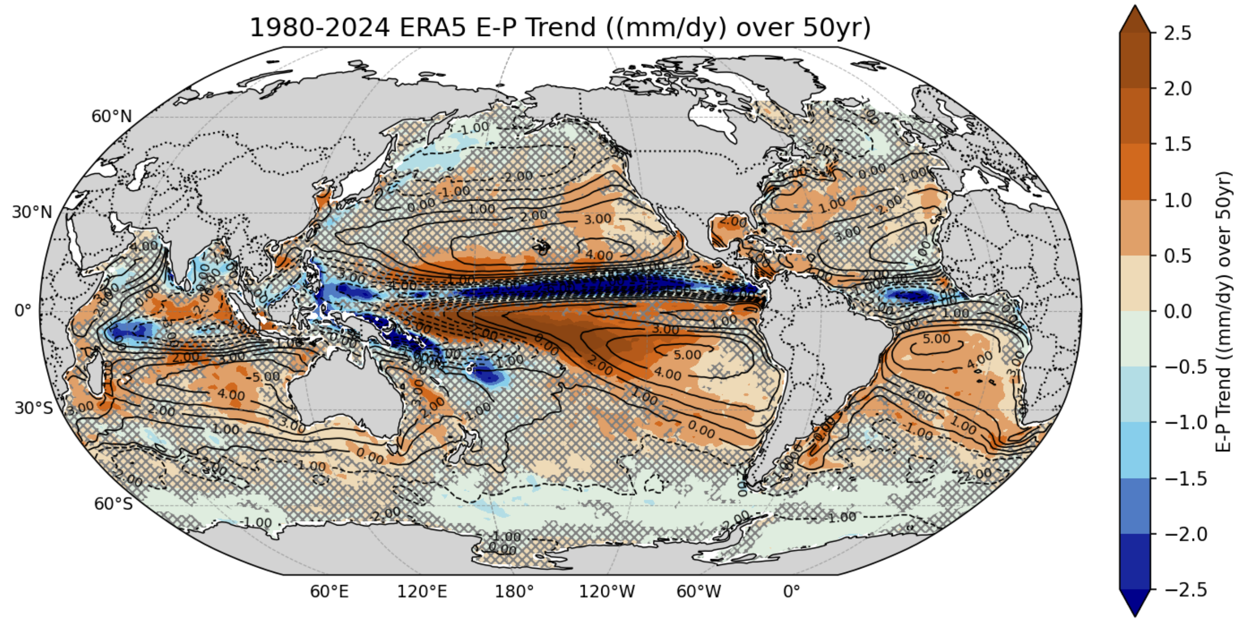

Figure C.4: The 1980-2024 linear trend in ERA5 E-P standardized to a 50-year time period. The units are in mm/day over 50 years. Orange shadings represent regions of increasing E-P, blue regions represent regions of decreasing E-P. Hatchings represent regions where the trend was not significant at the 95% level using the modified Mann-Kendall test. Black contours represent the climatological E-P mean and white regions had insufficient data for a trend to be computed.

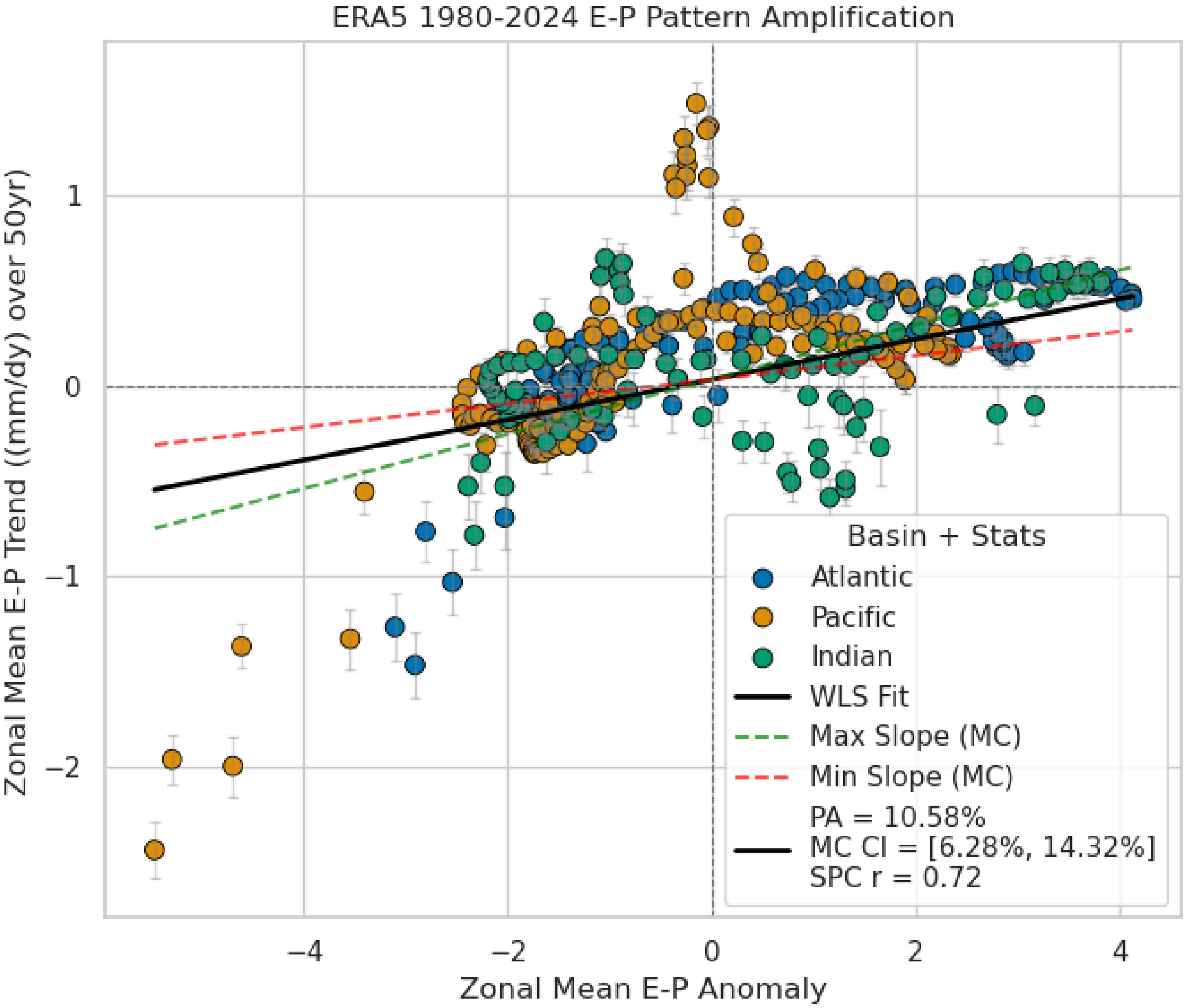

Figure C.5: The 1980-2024 ERA-5 E-P pattern amplification and spatial pattern correlation, standardized to a 50-year time period. See section 4.2.2 for full description of pattern amplifications and spatial pattern correlations.

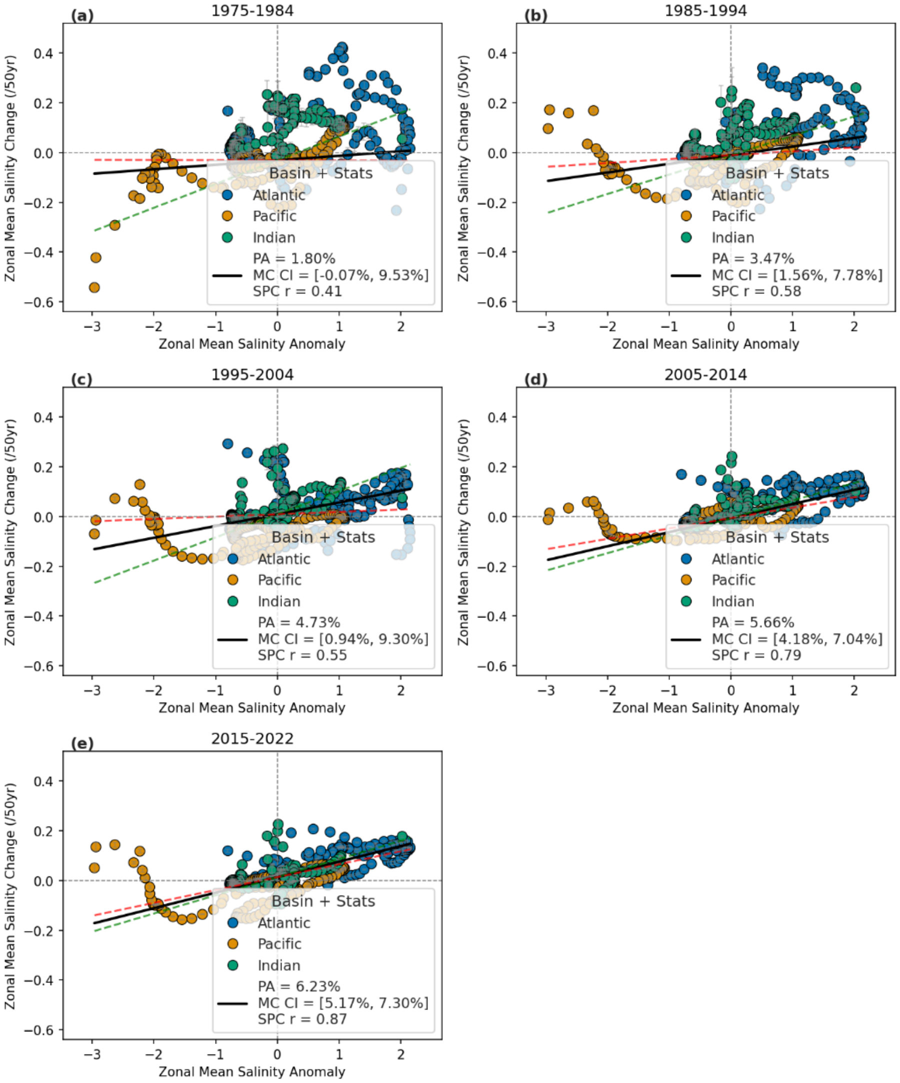

Figure C.6: Near-surface salinity pattern amplification and spatial pattern correlations for the differences between the 1965-1974 decadal climatology and a) 1975-1984, b) 1985-1994, c) 1995-2004, d) 2005-2014, and e) 2015-2022. The different colored dots represent the zonally-averaged differences between the climatology and the 1965-1974 climatology and the climatological near-surface salinity anomalies for each ocean basin (Atlantic = Blue, Pacific = Orange, Green = Indian) along each 1-degree latitudinal belts within that basin. The black line represents the weighted least squares regression, and the red and green lines represent the 95% confidence interval based on the minimum and maximum slopes from 500 Monte Carlo simulations. The climatologies are from the World Ocean Atlas 2023 (Reagan et al., 2024b).

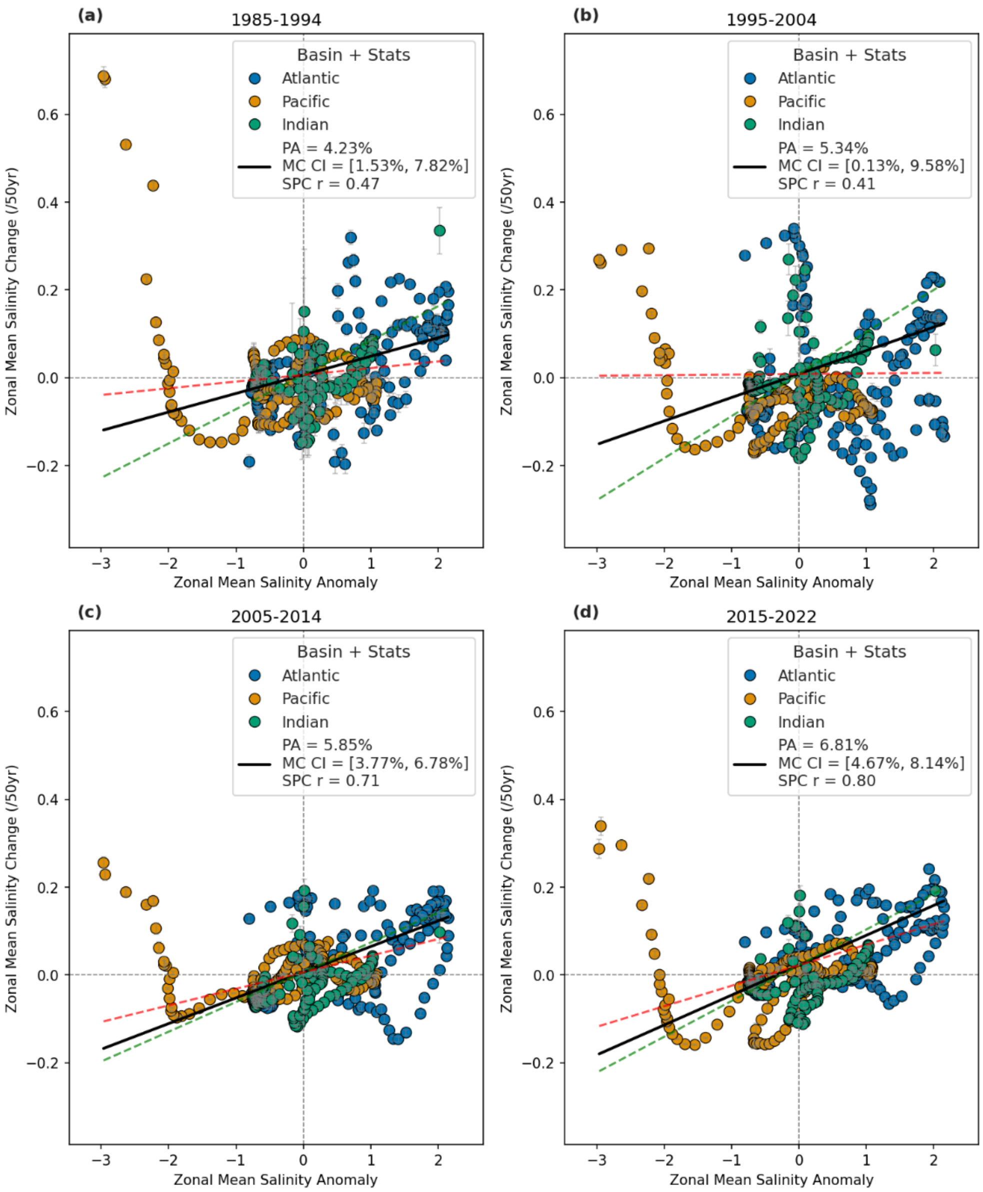

Figure C.7: Same as Fig C.6, but using 1975-1984 decadal climatology as baseline.

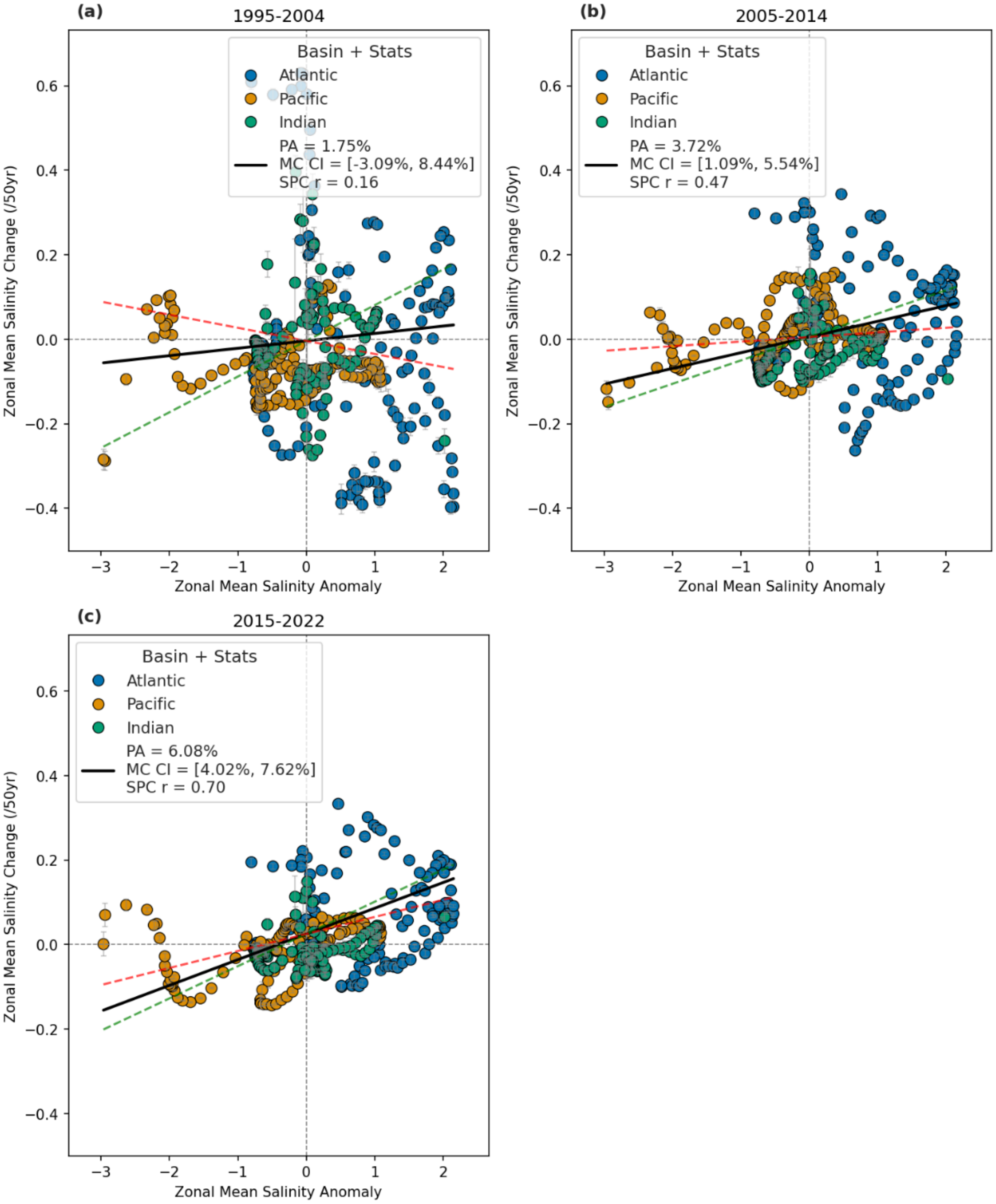

Figure C.8: Same as Fig C.6, but using 1985-1994 decadal climatology as baseline.

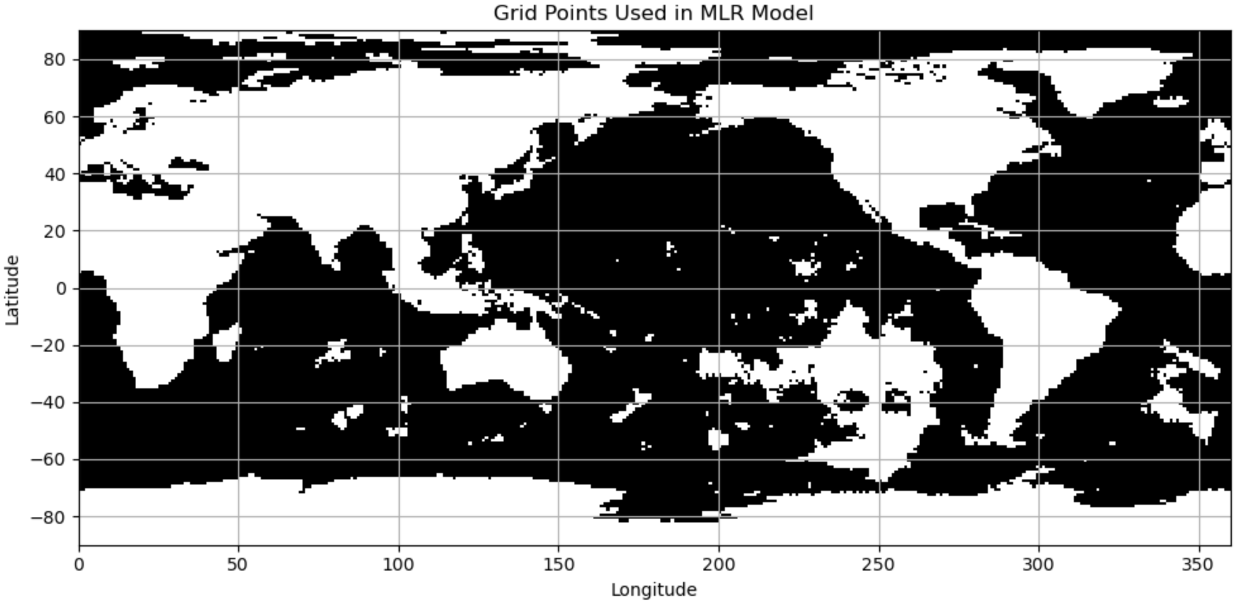

Figure C.9: The grid points included in the multiple linear regression model used to estimate the influence of natural variability over the 1957/1961-2019/2023 pentadal salinity time period (see Appendix C.4). Grid points that were included are shaded black; grid points that were not included are shaded white. For a grid point to be included in the MLR model for the pentadal salinity analysis, a minimum of 48/63 (>=75%) pentads would need to have at least one observation within the smallest radius of influence (446km) of the objective analysis used to construct the salinity anomaly fields.

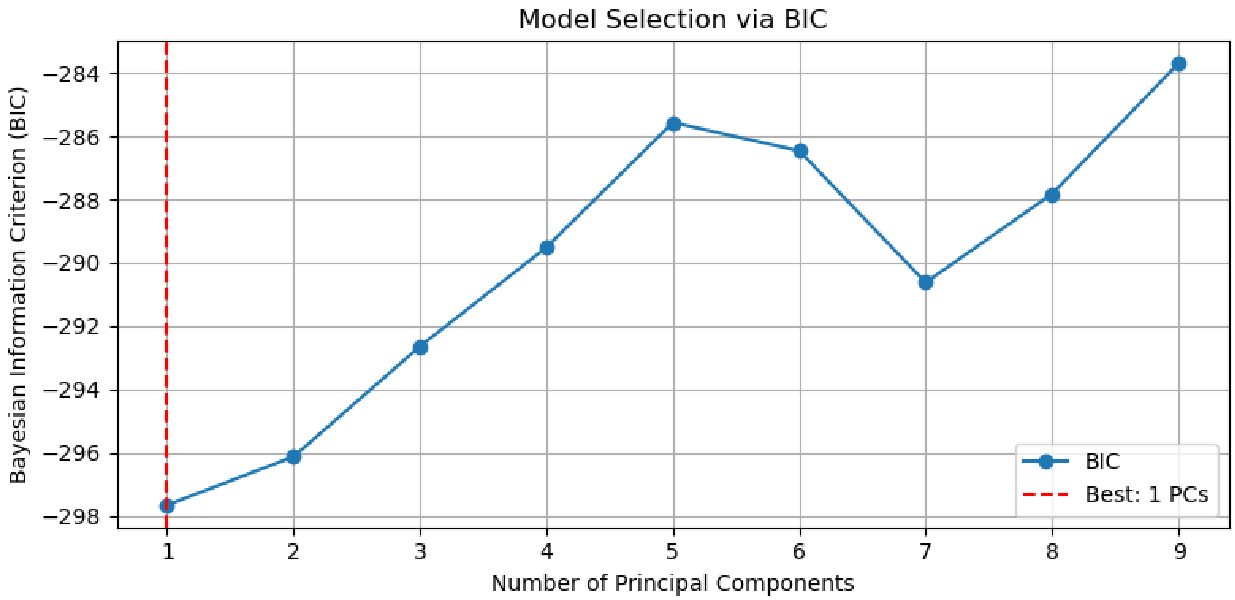

Figure C.10: The Bayesian Information Criterion (BIC) score for each MLR model developed with 1 to N principal components for the 63-year pentadal salinity analysis. While the first two PCs were significant at the 95% level, the first PC provided the lowest BIC score and is the model that was chosen.

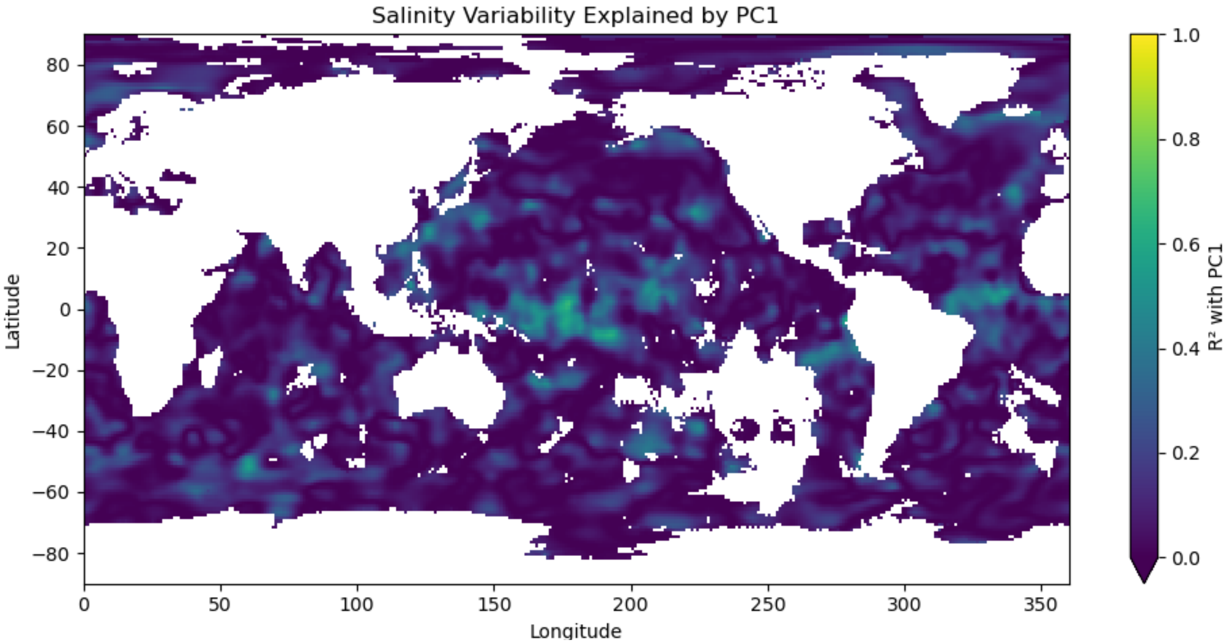

Figure C.11: The amount of variance explained by the MLR model developed using the first PC of the climate indices for the 1957/1961-2019/2023 pentadal salinity anomalies. The highest values are mostly situated in the tropics signifying the tropical indices (e.g., SOI, DMI, PDO etc.) play an important role in regulating salinity anomalies in this area and dominate the first principal component.

References:

Abe, H., & Ebuchi, N. (2014). Evaluation of sea-surface salinity observed by Aquarius. *Journal of Geophysical Research-Oceans*, *119*(11), 8109-8121. https://doi.org/10.1002/2014jc010094

Adler, R. F., Huffman, G. J., Chang, A., Ferraro, R., Xie, P. P., Janowiak, J., Rudolf, B., Schneider, U., Curtis, S., Bolvin, D., Gruber, A., Susskind, J., Arkin, P., & Nelkin, E. (2003). The version-2 global precipitation climatology project (GPCP) monthly precipitation analysis (1979-present). *Journal of Hydrometeorology*, *4*(6), 1147-1167. https://doi.org/10.1175/1525-7541(2003)004<1147:Tvgpcp>2.0.Co;2

Antonov, J. I., Seidov, D., Boyer, T. P., Locarnini, R. A., Mishonov, A. V., Garcia, H. E., Baranova, O. K., Zweng, M. M., & Johnson, D. R. (2010). "World Ocean Atlas 2009, Volume 2: Salinity." NOAA Atlas NESDIS 69: 1-184.

Balaguru, K., Foltz, G. R., Leung, L. R., Kaplan, J., Xu, W. W., Reul, N., & Chapron, B. (2020). Pronounced Impact of Salinity on Rapidly Intensifying Tropical Cyclones. *Bulletin of the American Meteorological Society*, *101*(9), E1497-E1511. https://doi.org/10.1175/Bams-D-19-0303.1

Barnes, S. L. (1964). A Technique for Maximizing Details in Numerical Weather Map Analysis. *Journal of Applied Meteorology and Climatology*, *3*(4), 396-409. https://doi.org/10.1175/1520-0450(1964)003<0396:ATFMDI>2.0.CO;2

Bengtsson, L., Hodges, K. I., & Roeckner, E. (2006). Storm tracks and climate change. *Journal of Climate*, *19*(15), 3518-3543. https://doi.org/10.1175/Jcli3815.1

Bosilovich, M. G., Robertson, F. R., Takacs, L., Molod, A., & Mocko, D. (2017). Atmospheric Water Balance and Variability in the MERRA-2 Reanalysis. *Journal of Climate*, *30*(4), 1177-1196. https://doi.org/10.1175/Jcli-D-16-0338.1

Boutin, J., Martin, N., Reverdin, G., Yin, X., & Gaillard, F. (2013). Sea surface freshening inferred from SMOS and ARGO salinity: impact of rain. *Ocean Science*, *9*(1), 183-192. https://doi.org/10.5194/os-9-183-2013

Boutin, J., Martin, N., Yin, X. B., Font, J., Reul, N., & Spurgeon, P. (2012). First Assessment of SMOS Data Over Open Ocean: Part II-Sea Surface Salinity. *Ieee Transactions on Geoscience and Remote Sensing*, *50*(5), 1662-1675. https://doi.org/10.1109/Tgrs.2012.2184546

Boutin, J., Reul, N., Koehler, J., Martin, A., Catany, R., Guimbard, S., Rouffi, F., Vergely, J. L., Arias, M., Chakroun, M., Corato, G., Estella-Perez, V., Hasson, A., Josey, S., Khvorostyanov, D., Kolodziejczyk, N., Mignot, J., Olivier, L., Reverdin, G.,…Mecklenburg, S. (2021a). Satellite-Based Sea Surface Salinity Designed for Ocean and Climate Studies. *Journal of Geophysical Research: Oceans*, *126*(11), e2021JC017676. https://doi.org/10.1029/2021JC017676

Boutin, J., Vergely, J. L., Dinnat, E. P., Waldteufel, P., D'Amico, F., Reul, N., Supply, A., & Thouvenin-Masson, C. (2021b). Correcting Sea Surface Temperature Spurious Effects in Salinity Retrieved From Spaceborne L-Band Radiometer Measurements. *Ieee Transactions on Geoscience and Remote Sensing*, *59*(9), 7256-7269. https://doi.org/10.1109/TGRS.2020.3030488

Boyer, T. P., Antonov, J. I., Baranova, O. K., Coleman, C., Garcia, H. E., Grodsky, A., Johnson, D. R., Locarnini, R. A., Mishonov, A. V., O'Brien, T. D., Paver, C. R., Reagan, J. R., Seidov, D., Smolyar, I. V., & Zweng, M. M. (2013). "World Ocean Database, Volume 1: Introduction." NOAA Atlas NESDIS 72: 1-209.

Boyer, T. P., & Levitus, S. (2002). Harmonic analysis of climatological sea surface salinity. *Journal of Geophysical Research-Oceans*, *107*(C12). https://doi.org/10.1029/2001jc000829

Boyer, T. P., Levitus, S., Antonov, J. I., Locarnini, R. A., & Garcia, H. E. (2005). Linear trends in salinity for the World Ocean, 1955-1998. *Geophysical Research Letters*, *32*(1). https://doi.org/10.1029/2004gl021791

Broecker, W. S. (1991). The Great Ocean Conveyor. *Oceanography*, *4*, 79-89.

Buckley, M. W., & Marshall, J. (2016). Observations, inferences, and mechanisms of the Atlantic Meridional Overturning Circulation: A review. *Reviews of Geophysics*, *54*(1), 5-63. https://doi.org/10.1002/2015rg000493

Byrne, M. P., & O'Gorman, P. A. (2015). The Response of Precipitation Minus Evapotranspiration to Climate Warming: Why the "Wet-Get-Wetter, Dry-Get-Drier" Scaling Does Not Hold over Land. *Journal of Climate*, *28*(20), 8078-8092. https://doi.org/10.1175/Jcli-D-15-0369.1

Chang, E. K. M., Lee, S. Y., & Swanson, K. L. (2002). Storm track dynamics. *Journal of Climate*, *15*(16), 2163-2183. https://doi.org/10.1175/1520-0442(2002)015<02163:Std>2.0.Co;2

Cheng, L. J., Trenberth, K. E., Gruber, N., Abraham, J. P., Fasullo, J. T., Li, G. C., Mann, M. E., Zhao, X. M., & Zhu, J. (2020). Improved Estimates of Changes in Upper Ocean Salinity and the Hydrological Cycle. *Journal of Climate*, *33*(23), 10357-10381. https://doi.org/10.1175/Jcli-D-20-0366.1

Chou, C., & Neelin, J. D. (2004). Mechanisms of global warming impacts on regional tropical precipitation. *Journal of Climate*, *17*(13), 2688-2701. https://doi.org/10.1175/1520-0442(2004)017<2688:Mogwio>2.0.Co;2

Chou, C., Neelin, J. D., Chen, C. A., & Tu, J. Y. (2009). Evaluating the "Rich-Get-Richer" Mechanism in Tropical Precipitation Change under Global Warming. *Journal of Climate*, *22*(8), 1982-2005. https://doi.org/10.1175/2008jcli2471.1

de Boyer Montégut, C., Madec, G., Fischer, A. S., Lazar, A., & Iudicone, D. (2004). Mixed layer depth over the global ocean:: An examination of profile data and a profile-based climatology -: art. no. C12003. *Journal of Geophysical Research-Oceans*, *109*(C12). https://doi.org/10.1029/2004jc002378

Dee, D. P., Uppala, S. M., Simmons, A. J., Berrisford, P., Poli, P., Kobayashi, S., Andrae, U., Balmaseda, M. A., Balsamo, G., Bauer, P., Bechtold, P., Beljaars, A. C. M., van de Berg, L., Bidlot, J., Bormann, N., Delsol, C., Dragani, R., Fuentes, M., Geer, A. J.,…Vitart, F. (2011). The ERA-Interim reanalysis: configuration and performance of the data assimilation system. *Quarterly Journal of the Royal Meteorological Society*, *137*(656), 553-597. https://doi.org/10.1002/qj.828

Delcroix, T. (1998). Observed surface oceanic and atmospheric variability in the tropical Pacific at seasonal and ENSO timescales: A tentative overview. *Journal of Geophysical Research-Oceans*, *103*(C9), 18611-18633. https://doi.org/10.1029/98jc00814

Dixon, K. W., Delworth, T. L., Spelman, M. J., & Stouffer, R. J. (1999). The influence of transient surface fluxes on North Atlantic overturning in a coupled GCM climate change experiment. *Geophysical Research Letters*, *26*(17), 2749-2752. https://doi.org/10.1029/1999gl900571

Douville, H., & Cheng, L. (2024). Asymmetric Sea Surface Salinity Response to Global Warming: "Fresh Gets Fresher but Salty Hesitates". *Geophysical Research Letters*, *51*(15). https://doi.org/10.1029/2023GL107944

Drucker, R., & Riser, S. C. (2014). Validation of Aquarius sea surface salinity with Argo: Analysis of error due to depth of measurement and vertical salinity stratification. *Journal of Geophysical Research-Oceans*, *119*(7), 4626-4637. https://doi.org/10.1002/2014jc010045

Durack, P. J. (2015). Ocean Salinity and the Global Water Cycle. *Oceanography*, *28*(1), 20-31. https://doi.org/10.5670/oceanog.2015.03

Durack, P. J., & Wijffels, S. E. (2010). Fifty-Year Trends in Global Ocean Salinities and Their Relationship to Broad-Scale Warming. *Journal of Climate*, *23*(16), 4342-4362. https://doi.org/10.1175/2010jcli3377.1

Durack, P. J., Wijffels, S. E., & Matear, R. J. (2012). Ocean Salinities Reveal Strong Global Water Cycle Intensification During 1950 to 2000. *Science*, *336*(6080), 455-458. https://doi.org/10.1126/science.1212222

Eiras-Barca, J., Brands, S., & Miguez-Macho, G. (2016). Seasonal variations in North Atlantic atmospheric river activity and associations with anomalous precipitation over the Iberian Atlantic Margin. *Journal of Geophysical Research-Atmospheres*, *121*(2), 931-948. https://doi.org/10.1002/2015jd023379

Evans, M. N., Kaplan, A., Cane, M. A., & Villalba, R. (2001). Chapter 4 - Globality and Optimality in Climate Field Reconstructions from Proxy Data. In V. Markgraf (Ed.), *Interhemispheric Climate Linkages* (pp. 53-72). Academic Press. https://doi.org/10.1016/B978-012472670-3/50007-0

Ferreira, D., Cessi, P., Coxall, H. K., de Boer, A., Dijkstra, H. A., Drijfhout, S. S., Eldevik, T., Harnik, N., McManus, J. F., Marshall, D. P., Nilsson, J., Roquet, F., Schneider, T., & Wills, R. C. (2018). Atlantic-Pacific Asymmetry in Deep Water Formation. *Annual Review of Earth and Planetary Sciences, Vol 46*, *46*, 327-352. https://doi.org/10.1146/annurev-earth-082517-010045

Fichefet, T., Poncin, C., Goosse, H., Huybrechts, P., Janssens, I., & Le Treut, H. (2003). Implications of changes in freshwater flux from the Greenland ice sheet for the climate of the 21st century. *Geophysical Research Letters*, *30*(17). https://doi.org/10.1029/2003gl017826

Ficklin, D. L., Null, S. E., Abatzoglou, J. T., Novick, K. A., & Myers, D. T. (2022). Hydrological Intensification Will Increase the Complexity of Water Resource Management. *Earths Future*, *10*(3). https://doi.org/10.1029/2021EF002487

Fore, A. G., Yueh, S. H., Tang, W. Q., Stiles, B. W., & Hayashi, A. K. (2016). Combined Active/Passive Retrievals of Ocean Vector Wind and Sea Surface Salinity With SMAP. *Ieee Transactions on Geoscience and Remote Sensing*, *54*(12), 7396-7404. https://doi.org/10.1109/Tgrs.2016.2601486

Gelaro, R., McCarty, W., Suárez, M. J., Todling, R., Molod, A., Takacs, L., Randles, C. A., Darmenov, A., Bosilovich, M. G., Reichle, R., Wargan, K., Coy, L., Cullather, R., Draper, C., Akella, S., Buchard, V., Conaty, A., da Silva, A. M., Gu, W.,…Zhao, B. (2017). The Modern-Era Retrospective Analysis for Research and Applications, Version 2 (MERRA-2). *Journal of Climate*, *30*(14), 5419-5454. https://doi.org/10.1175/Jcli-D-16-0758.1

Giorgi, F., & Bi, X. Q. (2009). Time of emergence (TOE) of GHG-forced precipitation change hot-spots. *Geophysical Research Letters*, *36*. https://doi.org/10.1029/2009gl037593

Gordon, A. L. (1986). Inter-Ocean Exchange of Thermocline Water. *Journal of Geophysical Research-Oceans*, *91*(C4), 5037-5046. https://doi.org/10.1029/JC091iC04p05037

Gould, W. J., & Cunningham, S. A. (2021). Global-scale patterns of observed sea surface salinity intensified since the 1870s. *Communications Earth & Environment*, *2*(1). https://doi.org/10.1038/s43247-021-00161-3

Gregory, J. M., Dixon, K. W., Stouffer, R. J., Weaver, A. J., Driesschaert, E., Eby, M., Fichefet, T., Hasumi, H., Hu, A., Jungclaus, J. H., Kamenkovich, I. V., Levermann, A., Montoya, M., Murakami, S., Nawrath, S., Oka, A., Sokolov, A. P., & Thorpe, R. B. (2005). A model intercomparison of changes in the Atlantic thermohaline circulation in response to increasing atmospheric CO concentration. *Geophysical Research Letters*, *32*(12). https://doi.org/10.1029/2005gl023209

Gutenstein, M., Fennig, K., Schröder, M., Trent, T., Bakan, S., Roberts, J. B., & Robertson, F. R. (2021). Intercomparison of freshwater fluxes over ocean and investigations into water budget closure. *Hydrology and Earth System Sciences*, *25*(1), 121-146. https://doi.org/10.5194/hess-25-121-2021

Hamed, K. H., & Rao, A. R. (1998). A modified Mann-Kendall trend test for autocorrelated data. *Journal of Hydrology*, *204*(1-4), 182-196. https://doi.org/10.1016/S0022-1694(97)00125-X

Haskins, R. K., Oliver, K. I. C., Jackson, L. C., Wood, R. A., & Drijfhout, S. S. (2020). Temperature domination of AMOC weakening due to freshwater hosing in two GCMs. *Climate Dynamics*, *54*(1-2), 273-286. https://doi.org/10.1007/s00382-019-04998-5

Hawkins, E., & Sutton, R. (2012). Time of emergence of climate signals. *Geophysical Research Letters*, *39*. https://doi.org/10.1029/2011gl050087

Hay, W. W., Migdisov, A., Balukhovsky, A. N., Wold, C. N., Flögel, S., & Söding, E. (2006). Evaporites and the salinity of the ocean during the Phanerozoic:: Implications for climate, ocean circulation and life. *Palaeogeography Palaeoclimatology Palaeoecology*, *240*(1-2), 3-46. https://doi.org/10.1016/j.palaeo.2006.03.044

Hegerl, G. C., Black, E., Allan, R. P., Ingram, W. J., Polson, D., Trenberth, K. E., Chadwick, R. S., Arkin, P. A., Sarojini, B. B., Becker, A., Dai, A. G., Durack, P. J., Easterling, D., Fowler, H. J., Kendon, E. J., Huffman, G. J., Liu, C. L., Marsh, R., New, M.,…Zhang, X. B. (2015). Challenges in Quantifying Changes in the Global Water Cycle. *Bulletin of the American Meteorological Society*, *96*(7), 1097-1115. https://doi.org/10.1175/Bams-D-13-00212.1

Held, I. M., & Soden, B. J. (2006). Robust responses of the hydrological cycle to global warming. *Journal of Climate*, *19*(21), 5686-5699. https://doi.org/10.1175/Jcli3990.1

Henocq, C., Boutin, J., Petitcolin, F., Reverdin, G., Arnault, S., & Lattes, P. (2010). Vertical Variability of Near-Surface Salinity in the Tropics: Consequences for L-Band Radiometer Calibration and Validation. *Journal of Atmospheric and Oceanic Technology*, *27*(1), 192-209. https://doi.org/10.1175/2009jtecho670.1

Hersbach, H., Bell, B., Berrisford, P., Hirahara, S., Horányi, A., Muñoz-Sabater, J., Nicolas, J., Peubey, C., Radu, R., Schepers, D., Simmons, A., Soci, C., Abdalla, S., Abellan, X., Balsamo, G., Bechtold, P., Biavati, G., Bidlot, J., Bonavita, M.,…Thépaut, J. N. (2020). The ERA5 global reanalysis. *Quarterly Journal of the Royal Meteorological Society*, *146*(730), 1999-2049. https://doi.org/10.1002/qj.3803

Hirabayashi, Y., Kanae, S., Emori, S., Oki, T., & Kimoto, M. (2008). Global projections of changing risks of floods and droughts in a changing climate. *Hydrological Sciences Journal-Journal Des Sciences Hydrologiques*, *53*(4), 754-772. https://doi.org/10.1623/hysj.53.4.754

Hoskins, B. J., & Hodges, K. I. (2002). New perspectives on the Northern Hemisphere winter storm tracks. *Journal of the Atmospheric Sciences*, *59*(6), 1041-1061. https://doi.org/10.1175/1520-0469(2002)059<1041:Npotnh>2.0.Co;2

Hosoda, S., Suga, T., Shikama, N., & Mizuno, K. (2009). Global Surface Layer Salinity Change Detected by Argo and Its Implication for Hydrological Cycle Intensification. *Journal of Oceanography*, *65*(4), 579-586. https://doi.org/10.1007/s10872-009-0049-1

Huffman, G. J., Adler, R. F., Bolvin, D. T., & Gu, G. J. (2009). Improving the global precipitation record: GPCP Version 2.1. *Geophysical Research Letters*, *36*. https://doi.org/10.1029/2009gl040000

IOC, SCOR, & IAPSO (2010). "The international thermodynamic equation of seawater – 2010: Calculation and use of thermodynamic properties." Intergovernmental Oceanographic Commission, Manuals and Guides 56: 196pp.

Johns, W. E., Baringer, M. O., Beal, L. M., Cunningham, S. A., Kanzow, T., Bryden, H. L., Hirschi, J. J. M., Marotzke, J., Meinen, C. S., Shaw, B., & Curry, R. (2011). Continuous, Array-Based Estimates of Atlantic Ocean Heat Transport at 26.5°N. *Journal of Climate*, *24*(10), 2429-2449. https://doi.org/10.1175/2010jcli3997.1

Johnson, D. R., Boyer, T. P., Garcia, H. E., Locarnini, R. A., Baranova, O. K., & Zweng, M. M. (2013). "World Ocean Datbase 2013, Volume 2: User's Manual." NODC Internal Report 22: 1-172.

Johnson, G. C., Lyman, J. M., Lagerloef, G. S. E., & Kao, H.-Y. (2013). [Global Oceans] Sea Surface Salinity [in *State of the Climate in 2012*]. *Bulletin of the American Meteorological Society*, *94*(8), S57-S60. https://doi.org/10.1175/2013BAMSStateoftheClimate.1

Kalnay, E., Kanamitsu, M., Kistler, R., Collins, W., Deaven, D., Gandin, L., Iredell, M., Saha, S., White, G., Woollen, J., Zhu, Y., Chelliah, M., Ebisuzaki, W., Higgins, W., Janowiak, J., Mo, K. C., Ropelewski, C., Wang, J., Leetmaa, A.,…Joseph, D. (1996). The NCEP/NCAR 40-year reanalysis project. *Bulletin of the American Meteorological Society*, *77*(3), 437-471. https://doi.org/10.1175/1520-0477(1996)077<0437:Tnyrp>2.0.Co;2

Kendall, M. G. (1970). *Rank correlation methods* (4th ed.). Griffin.

Kerr, Y. H., Waldteufel, P., Wigneron, J. P., Delwart, S., Cabot, F., Boutin, J., Escorihuela, M. J., Font, J., Reul, N., Gruhier, C., Juglea, S. E., Drinkwater, M. R., Hahne, A., Martín-Neira, M., & Mecklenburg, S. (2010). The SMOS Mission: New Tool for Monitoring Key Elements of the Global Water Cycle. *Proceedings of the Ieee*, *98*(5), 666-687. https://doi.org/10.1109/Jproc.2010.2043032

Knauss, J. A. (1997). *Introduction to physical oceanography* (2nd ed.). Prentice Hall.

Lagerloef, G. (2013). *Aquarius salinity validation analysis: Data version 2.0*. Aquarius Proj. Doc. AQ-014-PS-0016.

Lagerloef, G., Colomb, F. R., Le Vine, D., Wentz, F., Yueh, S., Ruf, C., Lilly, J., Gunn, J., Chao, Y., deCharon, A., Feldman, G., & Swift, C. (2008). The Aquarius/Sac-D Mission: Designed to Meet the Salinity Remote-Sensing Challenge. *Oceanography*, *21*(1), 68-81. https://doi.org/10.5670/oceanog.2008.68

Lagerloef, G., Schmitt, R., Schanze, J., & Kao, H. Y. (2010). The Ocean and the Global Water Cycle. *Oceanography*, *23*(4), 82-93. https://doi.org/10.5670/oceanog.2010.07

Lagerloef, G. S. E., Swift, C. T., & Le Vine, D. M. (1995). Sea Surface Salinity: The Next Remote Sensing Challenge. *Oceanography*, *8*. https://doi.org/10.5670/oceanog.1995.17

Large, W. G., & Yeager, S. G. (2009). The global climatology of an interannually varying air-sea flux data set. *Climate Dynamics*, *33*(2-3), 341-364. https://doi.org/10.1007/s00382-008-0441-3

Lee, T. (2016). Consistency of Aquarius sea surface salinity with Argo products on various spatial and temporal scales. *Geophysical Research Letters*, *43*(8), 3857-3864. https://doi.org/10.1002/2016gl068822

Lee, T., Lagerloef, G., Gierach, M. M., Kao, H. Y., Yueh, S., & Dohan, K. (2012). Aquarius reveals salinity structure of tropical instability waves. *Geophysical Research Letters*, *39*. https://doi.org/10.1029/2012gl052232

Levitus, S., Antonov, J. I., Boyer, T. P., Baranova, O. K., Garcia, H. E., Locarnini, R. A., Mishonov, A. V., Reagan, J. R., Seidov, D., Yarosh, E. S., & Zweng, M. M. (2012). World ocean heat content and thermosteric sea level change (0-2000 m), 1955-2010. *Geophysical Research Letters*, *39*. https://doi.org/10.1029/2012gl051106

Lewis, E. L. (1982). The Practical Salinity Scale of 1978 and Its Antecedents. *Marine Geodesy*, *5*(4), 351-357.

Lewis, E. L., & Perkin, R. G. (1981). The Practical Salinity Scale 1978 - Conversion of Existing Data. *Deep-Sea Research Part a-Oceanographic Research Papers*, *28*(4), 307-328. https://doi.org/10.1016/0198-0149(81)90002-9

Li, L. F., Schmitt, R. W., & Ummenhofer, C. C. (2022). Skillful Long-Lead Prediction of Summertime Heavy Rainfall in the US Midwest From Sea Surface Salinity. *Geophysical Research Letters*, *49*(13). https://doi.org/10.1029/2022GL098554

Li, L. F., Schmitt, R. W., Ummenhofer, C. C., & Karnauskas, K. B. (2016a). Implications of North Atlantic Sea Surface Salinity for Summer Precipitation over the US Midwest: Mechanisms and Predictive Value. *Journal of Climate*, *29*(9), 3143-3159. https://doi.org/10.1175/Jcli-D-15-0520.1

Li, L. F., Schmitt, R. W., Ummenhofer, C. C., & Karnauskas, K. B. (2016b). North Atlantic salinity as a predictor of Sahel rainfall. *Science Advances*, *2*(5). https://doi.org/10.1126/sciadv.1501588

Liu, T., Schmitt, R. W., & Li, L. (2018). Global Search for Autumn-Lead Sea Surface Salinity Predictors of Winter Precipitation in Southwestern United States. *Geophysical Research Letters*, *45*(16), 8445-8454. https://doi.org/10.1029/2018gl079293

Mann, H. B. (1945). Nonparametric tests against trend. *Econometrica*, *13*(3), 245-259. https://doi.org/10.2307/1907187

Mantua, N. J., Hare, S. R., Zhang, Y., Wallace, J. M., & Francis, R. C. (1997). A Pacific interdecadal climate oscillation with impacts on salmon production. *Bulletin of the American Meteorological Society*, *78*(6), 1069-1079. https://doi.org/10.1175/1520-0477(1997)078<1069:Apicow>2.0.Co;2

Marsh, R., Hazeleger, W., Yool, A., & Rohling, E. J. (2007). Stability of the thermohaline circulation under millennial CO forcing and two alternative controls on Atlantic salinity. *Geophysical Research Letters*, *34*(3). https://doi.org/10.1029/2006gl027815

Meissner, T., Wentz, F. J., & Le Vine, D. M. (2018). The Salinity Retrieval Algorithms for the NASA Aquarius Version 5 and SMAP Version 3 Releases. *Remote Sensing*, *10*(7).

Millero, F. J., Feistel, R., Wright, D. G., & McDougall, T. J. (2008). The composition of Standard Seawater and the definition of the Reference-Composition Salinity Scale. *Deep-Sea Research Part I-Oceanographic Research Papers*, *55*(1), 50-72. https://doi.org/10.1016/j.dsr.2007.10.001

Mishonov, A., Seidov, D., & Reagan, J. (2024). Revisiting the multidecadal variability of North Atlantic Ocean circulation and climate. *Frontiers in Marine Science*, *11*. https://doi.org/10.3389/fmars.2024.1345426

Mishonov, A. V., Boyer, T. P., Baranova, O. K., Bouchard, C. N., Cross, S. L., Garcia, H. E., Locarnini, R. A., Paver, C. R., Reagan, J. R., Wang, Z., Seidov, D., Grodsky, A. I., & Beauchamp, J. G. (2024). "World Ocean Database 2023." NOAA atlas NESDIS 97. https://doi.org/10.25923/z885-h264

O'Gorman, P. A., Allan, R. P., Byrne, M. P., & Previdi, M. (2012). Energetic Constraints on Precipitation Under Climate Change. *Surveys in Geophysics*, *33*(3-4), 585-608. https://doi.org/10.1007/s10712-011-9159-6

Polade, S. D., Pierce, D. W., Cayan, D. R., Gershunov, A., & Dettinger, M. D. (2014). The key role of dry days in changing regional climate and precipitation regimes. *Scientific Reports*, *4*. https://doi.org/10.1038/srep04364

Polson, D., Hegerl, G. C., Zhang, X. B., & Osborn, T. J. (2013). Causes of Robust Seasonal Land Precipitation Changes. *Journal of Climate*, *26*(17), 6679-6697. https://doi.org/10.1175/Jcli-D-12-00474.1

Preisendorfer, R. W. (1988). *Principal component analysis in meteorology and oceanography* (C. D. Mobley, Ed.). Elsevier. http://www.elsevier.com/journals

Qu, T. D., Song, Y. T., & Maes, C. (2014). Sea surface salinity and barrier layer variability in the equatorial Pacific as seen from Aquarius and Argo. *Journal of Geophysical Research-Oceans*, *119*(1), 15-29. https://doi.org/10.1002/2013jc009375

Rahmstorf, S., & Ganopolski, A. (1999). Long-term global warming scenarios computed with an efficient coupled climate model. *Climatic Change*, *43*(2), 353-367. https://doi.org/10.1023/A:1005474526406

Ramos, A. M., Nieto, R., Tomé, R., Gimeno, L., Trigo, R. M., Liberato, M. L. R., & Lavers, D. A. (2016). Atmospheric rivers moisture sources from a Lagrangian perspective. *Earth System Dynamics*, *7*(2), 371-384. https://doi.org/10.5194/esd-7-371-2016

Reagan, J., Boyer, T., Antonov, J., & Zweng, M. (2014). Comparison analysis between Aquarius sea surface salinity and World Ocean Database in situ analyzed sea surface salinity. *Journal of Geophysical Research-Oceans*, *119*(11), 8122-8140. https://doi.org/10.1002/2014jc009961

Reagan, J., Boyer, T., Schmid, C., & Locarnini, R. (2016). Subsurface Salinity [subsection in 'State of the Climate in 2015']. *Bulletin of the American Meteorological Society*, *97*(8), S72-S74. https://doi.org/10.1175/2016BAMSStateoftheClimate.1

Reagan, J., Boyer, T., Schmid, C., & Locarnini, R. (2017). Subsurface Salinity [subsection in 'State of the Climate in 2016']. *Bulletin of the American Meteorological Society*, *98*(8), S72-S75. https://doi.org/10.1175/2017BAMSStateoftheClimate.1

Reagan, J., Boyer, T., Schmid, C., & Locarnini, R. (2018a). Subsurface Salinity [subsection in 'State of the Climate in 2017']. *Bulletin of the American Meteorological Society*, *99*(8), S77-S81. https://doi.org/10.1175/2018BAMSStateoftheClimate.1

Reagan, J., Boyer, T., Schmid, C., & Locarnini, R. (2019). Subsurface Salinity [subsection in 'State of the Climate in 2018']. *Bulletin of the American Meteorological Society*, *100*(9), S79-S81. https://doi.org/10.1175/2019BAMSStateoftheClimate.1

Reagan, J., Boyer, T., Schmid, C., & Locarnini, R. (2020). Subsurface Salinity [subsection in 'State of the Climate in 2019']. *Bulletin of the American Meteorological Society*, *101*(8), S144-S148. https://doi.org/10.1175/2020BAMSStateoftheClimate.1

Reagan, J., Boyer, T., Schmid, C., & Locarnini, R. (2021). Subsurface Salinity [subsection in 'State of the Climate in 2020']. *Bulletin of the American Meteorological Society*, *102*(8), S162-S164. https://doi.org/10.1175/2021BAMSStateoftheClimate.1

Reagan, J., Boyer, T., Schmid, C., & Locarnini, R. (2022). Subsurface Salinity [subsection in 'State of the Climate in 2021']. *Bulletin of the American Meteorological Society*, *103*(8), S160-S162. https://doi.org/10.1175/2022BAMSStateoftheClimate.1

Reagan, J., Boyer, T., Schmid, C., & Locarnini, R. (2023). Subsurface Salinity [subsection in 'State of the Climate in 2022']. *Bulletin of the American Meteorological Society*, *104*(9), S165-S167. https://doi.org/10.1175/2023BAMSStateoftheClimate.1

Reagan, J., Boyer, T., Schmid, C., & Locarnini, R. (2024a). Subsurface Salinity [subsection in 'State of the Climate in 2023']. *Bulletin of the American Meteorological Society*, *105*(8), S175-S177. https://doi.org/10.1175/2024BAMSStateoftheClimate.1

Reagan, J., Seidov, D., & Boyer, T. (2018b). Water Vapor Transfer and Near-Surface Salinity Contrasts in the North Atlantic Ocean. *Scientific Reports*, *8*. https://doi.org/10.1038/s41598-018-27052-6

Reagan, J., Seidov, D., Wang, Z., Dukhovskoy, D., Boyer, T. P., Locarnini, R. A., Baranova, O. K., Mishonov, A. V., Garcia, H. E., Bouchard, C., Cross, S. L., & Paver, C. R. (2024b). "World Ocean Atlas 2023, Volume 2: Salinity." NOAA Atlas NESDIS 90. https://doi.org/10.25923/70qt-9574

Ren, L., Hackert, E., Arkin, P., & Busalacchi, A. J. (2014). Estimating the global oceanic net freshwater flux from Argo and comparing it with satellite-based freshwater flux products. *Journal of Geophysical Research-Oceans*, *119*(11), 7869-7881. https://doi.org/10.1002/2013jc009620

Ren, L., Speer, K., & Chassignet, E. P. (2011). The mixed layer salinity budget and sea ice in the Southern Ocean. *Journal of Geophysical Research-Oceans*, *116*. https://doi.org/10.1029/2010jc006634

Reul, N., Grodsky, S. A., Arias, M., Boutin, J., Catany, R., Chapron, B., D'Amico, F., Dinnat, E., Donlon, C., Fore, A., Fournier, S., Guimbard, S., Hasson, A., Kolodziejczyk, N., Lagerloef, G., Lee, T., Le Vine, D. M., Lindstrom, E., Maes, C.,…Yueh, S. (2020). Sea surface salinity estimates from spaceborne L-band radiometers: An overview of the first decade of observation (2010–2019). *Remote Sensing of Environment*, *242*, 111769. https://doi.org/10.1016/j.rse.2020.111769

Reverdin, G., Kestenare, E., Frankignoul, C., & Delcroix, T. (2007). Surface salinity in the Atlantic Ocean (30°S-50°N). *Progress in Oceanography*, *73*(3-4), 311-340. https://doi.org/10.1016/j.pocean.2006.11.004

Reverdin, G., Morisset, S., Boutin, J., & Martin, N. (2012). Rain-induced variability of near sea-surface T and S from drifter data. *Journal of Geophysical Research-Oceans*, *117*. https://doi.org/10.1029/2011jc007549

Reverdin, G., Olivier, L., Cabanes, C., Boutin, J., Thouvenin-masson, C., Vergely, J. L., Kolodziejczyk, N., Thierry, V., Khvorostyanov, D., & Jouannod, J. (2024). Missing Argo

Float Profiles in Highly Stratified Waters of the Amazon River Plume. *Journal of Atmospheric and Oceanic Technology*, *41*(3), 221-233. https://doi.org/10.1175/Jtech-D-23-0072.1

Riser, S. C., Ren, L., & Wong, A. (2008). Salinity in Argo: A Modern View of a Changing Ocean. *Oceanography*, *21*(1), 56-67. https://doi.org/10.5670/oceanog.2008.67

Risien, C. M., & Chelton, D. B. (2008). A Global Climatology of Surface Wind and Wind Stress Fields from Eight Years of QuikSCAT Scatterometer Data. *Journal of Physical Oceanography*, *38*(11), 2379-2413. https://doi.org/10.1175/2008jpo3881.1

Robertson, F. R., Bosilovich, M. G., Roberts, J. B., Reichle, R. H., Adler, R., Ricciardulli, L., Berg, W., & Huffman, G. J. (2014). Consistency of Estimated Global Water Cycle Variations over the Satellite Era. *Journal of Climate*, *27*(16), 6135-6154. https://doi.org/10.1175/Jcli-D-13-00384.1

Roemmich, D., Johnson, G. C., Riser, S., Davis, R., Gilson, J., Owens, W. B., Garzoli, S. L., Schmid, C., & Ignaszewski, M. (2009). The Argo Program: Observing the Global Ocean with Profiling Floats. *Oceanography*, *22*. https://doi.org/10.5670/oceanog.2009.36

Schanze, J. J., Schmitt, R. W., & Yu, L. L. (2010). The global oceanic freshwater cycle: A state-of-the-art quantification. *Journal of Marine Research*, *68*(3-4), 569-595. https://doi.org/10.1357/002224010794657164

Schmitt, R. W. (1995). The Ocean Component of the Global Water Cycle. *Reviews of Geophysics*, *33*, 1395-1409. https://doi.org/10.1029/95rg00184

Schmitt, R. W. (2008). Salinity and the Global Water Cycle. *Oceanography*, *21*(1), 12-19. https://doi.org/10.5670/oceanog.2008.63

Schmittner, A., Silva, T. A. M., Fraedrich, K., Kirk, E., & Lunkeit, F. (2011). Effects of Mountains and Ice Sheets on Global Ocean Circulation. *Journal of Climate*, *24*(11), 2814-2829. https://doi.org/10.1175/2010jcli3982.1

Seager, R., & Naik, N. (2012). A Mechanisms-Based Approach to Detecting Recent Anthropogenic Hydroclimate Change. *Journal of Climate*, *25*(1), 236-261. https://doi.org/10.1175/Jcli-D-11-00056.1

Seager, R., Naik, N., & Vecchi, G. A. (2010). Thermodynamic and Dynamic Mechanisms for Large-Scale Changes in the Hydrological Cycle in Response to Global Warming. *Journal of Climate*, *23*(17), 4651-4668. https://doi.org/10.1175/2010jcli3655.1

Seidov, D., & Haupt, B. J. (2002). On the role of inter-basin surface salinity contrasts in global ocean circulation. *Geophysical Research Letters*, *29*(16). https://doi.org/10.1029/2002gl014813

Seidov, D., & Haupt, B. J. (2003). Freshwater teleconnections and ocean thermohaline circulation. *Geophysical Research Letters*, *30*(6). https://doi.org/10.1029/2002gl016564

Seidov, D., & Haupt, B. J. (2005). How to run a minimalist's global ocean conveyor. *Geophysical Research Letters*, *32*(7). https://doi.org/10.1029/2005gl022559

Seidov, D., Mishonov, A., Reagan, J., & Parsons, R. (2019). Resilience of the Gulf Stream path on decadal and longer timescales. *Scientific Reports*, *9*. https://doi.org/10.1038/s41598-019-48011-9

Shaw, T. A., Baldwin, M., Barnes, E. A., Caballero, R., Garfinkel, C. I., Hwang, Y. T., Li, C., O'Gorman, P. A., Rivière, G., Simpson, I. R., & Voigt, A. (2016). Storm track processes and the opposing influences of climate change. *Nature Geoscience*, *9*(9), 656-+. https://doi.org/10.1038/Ngeo2783

Shi, H. Y., Du, L., & Ni, X. B. (2024). Amplified vertical salinity contrasts in the northwestern tropical Pacific under ocean warming. *Climate Dynamics*, *62*(12), 10465-10481. https://doi.org/10.1007/s00382-024-07443-4

Singh, H. K. A., Donohoe, A., Bitz, C. M., Nusbaumer, J., & Noone, D. C. (2016). Greater aerial moisture transport distances with warming amplify interbasin salinity contrasts. *Geophysical Research Letters*, *43*(16), 8677-8684. https://doi.org/10.1002/2016gl069796

Skliris, N., Marsh, R., Josey, S. A., Good, S. A., Liu, C. L., & Allan, R. P. (2014). Salinity changes in the World Ocean since 1950 in relation to changing surface freshwater fluxes. *Climate Dynamics*, *43*(3-4), 709-736. https://doi.org/10.1007/s00382-014-2131-7

Skliris, N., Zika, J. D., Nurser, G., Josey, S. A., & Marsh, R. (2016). Global water cycle amplifying at less than the Clausius-Clapeyron rate. *Scientific Reports*, *6*. https://doi.org/10.1038/srep38752

Stendardo, I., Rhein, M., & Steinfeldt, R. (2020). The North Atlantic Current and its Volume and Freshwater Transports in the Subpolar North Atlantic, Time Period 1993-2016. *Journal of Geophysical Research-Oceans*, *125*(9). https://doi.org/10.1029/2020JC016065

Stommel, H. (1961). Thermohaline Convection with 2 Stable Regimes of Flow. *Tellus*, *13*(2), 224-230. https://doi.org/10.1111/j.2153-3490.1961.tb00079.x

Stouffer, R. J., Seidov, D., & Haupt, B. J. (2007). Climate response to external sources of freshwater: North Atlantic versus the Southern Ocean. *Journal of Climate*, *20*(3), 436-448. https://doi.org/10.1175/Jcli4015.1

Stouffer, R. J., Yin, J., Gregory, J. M., Dixon, K. W., Spelman, M. J., Hurlin, W., Weaver, A. J., Eby, M., Flato, G. M., Hasumi, H., Hu, A., Jungclaus, J. H., Kamenkovich, I. V., Levermann, A., Montoya, M., Murakami, S., Nawrath, S., Oka, A., Peltier, W. R.,…Weber, S. L. (2006). Investigating the causes of the response of the thermohaline circulation to past and future climate changes. *Journal of Climate*, *19*(8), 1365-1387. https://doi.org/10.1175/Jcli3689.1

Swift, C. T., & Mcintosh, R. E. (1983). Considerations for Microwave Remote-Sensing of Ocean-Surface Salinity. *Ieee Transactions on Geoscience and Remote Sensing*, *21*(4), 480-491. https://doi.org/10.1109/Tgrs.1983.350511

Tang, W. Q., Yueh, S. H., Fore, A. G., Hayashi, A., Lee, T., & Lagerloef, G. (2014). Uncertainty of Aquarius sea surface salinity retrieved under rainy conditions and its implication on the water cycle study. *Journal of Geophysical Research-Oceans*, *119*(8), 4821-4839. https://doi.org/10.1002/2014jc009834

Team, A. S. (1998). "On the design and Implementation of Argo— An initial plan for the global array of profiling floats." Int. CLIVAR Proj. Off. Rep. 21: 1-32.

Tebaldi, C., & Friedlingstein, P. (2013). Delayed detection of climate mitigation benefits due to climate inertia and variability. *Proceedings of the National Academy of Sciences of the United States of America*, *110*(43), 17229-17234. https://doi.org/10.1073/pnas.1300005110

Terray, L., Corre, L., Cravatte, S., Delcroix, T., Reverdin, G., & Ribes, A. (2012). Near-Surface Salinity as Nature's Rain Gauge to Detect Human Influence on the Tropical Water Cycle. *Journal of Climate*, *25*(3), 958-977. https://doi.org/10.1175/Jcli-D-10-05025.1

Trenberth, K. E. (2011). Changes in precipitation with climate change. *Climate Research*, *47*(1-2), 123-138. https://doi.org/10.3354/cr00953

Uppala, S. M., Kållberg, P. W., Simmons, A. J., Andrae, U., Bechtold, V. D., Fiorino, M., Gibson, J. K., Haseler, J., Hernandez, A., Kelly, G. A., Li, X., Onogi, K., Saarinen, S., Sokka, N., Allan, R. P., Andersson, E., Arpe, K., Balmaseda, M. A., Beljaars, A. C. M.,…Woollen, J. (2005). The ERA-40 re-analysis. *Quarterly Journal of the Royal Meteorological Society*, *131*(612), 2961-3012. https://doi.org/10.1256/qj.04.176

Vinogradova, N. T., & Ponte, R. M. (2013). Small-Scale Variability in Sea Surface Salinity and Implications for Satellite-Derived Measurements. *Journal of Atmospheric and Oceanic Technology*, *30*(11), 2689-2694. https://doi.org/10.1175/Jtech-D-13-00110.1

Vinogradova, N. T., & Ponte, R. M. (2017). In Search of Fingerprints of the Recent Intensification of the Ocean Water Cycle. *Journal of Climate*, *30*(14), 5513-5528. https://doi.org/10.1175/Jcli-D-16-0626.1

Wainwright, C. M., Black, E., & Allan, R. P. (2021). Future Changes in Wet and Dry Season Characteristics in CMIP5 and CMIP6 Simulations. *Journal of Hydrometeorology*, *22*(9), 2339-2357. https://doi.org/10.1175/Jhm-D-21-0017.1

Wei, X. Y., & Zhang, R. (2024). Weakening of the AMOC and strengthening of Labrador Sea deep convection in response to external freshwater forcing. *Nature Communications*, *15*(1). https://doi.org/10.1038/s41467-024-54756-3

Woods, J. D. (1985). The World Ocean Circulation Experiment. *Nature*, *314*(6011), 501-511. https://doi.org/10.1038/314501a0

Wüst, G. O. (1936). "Verdunstung und Niederschlag auf dem Weltmeere." Länderkundliche Forschung: 347-359.

Xie, P., Boyer, T., Bayler, E., Xue, Y., Byrne, D., Reagan, J., Locarnini, R., Sun, F., Joyce, R., & Kumar, A. (2014). An in situ-satellite blended analysis of global sea surface salinity. *Journal of Geophysical Research-Oceans*, *119*(9), 6140-6160. https://doi.org/10.1002/2014jc010046

Yu, L., Jin, X., & Weller, R. A. (2008). *Multidecade Global Flux Datasets from the Objectively Analyzed Air-sea Fluxes (OAFlux) Project: Latent and sensible heat fluxes, ocean evaporation, and related surface meteorological variables*. Woods Hole Oceanographic Institution.

Yu, L. S. (2011). A global relationship between the ocean water cycle and near-surface salinity. *Journal of Geophysical Research-Oceans*, *116*. https://doi.org/10.1029/2010jc006937

Yu, L. S., Jin, X. Z., Josey, S. A., Lee, T., Kumar, A., Wen, C. H., & Xue, Y. (2017). The Global Ocean Water Cycle in Atmospheric Reanalysis, Satellite, and Ocean Salinity. *Journal of Climate*, *30*(10), 3829-3852. https://doi.org/10.1175/Jcli-D-16-0479.1

Yueh, S. H., & Chaubell, J. (2012). Sea Surface Salinity and Wind Retrieval Using Combined Passive and Active L-Band Microwave Observations. *Ieee Transactions on Geoscience and Remote Sensing*, *50*(4), 1022-1032. https://doi.org/10.1109/Tgrs.2011.2165075

Zhang, X. B., Zwiers, F. W., Hegerl, G. C., Lambert, F. H., Gillett, N. P., Solomon, S., Stott, P. A., & Nozawa, T. (2007). Detection of human influence on twentieth-century precipitation trends. *Nature*, *448*(7152), 461-U464. https://doi.org/10.1038/nature06025

Zika, J. D., Skliris, N., Blaker, A. T., Marsh, R., Nurser, A. J. G., & Josey, S. A. (2018). Improved estimates of water cycle change from ocean salinity: the key role of ocean warming. *Environmental Research Letters*, *13*(7). https://doi.org/10.1088/1748-9326/aace42

Zinc, S., Boutin, J., Waldteufel, P., Vergely, J. L., Pellarin, T., & Lazure, P. (2007). Issues about retrieving sea surface salinity in coastal areas from SMOS data. *Ieee Transactions on Geoscience and Remote Sensing*, *45*(7), 2061-2072. https://doi.org/10.1109/Tgrs.2007.894934

Zweng, M. M., Reagan, J. R., Antonov, J. I., Locarnini, R. A., Mishonov, A. V., Boyer, T. P., Garcia, H. E., Baranova, O. K., Johnson, D. R., Seidov, D., & Biddle, M. M. (2013). "World Ocean Atlas 2013, Volume 2: Salinity." NOAA Atlas NESDIS 74: 1-39.